ASME
SETTING THE STANDARD

Transactions of the ASME, Journal of Fluids Engineering (ISSN 0098-2202) is published monthly by The American Society of Mechanical Engineers, Three Park Avenue, New York, NY 10016. Periodicals postage paid at New York, NY and additional mailing offices.
POSTMASTER: Send address changes to Transactions of the ASME, Journal of Fluids Engineering, c/o THE AMERICAN SOCIETY OF MECHANICAL ENGINEERS, 22 Law Drive, Box 2300, Fairfield, NJ 07007-2300.
CHANGES OF ADDRESS must be received at Society headquarters seven weeks before they are to be effective. Please send old label and new address.
STATEMENT from By-Laws. The Society shall not be responsible for statements or opinions advanced in papers or ... printed in its publications (B7.1, Par. 3).

Journal of Fluids Engineering

Published Monthly by ASME

VOLUME 130 • NUMBER 4 • APRIL 2008

RESEARCH PAPERS

Flows in Complex Systems

Fundamental Issues and Canonical Flows

Multiphase Flows

Techniques and Procedures

(Contents continued on inside back cover)

This journal is printed on acid-free paper, which exceeds the ANSI Z39.48-1992 specification for permanence of paper and library materials. ♾™
♻ 85% recycled content, including 10% post-consumer fibers.

Journal of Fluids Engineering Volume 130, Number 4 APRIL 2008

TECHNICAL BRIEFS

The ASME Journal of Fluids Engineering is abstracted and indexed in the following:

Applied Science & Technology Index, Chemical Abstracts, Chemical Engineering and Biotechnology Abstracts (Electronic equivalent of Process and Chemical Engineering), Civil Engineering Abstracts, Computer & Information Systems Abstracts, Corrosion Abstracts, Current Contents, Ei EncompassLit, Electronics & Communications Abstracts, Engineered Materials Abstracts, Engineering Index, Environmental Engineering Abstracts, Environmental Science and Pollution Management, Excerpta Medica, Fluidex, Index to Scientific Reviews, INSPEC, International Building Services Abstracts, Mechanical & Transportation Engineering Abstracts, Mechanical Engineering Abstracts, METADEX (The electronic equivalent of Metals Abstracts and Alloys Index), Petroleum Abstracts, Process and Chemical Engineering, Referativnyi Zhurnal, Science Citation Index, SciSearch (The electronic equivalent of Science Citation Index), Shock and Vibration Digest, Solid State and Superconductivity Abstracts, Theoretical Chemical Engineering

Turbulence and Secondary Flows in an Axial Flow Fan With Variable Pitch Blades

Jesús Manuel Fernández Oro
e-mail: jesusfo@uniovi.es

Rafael Ballesteros-Tajadura

Eduardo Blanco Marigorta

Katia María Argüelles Díaz

Carlos Santolaria Morros

Área de Mecánica de Fluidos,
Universidad de Oviedo,
Campus de Viesques,
33271 Gijón (Asturias), Spain

This paper analyzes the structure of turbulence and secondary flows at the exit of an axial flow fan with variable pitch blades. The influence of changing the blades' pitch angle over the turbulent structures is assessed by means of turbulence intensity values and integral length scales, obtained by using hot-wire anemometry for several test conditions. Since total unsteadiness is composed of both periodic and random unsteadiness, it is necessary to filter deterministic unsteadiness from the raw velocity traces in order to obtain turbulence data. Consequently, coherent flow structures were decoupled and thus, levels of turbulence—rms values of random fluctuations—were determined using a filtering procedure that removes all the contributions stemming from the rotational frequency, the blade passing frequency, and its harmonics. The results, shown in terms of phase-averaged distributions in the relative frame of reference, revealed valuable information about the transport of the turbulent structures in the unsteady, deterministic flow patterns. The anisotropic turbulence generated at the shear layers of the blade wakes was identified as a major mechanism of turbulence generation, and significant links between the blade pitch angle and the wake turbulent intensity were established. In addition, the autocorrelation analysis of random fluctuations was also used to estimate integral length scales—larger eddy sizes—of turbulence, providing useful data for computational fluid dynamics applications based on large eddy simulation algorithms. Finally, contours of radial vorticity and helicity gave a detailed picture of the vortical characteristics of the flow patterns, and the definition of secondary flow as the deviation of the streamwise component from the inviscid kinematics was introduced to determine the efficiency of the blade design in the energy exchange of the rotor. [DOI: 10.1115/1.2903523]

Introduction

The overall performance of axial turbomachinery is strongly influenced by the level of unsteadiness and turbulence generated inside the blade passages. In the case of axial compressors, much research effort has been focused on understanding the transitional flow over blade surfaces, because it is essential to describe the performance of the blades embedded in an axial stage (Henderson et al. [1]). Actually, it is well known that different mechanisms may lead to set off the transition from laminar to turbulent flow over the blades. Such mechanisms can be related to periodic disturbances, establishing a "wake-induced" transition when upstream wakes impinge on the blades, or simply induced by high freestream turbulence, initiating a "bypass" transition derived from instabilities in the external flow (Mailach et al. [2]). As far as this is concerned, it is important to segregate the relative influence of both mechanisms on the development of the unsteady boundary layers on the blades.

The flow field inside a turbomachine is highly complex and unsteady, and composed of all-range fluctuations of varying natures. Typically, the largest time scales are related to a fraction of the rotational speed, while the lowest time scales are those derived from the smallest dissipative eddies of the inner turbulence. Inherently, this implies that the total unsteadiness of any velocity trace can be segregated into a deterministic, nonchaotic component, usually known as "unsteadiness," and a pure random, stochastic element referred to as "turbulence." The identification of both components requires of a filtering (frequency domain) or an averaging (time domain) procedure, which must specify the time scale that separates periodic events from random disturbances (typically, the blade passing frequency—BPF).

The simplest method to remove periodic fluctuations consists of ensemble averaging the velocity traces and then subtracting their processed signals from the original data (Lakshminarayana [3]). This phase-locked sampling and ensemble-averaging technique is a well-established framework that enables us to reconstruct unsteady flow fields from instantaneous signals. Hence, many authors have employed this technique with success in the past two decades in the case of both centrifugal (Ubaldi et al. [4], Sinha et al. [5]) and axial turbomachinery ([1], Uzol et al. [6], Cherret et al. [7]). This exact definition gives valuable results, especially when interest is placed on the phase-averaged flow. Unfortunately, this technique is just filtering all the unsteadiness related to the BPF. Other "large-scale" unsteadiness with periodic features, such as vortex shedding, unsteadiness of separation points, misalignment of the blades, or fluttering of separated flows, is not removed by using this method. In practice, this is because there is no exact frontier separating the periodic unsteadiness of large-scale fluctuations from the large-scale eddies of random turbulence. Consequently, it is also necessary to include some other filtering procedure to remove definitively all the periodic unsteadiness from the raw data.

On the other hand, frequential methods, based on a discrete filtering of the instantaneous signals, allow a selective removal of time scales or even a complete elimination of certain ranges. Thus, some authors have defined a cutoff frequency to extract just "small-scale" fluctuations, although neglecting much of the turbulent energy of large-scale eddies (Goto [8] defined a high-pass filter of 1.5 times the BPF; Senkter et al. [9,10] employed a filter of 0.2 times the BPF). In order to avoid this inconvenience, an alternative solution is the identification of relevant peaks (at the rotational frequency, at the BPF and all higher harmonics) in the

Contributed by the Fluids Engineering Division of ASME for publication in the JOURNAL OF FLUIDS ENGINEERING. Manuscript received July 24, 2007; final manuscript received January 4, 2008; published online April 1, 2008. Assoc. Editor Chunill Hah.

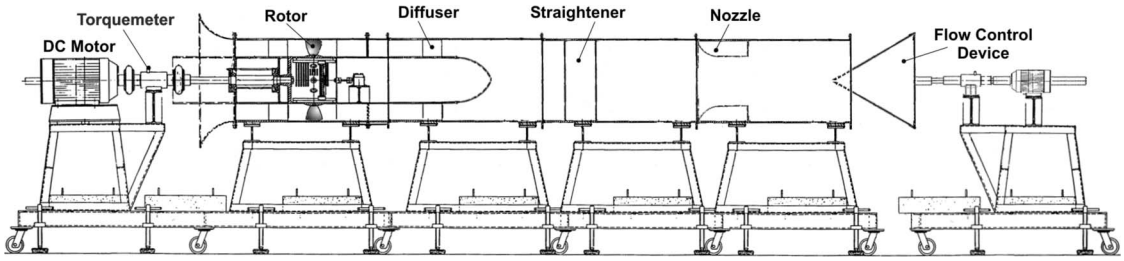

Fig. 1 Test facility

Fourier transform of the signal. Afterwards, these peaks, representing periodic events, are digitally filtered out by setting their amplitudes to zero. The truncated power spectrum is then transformed back into the time domain to give the turbulent signal (Camp et al. [11], Ballesteros et al. [12]).

In recent years, an increasing number of experimental investigations in axial turbomachinery have studied in detail the physical aspects of both turbulence and unsteady flow patterns. Since much of this investigation has been concerned with compressors and gas turbines, there are few relevant works in the literature regarding flow unsteadiness and turbulence in low-speed axial fans used for industrial purposes. Thus, a challenging task for the authors is to provide valuable results and analysis on these topics for this type of low-speed turbomachinery. Using a complete set of experimental data, encouraging results of the complexity of the flow structure at the exit of an axial fan with variable pitch blades (Ballesteros et al. [13]) led us to study in detail the characteristics of the total unsteadiness of the flow (Velarde-Suárez et al. [14]). Our recent experiments have led to the investigation of the structure of turbulence and unsteady flows in the case of single-staged fans (Fernández Oro et al. [15,16]), by analyzing the impact of the axial gap between the rows in the picture of turbulence. Now, we focus on the influence of variations of the blades' pitch angle in the generation and transport of turbulence and secondary flows.

In short, this paper presents an analysis of the structure of turbulence data, obtained using hot-wire anemometry, in a low-speed axial fan with variable pitch blades. Experimental measurements have been conducted modifying the pitch angle of the blades (up to four positions) for three different operating conditions. Velocity components have been obtained at ten radial positions by means of a triple-wire probe for every test. A digital filtering procedure in the frequency domain (adapted from Ref. [16]) has been employed to segregate random fluctuations from periodic disturbances downstream of the rotor. As a result, distributions and maps of turbulence intensity in the relative frame of reference are presented downstream of the rotor. The impact of both operating conditions and blade pitch angle on the transport and generation of turbulence has been characterized. Finally, the definition of secondary flows and the determination of helicity distributions have been appropiate to complete the description of the vortical features of the flow, mostly at off-design conditions.

Experimental Setup and Processing Techniques

Experimental Facility: Low-Speed Axial Fan With Variable Pitch Blades. The experimental measurements of the unsteady flow field were conducted on a low-speed axial fan with variable pitch blades. It is operated in an open-loop facility that includes a flow control device at the facility discharge to modify the operating conditions. A Venturi nozzle (constructed according to normative standard BS848) is embedded inside the duct to measure the volumetric flow rate, and a bell-mouth inlet is introduced to assure uniform inlet flow. Figure 1 shows a sketch of the experimental facility.

The fan analyzed is an eight-blade rotor based on the NACA-65 family and designed to provide a free vortex distribution of the absolute tangential velocity component. The rotor has a 600 mm tip diameter and a 380 mm hub diameter. The tip clearance is 2% of the blade height. Basic geometrical parameters of the blades are listed in Fig. 2. In this paper, the blade pitch angle refers to the blade setting (i.e., a fixed angular position of the blade) at the hub (see Fig. 2). The rotor allows for the manual changing of the blade pitch angle. The fan, rotating at 3000 rpm, is driven by a dc 36 kW motor.

The experimental data set is composed of 12 cases; specifically, four different blade pitch angles running at three different operating conditions (marked in Fig. 3 with the legend "Hot-Wire Measurements"). The blade pitches that were tested (with respect to the tangential direction) correspond to 52.5 deg (design geometry, denoted in the figures as "0°"), 43.5 deg and 48 deg (negative variations of −9 deg and −4.5 deg, respectively, denoted in the figures as "−9°" and "−4.5°"), and finally 57 deg (positive variation of +4.5 deg, denoted in the figures as "+4.5°"). The design geometry provides the highest efficiency—slightly higher than 80%—(see Fig. 3), while this regulation method guarantees an important increment of the operative range. The three operating

Radius (mm)	Solidity	Pitch (deg.)	Camber (deg.)	Thickness-to-chord ratio (%)
190	1.052	52.50	42.97	12.0
200	0.989	47.68	36.80	10.5
210	0.934	43.50	32.00	9.2
220	0.884	39.79	27.80	8.1
230	0.838	36.82	25.20	7.3
240	0.796	34.28	23.30	6.6
250	0.760	32.18	21.80	6.1
260	0.726	30.28	20.70	5.8
270	0.694	28.82	19.80	5.5
280	0.665	28.00	19.20	5.2
290	0.639	27.58	18.85	5.1
300	0.615	27.40	18.66	5.0

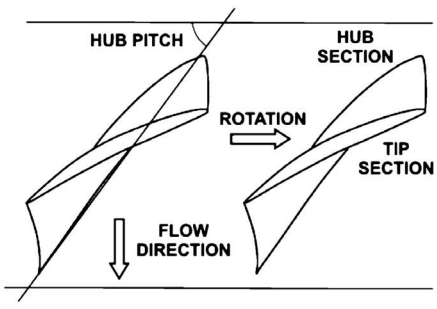

Fig. 2 Rotor blade characteristics (design)

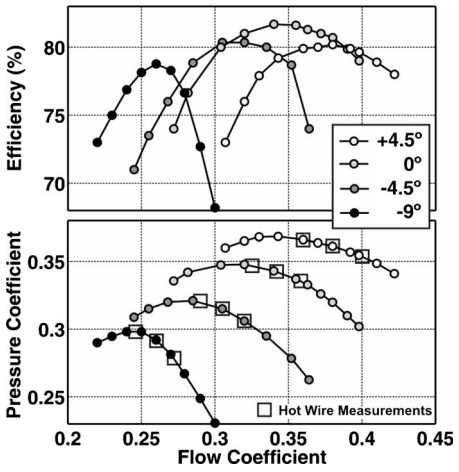

Fig. 3 Fan performance curves

points that were measured correspond to the best efficiency point (Q_o) of each pitch angle, and a lower and a higher flow rate, $0.95xQ_o$ and $1.05xQ_o$.

Measurement Techniques: Triple Hot-Wire Anemometry. The experimental data have been obtained using triple hot-wire anemometry. This technique gives a relatively high frequency response to velocity fluctuations, so flow disturbances at BPF (400 Hz) can be perfectly captured. The hot-wire probe is composed of three tungsten filament wires of 5 μm diameter and 1.5 mm length. The wires are orthogonal to each other forming a regular quadrant in space (Fig. 4). The inclination of the wires is 30 deg with respect to a plane normal to the prongs. Output signals of the wires are connected to a TSI IFA100 constant temperature anemometer, as represented in Fig. 4. The frequency response of the wires was estimated to be about 20 kHz. More details about the calibration setup and the uncertainty ranges of the probe can be found in Ref. [13].

The flow field measurements have been taken at inlet and outlet rotor planes, 120 mm upstream and 142 mm downstream of the blade axis. In both planes, ten radial positions were selected (Fig. 4) to acquire the velocity components and one pulse of a trigger signal per rotor revolution. This trigger enables a correct identification of every rotor phase when ensemble averaging in the post-processing. Therefore, accurate data sets can be rearranged from every velocity trace in order to phase average the instantaneous signals. To avoid aliasing of the signals, the data sampling rate was fixed at 12.8 kHz per channel, in order to obtain a good resolution of the jet-wake structure. The acquisition length for every realization was fixed at 2304 points per channel (i.e., nine complete rotor turns stored in every single measuring point).

Data Processing Techniques

Ensemble Averaging. The velocity traces have been processed in order to segregate periodic fluctuations from random unsteadiness. This may be expressed as

$$u(\mathbf{r},T) = \tilde{U}(\mathbf{r},t) + u'(\mathbf{r},T) \tag{1}$$

where the deterministic velocity is obtained by *ensemble averaging* (or phase averaging when observed in the relative frame of reference) the 72 blade passages recorded for every velocity trace:

$$\tilde{U}(\mathbf{r},t) = \frac{1}{M}\sum_{m=1}^{M} u(\mathbf{r},T)\big|_m, \quad T = t + \frac{2\pi}{\Omega B}(m-1) \tag{2}$$

The variable $\mathbf{r}$ represents the spatial coordinates and t defines each of the instantaneous realizations defined over the rotor blade passing period. B is the number of blades and T computes the total acquisition time. Bearing in mind that the temporal evolution in the absolute frame of reference is directly related to the circumferential gradients in the relative frame of reference (Lyman [17]), it is obvious that the ensemble-averaged velocity field observed by a stationary probe downstream of the rotor is the blade-to-blade distribution of the velocity components in the rotor passage. Hence, as long as there is no contribution of a previous stator or additional stages upstream of the rotor, velocity maps with a circumferential periodicity equal to the rotor pitch can be directly drawn.

FFT Filtering. In many cases, it may occur that the instantaneous velocity includes other "large-scale" unsteadiness that is periodic but not at the BPF. The existence of secondary flow patterns, such as sawing movement of the tip leakage vortex, fluttering of separated flows, or unstable separation points [8], implies that the ensemble-averaging technique does not remove all the periodicity components of the instantaneous velocity. As a result, the random component u' defined in Eq. (1) is not realistically describing pure turbulence, so an additional filtering method is needed to remove all the periodicity.

Figure 5 (left column) shows the power spectra of both periodic and random components of a velocity trace measured downstream of the rotor. The corresponding time evolutions of the velocity signals are also included in the figure over a complete rotor revolution (right column). All the representations have been made nondimensional by the time-mean velocity value. Complementarily, levels of unsteadiness and turbulence intensities are also defined (gray distributions referred to the right y axis) to provide an order of magnitude for the different variables. In the subplot Fig. 5(a), peaks corresponding to the BPF and its harmonics are clearly visible in the spectrum of the instantaneous velocity. Also, the contribution of periodic unsteadiness related to the machine's rotational frequency ($\Omega/2\pi$) is observable in the spectrum. Next, in subplot Fig. 5(b), the power spectrum of ensemble-averaged velocity shows a perfect periodic nature with the BPF. As a result,

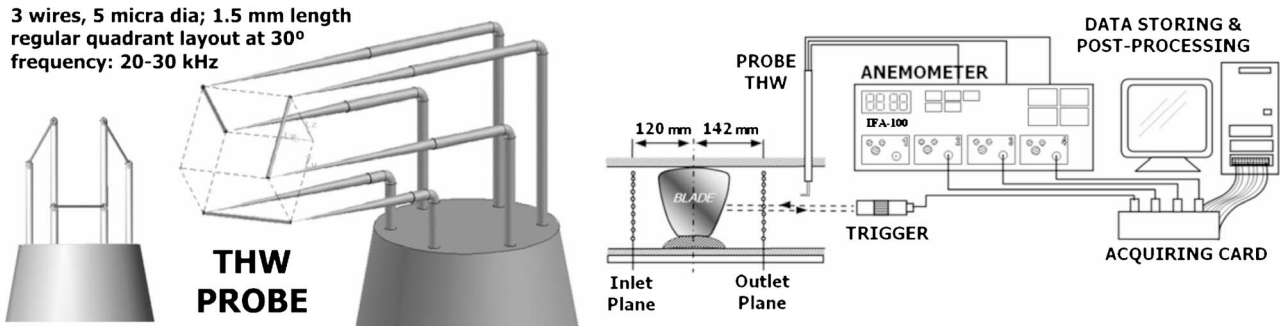

Fig. 4 Sketch of the triple hot-wire probe. Measurement chain.

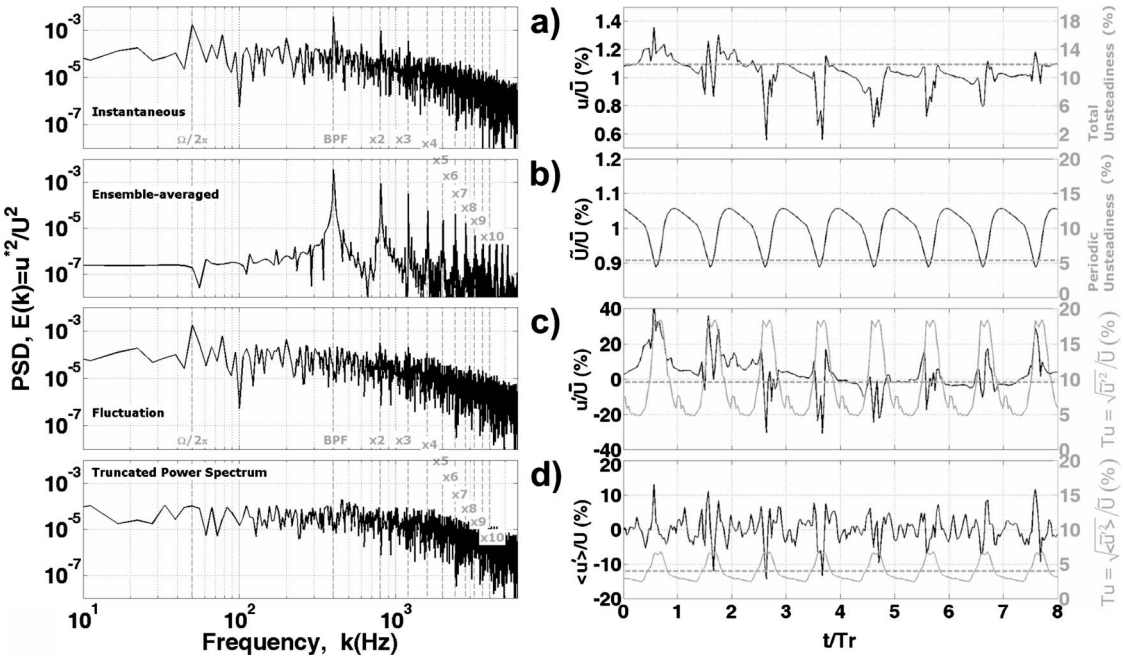

Fig. 5 Power spectra and time evolutions of different velocity components of an individual trace measured downstream of the rotor. u^* corresponds to (*a*) instantaneous, $u^*=u$; (*b*) ensemble averaged, $u^*=\tilde{U}$; (*c*) fluctuation, $u^*=u'$; and (*d*) filtered, $u^*=\langle u' \rangle$.

there is no contribution to large scales below 400 Hz, while higher harmonics appear to configure the particular shape of the blade-to-blade periodic velocity (right column of subplot (*b*)). Subtracting the ensemble-averaged velocity from the instantaneous signal, the pure fluctuation is expected to be obtained in subplot Fig. 5(*c*). Nevertheless, the power spectrum does not show the characteristic broadband distribution along the whole range of frequencies that should appear in the case of pure randomness. In particular, high-order periodicity is not totally removed by the ensemble-averaging technique. Thus, from the second harmonic on, there is still a certain reminiscence of periodic unsteadiness at BPF harmonics, though the fundamental peak of BPF has been filtered out by the procedure. Furthermore, even the rotational frequency periodicity is present in the fluctuation because the ensemble-averaging definition (2) cannot distinguish between rotor revolutions. This observation underlines that temporal averaging alone is not sufficient to eliminate all the periodicities. The power spectrum, $E(k)$, is the distribution of energy across the different eddy sizes, but every eddy size is really contributing across the full range of wave numbers (Davidson [18]). In addition, periodic disturbances are superimposed to that sea of all-range eddies in a similar fashion. Thus, the combination of both energy densities produces a high-complex structure with no exact frontier separating the periodic unsteadiness of large-scale fluctuations from the large-scale eddies of random turbulence. Moreover, the ensemble averaging considers that such a frontier can be established at the BPF wave number, and as a consequence, residual energy of large-scale fluctuations (or high-order periodicities) is masked as large-scale turbulence.

Consequently, these considerations suggest the need to introduce a frequential procedure to identify all the periodic events in the power spectrum and digitally filter them out by setting their amplitudes to zero. For that purpose, the methodology described in Refs. [11,12] has been adapted to the experimental data set of this particular axial fan. Using an iterative procedure, all the periodicity is removed from the instantaneous signal and a more realistic description of the turbulence is achieved. Hence, the subplot Fig. 5(*d*) shows the truncated power spectrum of the instantaneous velocity trace after FFT filtering. Notice that both fluctuation (Fig. 5(*c*)) and truncated spectra (Fig. 5(*d*)) contain the same small-scale, turbulent budget, despite being derived from different procedures (see the broadband component of both spectra). Thus, the usefulness of the truncated spectrum is shown because only chaotic randomness remains in the FFT signal, and all strong periodic events (marked with gray dashed lines in the plots) are completely filtered out. Finally, the truncated power spectrum is then transformed back into the time domain giving the turbulence signal (see right column of Fig. 5(*d*)).

To conclude the discussion, a few comments are now added here regarding the time evolution of the velocity components that illustrate the segregation process that leads to the description of pure turbulence. The subplot Fig. 5(*a*) shows the instantaneous velocity trace over a complete rotor revolution. The velocity deficit does not show an exact repeating pattern in every wake due to the strong degree of randomness within the velocity trace; besides, a level of total unsteadiness can be defined by computing the root mean square (rms) value of the wakes' total fluctuation. In this particular trace, it gives a reference level of approximately 12%, while inflow turbulence (shown later) is just around 1.5%. Introducing a statistical approach by means of ensemble averaging, all the velocity deficits are reduced to a single blade-to-blade deterministic fluctuation, which is shown in subplot Fig. 5(*b*) (replotted eight times). All the randomness has been filtered out, and total variations are therefore reduced. As a consequence, the level of unsteadiness of this statistical pattern is reduced approximately to roughly 6%. Afterwards, the temporal subtraction of previous traces to each other provides the quasirandom fluctuation in the right column of subplot Fig. 5(*c*). In order to analyze the circumferential structure of the turbulence from blade-to-blade in the relative frame of reference, the rms value of this fluctuation is divided by the deterministic flow. This definition is essential to reveal how turbulence is transported by the unsteady deterministic flow of the wakes, otherwise time averaged. Its mathematical expression is stated formally in the following epigraph—Eq. (3). The result shows a background level of turbulence between the wakes (centered on 5%) and large variations (up to 18%) only on the velocity deficits. This means that there is a sudden increase in the turbulence level in the wakes, whereas calm regions are estab-

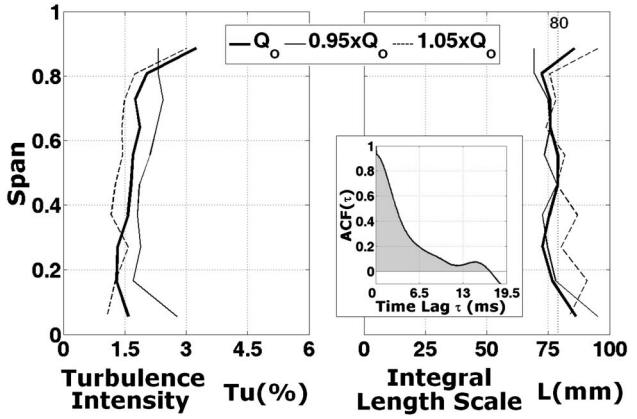

Fig. 6 Turbulence level and integral length scale of streamwise velocity of the inlet flow

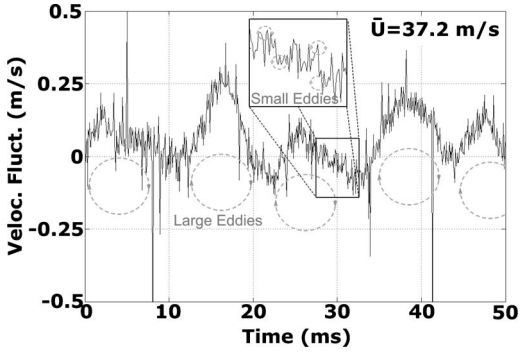

Fig. 7 Simplified sketch of the contribution of large and small eddies in the random fluctuations of the velocity traces for fully developed turbulence (adapted from Ref. [18])

lished between the wakes. As discussed earlier, these results are not completely accurate. In fact, they are overestimated because of the massive presence of residual large-scale periodicity in the shear layers of the wakes. On the contrary, the filtered fluctuation exhibits a more realistic random fluctuation, even in the calm regions between the wakes. Just 7% of random fluctuation is measured in the rotor wakes, and the background levels are also reduced to approximately 3%.

Description of Turbulence. Different variables can be used to describe the level and the spatial distribution of the turbulent flow. The *turbulence intensity* expresses the "strength" of the turbulent motion. It is defined as

$$\mathrm{Tu}(\mathbf{r},t) = \frac{\sqrt{\widetilde{u'^2}}}{\widetilde{U}} = \frac{1}{\widetilde{U}}\sqrt{\frac{1}{M}\sum_{m=1}^{M} u'^2|_m} \tag{3}$$

where the hat denotes the ensemble-averaging value of the random fluctuations to the square. In turbomachinery, the rms of the fluctuations is divided by the deterministic fluctuation, $\widetilde{U}$, in order to obtain the blade-to-blade turbulent field. As indicated above, this definition reveals the transport of the turbulent structures in the unsteady flow patterns. In the case of there being no deterministic fluctuations, the ensemble averaging would be replaced by a time averaging.

The *integral length scale* gives an idea of the spatial dimension of the largest eddy size of the turbulent structure. As described in Ref. [4] and Huyer et al. [19], if all the periodic events are removed from a velocity trace, then the autocorrelation function will show no oscillations, so the integral length scale L can be estimated by this expression:

$$L = \bar{U}\int_0^{\infty} \mathrm{ACF}(\tau)d\tau, \quad \mathrm{ACF}(\tau) = \frac{\overline{u'(t)\cdot u'(t+\tau)}}{\overline{u'^2}} \tag{4}$$

where the overbar denotes the time-averaged value, and τ is the time lag that is used to construct the ACF. This formulation supposes the validity of Taylor's hypothesis (the average eddy size lies through the correlation of two velocity signals). Obviously, the time lag depends directly on the data sampling rate, so an average eddy size of a wave number larger than the sampling rate cannot be measured.

Experimental Results and Discussion

Inflow Turbulence. Figure 6 shows the turbulence level and the integral length scale of the streamwise velocity along the radial coordinate at the inlet. Since the measuring plane (Fig. 4) is placed 120 mm upstream from the rotor, there are no periodic events involved in the velocity traces. As a consequence, both ensemble averaging and FFT filtering are not necessary in this case. The plot compares the three different operating points (higher efficiency, Q_o, and lower and higher flow rates, $0.95xQ_o$ and $1.05xQ_o$) for the design pitch angle (0 deg). There are no significant variations in the level of turbulence with the mass flow rate because Re is high enough (in the range of 6×10^5) to make turbulence statistically independent of low Re changes. As expected, the results show a clear spanwise uniformity, except for the casing viscous region where the levels are slightly increased. A typical value of 1.5% is obtained for the freestream region, which is totally representative for this type of open-loop facilities. Complementarily, the distribution of the integral length scale presents an appreciable radial disparity due to the inherent randomness of these fluctuations. However, for this Reynolds number range, the characteristic scale of larger eddies turned on to be in the order of 80 mm, with a noticeable spanwise uniformity. As expected, these larger eddies have velocity and length scales comparable to the global scales of the flow, because the integral value is a fraction of the duct diameter (approximately 13% of 600 mm). To illustrate this estimation, the figure includes the autocorrelation function of one radial point, needed to estimate the integral scale. To evaluate the area under the ACF, the first zero in the autocorrelation is usually taken as the upper limit of integration in Eq. (4) [11,20]. All these results are in clear agreement with previous predictions obtained by the authors in the case of single-staged axial fans: 1.5% of inlet turbulence and a 16% of the outer diameter as the typical integral length scale [16].

The idea of the integral length scale as a characteristic value of the larger eddies of the flow is revisited in Fig. 7. This figure shows a short fragment of the random fluctuations obtained from a particular velocity trace at the inlet. The amplitude of the fluctuations, about 0.5 m/s, represents 1.3% of the mean velocity (in agreement with the average turbulence level shown in Fig. 6). Notice that the temporal signals captured by the stationary probe are really showing the structure of the flow passing by. Thus, when a small eddy transported by the mean flow reaches the probe, it leaves an abrupt, sharp fingertip in the trace, since it takes a short time to pass through. On the contrary, the contribution of the largest eddies is more like a large, background fluctuation, because they take a long time to pass by. This is represented in the figure, where large eddies are identified by repetitive background oscillations. The integral length scale can be roughly estimated as the distance covered by these large eddies when transported by the mean flow at its averaged velocity, resulting in a value in the order of 0.1 m. This reasoning is totally coherent with the order of magnitude of the radial distribution in Fig. 6. Obviously, this one-dimensional description is quite a simplistic approach to the complex picture of turbulence, but it gives a very useful idea of the turbulent scales involved in the flow.

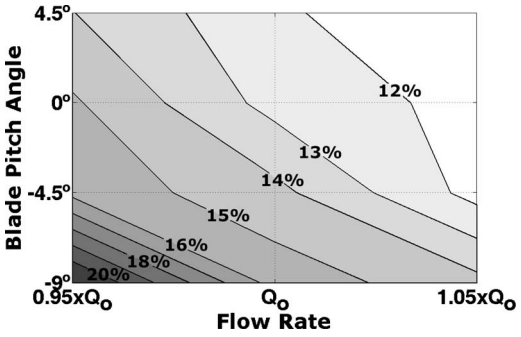

Fig. 8 Diagram of total unsteadiness rotor downstream. Influence of both blade pitch angle and operating conditions.

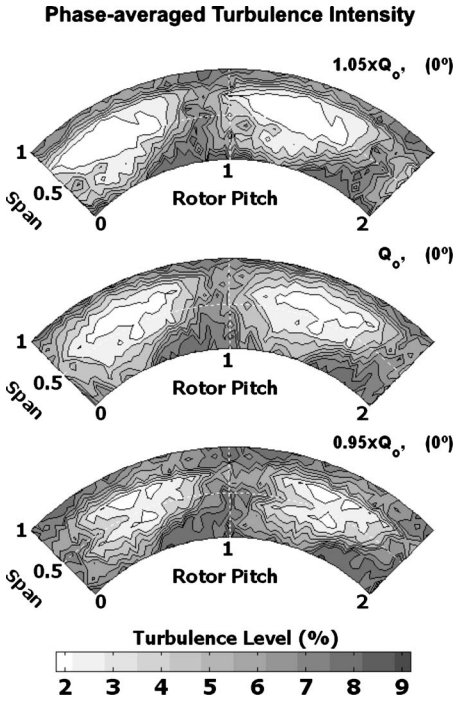

Fig. 9 Blade-to-blade distribution of turbulence intensity in the relative frame of reference. Influence of the operating conditions in the design geometry.

Unsteadiness and Turbulence at the Rotor Exit. The vortical nature of the shear layers confining the velocity deficit of the wakes is a major source of total unsteadiness. However, previous results published by the authors in Ref. [14] have demonstrated that higher levels of unsteadiness can be observed at the hub and casing regions, so small-scale turbulence inside the casing viscous regions also involves a relevant contribution. Moreover, the analysis of all the test cases revealed that these levels are even higher when running at off-design conditions and especially when pitch blade angles different from the nominal one are employed. Figure 8 is introduced at this point to summarize the influence of the pitch blade angle and the operating conditions in the level of total unsteadiness measured at midspan locations. In particular, this diagram presents the interpolated levels of total unsteadiness as a function of both parameters. Basically, these results show that the lower the blade pitch angle, the higher the levels of total unsteadiness. Also, reduced flow rates lead to major angles of incidence (less margin to prevent stall is available), and therefore, major flow separation may occur near the trailing edge resulting in a significant level of disorder at the rotor exit. Moreover, a reduction of the blade pitch angle produces a contraction in the crossed area of the passage, leading to more constricted flows and overall increase of volumetric oscillations and instabilities in the flow structures.

To observe the trends that the pure turbulence exhibits with both parameters, the FFT filtering procedure has been included in the postprocessing in order to guarantee an accurate decoupling method. Hence, some considerations of the turbulence structure downstream of the rotor are now illustrated (Fig. 9). Phase-averaged turbulence in the relative frame of reference is represented for different operating conditions in the case of the nominal angle of stagger. The whole spatial distribution (radial and tangential) is shown all along the rotor passage (replotted twice for convenience), viewed in downstream direction. As expected, all the maps present a core with low turbulence intensities (2%), limited by the rotor wakes (rotating counterclockwise in the fixed reference frame), and both hub and tip boundary layers with higher levels (up to 9%). It can be observed that if the flow rate decreases, the wakes get thicker, mainly in the tip region, following the same trend as the primary flow pattern [13]: For a same increment of the incidence angle, it implies a relative higher increase of the deflection at the tip, higher loads and major turbulent flow separation at the trailing edge (TE). Also, the overall levels are gradually increased, resulting in a higher level of disturbance. This fact fits in with previous results showing total unsteadiness in Ref. [14], indicating a higher disturbance level at high loads. Moreover, it is well known that this kind of major disturbances are derived from higher wake dispersion at low flow rates [1], so high velocity fluctuations are established and major generation of turbulence is confirmed.

More significant is the analysis of the influence of the blade pitch angle in the turbulent structures of the rotor (Fig. 10). Notice that Q_o differs for each blade pitch angle, corresponding to the best efficiency point of −9 deg to +4.5 deg, respectively. In this case, the spatial distribution of the turbulent structures is strongly influenced by the progressive reduction of the blade pitch angle. The low-turbulent core suffers a remarkable decrease as a consequence of a higher blockage derived from the enlargement of the tip boundary layer and the dispersion of the rotor wakes. These results are again in agreement with previous analyses of the flow patterns, suggesting a clear relation between the wake fluid and the generation of anisotropic turbulence at the wakes' shear layers. In other words, the distribution of the wake fluid is conditioning the shape and intensity of the blade-to-blade turbulent structures, establishing zones with low turbulence where freestream, high velocity regions are predominant, and high-turbulent structures where blockage mechanisms induce flow instabilities.

Assuming that all the periodic events have been filtered out in the postprocessing of the outlet measurements, an attempt was made to estimate the integral length scale of the turbulent flow. Initially, we would expect to observe an influence of both hub and casing boundary layers on the integral length scale. However, endwall effects are much smaller than the contribution coming from the periodic passing of rotor wakes, because of the spanwise uniformity of the results (Fig. 11). Also, all the radial distributions shown in the plot (either as a function of the operating conditions or modified by the pitch angle configuration) give a precise idea of the independence of the integral scale with respect to these parameters. As a consequence, it seems that the integral value is simply a characteristic of the flow scales (typically a fraction of the blade chord). On the other hand, the overall range of large-scale eddies is drastically reduced from the inlet, because of the continuous chopping mechanism of the rotor blades. Those large eddies (around 80 mm in Fig. 6) are broken up into smaller ones inside the rotor passages. In addition, the rotor wake fluid periodically crosses the measurement point and lowers the time-mean integral length scale [1], producing a typical value of 15 mm, which is in perfect agreement with previous estimations of the authors for this type of axial fans [16].

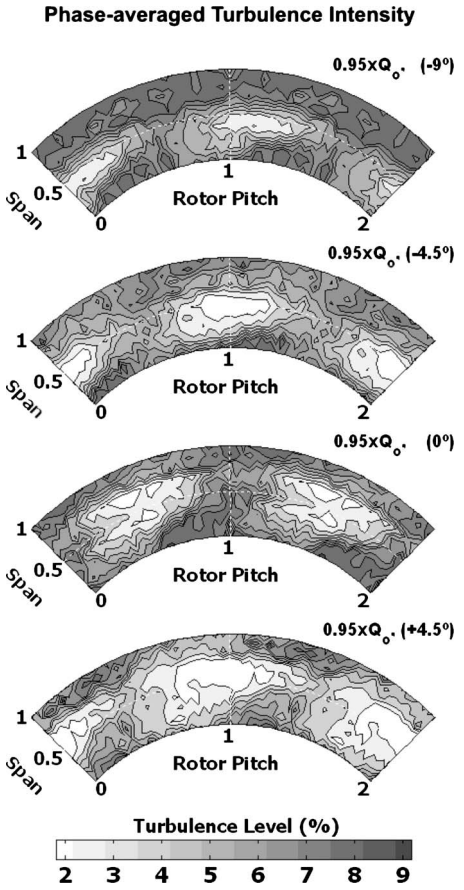

Fig. 10 Blade-to-blade distribution of turbulence intensity in the relative frame of reference. Influence of the blade pitch angle at off-design conditions.

Further considerations about the turbulent structure of the wakes' shear layers can be made by analyzing the vortical structure of the flow at the rotor exit. All turbulent flows are rotational and exhibit high levels of fluctuating vorticity concentrated in regions with strong coherence (e.g., in the wakes). For that purpose, distributions of radial vorticity have been obtained below in order to describe the vortical dynamics of the turbulent motion. Since the experiments provide all the velocity components in a traverse sector (in the relative flow, the circumferential nonuniformities are available), only in-plane radial and tangential derivatives can be computed to obtain the relative vorticity distributions. Therefore, all the streamwise variations of the velocity components are neglected in

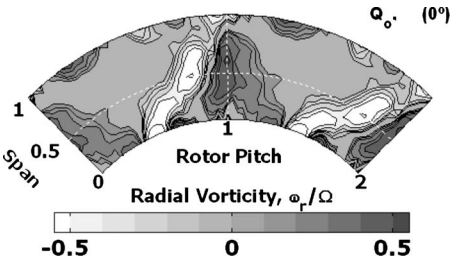

Fig. 12 Contours of radial vorticity at the rotor exit. Design conditions.

$$\frac{\omega_r}{|\Omega|} = \frac{1}{\Omega}\left(\frac{1}{r}\frac{\partial V_{ax}}{\partial \theta} - \frac{\partial V_\theta}{\partial z}\right) \tag{5}$$

Of course, this is an important restriction because out-of-plane (3D) effects may have an important impact on the distribution of radial vorticity. However, valuable information can be still obtained from the circumferential variation of the axial velocity. Hence, Fig. 12 shows the spatial distribution of radial vorticity—normalized by the rotational speed—in the relative flow for design conditions. The contribution of both hub and tip boundary layers is practically filtered out in this component, because their turbulent dynamics are mainly manifested in the tangential direction. Regions with positive and negative values indicate the presence of the wakes' shear layers. Positive levels are due to an increment of vorticity when moving tangentially (entering in the wake), while negative levels are a consequence of the change in the vorticity sign (leaving the wake). Considerable regions with no vorticity (gray zones in the map), especially from midspan to the outer half of the passage, reveal that the flow is behaving inviscidly there. Obviously, those regions are coincident with the low-turbulent core of the middle map in Fig. 9.

Figure 13 presents the influence of operating conditions and the blade pitch angle in the blade-to-blade distribution of radial vorticity at midspan. The inner and outer radial positions are more doubtful, since the flow is highly three dimensional there, so only an analysis of the midspan features has been attempted here. Results from the complete series of cases exhibit a common feature: the contribution of the rotor wakes is practically covering the whole rotor pitch. In fact, though large regions with inviscid characteristics appear in the outer half of the passage (i.e., Fig. 12), at midspan there is a considerable increment of the width of the wakes, which also gradually increases toward the hub (observed in previous maps of turbulent intensity). Therefore, low-turbulent

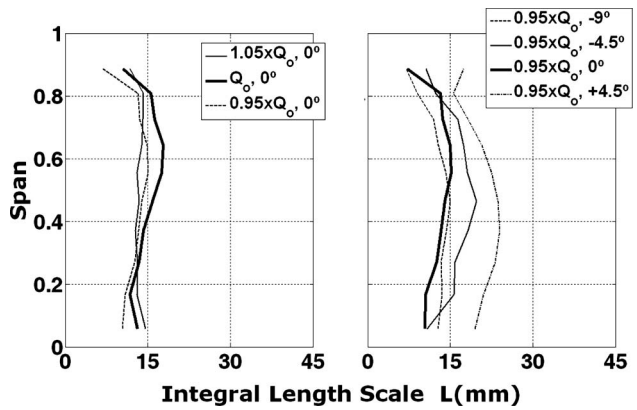

Fig. 11 Radial distribution of integral length scales at the rotor exit. Influence of operating conditions and blade pitch angle.

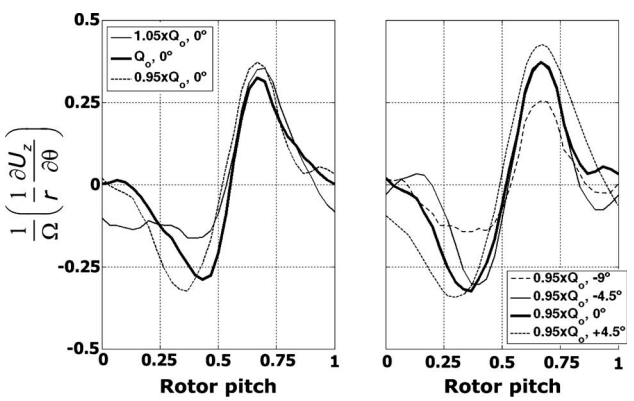

Fig. 13 Blade-to-blade distributions of radial vorticity at midspan. Influence of operating conditions and blade pitch angle.

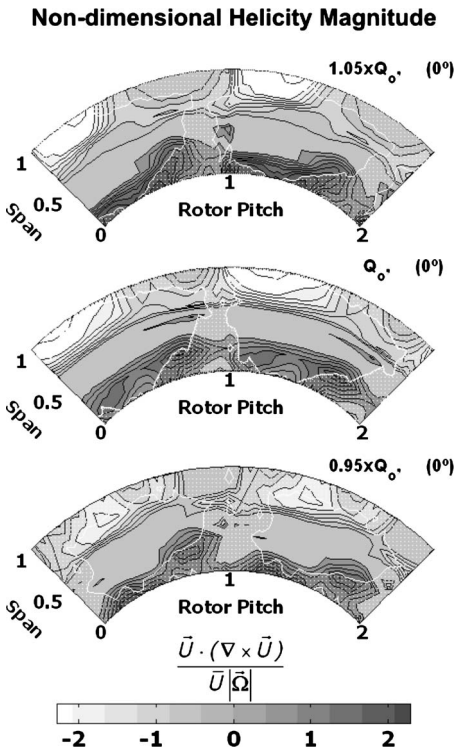

Fig. 14 Nondimensional helicity distributions at the rotor exit. Influence of operating conditions.

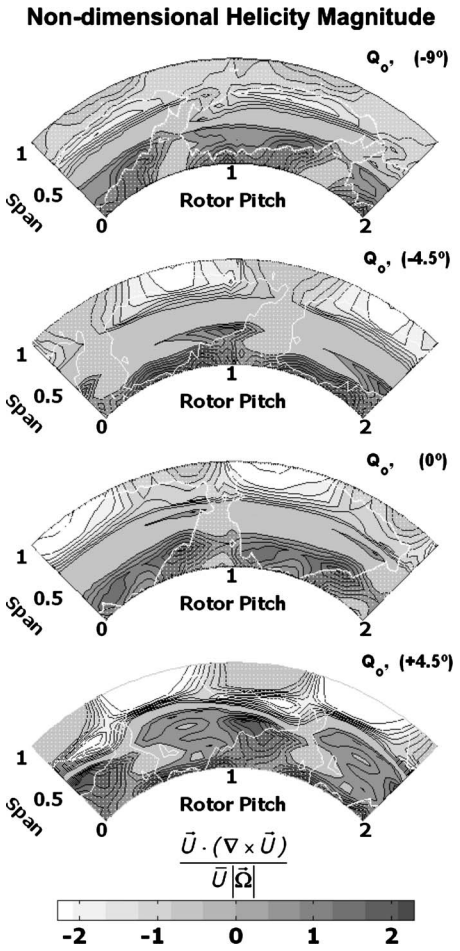

Fig. 15 Nondimensional helicity distributions at the rotor exit. Influence of blade pitch angle.

regions are established basically from midspan to 80% of the span, only partially shifted to central positions when blocked due to the large casing boundary layers at lower pitch angles (upper maps in Fig. 10). Meanwhile, radial vorticity at midspan is presented for all the test cases as an important source of turbulence associated with the unsteady shear layers of the wakes. Overall trends indicate that as the blade pitch angle is increased, the generation of radial vorticity is higher at midspan. The explanation lies in the progressive blockage of the tip boundary layer, which shifts the low turbulence core toward the midspan, as recently discussed. On the contrary, higher flow rates lead to lower radial vorticity, especially at the pressure side (PS) of the blades, as a direct consequence of the minor disorder of the flow structures downstream of the rotor.

Secondary Flows at the Rotor Exit. In the following section, we study in detail the structure of the relative flow to obtain information on the secondary flow patterns. For that purpose, helicity maps have been obtained and overlaid on to the shape of the rotor wakes in order to find a relationship between helicity distributions and the spatial evolution of the wakes.

Helicity is an instantaneous variable, which accounts for secondary flows, since it provides information on the vorticity aligned with the fluid stream. Hence, this magnitude is useful to describe flow fields with helical behavior. It is defined as the dot product of the vorticity and the velocity vectors, that is, $\mathbf{U}\cdot(\nabla\times\mathbf{U})$, and is usually made nondimensional by means of an average streamwise velocity and the rotational speed of the fan.

Figure 14 analyzes the influence of the operating conditions in the helicity distribution in the case of the design geometry. The rotor wakes are weft printed, so it is possible to track the evolution of the helicity patterns from both PS and suction side (SS) of the blades. In the proximity of the midspan, large regions with no helicity (colored in soft gray) demonstrate that there are no significant vortical structures (vortices) there for any of the three cases represented. At the hub, positive values indicate the generation of passage vortices associated with both sides of the blades, the one on the PS being more important. Meanwhile, the bulk of the wake fluid presents a notable lack of helicity. At the tip, a low-helicity region toward the SS is a clear indicator of the presence of leakage flow. Notice that there is a gradual shift of the center of the leakage flow toward the PS of the consecutive blade as the flow rate is decreased. This feature is in perfect agreement with previous results of Jang et al. [21] when studying the behavior of the tip leakage flow in the case of similar axial flow fans. Their results also revealed that a reduction in the flow rate leads to a major dispersion of the low-velocity region associated with the trough of the leakage vortex. As a consequence, the helicity core of the leakage flow presents a progressive tangential enlargement when operating at low flow-rate conditions, according to the figure. Complementarily, the helicity magnitude of the leakage flow core is also reduced in analogous fashion, indicating a clear influence of the boundary layer blockage on the tip vortex evolution: i.e., viscous effects of endwall boundary layer dominate, thereby decreasing the role of the leakage flow (Lakshminarayana [22]).

To illustrate the influence of the blade pitch angle on the establishment of the leakage flow, Fig. 15 shows the helicity maps at nominal conditions for different blade pitch angles. Basically, previous comments on Fig. 14 are also valid in this new context. In particular, notice that the regulation (decrease) of the flow rate by means of a lower pitch angle implies the same effects for the leakage flow as before. On the one hand, the core of low helicity is gradually shifted by the relative mean flow toward the PS of the consecutive blade. On the other hand, the enlargement of the casing boundary layer, which involves an important blockage of the flow, is causing a weakening of the leakage flow. This is espe-

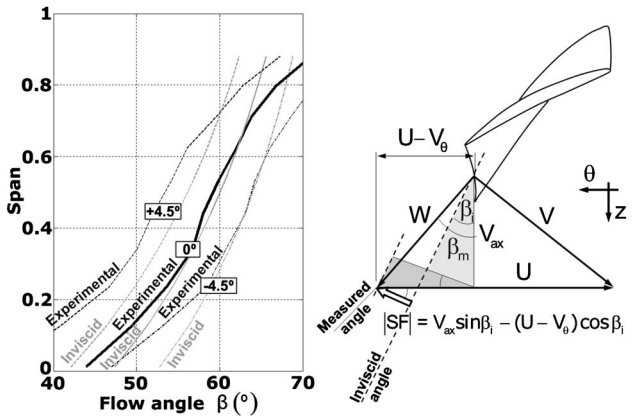

Fig. 16 Definition of SFs

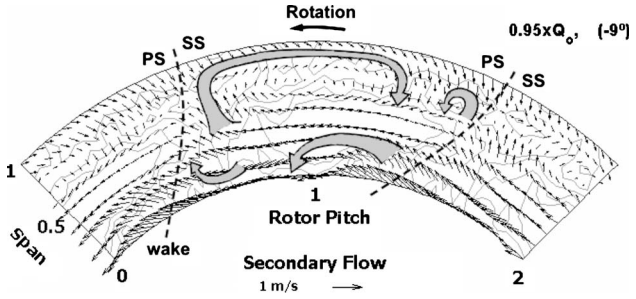

Fig. 17 Secondary velocity vectors

cially critical when operating at a pitch angle of −9 deg, because of the establishment of an extremely thick annulus wall boundary layer. As a result, the leakage flow is drastically stretched toward the midspan, contributing to a higher level of disorder and small-scale turbulence of the flow structure.

Finally, the development of secondary flows is presented using plots of secondary velocity vectors in the rotor passage. Many authors have proposed different methods to define it. Hawthorne [23] stated that a secondary flow arises when the flow exhibits a component of absolute vorticity in the direction of the relative streamline (i.e., the helicity). Other researchers have tried to split primary from secondary flows in spite of them being really interacting on each other. Bradshaw [24,25] considered that due to the viscous effects, endwalls divert primary flow, giving rise to an additional component called secondary flow. From this point of view, the secondary flows are defined as the departure of the local relative velocity vector from the local streamwise direction. However, in a geometrically complex channel, the streamwise direction can be defined in several different ways, and each definition will yield a slightly different result for the secondary flow (Hathaway et al. [26]).

In the present work, it has been assumed that the secondary flow vectors are those that represent departures from inviscid flow fields, according to Ref. [8]. Figure 16 illustrates the kinematic considerations that were followed to define the cross-flow component of the secondary flow (SF). Hence, the measured flow angle at the rotor exit (β_m) was compared spanwise to an inviscid flow angle (β_i)—plot in Fig. 16, showing the results at design conditions for several pitch angles. The inviscid angle was calculated from the total pressure increment of the rotor, assuming a free vortex flow pattern from hub to tip. The good agreement between the inviscid (design) parameters and the measured angle, mainly at central positions, seems to ratify this kinematic choice. Additionally, the radial equilibrium imposed on the blades' design should guarantee zero radial velocities for the inviscid flow. Therefore, the radial-flow component of the SF was directly identified with the radial velocity component measured in the tests.

Such a definition of the SF enables us to analyze the flow that is not participating in the energy conversion process as designed. For instance, at the tip, the flow is underturned—the measured angles in Fig. 16 are higher than the inviscid ones, so the flow is poorly deflected by the blades—which induces less tangential component of absolute velocity and provides less energy exchange. On the contrary, the flow in the hub section is overturned, leading to an excess of energy that must be dissipated somehow. Since the energy that is necessary to balance the input of shaft power is fulfilled, the rest turns into turbulence, enlarging the wakes and increasing the flow disorder, as shown previously in Fig. 10.

Figure 17 summarizes most of the SFs revealed in this investigation. To that end, a case with a low blade pitch angle running at off-design conditions has been used to point out the presence of significant vortices. The map, viewed in downstream direction as usual, includes curved arrows marking such vortices. A common feature is that the vectors of outer positions are pointing clockwise (towards the rotation), while vectors on inner radii are pointing counterclockwise. In fact, this is a direct consequence of the deviations of the measured angles from the streamwise direction. Indeed, the tangential component of the secondary vector, previously named as "cross-flow" component, is closely related to the deviation of the flow from inviscid mechanisms. Meanwhile, the radial component, directly adopted from the measurements, is more related to the real three dimensionality of the flow, mainly at endwall positions. To illustrate the flow migration induced by the SF structures, the turbulent wakes have been also introduced into the plots. As expected, the flow inside the wakes boundary layers is driven from the hub to the shroud [4,22]. In addition, the leakage flow is clearly recognizable as a huge loop—rotating clockwise—that covers practically all the outer half of the passage. The large extension of the vortex derives from the stretching mechanism set off by the enlargement of the casing boundary layer, as explained above. Other secondary vortices, like those located close to the PS at the tip and nearby the SS at the hub, are probably passage vortices derived from secondary vorticity, confined to the passage corners because of the higher strength of the other viscous structures.

Figure 18 evaluates the overall trends of SFs when modifying operating conditions or blade row parameters. At the design blade pitch angle, SFs are only important in the endwall regions as well as in the rotor wake fluid. Other operating conditions for the design geometry exhibit similar patterns (not shown here). This fact reveals a satisfactory well-structured flow with low levels of three dimensionality in large regions around the midspan (recall the good agreement of the flow angles at 0 deg in Fig. 16). However, when the blade pitch angle is changed, SFs are clearly activated. At a positive pitch angle of +4.5 deg, there is a noticeable disorder of the flow structures (mainly derived from the difference between the blade angles in Fig. 16), though this is not transferred to the turbulence intensity, that presented moderate levels in Fig. 10. Instead, spots of high helicity at midspan in the bottom map of Fig. 15 are matched with a core of secondary vectors pointing radially inwards on the PS. This effect is predominant in the flow structure, even reducing the impact of the leakage flow. Precisely, in consonance with the helicity maps of Fig. 15, the other vector plots (0 deg and −4.5 deg) confirm the tangential enlargement of the leakage flow when the blade pitch angle is reduced.

Conclusions

The analysis of the structure of turbulence and SFs in a low-speed axial fan with variable pitch blades has been carried out by means of an experimental investigation. Turbulent intensities and integral length scales in addition to helicity and secondary velocity vectors have been determined using a triple hot-wire probe in

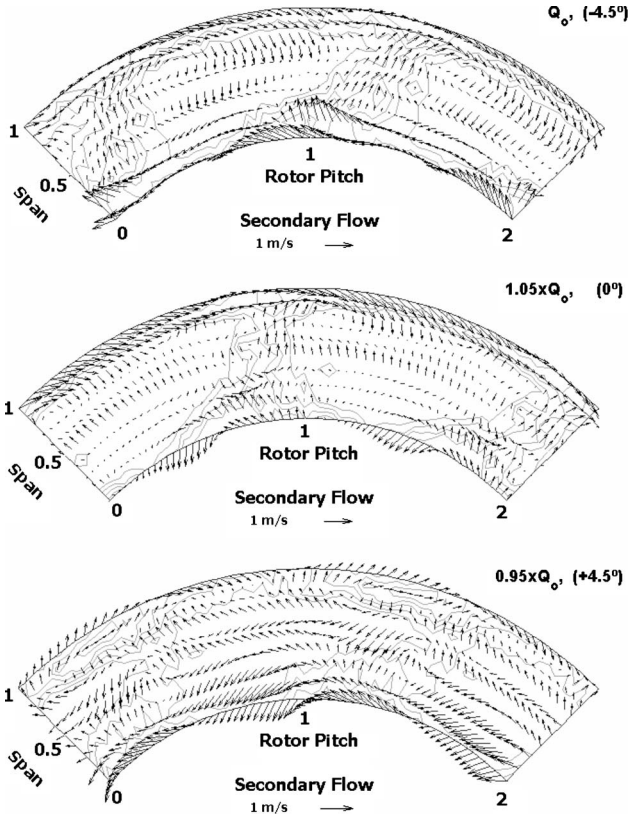

Fig. 18 SF patterns at off-design conditions

the measuring locations. In order to decouple periodic, unsteady flow from random turbulence, it was necessary to introduce a FFT filtering procedure to remove all the periodicity in the velocity traces. Additionally, ensemble averaging was used to highlight the transport of the turbulent structures by the unsteady jet-wake patterns. By studying the influence of other parameters, such as the variation of the operating point or the impact of the pitch angle in the turbulent structures, it was possible to obtain a detailed picture of the flow turbulence. Finally, the definition of SFs as the deviation from inviscid kinematics enabled us to investigate the efficiency of the blade design in the energy exchange of the rotor.

The results of turbulence intensities and integral length scales have shown good agreement with other results reported in the literature in the case of similar low-speed axial fans and compressors. The estimation of those length scales provides useful data to define good practices for both numerical discretization and turbulence modeling when developing CFD applications for axial flow fans.

At the rotor exit, the influence of different parameters has revealed the impact of the operating conditions on the levels of turbulence intensity. Thus, a reduction of the mass flow rate or a decrease of the blade pitch angle was found to set off higher disorder and important flow instabilities, thus increasing the global levels of turbulence. An excessive overturning of the primary flow at the hub has been characterized as a specific source of turbulence, which leads to thicker wake shear layers and major flow disorder. Moreover, as a direct consequence of the deviation of the primary flow from the design kinematics, the performance curves are also modified, resulting in more stepped curves with narrow high-efficiency regions. This implies that wide operating ranges can be obtained using variable pitch blades, but at the expense of poor overall performance and higher turbulence levels. In addition, the contribution of small-scale turbulence, derived from a significant thickening of the casing boundary layer, has played a major role when describing SF structures. In particular, we saw the strong influence of the blockage of the annulus wall boundary layer in both position and intensity of the leakage flow. Other typical structures related to SFs in the literature, such as passage vortices, have been also identified and described in the results.

In summary, traverse maps of the flow patterns in the relative frame of reference have illustrated the basic characteristics of all the turbulent phenomena involved in the rotor passages, describing the complexity of the unsteady transport of chaotic randomness and SF.

Acknowledgment

This work was supported by the Research Project "Characterization of the Generation of Aerodynamic Noise due to the Interaction between the Rotor Blades and the Guide Vanes in Axial Flow Fans," Ref. No. DPI2006-15720, CICYT.

Nomenclature

ACF = autocorrelation function
B = number of rotor blades
BPF = blade passing frequency, s^{-1}
E = spectrum of turbulent energy, m^2/s^2
FFT = fast Fourier transform
H = helicity, m/s^2
k = frequency or eddy wave number, s^{-1}
L = integral length scale, mm
LE = leading edge
m, M = number of stored rotor blades periods
Q, Q_o = flow rate and design flow rate, m^3/s
$\mathbf{r}$ = spatial position in cylindrical coordinates
r = radial coordinate, m
Re = reference Reynolds number
t = time, s
T = total acquisition time, s
T_r = rotor blade passing period, s
Tu = turbulence intensity, %
u = instantaneous velocity, m/s
u' = random velocity fluctuation, m/s
$\tilde{U}$ = deterministic velocity component, m/s
U = deterministic velocity fluctuation, m/s
$\bar{U}$ = mean velocity, m/s
z = axial coordinate, m

Greek Letters

β = relative flow angle, deg
θ = angular coordinate, rad
τ = time lag, s
Ω = rotational speed, rad/s

Superscripts and Subscripts

$\langle\ \rangle$ = FFT filtering
$\sim$ = ensemble averaging
$-$ = time averaging
i = inviscid
m = measured

References

[1] Henderson, A. D., Walker, G., and Hughes, J. D., 2006, "The Influence of Turbulence on Wake Dispersion and Blade Row Interaction in an Axial Compressor," ASME J. Turbomach., **152**, pp. 150–157.
[2] Mailach, R., and Vogeler, K., 2004, "Aerodynamic Blade Row Interactions in an Axial Compressor—Part I: Unsteady Boundary Layer Development," ASME J. Turbomach., **126**, pp. 35–44.
[3] Lakshminarayana, B., 1981, "Techniques for Aerodynamic and Turbulence Measurements in Turbomachinery Rotors," ASME J. Eng. Power, **103**, pp. 374–392.
[4] Ubaldi, M., Zunino, P., and Cattanei, A., 1993, "Relative Flow and Turbulence Measurements Downstream of a Backward Centrifugal Impeller," ASME J. Turbomach., **115**, pp. 543–551.
[5] Sinha, M., and Katz, J., 2000, "Quantitative Visualization of the Flow in a

Centrifugal Pump With Diffuser Vanes—I: On Flow Structures and Turbulence," ASME J. Fluids Eng., **122**, pp. 97–107.
[6] Uzol, O., Chow, Y.-C., Katz, J., and Meneveau, C., 2002, "Experimental Investigation of Unsteady Flow Field Within a Two-Stage Axial Turbomachine Using Particle Image Velocimetry," ASME J. Fluids Eng., **124**, pp. 542–552.
[7] Cherret, M. A., and Bryce, J. D., 1992, "Unsteady Visocus Flow in High-Speed Core Compressor," ASME J. Turbomach., **114**, pp. 287–294.
[8] Goto, A., 1992, "Three-Dimensional Flow and Mixing in an Axial Flow Compressor With Different Rotor Tip Clearances," ASME J. Turbomach., **114**, pp. 675–685.
[9] Senkter, A., and Riess, W., 1998, "Measurement of Unsteady Flow and Turbulence in a Low Speed Axial Compressor," Exp. Therm. Fluid Sci., **17**, pp. 124–131.
[10] Senkter, A., and Riess, W., 2000, "Experimental Investigation of Turbulent Wake-Blade Interaction in Axial Compressors," Int. J. Heat Fluid Flow, **21**, pp. 285–290.
[11] Camp, T. R., and Shin, H.-W., 1995, "Turbulence Intensity and Length Scale Measurements in Multistage Compressors," ASME J. Turbomach., **117**, pp. 38–46.
[12] Ballesteros, R., Velarde, S., and Santolaria, C., 2002, "Turbulence Intensity Measurements in a Forward-Curved Blades Centrifugal Fan," *Proceedings of the 21st IAHR Symposium on Hydraulic Machinery and Systems*, Lausanne.
[13] Ballesteros, R., Blanco, E., and Santolaria, C., 1995, "Blade Pitch Influence at the Exit Flow Field of an Axial Flow Fan," ASME Paper No. 95-GT-191.
[14] Velarde-Suárez, S., Ballesteros-Tajadura, R., Santolaria-Morros, C., and Blanco-Marigorta, E., 2002, "Total Unsteadiness Downstream of an Axial Flow Fan With Variable Pitch Blades," ASME J. Fluids Eng., **124**, pp. 280–283.
[15] Fernández Oro, J. M., Argüelles Díaz, K. M., Santolaria Morros, C., and Blanco Marigorta, E., 2007, "Unsteady Flow and Wake Transport in a Low-Speed Axial Fan With Inlet Guide Vanes," ASME J. Fluids Eng., **129**, pp. 1015–1029.
[16] Fernández Oro, J. M., Argüelles Díaz, K. M., Santolaria Morros, C., and Blanco Marigorta, E., 2007, "On the Structure of Turbulence in a Low-Speed Axial Fan With Inlet Guide Vanes," Exp. Therm. Fluid Sci., **32**(1), pp. 316–331.
[17] Lyman, F. A., 1993, "On the Conservation of Rothalpy in Turbomachines," ASME J. Turbomach., **115**, pp. 520–526.
[18] Davidson, P. A., 2004, *Turbulence: an Introduction for Scientists and Engineers*, Oxford University Press, New York.
[19] Huyer, S. A., and Snarski, S. R., 2003, "Analysis of a Turbulent Propeller Inflow," ASME J. Fluids Eng., **123**, pp. 533–542.
[20] Barrett, M. J., and Keith Hollingsworth, D., 2001, "On the Calculation of Length Scales for Turbulent Heat Transfer Correlation," ASME J. Heat Transfer, **123**, pp. 878–883.
[21] Jang, C. M., Sato, D., and Fukano, T., 2005, "Experimental Analysis on Tip Leakage and Wake Flow in an Axial Flow Fan According to Flow Rates," ASME J. Fluids Eng., **127**, pp. 322–329.
[22] Laksminarayana, B., 1996, *Fluid Dynamics and Heat Transfer of Turbomachinery*, Wiley, New York.
[23] Hawthorne, W. R., 1974, "Secondary Vorticity in Stratified Compressible Fluids in Rotating Systems," *CUED/A-Turbo/TR 63*, University of Cambridge.
[24] Bradshaw, P., 1987, "Turbulent Secondary Flows." Annu. Rev. Fluid Mech., **19**, pp. 53–74.
[25] Bradshaw, P., 1996, "Turbulence Modelling with Application to Turbomachinery," Prog. Aerosp. Sci., **32**, pp. 575–624.
[26] Hathaway, M. D., Chriss, R. M., Wood, J. R., and Strazisar, A. J., 1993, "Experimental and Computational Investigation of the NASA Low-Speed Centrifugal Compressor Flow Field," ASME J. Turbomach., **115**, pp. 527–542.

Vorticity Dynamics in Axial Compressor Flow Diagnosis and Design

Yantao Yang[1]
Hong Wu[2]
Qiushi Li[2]
Sheng Zhou[2]
Jiezhi Wu[1,3]
e-mail: jzwu@mech.pku.edu.cn

Institute of Engineering Research,
Peking University,
Beijing, 100871, P.R.C.

It is well recognized that vorticity and vortical structures appear inevitably in viscous compressor flows and have strong influence on the compressor performance. However, conventional analysis and design procedure cannot pinpoint the quantitative contribution of each individual vortical structure to the integrated performance of a compressor, such as the stagnation-pressure ratio and efficiency. We fill this gap by using the so-called derivative-moment transformation, which has been successfully applied to external aerodynamics. We show that the compressor performance is mainly controlled by the radial distribution of azimuthal vorticity, of which an optimization in the through-flow design stage leads to a simple Abel equation of the second kind. The satisfaction of the equation yields desired circulation distribution that optimizes the blade geometry. The advantage of this new procedure is demonstrated by numerical examples, including the posterior performance check by 3D Navier–Stokes simulation. [DOI: 10.1115/1.2903814]

1 Introduction

It has been well recognized that the vorticity and vortices have inevitable appearance in compressor flows. The vorticity is mainly generated due to the no-slip condition and forms boundary layers at the surfaces of hub and shroud, as well as the surface of the rotor and stator blades. It is also generated behind curved shock waves, near the tip of the rotor blade. The boundary layers may separate to form concentrated vortices at adverse pressure gradient, in particular, caused by their interaction with shock waves. The distribution and unsteady evolution of the vorticity field and vortical structures have strong influence on the compressor performance under both designed and off-design conditions. The advances of computational fluid dynamics (CFD) and experimental techniques have now made it possible for analysts and designers to qualitatively identify the effects of these structures on the compressor performance and relevant physical mechanisms, and then to take these effects into account as much as possible in modern design methods. However, in conventional analysis and design procedure, a critical physical link is still missing. The question is how to precisely pinpoint the quantitative contribution of each individual local flow structure and associated dynamic process to the compressor performance, which by nature is measured by integrated global quantities. Discovering this missing link is evidently of great significance for improving our ability in flow diagnosis, optimal configuration design, and flow control.

One of the possible methods to recover the missing link has now been developed and proved effective and widely applicable, which is systematically introduced in a book of Wu et al. [1]. The method is based on the so-called "derivative-moment transformation" (DMT), which is the extension of the integration by parts in elementary calculus,

$$\int_a^b f(x)dx = [xf(x)]|_a^b - \int_a^b xf'(x)dx \tag{1}$$

to two and three dimensions via the Gauss and Stokes theorems. Then a series of unconventional DMT-based expressions for various integrated aerodynamic performances can be derived. The special advantage of these expressions is that the new integrand explicitly contains the derivatives of flow quantities that can directly reflect local dynamic processes and structures (e.g., vortices and shocks) responsible for the integrated performances. The method has been extensively applied to innovative diagnosis of the total force and moment acting on an arbitrary body in external flows, and its application to internal flows has also been initiated (for reviews see Ref. [1] and Wu et al. [2]). This DMT method will also be the basis of the present investigation.

To briefly introduce the central idea of DMT-based theories and for later reference, we present two kinds of DMT formulas to be used for compressor flows. Formulas in component form will be expressed in terms of cylindrical coordinates (r, θ, z).

The first kind of formulas follows from a DMT identity for the integral of any function $f(r, \theta, z)$ over a cross-sectional plane S_0 at any axial location z_0, say. Let $R_1(z)$ and $R_2(z)$ be the radii of generators of the hub and shroud, respectively; the identity reads

$$\int_{S_0} frdrd\theta = \frac{1}{2}\left[\int_0^{2\pi} (fr^2)|_{R_1}^{R_2} d\theta - \int_{S_0} r^2 \frac{\partial f}{\partial r} drd\theta\right] \quad \text{at } z = z_0 \tag{2}$$

To gain a feeling of this formula, consider the mass flux Q of a viscous incompressible flow in a circular cylindrical pipe, as shown in Fig. 1. Assume for simplicity that the flow is axisymmetric and unidirectional, with velocity $u_z(r)$. Then setting $f = \rho u_z$ in Eq. (2) yields, on any cross-sectional plane S,

$$Q = \int_S \rho u_z dS = \frac{1}{2}\int_S r\rho\omega_\theta dS \tag{3}$$

where we used $\omega_\theta = -\partial u_z/\partial r$ and the no-slip condition on pipe wall. We see at once that the azimuthal vorticity ω_θ is a key quantity. To enhance the mass flux, the positive ω_θ should locate at as large r as possible, namely, be confined to the boundary layer (BL in Fig. 1) of the pipe. Then in the core region away from the BL, the flow will be uniform and irrotational. Note that this is

[1]Also at State Key Laboratory for Turbulence and Complex Systems, College of Engineering, Peking University, Beijing, 100871, China.
[2]Also at National Key Laboratory on Aero-engines School of Jet Propulsion, Beijing University of Aeronautics and Astronautics, Beijing, 100083, China.
[3]Also at The University of Tennessee Space Institute, Tullahoma, TN 37388.

Contributed by the Fluids Engineering Division of ASME for publication in the JOURNAL OF FLUIDS ENGINEERING. Manuscript received November 29, 2006; final manuscript received November 7, 2007; published online April 3, 2008. Assoc. Editor: Chunill Hah.

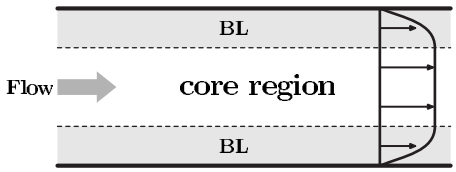

Fig. 1 The sketch of the pipe flow and the partition. The flow is along the *z*-axis and the vertical line denotes the cross plane *S*.

especially possible for averaged turbulent flows. Thus, we may write $S=S_{\mathrm{BL}}+S_{\mathrm{core}}$ and $Q=Q^{\dagger}_{\mathrm{BL}}+Q^{\dagger}_{\mathrm{core}}$, with

$$Q^{\dagger}_{\mathrm{BL}}=\frac{1}{2}\int_{S_{\mathrm{BL}}} r\rho\omega_{\theta}dS=Q, \quad Q^{\dagger}_{\mathrm{core}}=\frac{1}{2}\int_{S_{\mathrm{core}}} r\rho\omega_{\theta}dS=0 \tag{4}$$

Here, the dagger reminds that, like any DMT formulas, the integrand of $Q^{\dagger}$ is no longer the local mass flux. However, now $Q^{\dagger}_{\mathrm{BL}}$ shows that for viscous flow the local structure (vorticity moment in BL) alone can fully express the whole Q (in what follows the dagger in DMT-based formulas will be saved). Evidently, Eq. (3) can be easily extended to flow between two concentric circular cylinders, for which the negative ω_{θ} should locate at as small r as possible to enhance the flux; namely, it should be confined in the BL of the inner cylinder wall.

The second kind of DMT formulas are based on the concept of the boundary vorticity flux (BVF)

$$\boldsymbol{\sigma}\equiv\nu\mathbf{n}\cdot\nabla\boldsymbol{\omega}=\nu\frac{\partial\boldsymbol{\omega}}{\partial n} \tag{5}$$

where ν is the kinematic viscosity and $\mathbf{n}$ the unit normal vector pointing out of the fluid. The BVF measures the vorticity creation rate at solid surfaces, and hence controls the development of boundary layers. Its behavior also has close relation to flow separation [1] including that induced by a shock wave. On an accelerating body surface, applying the tangential components of the Navier–Stokes (NS) equation to the surface indicates that the BVF consists of the contributions of wall acceleration $\mathbf{a}$, on-wall tangent pressure gradient, and a three-dimensional viscous correction: $\boldsymbol{\sigma}=\boldsymbol{\sigma}_a+\boldsymbol{\sigma}_p+\boldsymbol{\sigma}_{\mathrm{vis}}$, with [1]

$$\boldsymbol{\sigma}_a=\mathbf{n}\times\mathbf{a}, \quad \boldsymbol{\sigma}_p=\frac{1}{\rho}\mathbf{n}\times\nabla p, \quad \boldsymbol{\sigma}_{\mathrm{vis}}=\nu(\mathbf{n}\times\nabla)\times\boldsymbol{\omega} \tag{6}$$

Then, according to a DMT identity for surface integrals, the total force and moment can be expressed by the first and second integrated moments of $\boldsymbol{\sigma}_p$ and $\boldsymbol{\sigma}_{\mathrm{vis}}$, respectively, where $\boldsymbol{\sigma}_{\mathrm{vis}}$ can be neglected at large Reynolds numbers for the design purpose. Consequently, the axial moment acting on a rotor blade surface S_b (which, multiplied by rotor's angular velocity Ω_z, represents the power input) has a DMT form given by (Eq. (11.101) of Ref. [1])

$$M_z=-\frac{1}{2}\int_{S_b}\rho r^2\sigma_{pz}dS+\frac{1}{2}\oint_{\partial S_b} pr^2dz \tag{7}$$

where ∂S_b is the closed boundary curve of the blade at its juncture with the hub. Because the BVF peaks are highly localized at very narrow areas of the blade surface and have easily identifiable favorable or adverse effect on M_z, one's attention in optimal blade design can be well focused to these local areas.

Li and Guo [3] were the first to apply DMT-based theories to diagnose axial compressor flows and thereby improve the rotor blade design (see the review of Ref. [1]). On the one hand, they specified f in Eq. (2) as the stagnation-pressure flux (to be defined below). Based on the data obtained by three-dimensional (3D) NS simulation, these authors examined the distribution of all terms of the transformed integrand on sectional planes at many z stations. Similar to Eq. (3), their numerical example showed that the distribution of azimuthal vorticity ω_{θ} dominates the performances. On the other hand, they applied Eq. (7) to analyze the effect of the σ_{pz} distribution over the rotor blade surfaces on the axial moment. With these two sets of local-dynamics information at hand, Li and Guo [3] were able to redesign the blade geometry of a low-pressure compressor to significantly enlarge its stall margin under small flow-rate condition.

Having the aforementioned preliminary progress on the application of DMT method in compressor flow, it is of great interest to further explore the following questions.

1. Does the dominance of ω_{θ} in compressor flows happen only in specific situations, or as a generic phenomenon? If the answer is the latter, what is the underlying physics?
2. After the most favorable ω_{θ} distribution on sectional planes is identified, can it be built into an optimal design procedure as a key constraint?
3. After the most favorable σ_{pz} distribution over the surfaces of blade, hub, and shroud is identified, can it also be built into an optimal design procedure as a key constraint?

In this paper, we give positive answers to the first two questions, leaving the third question to a separate companion paper [4]. The organization of the present paper is as follows.

First, we present a DMT-based theory (Sec. 2) to establish the explicit link between the compressor performance and the local dynamics. We then show that, given the kinetic energies associated with three velocity components, the distribution of azimuthal vorticity indeed dominates the compressor performances generically, though approximately.

Second, we focus on the core region of the compressor flow as sketched in Fig. 1, where the explicit viscous effect can be neglected. This is the region where the inviscid and axisymmetric through-flow design (TFD) procedure applies. We present a thorough vorticity-dynamics analysis of this TFD model flow in Sec. 3. For an assumed viscous-force model that can preserve the rothalpy [5], the optimal ω_{θ} distribution implies a new constraint to the TFD, of which the satisfaction determines the optimal blade geometry under the considered approximation.

Third, we demonstrate the advantage of this new TFD procedure by a numerical example (Sec. 4), including the TFD of the rotor blades and the posterior check of the performances by 3D Reynolds-averaged NS (RANS) simulation. Some brief concluding remarks are made in Sec. 5.

2 Compressor Performance and Local Flow Structures

2.1 Modified Performance Measure for Local-Dynamics Analysis. Throughout this paper, we consider steady viscous flow of calorically perfect gas in an axial compressor. In engineering community, the compressor performance is mainly measured by the increment of the stagnation temperature and pressure,

$$T^*=T\left(1+\frac{\gamma-1}{2}M^2\right), \quad P^*=p\left(1+\frac{\gamma-1}{2}M^2\right)^{\gamma/\gamma-1} \tag{8}$$

Specifically, let ρ be the fluid density, and S_i with $i=1,2$ be the cross planes at the inlet and exit of a compressor, respectively, with axis along the z direction. Then the mass flux is

$$Q=\int_{S_1}\rho u_z dS=\int_{S_2}\rho u_z dS \tag{9}$$

and the spatially averaged values of stagnation temperature $\overline{T^*}$ and stagnation pressure $\overline{P^*}$ are defined using the mass-flux averaged T^* and P^*, which may also be viewed as the T^*-weighted and P^*-weighted mass-flux integrals normalized by Q:

$$\overline{T^*}_i = \frac{1}{Q}\int_{S_i} \rho T^* u_z dS, \quad \overline{P^*}_i = \frac{1}{Q}\int_{S_i} \rho P^* u_z dS \tag{10}$$

With these mean quantities, one takes the stagnation-pressure ratio $\overline{P^*}_2/\overline{P^*}_1$ and the adiabatic efficiency

$$\eta = \frac{(\overline{P^*}_2/\overline{P^*}_1)^{\gamma-1/\gamma} - 1}{(\overline{T^*}_2/\overline{T^*}_1) - 1} \tag{11}$$

as the major measures of the compressor performance. The input rate of work ΩM_z is also an important measure, of which the optimization will be addressed in the companion paper [4].

Now, like external-flow problems, in order to reveal the dependence of the compressor performance on the local dynamics, we need to transform the integrand of Eq. (10) by proper DMT so that the new integrand can be reexpressed by local quantities naturally appearing in the differential equations of mass, momentum, and energy. To this end, it is convenient to replace mean stagnation quantities, such as $\overline{P^*}_i$ and $\overline{T^*}_i$, which do not appear in the viscous dynamic equations, by their close analogies which do, as our "modified" or "working" performance measures. In particular, instead of $\overline{P^*}$, we will consider the *stagnation-pressure flux* (SPF),

$$\mathrm{SPF} = \int_S P^* u_z dS \tag{12}$$

as a major modified performance. Here, P^* can be easily related to the static pressure p by the Taylor expansion of Eq. (8) for $\gamma = 1.4$, which converges for the local Mach number $M < 5$:

$$P^* = p + \frac{1}{2}\rho|\mathbf{u}|^2[1 + f(M)], \quad f(M) = \frac{M^2}{4} + \frac{M^4}{40} + \ldots \tag{13}$$

where $f(M) = O(M^2)$ is a compressibility correction factor. Unlike the sectional-plane integral of $\rho P^* u_z$, the integral of $P^* u_z$ except $f(M)$ can appear in the integrated kinetic-energy equation, to which the DMT can be effectively applied. Evidently, improving SPF at the exit can increase both $\overline{P_2^*}/\overline{P_1^*}$ (up to a factor of ρ) and the ratio of $\overline{P^*}$ to the reversible work on the fluid. Therefore, in what follows, we will focus exclusively on the SPF, but in the posterior check of the compressor performances, we will go back to the stagnation-pressure ratio $\overline{P_2^*}/\overline{P_1^*}$ and adiabatic efficiency defined by Eq. (11).

2.2 Local Flow Structure Influencing the Stagnation-Pressure Flux. Following Li and Guo [3], we now apply Eq. (2) to transform the integrand of Eq. (12). The result is more complicated than Eq. (3) since not only the flow is compressible with variable hub and shroud radii but also the integrand $P^* u_z$ is more involved than ρu_z. In addition to the appearance of ω_θ as in Eq. (3), there appears a $\partial P^*/\partial r$, which except $f(M)$ can be replaced by other terms in the radial component of the momentum equation. After some algebra (for details see [6]), Eq. (12) is cast to

$$\begin{aligned}\mathrm{SPF} = {} & \frac{1}{2}\int_S r^2(P^* + \rho u_z^2)\omega_\theta dr d\theta - \frac{1}{2}\int_S r^2 \rho u_\theta u_z \omega_z dr d\theta \\ & - \frac{1}{4}\int_S r^2 u_z |\mathbf{u}|^2 \frac{\partial \rho}{\partial r} dr d\theta - \frac{1}{2}\int_S r^2 \rho \Psi dr d\theta \\ & - \frac{1}{2}\int_S r^2 P^* \frac{\partial u_r}{\partial z} dr d\theta + I_{\mathrm{isen}}\end{aligned} \tag{14}$$

where Ψ collects all viscous terms and

$$I_{\mathrm{isen}} = -\frac{1}{4}\int_S u_z r^2 \frac{\partial}{\partial r}(\rho|\mathbf{u}|^2 f(M)) dr d\theta \tag{15}$$

is an integrated compressibility correction. Unlike Eq. (12), Eq. (14) explicitly reveals the local flow structures (represented by vorticity peaks) and dynamic processes influencing the SPF. It is from Eq. (14) that Li and Guo [3] found the dominance of $r^2\omega_\theta$ to the SPF from their specific numerical examples.

If the flow is steady and axisymmetric, the key mechanisms influencing the compressor performance can stand out more clearly and the asserted dominant role of ω_θ can be generally confirmed. In this case, Eq. (14) is simplified to (see Appendix A for derivation)

$$\begin{aligned}\mathrm{SPF} = {} & \pi\int_{R_1}^{R_2} r^2 E_2 \omega_\theta dr - \pi\int_{R_1}^{R_2} r^2 E_1 \frac{\partial u_r}{\partial z} dr - \frac{\pi}{2}\int_{R_1}^{R_2} r^2 u_z q^2 \frac{\partial \rho}{\partial r} dr \\ & - \pi\int_{R_1}^{R_2} r^2 \rho \Psi dr + I_{\mathrm{isen}}\end{aligned} \tag{16}$$

where

$$E_1(r,z) = P^* - \frac{1}{2}\rho u_\theta^2 > 0 \tag{17a}$$

$$E_2(r,z) = P^* + \frac{1}{2}\rho(2u_z^2 - u_\theta^2) = E_1 + \rho u_z^2 > E_1 \tag{17b}$$

$$q^2 = u_r^2 + u_z^2 \tag{17c}$$

In particular, in the neighborhood of the exit sectional plane S_2 of the compressor, the shroud and hub are parallel to the z axis. Thus, the flow is basically along that direction and one has

$$\left|\frac{\partial}{\partial r}\right| \gg \left|\frac{\partial}{\partial z}\right|, \quad |u_r| \ll |u_z|$$

Besides, the variation of the density, viscous effect, and the $f(M)$ term are relatively small. Therefore, it follows at once that generically the first term on the right-hand side of Eq. (16) is a major contributor to SPF:

$$(\mathrm{SPF})_{\mathrm{exit}} \simeq \pi\int_{R_1}^{R_2} r^2 E_2 \omega_\theta dr \tag{18}$$

This expression verifies that the numerical finding of the dominance of ω_θ in the compressor performances [3] indeed reflects a general phenomenon.

3 Vorticity Dynamics in Through-Flow Design

The TFD is an iterative procedure based on the inviscid, steady, and axisymmetric flow model. In this procedure, the effects of blades and entropy variation are mimicked by "blade body force" and "viscous body force," and the distribution of circulation (swirl) $\Gamma = ru_\theta$ and the entropy gradient are prescribed as the input of the TFD to start the numerical iterative solution of the Euler equation. The vorticity components on the meridian plane are related to Γ by the kinematic relation

$$\omega_r = -\frac{1}{r}\frac{\partial \Gamma}{\partial z}, \quad \omega_z = \frac{1}{r}\frac{\partial \Gamma}{\partial r} \tag{19}$$

which ensures the solenoidal feature of the vorticity. The inviscid nature of TFD makes it applicable to the core flow only, which is precisely the concern of this paper. Thus, our analysis in this section will be within the framework of TFD. The goal is to derive an analytical condition for the optimal Γ distribution which, through the aforementioned iteration, will in turn determine an optimal blade geometry (via the ratio u_θ/u_z) that can maximize the SPF and minimize the viscous loss of the compressor flow.

3.1 Optimal Distribution of ω_θ. We start from an important observation of Eq. (18). In this relation, we can write

$$E_2 = P^* - \frac{\rho}{2}\frac{\Gamma^2}{r^2} + \rho u_z^2 > 0$$

where $\Gamma^2/2r^2$ is to be optimized through the iteration procedure of TFD. Then, if the boundary layers of the shroud and hub remain fully attached, Eq. (3) indicates that the mass flux will be maximum, which will also maximize the axial kinetic energy $\rho u_z^2/2$. Thus, in Eq. (18), the maximum SPF and optimal E_2 may be simultaneously achieved, and the key here is to solely maximize $r^2\omega_\theta$ at each z station. As already seen in the context of Eqs. (3) and (4), this requirement is nothing but again the boundary layers on the shroud and hub be fully attached even though a compressor inevitably works under an adverse pressure gradient. According to the partition of the cross section S into BL region S_{BL} and core region S_{core}, one may impose an extremal condition

$$(r^2\omega_\theta)_{\mathrm{exit}} = \text{minimal over the core region} \tag{20}$$

as a projective function in a variational calculus. In order to ease our analysis to see more clearly the basic physics, here we follow Eq. (4) to impose a much simpler but *idealized* condition that may not be exactly achieved in real flow:

$$\omega_\theta = 0 \quad \text{over the core region} \tag{21}$$

which, under the approximation of Eq. (18), is equivalent to

$$(\mathrm{SPF})_{\mathrm{exit}} \simeq \frac{1}{2}\int_{S_{\mathrm{BL}}} rE_2\omega_\theta dS = (\mathrm{SPF}_{\mathrm{BL}})_{\mathrm{exit}}, \quad (\mathrm{SPF}_{\mathrm{core}})_{\mathrm{exit}} = 0 \tag{22}$$

Before we proceed, it is necessary to recall how ω_θ is generated and evolves in the flow field. In contrast to ω_r and ω_z, which are solely determined by the Γ distribution, ω_θ has two types of physical origins. First and in full generality, as has been pointed out in Sec. 1, for any viscous flow (including the limiting case with $\nu \to 0$), ω_θ is created at the shroud and hub surface via the azimuthal component of the BVF (5). Since a detailed analysis of the topics related to BVF and near-wall viscous flow is the subject of the companion paper [4], here we only stress that the boundary creation of ω_θ is inevitable, and one's task is to optimally manage the boundary layers under an adverse pressure gradient in compressor's working condition. Second, in the interior of the flow (the "core flow"), three mechanisms will produce ω_θ: the tilting of other vorticity components to the $\mathbf{e}_\theta$ direction, a nonconservative body force $\mathbf{F}$, and the baroclinicity caused by entropy gradient. These mechanisms are seen from the azimuthal component of the vorticity transport equation (see Ref. [1], Sec. 6.1):

$$\frac{D}{Dt}\left(\frac{\omega_\theta}{\rho r}\right) = \frac{1}{\rho r^4}\frac{\partial \Gamma^2}{\partial z} + \frac{1}{\rho r}(\nabla \times \mathbf{F})_\theta + \frac{1}{\rho r}(\nabla T \times \nabla s)_\theta \tag{23}$$

where $\mathbf{F}$ is an axisymmetric body force per unit mass, T is the temperature, and s is the specific entropy. In TFD, it is a common practice to set $\mathbf{F} = \mathbf{F}_B + \mathbf{F}_v$, which mimic the effect of the rotor blades that do work to the flow and the energy loss due to the viscosity, respectively (for more discussion see the next section). By Eq. (19), the first term on the right-hand side of Eq. (23) represents the mechanism of ω_r tilting toward the azimuthal direction. Note that, unlike the ω_θ in the shroud and hub boundary layers, in principle, the interior ω_θ creation can be well controlled to maximally reach the desired goal (20) or (21).

3.2 ω_θ-Γ Relation in Rothalpy-Preserving Flow. Because the TFD has a Γ-distribution as input, to achieve an optimal TFD that satisfies Eq. (20) or (21), a key issue is to find an explicit relation between the prescribed Γ distribution and its associated ω_θ field. We start from the Crocco equation with body force $\mathbf{F} = \mathbf{F}_B + \mathbf{F}_v$ as introduced in Eq. (23):

$$\boldsymbol{\omega} \times \mathbf{u} = -\nabla H + T\nabla s + \mathbf{F} \tag{24}$$

where

$$H = e + \frac{p}{\rho} + \frac{1}{2}|\mathbf{u}|^2 \tag{25}$$

is the total enthalpy with e being the internal energy. Here, the form of $\mathbf{F}$ and its splitting into $\mathbf{F}_B$ and $\mathbf{F}_v$ inevitably contain some arbitrariness. To be specific, we follow Damle [5] to set $\mathbf{F}_B$ and $\mathbf{F}_v$ normal and parallel, respectively, to the relative velocity $\mathbf{W} = \mathbf{u} - \Omega r\mathbf{e}_\theta$ viewed in the frame rotating with the rotor:

$$\mathbf{F}_B \cdot \mathbf{W} = 0, \quad \mathbf{F}_v = F_v\frac{\mathbf{W}}{|\mathbf{W}|} \tag{26}$$

Besides, in our design, we set $F_{Br} = 0$. Then, by using Eq. (19), the component form of Eq. (24) reads

$$u_z\omega_\theta = \frac{1}{2r^2}\frac{\partial(\Gamma^2)}{\partial r} - \frac{\partial H}{\partial r} + T\frac{\partial s}{\partial r} + F_r \tag{27a}$$

$$\mathbf{W} \cdot \nabla\Gamma = rF_\theta \tag{27b}$$

$$u_r\omega_\theta = -\frac{1}{2r^2}\frac{\partial(\Gamma^2)}{\partial z} + \frac{\partial H}{\partial z} - T\frac{\partial s}{\partial z} - F_z \tag{27c}$$

where use has been made of the fact that $\partial f/\partial\theta = 0$ for any f. On the other hand, by Eq. (26), the inner product of $\mathbf{u}$ and Eq. (24) gives

$$\mathbf{W} \cdot \nabla H = \Omega rF_\theta + \mathbf{W} \cdot (\mathbf{F}_v + T\nabla s)$$

Then by Eq. (27*b*), we obtain

$$\mathbf{W} \cdot \nabla(H - \Omega\Gamma) = \mathbf{W} \cdot (\mathbf{F}_v + T\nabla s) \tag{28}$$

Therefore, for inviscid and isentropic flow the well-known *rothalpy conservation* [7] follows at once:

$$H(r,z) - \Omega\Gamma(r,z) = H_0 \quad \text{alone relative streamlines} \tag{29}$$

where H_0 is the the total enthalpy of the incoming flow. The rate of work done by the rotor to the fluid, per unit mass, is represented by $\Omega\Gamma(r,z)$. For simplicity, we assume the that incoming flow is a uniform axial flow such that H_0 is constant. Since H_0 is uniform, before the trailing edge station z_{TE} of the rotor, Eq. (29) holds *in space* rather than only along the relative streamlines.

Now, note that Eq. (29) will still be saved for nonisentropic flow, provided that a balance is assumed between the mean viscous dissipation mimicked by $\mathbf{W} \cdot \mathbf{F}_v$ and entropy advection:

$$\mathbf{W} \cdot \mathbf{F}_v = -T\mathbf{W} \cdot \nabla s \tag{30}$$

Then combining Eq. (30) with Eqs. (24), (26), and (29), one obtains [5]

$$\mathbf{F}_v = -\frac{T(\mathbf{W} \cdot \nabla s)}{|\mathbf{W}|}\frac{\mathbf{W}}{|\mathbf{W}|} \tag{31}$$

A unique advantage of this rothalpy-preserving viscous-force model is that Eq. (29) permits an innovative ω_θ-Γ *relation*. Actually, by using the above results, whenever H_0 is uniform, *from either Eq. (27a) or (27c) and denoting* $A(r,z) \equiv \Gamma - \Omega r^2$, *one obtains*

$$\begin{aligned} r^2\omega_\theta &= \frac{1}{W_z}\left(A\frac{\partial\Gamma}{\partial r} + r^2T\frac{\partial s}{\partial r} + r^2F_{vr}\right) \\ &= \frac{1}{W_z}\left[A\frac{\partial\Gamma}{\partial r} + r^2T\frac{\partial s}{\partial r}\left(1 - \frac{W_r^2}{|\mathbf{W}|^2}\right) - r^2T\frac{\partial s}{\partial z}\frac{W_rW_z}{|\mathbf{W}|^2}\right] \end{aligned} \tag{32}$$

This equation establishes the exact relation between the (r,z) distributions of $r^2\omega_\theta$, Γ, and entropy gradient. While Eq. (23) describes a dynamic process by which the ω_r tilting generates ω_θ and in which $\partial\Gamma/\partial z$ is important, Eq. (32) implies that once the

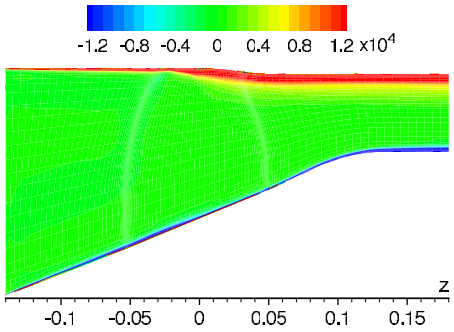

Fig. 2 A typical $\partial s/\partial r$ distribution on the meridian plane of the compressor, obtained by a 3D rotor-only RANS simulation.

flow is in a steady state the generated ω_θ will mainly depend on $\partial\Gamma/\partial r$ and u_z, which themselves depend on z.

3.3 Abel Equation of the Second Kind for Ideally Optimal Γ Distribution. The approximate DMT-based expression (18) for the the stagnation-pressure flux and the exact ω_θ-Γ relation (32) for the inviscid and axisymmetric model flow with rothalpy-preserving viscous force are the major theoretical results of the present paper. Indeed, the combination of Eq. (20) derived from Eqs. (18) and (32) leads at once to an innovative constraint for optimal blade design:

$$\frac{1}{W_z}\left(A\frac{\partial\Gamma}{\partial r}+r^2T\frac{\partial s}{\partial r}+r^2F_{vr}\right)=\text{minimal} \tag{33}$$

Or, ideally, Eq. (21) implies an equation relating the optimal distributions of Γ and ∇s:

$$A\frac{\partial\Gamma}{\partial r}=-r^2\left[T\frac{\partial s}{\partial r}\left(1-\frac{W_r^2}{|\mathbf{W}|^2}\right)-T\frac{\partial s}{\partial z}\frac{W_rW_z}{|\mathbf{W}|^2}\right] \tag{34}$$

This is a nonlinear first-order ordinary differential equation for $\Gamma(r)$ with z being a parameter. It belongs to the *Abel equation of the second kind*, having analytical solutions only if the source terms have certain special algebraic dependence on r.

Note that the derivation of Eq. (34) has used all components of the Crocco equation (24). Thus, it is not independent of any of these component equations nor the transport equation of ω_θ, Eq. (23). Consequently, the Abel equation (34) is the only constraint for determining the optimal $\Gamma(r,z)$. In other words, if H_0 is uniform, Eq. (34) is equivalent to the pair of Eqs. (27*a*) and (27*c*) with $\omega_\theta=0$, of which the vector form is

$$\frac{1}{2r^2}\nabla_\pi(\Gamma^2)=\nabla_\pi H-T\nabla_\pi s-\mathbf{F}_\pi \tag{35}$$

where subscript π refers to the components on the meridian (r,z) plane. While our test indicates that in numerical computation it is more convenient to use Eq. (35) as the constraint for optimal rotor blade design, the Abel equation (34) for $\Gamma(r;z)$ can provide good insight into the qualitative feature of this constraint and its solution behavior, which we discuss below.

First, the source terms on the right of Eq. (34) is solely from the entropy gradient, of which the component $\partial s/\partial r$ is normally dominating in a compressor. A typical contour plot of this component obtained by a 3D RANS simulation is shown in Fig. 2. We see that $\partial s/\partial r$ is significant only within the thin boundary layers of the hub and shroud, which is away from the core region, and behind the shock wave at the rotor cross sections, which is also quite localized. Therefore, it would be natural to further ignore the entropy gradient in the entire core region. Then by Eq. (34), there is either $A=0$ or $\partial\Gamma/\partial r=0$. The former implies that the fluid would corotate with the blade, so the added work by the rotor could merely produce radial and axial kinetic energies as well as change the pressure distribution. This is certainly not efficient, and only $\partial\Gamma/\partial r=0$ is the desired solution. Actually, assuming Γ be independent of r was precisely the basis of constant circulation or "irrotational" design used in the early development stage of TFD.

Under this simplified assumption, however, it is impossible to obtain a nontrivial constraint for optimal rotor blade. Indeed, if the r dependence of Γ is ignored for all r, then its z dependence would be deduced from nowhere, but our TFD practice showed that the z dependence of Γ dominates the blade performance (including the entropy-gradient distribution) and has to be found optimally. This trouble can also be seen by retaining ω_θ but ignoring $\partial\Gamma/\partial r$ in Eq. (32), yielding

$$W_z\omega_\theta=T\frac{\partial s}{\partial r}\left(1-\frac{W_r^2}{|\mathbf{W}|^2}\right)-T\frac{\partial s}{\partial z}\frac{W_rW_z}{|\mathbf{W}|^2}\quad\text{if }\Gamma=\Gamma(z) \tag{36}$$

so that the ω_θ and the entropy gradient must coexist locally. Therefore, if $\omega_\theta=0$ in the core region, Γ has to depend on both r and z to balance the entropy gradient. In fact, it is this (r,z) dependence of Γ that provides the chance to optimize the distribution of both Γ and entropy gradient. Note that although in compressor flows the radial velocity $|W_r|$ is normally much smaller than the magnitude of other two velocity components W_θ and W_z, and $|\partial s/\partial z|$ is much smaller than $|\partial s/\partial r|$, our numerical study indicates that at the blade tip the effect of $\partial s/\partial z$ is not negligible.

Second, as r varies, $A=\Gamma-\Omega r^2$ may change sign from positive to negative or vise versa. However, this can only happen in the region with zero entropy gradient, for otherwise Eq. (34) will be violated, implying the appearance of a singularity beyond which no solution can exist. An analysis on the possible appearance of this singularity and the domain range where $\omega_\theta=0$ is given in the Appendix B for various cases. It is precisely this singularity inside the core region, however, that implies a room for improving the blade performance. By the iterative TFD procedure to be described below, the singular point is pushed as much as possible to R_1 and R_2 to maximize the zero-ω_θ region. This must be associated with the weakening of the entropy-gradient peaks and/or narrowing of its range.

4 Application to Compressor Design: A Numerical Example

We now demonstrate the theoretical results developed in the preceding section by using the TFD procedure [8,9] to design a better rotor blade based on an old one. The performance of the new rotor blade is then tested by the 3D RANS simulation.

4.1 Numerical Simulation. We have shown in the preceding section that an optimal Γ-distribution should produce minimal ω_θ in the core region. We now apply this principle to the TFD simulation. For numerical convenience we use Eq. (35) as the constraint for optimizing $\Gamma(r,z)$, which is equivalent to Eq. (34) for constant H_0. On the right-hand side of Eq. (35), quantities such as H, T, and $\mathbf{F}$ are unknown before the flow field is solved. Thus, we employ an iterative procedure to achieve the optimal design. That is, every time after a TFD simulation is done, we use the flow quantities and Eq. (35) to solve a $\Gamma(r,z)$ distribution. With this new $\Gamma(r,z)$, another TFD simulation is conducted. This iteration is repeated until the procedure converges. The results represent an optimal design in the core flow region.

In each TFD simulation, the axisymmetric Euler equation is solved using the cell-centered finite-volume scheme with Runge–Kutta time stepping proposed by Jameson et al. [10], which is of second-order accuracy in space. Second and fourth difference artificial dissipations are added to prevent numerical oscillation. To accelerate convergence, local time step and residual smoothing are used. Both the inflow and outflow are subsonic in this study. The stagnation pressure, stagnation temperature, and two flow angles $\arctan(u_r/u_z)$ and $\arctan(u_\theta/u_z)$ are prescribed at the inflow boundary, and the static pressure is obtained using a first-order

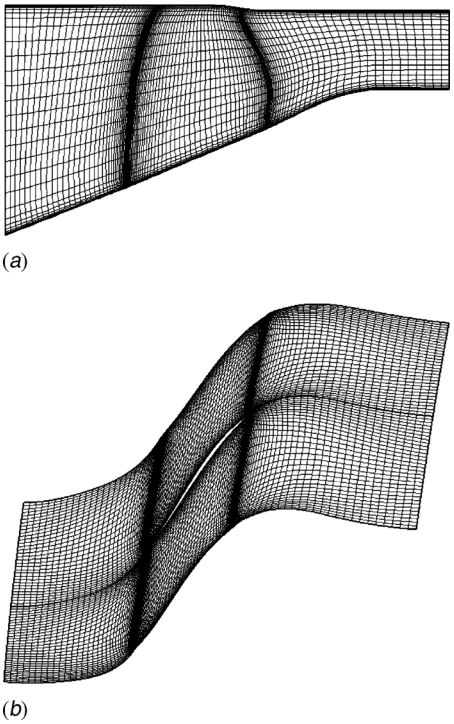

Fig. 3 3D computational mesh: (*a*) meridional plane mesh; (*b*) tip-section mesh

space-extrapolation technique. At the outlet boundary, only the static pressure is specified and the remaining four characteristic variables, such as density and velocity vector, are calculated using the aforementioned extrapolation technique. Besides, slip condition is imposed along the hub and shroud boundaries. Our TFD scheme has been validated by the 3D RANS simulation of a transonic fan stage. All these TFD and 3D RANS numerical results have previously been supported by our experiments, as reported in Ref. [11].

The performances of two rotors (without stators) before and after the optimal TFD are tested using 3D RANS simulations by the commercial software NUMECA on the same mesh shown in Fig. 3, with the one-equation S-A turbulence model. The dimension of the mesh is $65\times49\times129$ in circumferential, radial, and axial directions, respectively, and there are $65\times49\times65$ nodes in blade passage. The cell width of the grid near end wall and blade surface is set to ensure Y^+ (normal distance in wall unit) to be about 5.

4.2 Optimization of Γ and Performances. In Fig. 4(*a*), we plot the initial Γ distribution in our axisymmetric TFD, which linearly varies in both radial and axial directions. The optimized Γ contour is shown in Fig. 4(*b*). Here after, we shall refer the initial and optimized designs to Designs A and B, respectively. One can see that near the hub between the rotor and stator, the circulation increases after the optimization. At the middle of the channel, the radial variation of Γ becomes weaker, which is consistent with our theoretical analysis. A similar behavior change can be found in the 3D RANS simulation, as shown in Fig. 5, though the (r,z) dependence of Γ is no longer linear even for the Design A. The configuration of the blades are compared in Fig. 6 at two cross sections.

The performance curves of two rotors computed by 3D RANS are plotted in Fig. 7. Both the peak stagnation-pressure ratio and efficiency of Design B are improved compared to Design A, and Rotor B has a larger choke mass than A.

4.3 Azimuthal Vorticity and SPF. The following comparisons of SPF and azimuthal vorticity are to be made at the peak efficiency points.

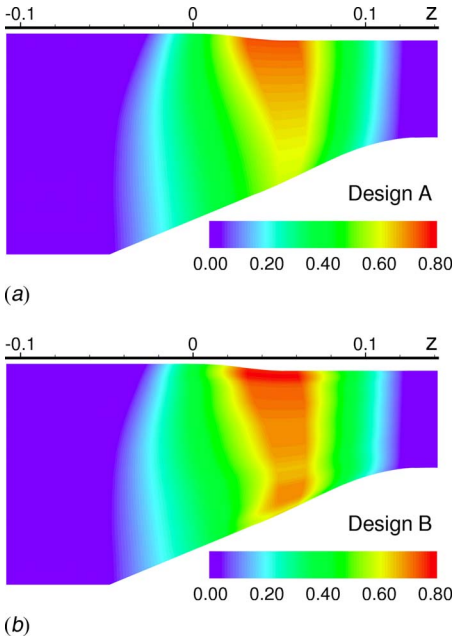

Fig. 4 Γ-distributions in TFD procedure. Nondimensionalized by $r_{tip}\sqrt{RT}$. (*a*) Initial Γ distribution; (*b*) optimal Γ distribution.

We have claimed that for an optimal Γ distribution, there should be less ω_θ in the core region, and the ω_θ peaks should be kept close to the hub and shroud surfaces. Figure 8 compares the ω_θ distributions obtained by 3D RANS for the two designs. One can see that Design B has thinner boundary layer than A, attaching more strongly to the shroud. The core region is thereby expanded. These are what we wished in the optimized TFD.

A careful examination of the shroud boundary layers before and after optimal design may illustrate how their thinning makes them attached more strongly to the wall. The zoom-in plot of Fig. 8(*a*) indicates that in Design A there is a thin recirculation layer with $\omega_\theta<0$ underneath the shroud boundary layer, unfavorable for the latter to keep fully attached. This layer extends about five meshes in wall-normal direction and is probably caused by the rotor tips. For Design B, the recirculation layer shrinks to within one layer mesh, and is much shorter in axial direction.

The approximate nature of TFD implies that in 3D RANS simulation, one cannot really find a core region with $\omega_\theta=0$ exactly. Figure 8(*b*) shows that some new ω_θ is produced in the middle channel of Design B, for example, the $\omega_\theta>0$ near the hub at z

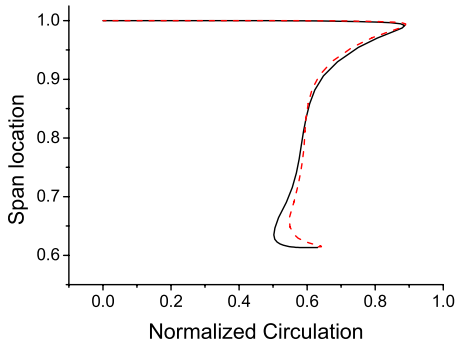

Fig. 5 Comparison of the radial distributions of Γ at the rotors' trailing edges of 3D simulations. The ordinates are nondimensionalized by $r_{tip}\sqrt{RT}$, and the height of rotor blade. Solid lines, Design A; dashed lines: Design B.

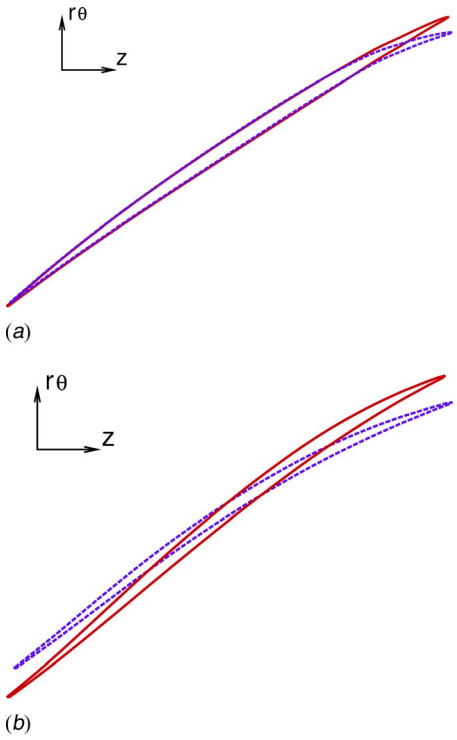

Fig. 6 Comparison of the configuration of two rotors, with the flow coming from lower left corner. Red solid, Design A; blue dashed, Design B. (*a*) 9% blade-height sections; (*b*) tip sections.

$\simeq 0.04$. However, in the vorticity magnitude there is several order smaller than that in boundary layers, having very minor effect on

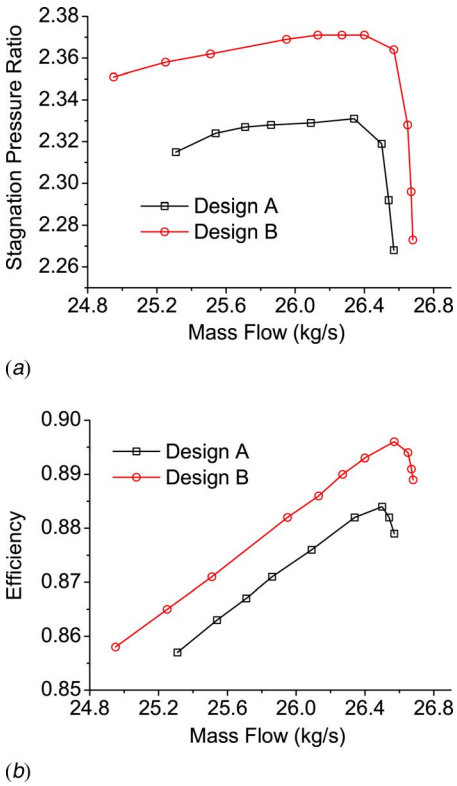

Fig. 7 Comparison of the performance curves of two rotors: (*a*) Stagnation-pressure ratio; (*b*) efficiency

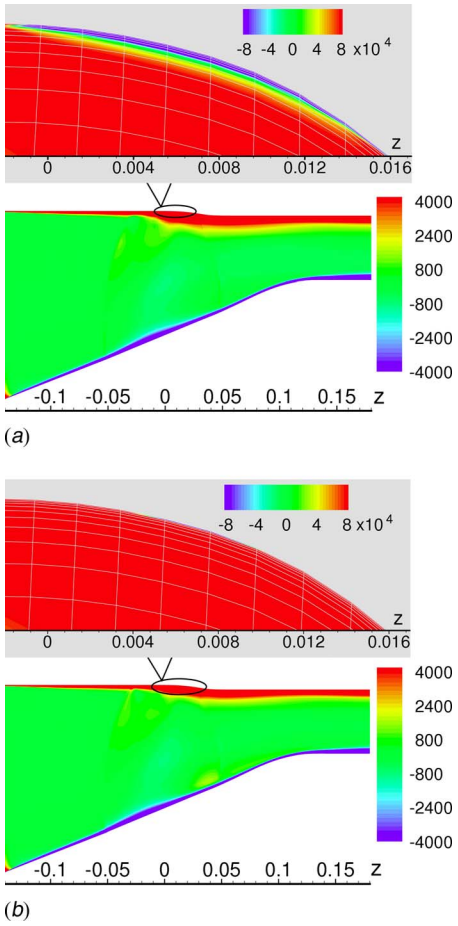

Fig. 8 ω_θ distributions on the meridian plane of two rotors of 3D RANS, with the corresponding zoom-in plots. In the zoom-in plots, the unit lengthes of ordinates are ten times larger than those of the abscissas for clarity, and the color bands are larger than the whole field plots. The computational meshes are also shown by the gray lines. (*a*) Design A; (*b*) Design B.

the total SPF.

The ultimate purpose of controlling azimuthal vorticity ω_θ via prescribed $\Gamma(r,z)$ distribution in TFD is to improve the SPF given by Eq. (14) in general and Eq. (16) for axisymmetric flow. In Eq. (14), the SPF integral consists of six terms. In Fig. 9, we plot the z dependence of these terms along with the total SPF, from Rotor's leading edge to trailing edge. For both Rotors A and B, the SPF increases smoothly, but from the total SPF curves alone, one cannot identify any effect of local dynamic processes and structures. In contrast, the six constituents of the SPF integral (14) do reflect local dynamics. Evidently, the ω_θ term is indeed the main contributor of SPF, in particular, as predicted before, at the exit the SPF is almost solely from the ω_θ term.

The magnitude of all other terms in Eq. (14) is much smaller than the first term. The second term (axial vorticity), third term (radial variation of density), and fifth term (axial gradient of radial velocity) make negative contribution somewhere. The fourth term (viscous term in the NS equation) is almost negligible. The sixth term, the effect of $f(M)$, has only a small effect at the rear part of the rotor.

In short, our theoretical assertion on the dominating role of ω_θ in SPF is reconfirmed. The SPF of Rotor B has a higher magnitude, see Fig. 9(*a*). Figure 9(*b*) reveals that the ω_θ term for Rotor B is larger than Rotor A at region $0<z<0.05$, which is exactly

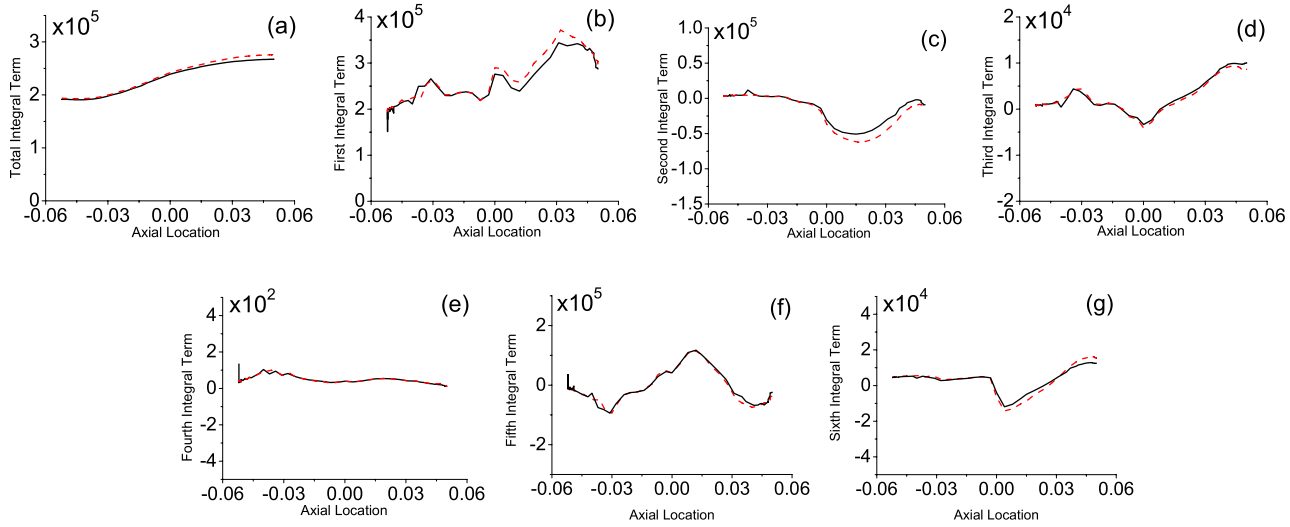

Fig. 9 Term-by-term comparison of SPF of Rotors A and B. Notice the scales of ordinates. Solid lines, Design A; dashed lines, Design B. (*a*) Total SPF, (*b*) the ω_θ term in Eq. (14), (*c*) $-(\int_W r^2 \rho u_\theta u_z \omega_z dr d\theta)/2$, (*d*) $-(1/4\int_W r^2 u_z |\mathbf{u}|^2 \partial\rho/\partial r dr d\theta)/4$, (*e*) $-(\int_W r^2 \rho \Psi dr d\theta)/2$, (*f*) $-(\int_W r^2 P^* \partial u_r/\partial z dr d\theta)/2$, and (*g*) I_{isen}.

where Rotor A produces negative ω_θ below the shroud boundary layer, as shown in Fig. 8(*a*). Figures 9(*c*)–9(*g*) show that the differences in other terms between the two rotors are relatively small.

These comparisons indicate that Design B has better ω_θ distribution, which indeed produces larger mass flux Q and the ratio $\overline{P_2^*}/\overline{P_1^*}$ than Rotor A, as shown by the performance curves in Fig. 7. Therefore, the goal of optimized TFD with constraint (34) or (35) is achieved.

5 Conclusion

The present work provides a vorticity-dynamics explanation of the underlying physics in compressor flow, along with flow diagnosis in terms of local dynamic processes and flow structures. A natural working criterion of the compressor performance, say, the SPF derived from the energy equation, is introduced for local-dynamics analysis and transformed to a form by DMT to exhibit the crucial flow structures. The most important structure is the azimuthal vorticity. The two kinds of ω_θ-creation mechanisms in the compressor, its creation inside the flow and its BVF at the solid walls, deserve careful analysis and control. For a simplified model in TFD, a simple ω_θ-Γ relation is found when the body-force model can preserve rotary enthalpy. This relation leads to a new constraint in optimal TFD procedure for enhancing SPF and the uniformity of the total enthalpy. The optimal TFD scheme is exemplified by the improvement of rotor performance. The results are further confirmed by the 3D RANS simulations.

Acknowledgment

The authors thank the kind help of Feng Mao and Li-Jun Xuan in the study of the Abel equation, and valuable discussions with Feng Liu, Wei-Dong Su, and Ming Guo, as well as the very useful comments of the referees. This work was supported in part by the Institute of Engineering Research of Peking University, with Program No. 204039.

Nomenclature

- (r,θ,z) = the cylinder coordinates with z the axial direction; when used as subscripts denote the corresponding components of a vector
- $\mathbf{e}_r,\mathbf{e}_\theta,\mathbf{e}_z$ = unit vectors of cylindrical coordinates
- e = internal energy
- $\mathbf{n}$ = unit normal vector of a surface, pointing out of the fluid if at a flow boundary
- p = static pressure
- q = velocity magnitude on the meridian plane, $q^2 = u_r^2 + u_z^2$
- s = specific entropy
- $\mathbf{u}$ = velocity vector in inertial frame of reference
- γ = the ratio of specific heats
- η = adiabatic efficiency
- ρ = density
- $\boldsymbol{\sigma}$ = boundary vorticity flux vector
- $\boldsymbol{\omega}$ = vorticity vector
- $\mathbf{F}$ = body force
- H = total enthalpy
- M = local Mach number
- P^* = stagnation pressure
- Q = mass flux
- T = temperature
- T^* = stagnation temperature
- $\mathbf{W}$ = relative velocity vector in the frame of reference rotating with the rotor, $\mathbf{W}=\mathbf{u}-\Omega r\mathbf{e}_\theta$
- S_1, S_2 = cross plane at compressor inlet and exit, respectively
- Γ = circulation
- Ω = angular velocity of the rotor
- SPF = stagnation-pressure flux

Appendix A: The Proof of Equation (16)

For axisymmetric flow, we use $\Gamma = ru_\theta$ and Eq. (19) to rewrite the sum of the second and third integrands on the right-hand side of Eq. (14):

$$\begin{aligned}
&\frac{1}{2}r^2\rho u_\theta u_z\omega_z + \frac{1}{4}r^2 u_z|\mathbf{u}|^2\frac{\partial\rho}{\partial r} \\
&\quad = \frac{1}{4}\left[\frac{\partial(\rho u_z\Gamma^2)}{\partial r} - \Gamma^2 u_z\frac{\partial\rho}{\partial r} - \rho\Gamma^2\frac{\partial u_z}{\partial r} + r^2 u_z|\mathbf{u}|^2\frac{\partial\rho}{\partial r}\right] \\
&\quad = \frac{1}{4}\left(\frac{\partial(\rho u_z\Gamma^2)}{\partial r} + r^2 u_z q^2\frac{\partial\rho}{\partial r}\right) + \frac{1}{4}\rho\Gamma^2\left(\omega_\theta - \frac{\partial u_r}{\partial z}\right) \qquad \text{(A1)}
\end{aligned}$$

Substituting Eq. (A1) into Eq. (14) and grouping similar terms yield

$$\mathrm{SPF} = \frac{1}{2}\int_S r^2 E_2 \omega_\theta dr d\theta - \frac{1}{2}\int_S r^2 E_1 \frac{\partial u_r}{\partial z} dr d\theta - \frac{1}{4}\int_S r^2 u_z q^2 \frac{\partial \rho}{\partial r} dr d\theta$$

$$- \frac{1}{2}\int_S r^2 \rho \Psi dr d\theta + I_{\mathrm{isen}} - \frac{1}{4}\int_S \frac{\partial(\rho u_z \Gamma^2)}{\partial r} dr d\theta \quad \text{(A2)}$$

where E_1, E_2, and q are defined in Eq. (17).

In axisymmetric flow, all scalar quantities are independent of θ, thus their integrations over θ simply causes a factor 2π. The last integral in Eq. (A2) can then be further integrated over r and vanishes due to the nonslip condition at the hub and shroud. Hence, Eq. (A2) leads to Eq. (16).

Appendix B: The Solvability Range of the Abel Equation

Consider an Abel equation with $\Omega = 1$ and a general source function $f(r)$:

$$A(r)\Gamma'(r) = -f(r), \quad A = \Gamma - r^2 \quad \text{(B1)}$$

Here, the parabola $\Gamma = r^2$ or $A = 0$, denoted by L, is a singular line: If the solution curve $\Gamma(r)$ ($\Gamma - curve$) touches L at r_0, then Eq. (B1) can no longer hold unless $f(r_0) = 0$. We examine the behavior of the Γ-curve as r approaches an assumed singularity at r_0. There are four possible cases.

(1) Assume $f > 0$ and $A < 0$ as r increases toward r_0. Then at a neighboring point $r = r_0 - \epsilon$ with positive $\epsilon \ll 1$, there is

$$A(r) = -\epsilon A_0' = -\epsilon(\Gamma_0' - 2r_0) < 0, \quad A\Gamma' = -\epsilon\Gamma_0'(\Gamma_0' - 2r_0) + O(\epsilon^2)$$

where there must be $\Gamma_0' > 2r_0$ (Γ increases faster than solid rotation). At this r, Eq. (B1) can be simplified to

$$\epsilon(\Gamma_0'^2 - 2r_0\Gamma_0') - (f_0 - \epsilon f_0') = 0$$

This yields

$$\Gamma_0' = r_0 \pm \sqrt{f_0/\epsilon + r_0^2 - f_0'} = \pm\sqrt{f_0/\epsilon} + O(1) \quad \text{(B2)}$$

where the negative sign should be dropped. Therefore, as r approaches r_0 or $\epsilon \to 0$, Γ runs up and hit L with singularly increasing slope.

We then assume Γ has gone across L such that at $r = r_0 + \epsilon$, there is

$$A(r) = \epsilon A_0' = \epsilon(\Gamma_0' - 2r_0) > 0, \quad A\Gamma' = \epsilon\Gamma_0'(\Gamma_0' - 2r_0) + O(\epsilon^2)$$

where since $f_0 > 0$, there should again be $\Gamma_0' > 2r_0$. Then Eq. (A1) becomes

$$\epsilon(\Gamma_0'^2 - 2r_0\Gamma_0') + (f_0 + \epsilon f_0') = 0$$

which yields

$$\Gamma_0' = r_0 \pm \sqrt{-f_0/\epsilon + r_0^2 - f_0'} = \pm i\sqrt{f_0/\epsilon} + O(1) \quad \text{(B3)}$$

Thus, no real root exists, contradicting the assumed $A > 0$. Hence, the Γ-curve cannot really cross L but only stick to it, making the left-hand side of Eq. (B1) vanish. This, however, implies that Eq. (B1) has no solution for $r > r_0$.

(2) Assume $f < 0$. Then Eq. (B1) implies that if $A(r_0 - \epsilon) > 0$, there must be $\Gamma_0' > 2r_0$, and vise versa if $A(r_0 - \epsilon) < 0$. In both cases, as r increases toward r_0, the Γ-curve will move away from L, and hence no singularity can exist at r_0.

(3) Assume $f < 0$ but r decreases toward r_0. Then the singularity exists and the solution will behave the same as Case (1) with $f > 0$ and r increases toward r_0. Namely, no solution exists for $r < r_0$.

(4) Assume $f > 0$ but r decreases toward r_0, then like Case (2) no singularity can occur.

References

[1] Wu, J. Z., Ma, H. Y., and Zhou, M. D., 2006, *Vorticity and Vortex Dynamics*, Springer, New York.

[2] Wu, J. Z., Lu, X. Y., and Zhuang, L. X., 2007, "Integral Force Acting on a Body Due to Local Flow Structures," J. Fluid Mech., **576**, pp. 265–286.

[3] Li, Q. S., and Guo, M., 2005, "Diagnosis and Design of A Low Speed Compressor Based on Local Dynamics," Progress in Natural Science, **15**(2), pp. 221–228, in Chinese.

[4] Li, Q. S., Wu, H., Guo, M., Zhou, S., and Wu, J. Z., "Vorticity Dynamics in Axial Compressor Flow Diagnosis and Design II: Near-Boundary Viscous Flow," unpublished.

[5] Damle, S. V., 1996, "Throughflow Method for Turbomachines Using Euler Solvers," Paper No. AIAA-96-0010.

[6] Guo, M., Li, Q. S., Hou, A. P., and Yuan, W., 2006, "A Diagnostic and Design Approach of Axial Compressor Based on Local Dynamics," *Proceedings of GT2006. ASME Turbo Expo 2006: Power for Land, Sea and Air*, Barcelona, Spain, May 8–11, Paper No. GT2006-91116.

[7] Wu, C. H., 1952, "A General Theory of Three-Dimensional Flow in Subsonic and Supersonic Turbo-Machines of Axial-, Radial-, and Mixed-Flow Types," NACA TN 2604.

[8] Ji, L. C., Meng, Q. G., and Zhou, S., 1999, "Time-Marching Method for Throughflow Computation of Turbomachinery," Journal of Aerospace Power, **14**(1), pp. 23–26, in Chinese.

[9] Shi, X., Zhao, Y. J., Ji, L. C., and Zhou, S., 2002, "Exploration and Analysis About Time-Marching Through-Flow Method," Journal of Engineering Thermophysics, **23**, pp. 50–53, in Chinese.

[10] Jameson, A., Schmidt, W., and Turkel, E., 1981, "Numerical Solutions of the Euler Equations by Finite Volume Methods Using Runge–Kutta Time Stepping Schemes," AIAA Paper No. 81-1259.

[11] Wu, H., Li, Q. S., Song, Y. H., Zhou, S., Wu, J. Z., and Yang, Y. T., 2006, "Vorticity Diagnosis in Throughflow Design of Highly Loaded Fan Rotor," *Proceedings of the First International Symposium on Jet Propulsion and Power Engineering*, Paper No. *ISJPPE-2006-5003*.

Mixing Flow Characteristics in a Vessel Agitated by the Screw Impeller With a Draught Tube

Yeng-Yung Tsui[1]
Professor
e-mail: yytsui@mail.nctu.edu.tw

Yu-Chang Hu
Graduate Student

Department of Mechanical Engineering,
National Chiao Tung University,
Hsinchu 300, Taiwan

The circulating flow in a vessel induced by rotating impellers has drawn a lot of interests in industries for mixing different fluids. It used to rely on experiments to correlate the performance with system parameters because of the theoretical difficulty to analyze such a complex flow. The recent development of computational methods makes it possible to obtain the entire flow field via solving the Navier–Stokes equations. In this study, a computational procedure, based on multiple frames of reference and unstructured grid methodology, was used to investigate the flow in a vessel stirred by a screw impeller rotating in a draught tube. The performance of the mixer was characterized by circulation number, power number, and nondimensionalized mixing energy. The effects on these dimensionless parameters were examined by varying the settings of tank diameter, shaft diameter, screw pitch, and the clearance between the impeller and the draught tube. Also investigated was the flow system without the draught tube. The flow mechanisms to cause these effects were delineated in detail. [DOI: 10.1115/1.2903815]

1 Introduction

The process of fluid mixing is commonly used in industries. To blend different fluids, a vessel is equipped with a rotational impeller. A swirling flow, i.e., a flow rotating about the vessel axis, is generated by the impeller. The function of the impeller is to ensure transport of a fluid element to anywhere in the tank. In order to fulfill this objective, axial vortices, i.e., loop flows circulating from the top region of the tank to the bottom region, must be induced. Thus, the flow in the tank is inevitably three dimensional. The contact surfaces between different fluids are then deformed by the three-dimensional flow. Since different fluid materials are mixed in the interface layer via molecular diffusion, the deformed and, thus, elongated contact surface leads to the enhancement of fluid mixing.

For low-viscosity fluids, the most commonly used impellers are the disk-type flat blade turbines and the pitched-blade turbines [1]. The low viscosity of the fluids and the smaller size, compared with the tank, render the turbine impellers suitable for high-speed rotation, which makes the flow field turbulent. Turbulent flows are helpful in fluid mixing because the contact surfaces between different fluids are greatly wrinkled by the turbulence fluctuations. At higher viscosities, these impellers lose their effectiveness due to the difficulty to achieve high shear conditions because large power consumption is demanded. Instead, helical ribbon impellers or screw impellers, rotating at low speeds, are preferred.

The screw impeller, despite its small diameter, produces significant secondary circulation when incorporating a draught tube and is the main concern of the present study. This mixer works in a similar manner to the screw extruder. However, the former functions to maximize pumping flow with a low pressure increase, whereas the latter works to maximize pressure rise with a low pumping capacity. In the past, most analyses of the pumping flow in the screw mixer are based on an analogy to the extruder. As seen in Refs. [2,3], the flow in a tube pumped by a screw can be mainly divided into a drag flow q_d and a pressure flow q_p,

$$q = q_d - q_p \tag{1}$$

The drag flow q_d resulting from the relative motion between the screw and the casing is a forward flow in the positive direction of the axis. It was treated as a fully developed flow between two parallel plates with one plate moving at the rotational speed to drive the fluid flow, which is similar to the well-known Couette flow. When the screw pump operates, pressures builds up in the pump, resulting in a high pressure at the outlet. The adverse pressure gradient brings about a back flow in the negative direction of the axis. This pressure flow q_p can be analyzed by assuming a Poiseuille flow between the plates.

The above simple models were also used to estimate power requirements. The power consumed by the drag flow is obtained via calculating the internal heat generation due to viscous dissipation. Both the flows in the channel direction and in the transverse direction need to be taken into consideration in estimating the energy dissipation. For the pressure flow, the power required is the power expended as flow energy in raising the pressure of the fluid, which is equal to the product of the pressure rise in the screw pump and the maximum pumping flow rate corresponding to zero pressure gradients.

For the pressure flow, the pressure rise between the inlet and the outlet of the screw pump needs to be known. In general, the pressure rise is determined from experiments. However, Sykora [4] used the frictional loss in the flow through the annular span between the draught tube and the tank to estimate this pressure rise. To account for the effects of the side walls and the curvature of the flow channel in the pump at low helical angles, shape factors were introduced [2,3].

In the past, most studies were done to correlate three key characteristic parameters (power number, mixing time, and circulation number) to geometric parameters, such as the tank diameter, the length of the screw, the pitch of the impeller, and the width of the impeller blade [4–10]. These correlations were expressed in dimensionless form to generalize their applicability. When geometric configurations are fixed, the dependence of the three characteristic parameters on the rotational speed of the screw impeller (n) or the Reynolds number (Re) can be summarized for Newtonian fluids as

$$N_P \,\mathrm{Re} = \mathrm{const} \tag{2}$$

[1]Corresponding author.

Contributed by the Fluids Engineering Division of ASME for publication in the JOURNAL OF FLUIDS ENGINEERING. Manuscript received January 31, 2007; final manuscript received October 18, 2007; published online April 3, 2008. Assoc. Editor:r Yu-Tai Lee.

$$N_Q = \text{const} \tag{3}$$

$$\tau_m n = \text{const} \tag{4}$$

where N_P is the power number, N_Q the circulation number, and τ_m the mixing time. These relationships are valid for $\text{Re} < 20$. For higher Reynolds numbers, the results of Carreau et al. [11] revealed that mixing time gradually decreases with Reynolds number. They also found that

$$\frac{N_p \,\text{Re}}{N_Q} = \text{const} \tag{5}$$

The circulation number increases from the value at low Reynolds numbers with increasing Re to eventually attain another constant value. It was concluded by them that the ratio of the mixing time to the circulation time (the time for the flow to complete a circulation loop in the vessel) is a constant.

In view of the above review, despite the fruitful achievement in relating the screw mixer performance to the system configuration settings, details about the flow field were not delineated in these experimental works and the simple analytical models cannot portray the flow field precisely. Mathematical methods, which solve the Navier–Stokes equations, give complete pictures of velocity and pressure fields and are thus useful to analyze the flow. Although they have already been widely employed in industrial applications, their use in simulating the screw mixer is very limited. As far as we are aware, only Kuncewicz et al. [12] adopted a numerical method to study the effects of the tank diameter and the pitch of the screw impeller on the mixer performance. In their simulations, the flow field was simplified by assuming it to be two dimensional. The action of the rotating impeller on the flow is realized by imposing a form drag force and a frictional drag force onto the momentum equations [13]. Two empirical coefficients, characterizing the two forces, need to be specified. Recently, the present authors developed a three-dimensional computational method, which is based on a fully conservative finite volume method and incorporates unstructured grid techniques. Multiple frames of reference were employed to tackle the rotation of the impeller. This method had been successfully used in the simulation of the vacuum pump of the Holweck type [14] and the mixer with pitched-blade turbines [15]. In this study, it is employed to examine the effects of various geometric parameters on the screw mixer with a draught tube.

2 Mathematical Method

A schematic sketch of an agitated system with a screw impeller together with a draught tube is shown in Fig. 1. For numerical calculations, the draught tube is divided into an inner part and an outer part. The outer part covers the clearance region between the impeller blade and the inner wall of the tube. In this clearance region and the bulk region outside the draught tube, the frame of reference is stationary. A rotational frame is imposed on the inner part of the tube to allow the blade of the impeller to sweep across this region. The flow field in the agitated vessel is assumed to be quasisteady, implying that the screw impeller is frozen at a specific position. The governing equations in the rotational frame can then be cast into the following form:

$$\frac{\partial[(U_j^* - U_{gj}^*)]}{\partial x_j^*} = 0 \tag{6}$$

$$\frac{\partial[(U_j^* - U_{gj}^*)(U_i^* - U_{gi}^*)]}{\partial x_j^*} = -\frac{\partial p^*}{\partial x_i^*} + \frac{1}{\text{Re}}\frac{\partial}{\partial x_j^*}\left(\frac{\partial(U_i^* - U_{gi}^*)}{\partial x_j^*}\right) - \varepsilon_{mni}\Omega_m U_{gn}^* - 2\varepsilon_{mni}\Omega_m (U_n^* - U_{gn}^*) \tag{7}$$

The above equations are expressed in dimensionless form in which the coordinates, velocities, and pressure are normalized as

$$x_j^* = \frac{x_j}{d}, \quad U_j^* = \frac{U_j}{nd}, \quad p^* = \frac{p}{\rho n^2 d^2} \tag{8}$$

where d is the diameter of the impeller, n the rotational frequency, and ρ the density of the fluid. The Reynolds number Re is defined as $\rho n d^2/\mu$, where μ is the molecular viscosity of the fluid. $U_j^* - U_{gj}^*$ represents the flow velocity with respect to the moving grid and $U_{gj}^* = \varepsilon_{jpq}\Omega_p x_q^*$ is the velocity of the moving grid rotating with the impeller. $\Omega_j (= 2\pi n e_j)$ is the angular velocity of the impeller. The effects of the rotational frame are represented by the body forces given in the last two terms in the momentum equation, corresponding to the centrifugal force and the Coriolis force. In the stationary frame of reference, the grid velocity $U_{gj}^* = 0$ and the body forces are dropped.

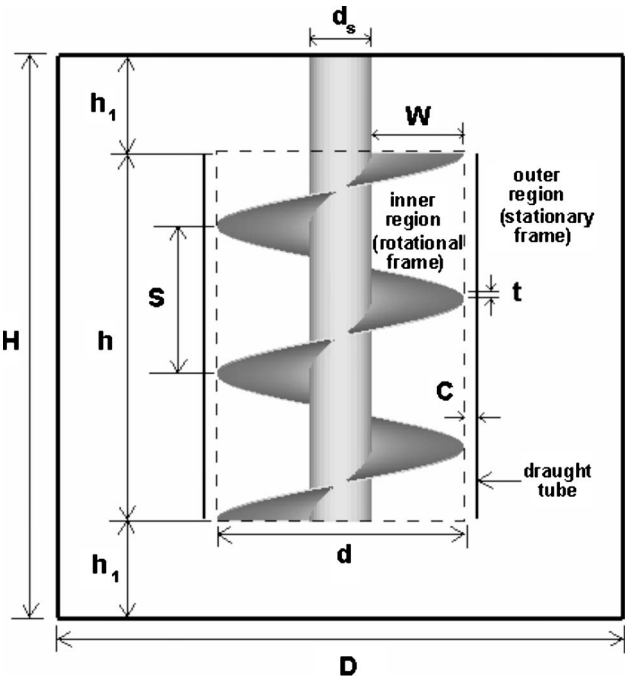

Fig. 1 A sketch of the mixing system

There is a need to have a comprehensive tool to handle various flow configurations encountered in industries. To meet this requirement, the authors have developed a general code in recent years such that the flow with irregular boundaries can be analyzed. The analytic tool is based on a fully conservative finite volume method applicable to unstructured grids, which are made of polyhedrons with arbitrary geometric topology. This method is briefly described in the following.

The transport equations are first integrated over a control volume which, in principle, can be of arbitrary geometry. With the aid of the divergence theorem, the volume integrals of the convection and diffusion terms are transformed into surface integrals. It is followed by the use of midpoint rule to yield discretization form

$$\sum_f [(\vec{U} - \vec{U}_g)_f \cdot \vec{s}_f]\phi_f = \sum_f \frac{1}{\text{Re}} \nabla \phi_f \cdot \vec{s}_f + q\Delta v \tag{9}$$

where the subscript f denotes the face values, $\vec{s}_f$ is the surface vector of the considered face, and ϕ represents the components of the relative velocity $(\vec{U} - \vec{U}_g)$. The last term in the equation represents all the terms apart from the convection and diffusion terms. The summation is taken over all the faces of the control surface.

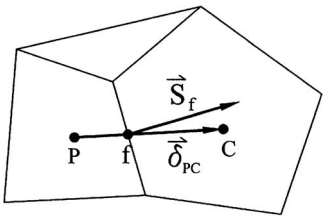

Fig. 2 Illustration of a principal node and a neighboring node with a common face

The convective value ϕ_f through each face is approximated by a high-order scheme,

$$\phi_f = \phi^{\mathrm{UD}} + \gamma(\nabla\phi)^{\mathrm{UD}} \cdot \vec{\delta} \tag{10}$$

where the superscript UD denotes the value evaluated at a node upstream of the face under consideration and $\vec{\delta}$ is the distance vector directed from the upwind node to the centroid of the face. In the equation, γ is a blending factor falling in the range between 0 and 1. For a value of 0, it simply degenerates into the upwind difference scheme. For $\gamma=1$, the scheme is second order accurate. In the present calculations, a value of 0.9 is assigned to γ.

The diffusive flux is further modeled by the following approximation:

$$\frac{1}{\mathrm{Re}} \nabla \phi_f \cdot \vec{s}_f = \frac{1}{\mathrm{Re}} \frac{s_f^2}{\vec{\delta}_{PC} \cdot \vec{s}_f} (\phi_C - \phi_P) + \frac{1}{\mathrm{Re}} \overline{\nabla \phi_f} \cdot \left(\vec{s}_f - \frac{s_f^2}{\vec{\delta}_{PC} \cdot \vec{s}_f} \vec{\delta}_{PC} \right) \tag{11}$$

where (see Fig. 2) the subscripts P and C denote the principal and the neighboring nodes sharing a common face f, and $\vec{\delta}_{PC}$ is a distance vector connecting these two nodes. The face gradient $\overline{\nabla \phi_f}$ is obtained via interpolation from the gradients at the two nodes.

In solving the discretized transport equations, the first terms on the right-hand side in Eqs. (10) and (11) are implicitly treated, while the second terms in the equations are tackled in an explicit manner using the deferred-correction procedure. It also needs to be noted that the computational molecules for the nodes in one frame immediately adjacent to the interface between the two reference frames include nodal points in the other frame. To correctly evaluate the momentum flux transported through the interface, the velocities at these neighboring nodes must be transformed onto the frame where the considered node is located.

After solving momentum equations, the resulting velocities must be adjusted, and the prevailing pressure must be upgraded in a way that the continuity equation is satisfied. The enforcement of conservation of mass results in a pressure-correction equation. The discretized momentum equations and the pressure-correction equation are sequentially solved in an iterative manner. Iterations are performed to account for the nonlinearities, the coupling between velocities and pressure, and the deferred-correction terms mentioned above. More details about the method can be found in Refs. [14,16].

3 Results and Discussion

A drawing of the mixing system with a screw-in-a-tube agitator is given in Fig. 1. A benchmark configuration of the mixing system has a screw impeller with diameter $d=126$ mm and length $h=1.5d$. The diameter D and the height H of the agitated tank are $D=H=2.3d$. The screw impeller has a shaft of diameter $d_S=0.254d$ and a clearance $C=0.05d$. The pitch of the screw impeller is $S=0.6d$. The width of the screw blade W is equal to $(d-d_S)/2$, and the distances between the impeller and both the top and the bottom of the tank are $h_1=(H-h)/2$. The impeller rotates at a speed of 59 rpm, which is equivalent to a Reynolds number of 1.52.

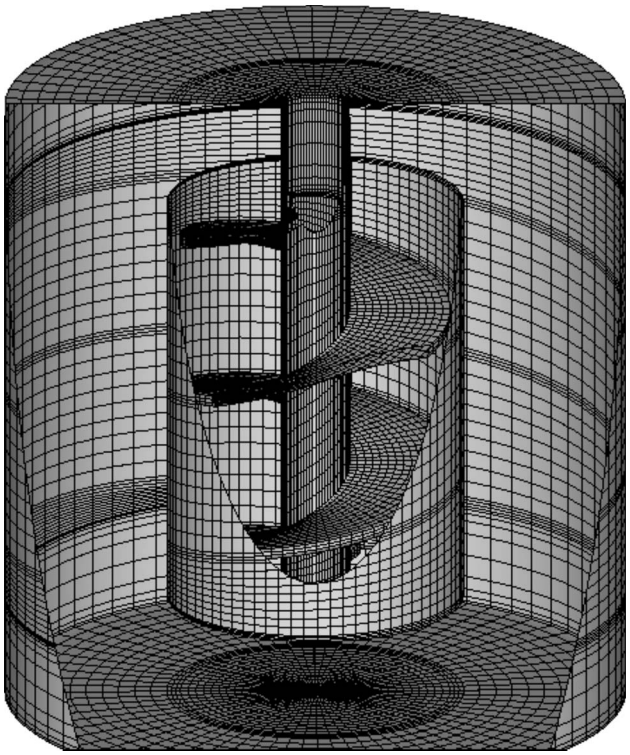

Fig. 3 A computational mesh

To generate unstructured grids, the computational domain is first divided into 80 blocks. In each block, an algebraic method is used to create a suitable grid. After the grids for all the blocks are constructed, the grid nodes are readdressed. An example of the resulting mesh is presented in Fig. 3. To examine grid effects on the mixing flow performance, grids with about 120,000, 200,000, 300,000, and 380,000 cells have been tested. It was found that the power number (defined by Eq. (14)) gradually increases with the cell number from 287 to 301.6. However, the difference between the two finest grids is only 0.4%. The circulation number (defined by Eq. (12)) is less sensitive to the choice of grid. It varies from 0.196 for the coarsest grid to 0.193 for the other grids. In the following, the grid with about 380,000 cells is adopted for calculations. The no-slip conditions are imposed on all the surfaces of the system. The flow in the vessel is assumed to be motionless as the initial condition.

The flow field, illustrated in Fig. 4, shows that fluid is drawn by the rotating impeller into the draught tube from the upper opening and emerges from the bottom end, followed by an upward flow outside the tube to complete a circulation loop. To validate the methodology, calculations have been conducted to compare with the measurements of Seichter et al. [8] and Seichter [9]. In the experiments, the liquids to be mixed were solutions of starch syrup in water, which exhibit a Newtonian behavior. The flow velocities were measured using a thermal resistor. To measure the torque, the mixing vessel was placed on a turntable. The torque produced by the rotating impeller was transmitted to a silon thread and compensated on a desk balance. There are two major differences between the experiments and the simulations. One is that the thickness of the impeller is not given in the experiments. Therefore, a guessed value for the thickness was used in simulations. The other is the upper surface of the flow in the vessel, which is open to air. However, it is assumed to be a solid wall in calculations. A comparison of the axial velocity in the annular

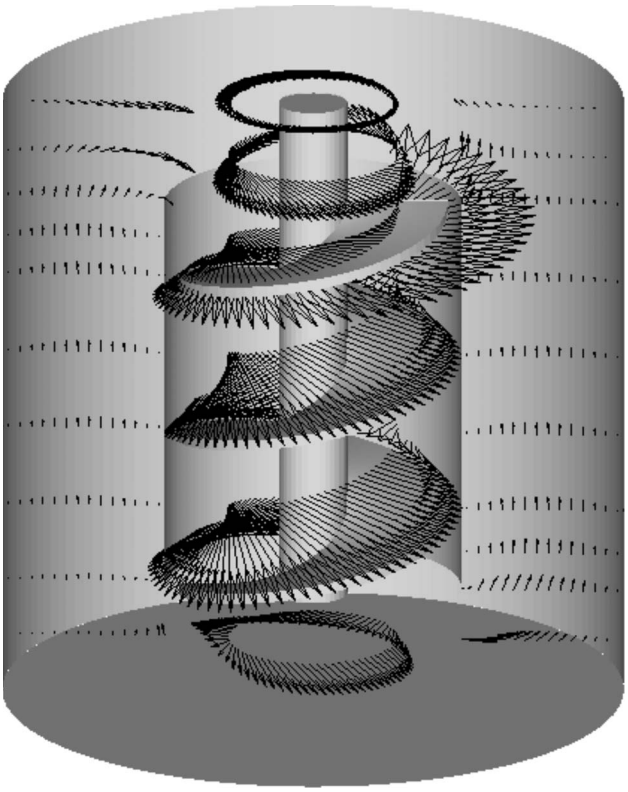

Fig. 4 Typical flow field

region outside the tube at the midheight plane is shown in Fig. 5. Three rotational speeds, corresponding to Re=0.92, 1.26, and 1.52, were under consideration. Since the thickness of the impeller blade was not clear, three values, corresponding to $t=1$ mm, 5 mm, and 8 mm, were chosen to test its effects. It is obvious from the figures that the larger the blade thickness, the lower the flow rate. Both the experiments and the predictions indicate that the flow in the annulus approaches a fully developed state with the velocity close to a parabolic profile. A further comparison between predictions and measurements for Re=1.52 is given in Table 1 in which the circulation number N_Q and the power number N_P^* are shown. The corresponding N_Q and N_P^* for Re=1.26 and 0.92 are

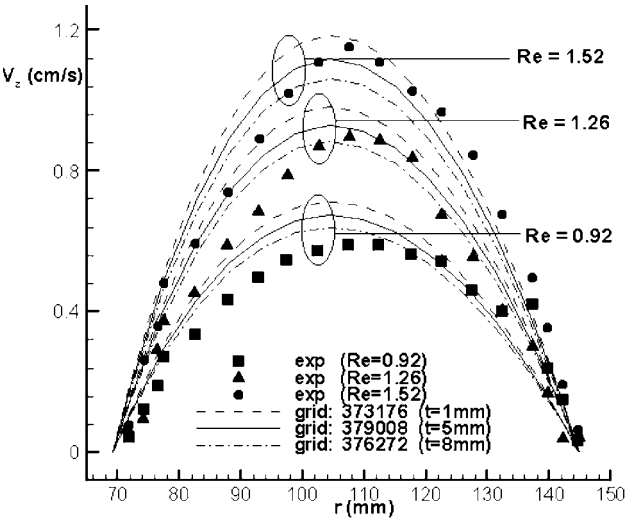

Fig. 5 Comparison of predicted and measured axial velocities in the annular region outside the tube

Table 1 Comparison between predicted and measured circulation numbers and power numbers for different blade thicknesses

	$t=1$ mm	$t=5$ mm	$t=8$ mm	Expt.
N_Q	0.204	0.193	0.183	0.178
N_P^*	242.6	301.6	341.6	306.1

almost the same as the values listed in Table 1 due to the fact these numbers are independent of the Reynolds number, as seen from Eqs. (2) and (3). For the largest thickness case, the predicted N_Q is close to the experimental data, but the predicted N_P^* is too high. For $t=5$ mm, the predicted N_P^* is in good agreement with the measurements and the predicted N_Q is only about 8% higher. Therefore, 5 mm of blade thickness, being about 4% of the impeller diameter, is used throughout the following results.

The performance of the mixer is characterized in terms of three dimensionless parameters: circulation number N_Q, power number N_P^*, and energy of mixing E.

The circulation number is defined by

$$N_Q = \frac{Q}{nd^3} \tag{12}$$

Here, Q is the volumetric flow rate through the draught tube. It is exactly the same as the flow rate in the annulus outside the tube due to mass conservation.

The power number is usually given as

$$N_P = \frac{P}{\rho n^3 d^5} \tag{13}$$

where P is the power consumed by the impeller. The power required to drive the impeller can be divided into two parts: one due to the pressure force acting on the impeller blade and the other due to the frictional force acting on the surfaces of the blade and the shaft. This power number is a function of Reynolds number. Another form of the power number can be expressed by

$$N_P^* = \frac{P}{\mu n^2 d^3} \tag{14}$$

These two expressions are related by

$$N_P^* = N_P \,\mathrm{Re} \tag{15}$$

As seen from Eq. (2), N_P^* is a constant for low Reynolds numbers.

A criterion to evaluate the effectiveness of the mixer is the energy of mixing E nondimensionalized as [12]

$$E = \frac{P\tau_m}{\mu n d^3} \tag{16}$$

where τ_m is the time needed for the mixing process to reach a homogenization state. To estimate the mixing time, unsteady flow simulations must be undertaken, which require large computational time. Alternatively, we can use the circulation time instead of the mixing time because it was observed that the time required for mixing is proportional to the time required for circulation [11]. The circulation time is given by

$$\tau_c = \frac{\Delta V}{Q} \tag{17}$$

where ΔV is the volume of the considered tank. By substituting $4\tau_c$ into Eq. (16) to replace τ_m [11], we can redefine E as

$$E = \pi \frac{N_P^*}{N_Q} \left(\frac{H}{D}\right) \left(\frac{D}{d}\right)^3 \tag{18}$$

It is noted that in the equation, N_P^*/N_Q represents the power required per unit of circulating flow. It can be used as an indicator for pumping effectiveness [15] but is not suitable for mixing effectiveness because the geometric size of the tank needs to be taken into account in the mixing process.

3.1 Effects of Tank Diameter. To examine the influence of the relative size of the stirred tank to the impeller, the diameter of the tank is gradually enlarged, while those of both the screw impeller and the draught tube remain unchanged. Its effects on the pumping capacity, power consumption, and mixing effectiveness are illustrated in Figs. 6(*a*)–6(*c*). In the figures, two sets of calculations corresponding to cases with a constant impeller shaft ($d_s/d=0.254$, where d is fixed) and a variable shaft ($d_s/D=0.11$) are presented. In the constant shaft case, the pump configuration is fixed, while the pump shaft diameter d_s will be increased with the enlarged tank in the variable shaft case. The inclusion of the latter is simply used to compare with the experiments of Seichter et al. [8] and the predictions of Kuncewicz et al. [12] because there are no data available for the former case for comparison. Considering the case with a fixed shaft, for small values of D close to d, the circulating flow rate N_Q is small because of the great frictional resistance of the narrow passage between the draught tube and the tank wall. The flow rate quickly builds up when the annular space is enlarged to $D/d=2.3$, followed by leveling off to a value of $N_Q=0.35$. Theoretically, the power number N_P^* is maximized as the tank diameter is reduced to the tube diameter because a very high pressure gradient is generated, but without any fluid flow. When the tank diameter is increased, the power requirement decreases sharply and then N_P^* reaches nearly a constant value of 225 after D becomes larger than $2.3d$. Also shown in Fig. 6(*b*) are the two parts of power number due to the pressure force ($N_{P,p}^*$) and the frictional force ($N_{P,f}^*$). For small tank diameters, $N_{P,p}^*$ quickly decreases and $N_{P,f}^*$ gradually increases. Both are attributed to the release of the flow in the annular region as D/d increases. At large diameters, power consumption is mainly attributed to the frictional loss, which is about three times the pressure loss. Figure 6(*c*) illustrates that the energy required for mixing is reduced first and then quickly increases when the tank is enlarged. There exists a minimum point at $D/d=2$. This value is smaller than the value of 2.3 at which the circulating flow rate becomes nearly a maximum and the power consumption a minimum. The results can be understood in view of Eq. (18) in which the mixing energy is proportional to D^3.

For the variable shaft case with $d_s/D=0.11$, the flow channel in the draught tube is narrowed as the shaft diameter increases with the enlarged tank, resulting in a reduction in N_Q and an increase in N_P^* when D is greater than $2.3d$. A similar trend for N_Q can be found in the results of Kuncewicz et al. [12]. However, the power number N_P^* increases with increasing D in the present calculations for D greater than $2.3d$ but continues to decrease in the calculations of Kuncewicz et al. It will be shown in Sec. 3.2 that an increase in shaft diameter will cause an increase in frictional force on the shaft surface, which leads to a large frictional loss. Therefore, the predictions of Kuncewicz et al. are not reliable. The cause of the decreasing behavior is thought to be due to their calculation procedure. As mentioned in the Introduction, in their two-dimensional calculations, two drag coefficients need to be specified to account for the action forces by the impeller. These coefficients were determined by some pilot tests to fit the experimental data and then used throughout the rest of the calculations. It is conjectured that these coefficients may require adjustment for the cases with large D/d. This may explain why their results have a good agreement with the measurements at low values of D/d.

The experimental data of Seichter et al. [8] are also included in the figures. There exist some differences between the present predications and the measurements. It needs to be emphasized that

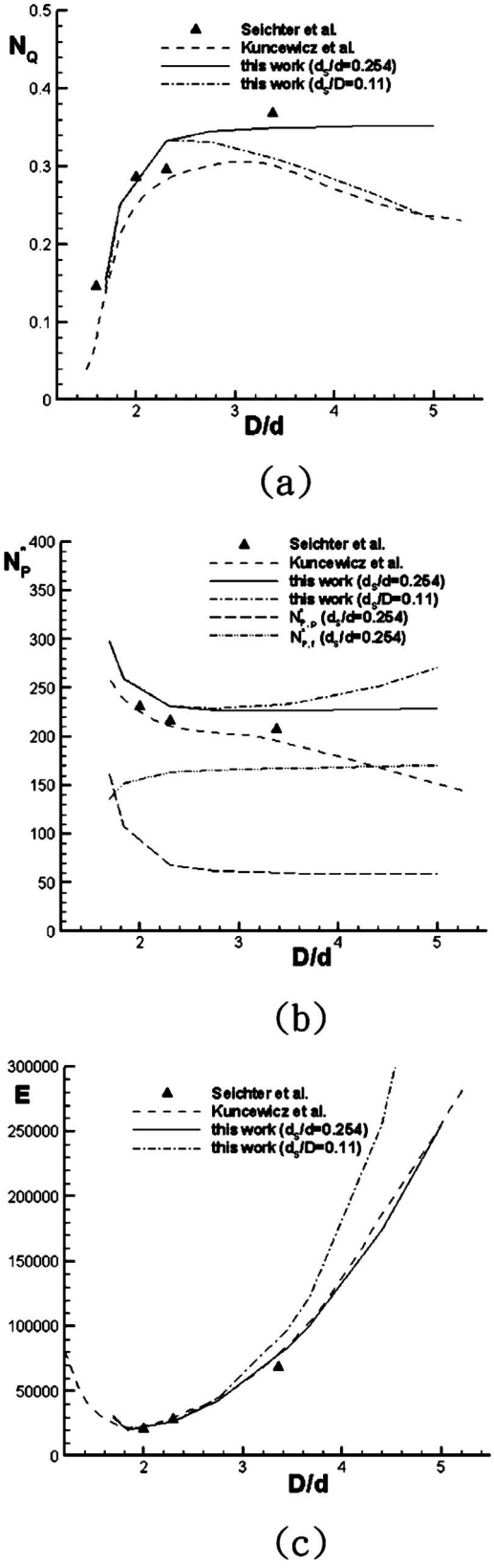

Fig. 6 Variation of (*a*) circulation number, (*b*) power number, and (*c*) mixing energy against tank diameter *D*

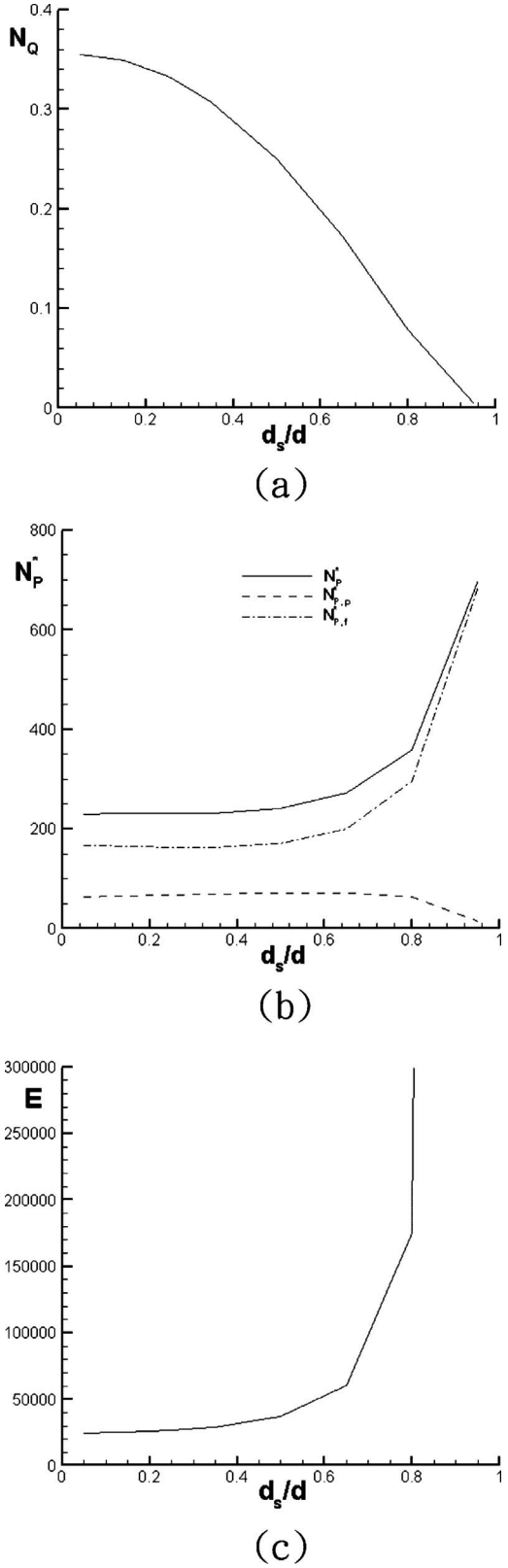

Fig. 7 Variation of (*a*) circulation number, (*b*) power number, and (*c*) mixing energy against shaft diameter d_s

the simulation cannot completely mimic the experiments. As discussed above, the thickness of the impeller blade and that of the draught tube were not clear in the experiments.

3.2 Effects of Shaft Diameter. As seen in Fig. 7(*a*), the circulating flow rate is reduced by enlarging the shaft. This is not unexpected because the height and, thus, the cross-sectional area of the flow channel in the tube decrease. The power number, shown in Fig. 7(*b*), remains almost a constant until $d_s/d=0.6$, followed by an increase. It is seen in the figure that the increase in the power number at large shaft diameters is due to the increase in frictional loss ($N^*_{P,f}$). The enlarged shaft causes an increase in the surface velocity and a reduction in the channel height. As a consequence, the shear stress in the channel is increased, which is evidenced in view of the radial variation of circumferential velocity V_θ shown in Fig. 8. Since the shaft surface area also increases with the shaft diameter, the frictional loss is greatly increased at large diameters. The required mixing energy, as shown in Fig. 7(*c*), gradually increases for low values of d_S until $d_S/d=0.6$. It is then followed by a rapid increase.

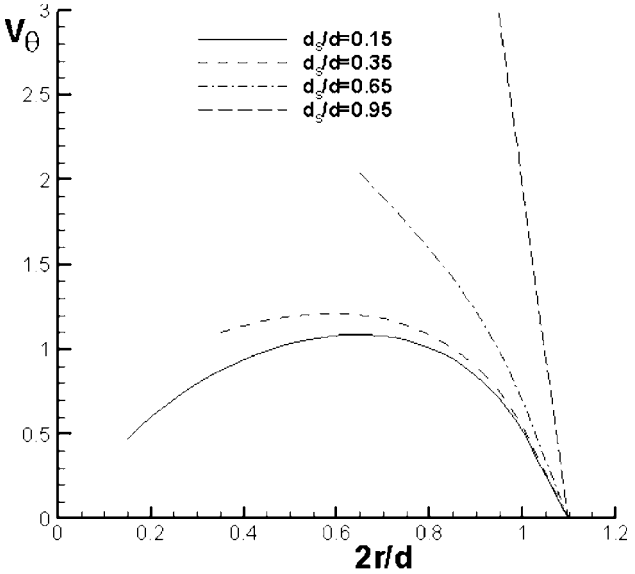

Fig. 8 Distribution of circumferential velocity along the radial direction in the draught tube for different shaft diameters

3.3 Effects of Impeller Pitch. A schematic drawing of the flow channel formed by the impeller blade and the draught tube is deployed onto a plane, as shown in Fig. 9, in which the clearance between the impeller and the tube is neglected. The length of the channel for one revolution of impeller blade is given by $L=S/\sin\alpha$, where α is the helical angle. The flow in the channel can be regarded as being driven by the internal wall of the tube moving in a direction opposite to that of the rotation. This moving wall velocity (V_w) can be divided into two components: one in the channel direction ($V_w \cos\alpha$) and the other in the transverse direc-

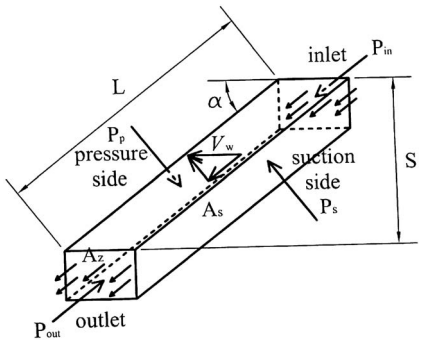

Fig. 9 A schematic drawing of the flow channel inside the draught tube

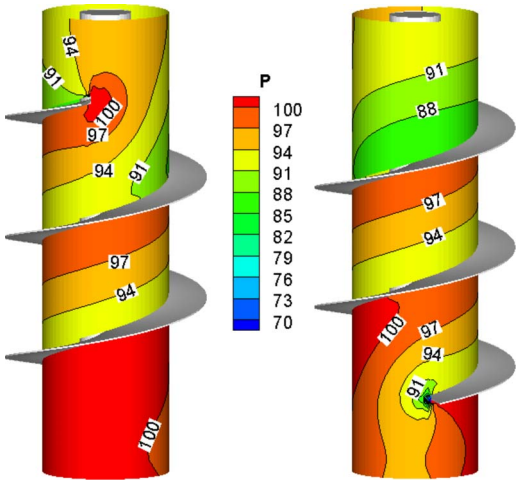

Fig. 10 Pressure distribution on the impeller shaft from two different view angles

tion ($V_w \sin \alpha$). A pressure rise between the inlet and the outlet is built up by the channel-direction flow and a pressure difference between the side walls by the transverse flow. These two pressure differences are related by considering the axial component of the force balance over the entire channel,

$$(p_{\text{out}} - p_{\text{in}})A_z = (p_p - p_s)A_s \cos \alpha - F_z \tag{19}$$

where p_{in} and p_{out} are the pressures at the inlet and the outlet, p_p and p_s are the pressures at the pressure side and the suction side, A_z is the cross-sectional area, A_s is the sidewall area, and F_z is the axial component of the frictional force exerted on the channel walls. In the equation, the momentum difference between the inlet and the outlet is neglected. It is obvious that the pressure difference between the sidewalls is linearly related to the pressure rise through the draught tube. As an illustration, the pressure contours distributed on the impeller shaft are presented in Fig. 10. The dimensionless average pressures at the inlet and exit of the tube are $p_{\text{in}}=91.6$ and $p_{\text{out}}=100.8$, while those on the two sides of the blade are $p_p=104$ and $p_s=87.9$. As a result, the pressure rise through the tube is $p_{\text{in}}-p_{\text{out}}=9.2$ and the pressure difference between the two blade sides is $p_p-p_s=16.1$. It is noted that there exists a high pressure zone at the leading edge of the blade at the entrance and a low pressure zone at the trailing edge at the exit. Near these two regions, reversed flows may result. However, its effect on the primary flow structure is insignificant.

The pitch, or the helical angle α, has two opposite effects on the flow. As seen in Fig. 9, by decreasing the helical angle, the velocity component of the moving wall in the channel direction is increased, being helpful to the fluid flow. However, the channel is narrowed and lengthened, resulting in greater frictional resistance. Hence, there exists an optimum pitch value for maximum flow. It is observed in Fig. 11(*a*) that this optimum value holds at $S/d=1.5$ in the present computations. For the two limiting cases with $\alpha=0$ deg and 90 deg, i.e., $S/d=0$ and ∞, there is no flow through the draught tube because in the former the impeller degenerates into a rotating cylinder, whereas in the latter the impeller blade becomes vertical. For the rotating cylinder case, a large amount of power is required to overcome the great frictional resistance that is prevailing. As shown in Fig. 11(*b*), the power requirement quickly decreases first, followed by leveling off to a constant value. When S is greater than $1.5d$, the constant value of N_P^* is 226 for $S/d=\infty$. It is also shown in the figure that the pressure part of the power number $N_{P,p}^*$ gradually approaches 226 while the frictional part $N_{P,f}^*$ gradually approaches zero. For the limiting case of the vertical blade, transverse flow prevails in the draught tube,

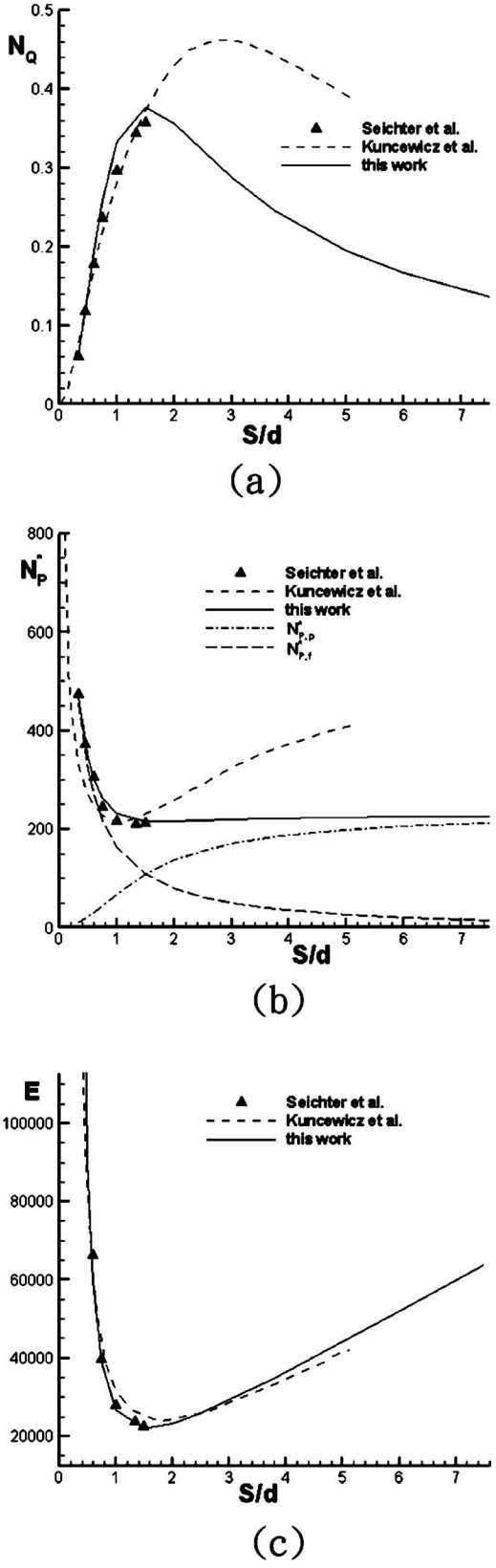

Fig. 11 Variation of (*a*) circulation number, (*b*) power number, and (*c*) mixing energy against screw impeller pitch *S*

which generates large pressure difference between the two sidewalls. The variation of mixing energy in Fig. 11(*c*) shows that the most efficient mixing occurs when $S/d=1.5$.

Compared with the measurements of Seichter et al. [8], the agreement is reasonably good. However, the calculations of Kuncewicz et al. [12] showed that both N_Q and N_P^* are much larger than the present predictions for high values of S. These overpredictions are believed to be due to the drag coefficients used in their model. However, despite the large differences in N_Q and N_P^*, the two calculations yield a close agreement in predicting the mixing energy E.

3.4 Effects of Clearance Gap. It was discussed that a pressure difference is generated between the two sidewalls by the transverse flow, as seen in Fig. 9. The sidewalls represent the two faces of the impeller blade. In practical applications, a passage, i.e., a clearance gap, exists to connect the two sides. Due to the existing pressure gradient, part of the fluid flows through the clearance from the pressure side to the suction side. This flow leakage causes a decrease in the sidewall pressure difference and, in turn, a decrease in pressure rise in the flow channel because they are related, as seen in Eq. (19). Consequently, the circulation number N_Q, the power number N_P^*, and the mixing energy E decrease with increasing clearance C, which are shown in Figs. 12(*a*)–12(*c*). It is seen from Fig. 12(*b*) that the clearance has a significant effect on the frictional force and, thus, the power consumption when the clearance is very small.

3.5 Effects of Draught Tube. A comparison has been made on a system with and without a draught tube by gradually increasing the tank size. It is known that without a tube, a surface vortex may be formed due to the swirling flow generated by the rotating impeller. This surface vortex flow does not exist in the present calculations by assuming that the upper surface is flat. According to Fig. 13(*a*), the circulation number N_Q for the case without a draught tube is almost linearly related to the tank diameter D in the considered range. For low values of D, the system with a draught tube is superior to that without one. However, it loses superiority when $D>4d$. For the sake of better understanding this result, the mean axial velocity profiles (averaged over the entire circumference) for $D/d=5.0$ at midheight of the tank are shown in Fig. 14. It is seen that by removing the tube, the downward flow induced by the impeller continuously extends to the region far away from the impeller, the point at which the axial velocity $V_z=0$ is the center of the circulation loop. The variation of this circulation center with the tank diameter is shown in Fig. 15. It is evident that the location of this circulation center is nearly proportional to the tank diameter. This explains the previous observation that the flow number N_Q is linearly related to D when the draught tube is not incorporated. It is interesting to notice that for the large tank with $D=5.0d$ shown in Fig. 14, a small amount of induced circulating fluid between the draught tube and the wall of the tank bypasses the tube and flows over the outside surface of the tube. As an illustration of the flow field, the streamlines on a vertical plane for the $D/d=5$ case is prepared in Fig. 16. With the draught tube, there exist small vortices near the inlet and the outlet regions just outside the tube together with the primary circulating loop flow. By removing the tube, the above observed vortices disappear. However, owing to the reduced strength of the downward pumping flow and the enlarged space, a vortex is formed beneath the impeller. It can be seen that without the restriction of the tube, the center of the induced looping flow moves away from the impeller, as discussed in the above.

The power number, shown in Fig. 13(*b*), is nearly a constant when the tank diameter D becomes greater than $2.5d$. The power consumption is much larger for the case with a draught tube, being about 2.2 times greater than that without a draught tube. This result is supported by the experiments of Chavan et al. [5]. The lower power consumption in the case without a draught tube is mainly ascribed to the large space between the impeller and the wall of the tank, which, in turn, leads to a reduction of pressure gradient and, thus, the power required, as discussed in Sec. 3.4.

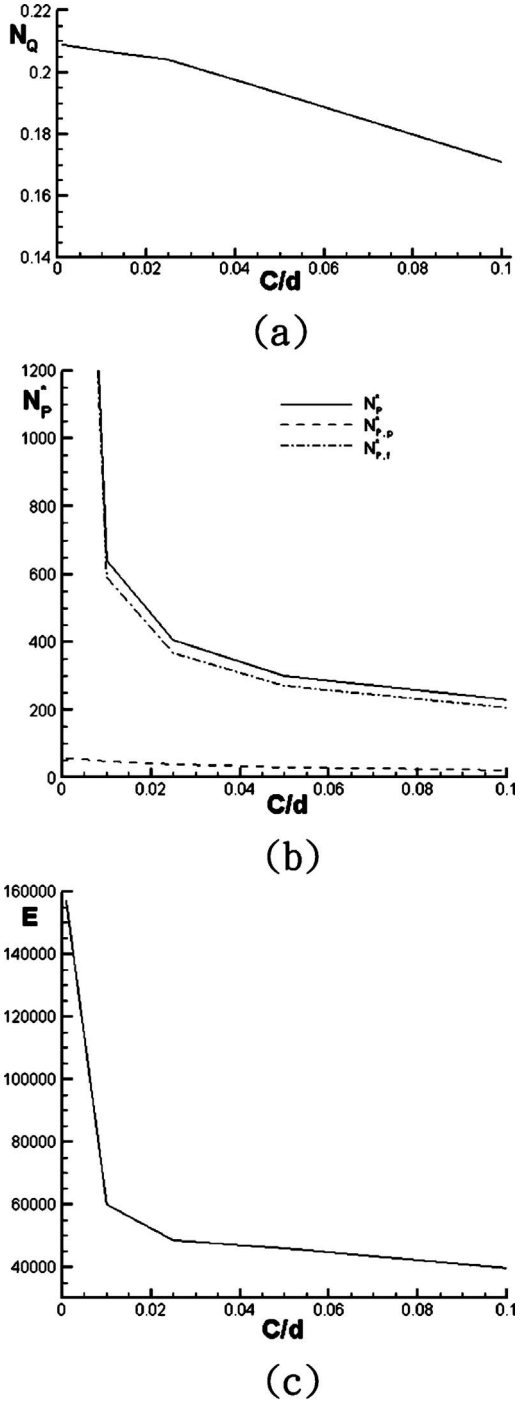

Fig. 12 Variation of (*a*) circulation number, (*b*) power number, and (*c*) mixing energy against clearance *C*

The mixing energy required, shown in Fig. 13(*c*), for the case with a draught tube is higher than that without a tube. The difference becomes very significant for large tanks.

4 Conclusions

A three-dimensional computational method has been employed to investigate the mixing flow stirred by a screw impeller with a draught tube. The main findings are summarized in the following.

(1) When the tank diameter is slightly greater than that of the draught tube, the narrow passage in the annular space outside the tube restricts the fluid flow and causes large power

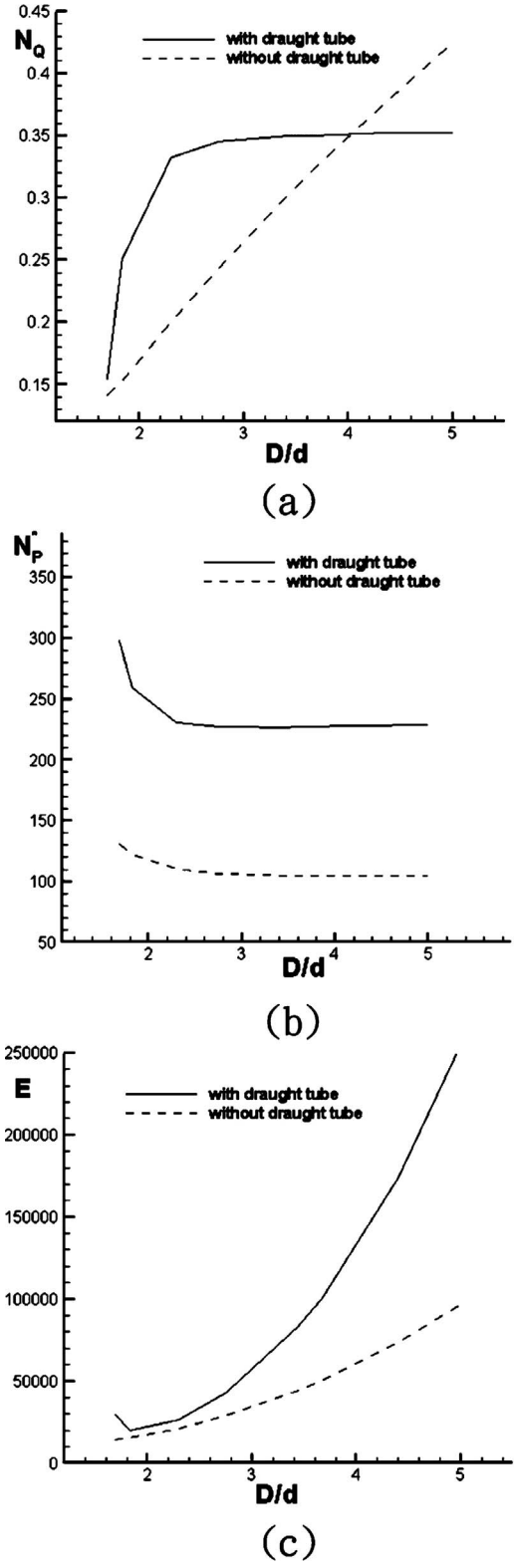

Fig. 13 Variation of (*a*) circulation number, (*b*) power number, and (*c*) mixing energy against tank diameter *D* for the screw impellers with and without a draught tube

consumption. Either the circulation number or the power number nearly reaches a constant for $D > 2.3d$. However, in terms of the total energy required for mixing, the optimum size of the tank occurs at $D=2d$.

(2) The increase in the shaft diameter leads to a decrease in channel height and, thus, reduction in fluid flow. The power requirement remains nearly a constant until $d_s=0.6d$. It is followed by an increase in power consumption due to the enhanced frictional force near the shaft surface.

(3) The flow inside the tube can be considered as a channel

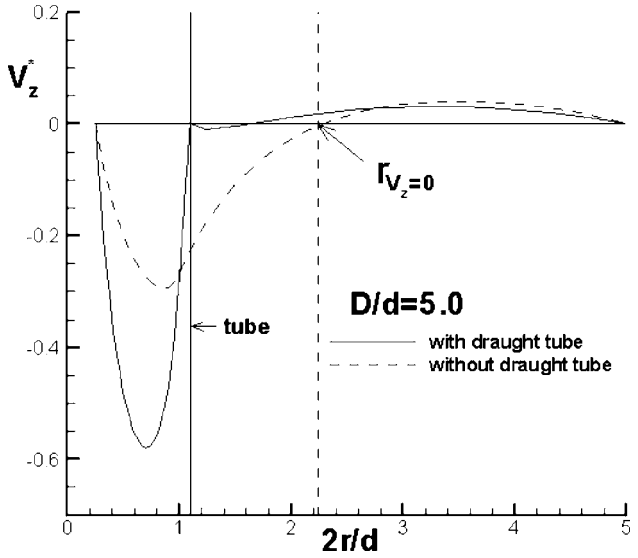

Fig. 14 Distribution of axial velocity along the radial direction for the screw impellers with and without a draught tube

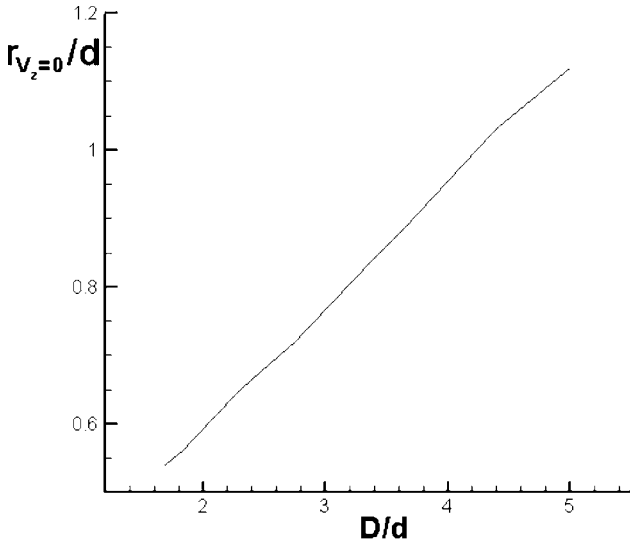

Fig. 15 Variation of circulation center with tank diameter for the case without a draught tube

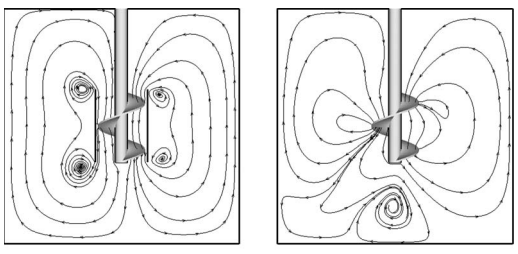

Fig. 16 Flow streamlines on a vertical plane for the screw mixer (*a*) with a draught tube and (*b*) without a draught tube

flow with a moving wall. When the impeller pitch decreases, the velocity component of the moving wall along the channel is increased, but the channel is lengthened and narrowed, resulting in larger frictional resistance. Thus, there exists an optimum value of pitch, which holds at $s/d=1.5$.

(4) The flow leakage from the pressure side to the suction side in the clearance gap brings about a reduction in the pressure difference between the two side surfaces of the impeller blade and, hence, reduces the pressure rise in the tube. As a consequence, both the flow rate and the power requirement decrease.

(5) Without a draught tube, the circulating flow rate is linearly proportional to the size of the tank. Therefore, for sufficiently large tanks, the induced flow rate becomes greater than the system with a draught tube. The linear relationship resulted from the radial movement of the center of the circulating flow. The power requirement for that without a draught tube is about half of that of the system with a draught tube. The lower power required is mainly due to the lower pressure gradients caused by the open space between the impeller and the wall of the tank.

Acknowledgment

This work was supported by the National Science Council of Taiwan, R.O.C. under the Contract No. NSC 96-2221-E-009-135-MY2.

Nomenclature

A_s = sidewall area of pumping channel
A_z = cross-sectional area of pumping channel
C = clearance
d = impeller diameter
d_s = shaft diameter
D = tank diameter
e_j = unit vector in the jth direction of Cartesian coordinates
E = mixing energy $(=\pi(N_p^*/N_Q)(H/D)(D/d)^3)$
f = the faces of the control surface
E_z = axial component of the frictional force exerted on pumping channel walls
h = impeller length
h_1 = distance between the impeller and the top and bottom of the tank
H = liquid height in the tank
L = length of the channel for one revolution of impeller blade
n = rotational frequency of the screw impeller
N_p = power number $(=P/\rho n^3 d^5)$
N_p^* = power number $(=P/\mu n^2 d^3)$
$N_{p,f}^*$ = power number due to frictional force
$N_{p,p}^*$ = power number due to pressure force
N_Q = circulation number $(=Q/nd^3)$
p = pressure
p_{in} = pressure at the inlet of the pumping channel
p_{out} = pressure at the outlet of the pumping channel
p_p = pressure at the pressure side of the pumping channel
p_s = pressure at the suction side of the pumping channel
P = power consumption for a mixing vessel
Q = volumetric flow rate
r = radial distance
Re = Reynolds number $(=\rho nd^2/\mu)$
S = screw pitch
$\mathbf{s}_f$ = surface vector of the considered face
t = thickness of the screw blade
U_{gj} = grid velocity
V_w = moving wall velocity
V_z = axial velocity
V_θ = circumferential velocity
W = blade width

Greek Symbols

α = helical angle of the pumping channel
γ = blending factor
$\vec{\delta}$ = distance vector directed from the upwind node to the centroid of the face
$\vec{\delta}_{PC}$ = distance vector connecting the principal and the neighboring nodes
μ = fluid viscosity
ρ = fluid density
τ_c = circulation time
τ_m = mixing time
Ω_j = angular velocity of the screw impeller

Subscripts

C = neighboring node
f = face value
P = principal node

Superscripts

UD = the value evaluated at a node upstream of the face
$*$ = dimensionless variables

References

[1] Tatterson, G. B., 1991, *Fluid Mixing and Gas Dispersion in Agitated Tanks*, McGraw-Hill, New York.
[2] Paton, J. B., Squires, P. H., Darnell, W. H., Cash, F. M., and Carley, J. F., 1959, "Chap. 4 Extrusion," *Processing of Thermoplastic Materials*, E. C. Bernhardt, ed., Van Nostrand Reinhold, New York.
[3] Carley, J. F., 1962, "Single-Screw Pumps for Polymer Melts," Chem. Eng. Prog., **58**(1), pp. 53–58.
[4] Sykora, S., 1966, "Mixing of Highly Viscous Liquids," Collect. Czech. Chem. Commun., **31**, pp. 2664–2678.
[5] Chavan, V. V., Jhaveri, A. S., and Ulbrecht, J., 1972, "Power Consumption for Mixing of Inelastic Non-Newtonian Fluids by Helical Screw Agitators," Trans. Inst. Chem. Eng., **50**, pp. 147–155.
[6] Chavan, V. V., and Ulbrecht, J., 1973, "Power Correlations for Close-Clearance Helical Impellers in Non-Newtonian Liquids," Ind. Eng. Chem. Process Des. Dev., **12**(4), pp. 472–476.
[7] Chavan, V. V., and Ulbrecht, J., 1973, "Internal Circulation in Vessels Agitated by Screw Impellers," Chem. Eng. J., **6**, pp. 213–223.
[8] Seichter, P., Dohnal, J., and Rieger, F., 1981, "Process Characteristics of Screw Impellers With a Draught Tube for Newtonian Liquids: The Power Input," Collect. Czech. Chem. Commun., **46**, pp. 2007–2020.
[9] Seichter, P., 1981, "Process Characteristics of Screw Impellers with a Draught Tube for Newtonian Liquids: Pumping Capacity of the Impeller," Collect. Czech. Chem. Commun., **46**, pp. 2021–2031.
[10] Seichter, P., 1981, "Process Characteristics of Screw Impellers With a Draught Tube for Newtonian Liquids: Time of Homogenization," Collect. Czech. Chem. Commun., **46**, pp. 2032–2042.
[11] Carreau, P. J., Paris, J., and Guerin, P., 1992, "Mixing of Newtonian and Non-Newtonian Liquids: Screw Agitator and Draft Coil System," Can. J. Chem. Eng., **70**, pp. 1071–1082.
[12] Kuncewicz, C., Szulc, K., and Kurasinski, T., 2005, "Hydrodynamics of the Tank With a Screw Impeller," Chem. Eng. Process., **44**, pp. 766–774.
[13] Kuncewicz, C., and Pietrzykowski, M., 2001, "Hydrodynamic Model of a Mixing Vessel With Pitched-Blade Turbines," Chem. Eng. Sci., **56**, pp. 4659–4672.
[14] Tsui, Y.-Y., and Jung, S.-P., 2006, "Analysis of the Flow in Grooved Pumps With Specified Pressure Boundary Conditions," Vacuum, **81**, pp. 401–410.
[15] Tsui, Y.-Y., Chou, J.-R., and Hu, Y.-C., 2006, "Blade Angle Effects on the Flow in a Tank Agitated by the Pitched-Blade Turbine," ASME J. Fluids Eng., **128**, pp. 774–782.
[16] Tsui, Y.-Y., and Pan, Y.-F., 2006, "A Pressure-Correction Method for Incompressible Flows Using Unstructured Meshes," Numer. Heat Transfer, Part B, **49**, pp. 43–65.

Plasma-Based Flow-Control Strategies for Transitional Highly Loaded Low-Pressure Turbines

Donald P. Rizzetta
e-mail: donald.rizzetta@wpafb.af.mil

Miguel R. Visbal
e-mail: miguel.visbal@wpafb.af.mil

Air Force Research Laboratory,
Computational Sciences Branch,
Aeronautical Sciences Division,
AFRL/RBAC,
Building 146, Room 225,
2210 Eighth Street,
Wright-Patterson AFB, OH 45433-7512

Recent numerical simulations have indicated the potential of plasma-based active flow control for improving the efficiency of highly loaded low-pressure turbines. The configuration considered in the current and earlier simulations correspond to previous experiments and computations for the flow at a Reynolds number of 25,000 based on axial chord and inlet conditions. In this situation, massive separation occurs on the suction surface of each blade due to uncovered turning, causing blockage in the flow passage. It was numerically demonstrated that asymmetric dielectric-barrier-discharge actuators were able to mitigate separation, thereby decreasing turbine wake losses. The present investigation extends this work by investigating a number of plasma-based flow control strategies. These include the chordwise location of actuation, spanwise periodic arrays of actuators, multiple actuation in the streamwise direction, and spanwise-direct actuation. The effect of alternate plasma-force models is also considered. Solutions were obtained to the Navier–Stokes equations, which were augmented by source terms used to represent plasma-induced body forces imparted by an actuator on the fluid. The numerical method utilized a high-fidelity time-implicit scheme, employing domain decomposition to carry out calculations on a parallel computing platform. A high-order overset grid approach preserved spatial accuracy in locally refined embedded regions. Features of the flowfields are described, and resultant solutions are compared to each other, with a previously obtained control case, and with the base line situation where no control was enforced.
[DOI: 10.1115/1.2903816]

Keywords: plasma-based flow control, low-pressure turbine, high-fidelity scheme

Introduction

Low-pressure turbines are commonly utilized in the propulsion systems of unmanned air vehicles (UAVs) employed for reconnaissance and combat purposes. Due to a reduction in atmospheric density during high-altitude cruise, such low-pressure turbines may encounter Reynolds numbers, based on blade axial chord and inlet conditions, below 25,000. In this situation, boundary layers along a large extent of blade surfaces can remain laminar, even in the presence of elevated freestream turbulence levels. The laminar boundary layers are then particularly susceptible to flow separation over the aft portion of blade suction surfaces, causing blockage in flow passages and a significant reduction in turbine efficiency.

Recent experiments of low-pressure turbines [1] have investigated the feasibility of increasing the interblade spacing, thereby raising the per blade loading. For practical applications, a higher loading can reduce the turbine part count and stage weight. Increased blade spacing, however, is accompanied by more extensive boundary-layer separation on the suction surface of each blade due to uncovered turning, resulting in a further reduction in efficiency and additional wake losses. Unless these adverse circumstances for highly loaded low-pressure turbines can be overcome, ceiling limitations may be imposed for prolonged UAV operations.

A number of experimental investigations by Bons et al. [2–4] and by Sondergaard et al. [1,5] have explored the use of both steady and pulsed vortex generator jets, which may be actuated upon demand, as a means of flow control in low-pressure turbines. When installed, these devices can remain idle at sea level where flow along the blades is attached and activated at altitude when separation occurs. Extensive measurements verified that vortex generator jets dramatically reduced separation, resulting in decreased losses and increased efficiency. As an alternative to vortex-generating jets, other experiments have considered the use of plasma-based actuators for controlling turbine flowfields [6–10]. In addition to the absence of more complex mechanical or pneumatic systems, such devices have relatively low power requirements and can operate over a broad range of frequencies. Plasma actuation has also been considered in a number of other experimental studies including rotorcraft blade control [11], lift enhancement for stationary and oscillating airfoils [12–14], plasma flaps and slats [15], dynamic stall [16], tip clearances in turbine blades [17], bluff-body flows [18], and aerodynamic control of UAVs [19].

Advances in the speed and storage capacity of high-performance computing systems have allowed numerical simulation to emerged as a viable means for the investigation of flows through low-pressure turbines [20–29]. Computational studies have also been performed for the application of plasma-based actuators to flow control problems. Because these problems are typically characterized by transitional and turbulent flowfields, high-fidelity time-accurate three-dimensional approaches are required to properly account for the physical processes inherent in their description. Specification of plasma effects derived from fundamental principles is therefore computationally prohibitive. Thus, numerical simulations primarily have incorporated a simplified phenomenological model to represent plasma-induced body forces imparted by the actuator on the fluid field. This technique has allowed calculations for the control of wing sections [30], delta wings [31], wall-bounded flows [32], and other configurations.

Dielectric-barrier-discharge (DBD) actuators typically operate

Contributed by the Fluids Engineering Division of ASME for publication in the JOURNAL OF FLUIDS ENGINEERING. Manuscript received June 21, 2007; final manuscript received October 16, 2007; published online April 4, 2008. Assoc. Editor: Paul Durbin. Paper presented at the 37th AIAA Fluid Dynamics Conference and Exhibit, Miami, FL, June 25–28, 2007.

in the low radio frequency range (1–10 kHz) with voltage amplitudes of 5–10 kV. Experimental measurements indicate that time-averaged plasma-induced body forces generated by DBD devices are the dominant mechanism for exerting control. An overview of the design, optimization, and application of these actuators has been given by Corke and Post [8]. The investigation of Rizzetta and Visbal [33] provided companion simulations to both previous experiments and computations of plasma-based flow-control applications by exploring the use of a single asymmetric DBD actuator to mitigate separation on the suction surface of a highly loaded low-pressure turbine. Although the turbine blade geometry in that study corresponded to plasma-control experiments of Huang et al. [7,10], the interblade spacing was greater. Thus, no comparison with measured data was possible. The configuration, however, was identical to that of previous simulations for vortex-generating jet control of turbines [28,29]. The magnitude of the plasma-induced body force required for such control was examined, and both continuous and pulse-modulated actuations were considered. Novel use of counterflow actuation was also investigated.

The present work extends the simulations of Rizzetta and Visbal [33] by analyzing several DBD plasma-based flow-control strategies for the identical highly loaded low-pressure turbine configuration. Specifically, these include the chordwise location of actuators relative to separation, the use of spanwise periodic arrays of actuators, multiple actuations in the streamwise direction, and spanwise-direct actuation. The effect of alternate plasma-force models is also considered. Features of the flowfields are described, and resultant solutions are compared to each other, with a previously obtained control case, and with the base line situation where no control was enforced. Control effectiveness is quantified by calculation of the integrated wake total pressure loss coefficient.

Governing Equations and Numerical Method

The governing fluid equations are taken as the unsteady three-dimensional compressible unfiltered Navier–Stokes equations. After introducing a curvilinear coordinate transformation to a body-fitted system, the equations are cast in the following nondimensional conservative form:

$$\frac{\partial}{\partial t}\left(\frac{1}{\mathcal{J}}\mathbf{Q}\right)+\frac{\partial}{\partial \xi}\left(\mathbf{F}-\frac{1}{\mathrm{Re}_\infty}\mathbf{F}_v\right)+\frac{\partial}{\partial \eta}\left(\mathbf{G}-\frac{1}{\mathrm{Re}_\infty}\mathbf{G}_v\right)+\frac{\partial}{\partial \zeta}\left(\mathbf{H}-\frac{1}{\mathrm{Re}_\infty}\mathbf{H}_v\right)=D_c q_c \mathbf{S} \tag{1}$$

Here, t is the time, ξ, η, and ζ are the computational coordinates, $\mathbf{Q}$ is the vector of dependent variables, $\mathbf{F}$, $\mathbf{G}$, and $\mathbf{H}$ are the inviscid flux vectors, $\mathbf{F}_v$, $\mathbf{G}_v$, and $\mathbf{H}_v$ are the viscous flux vectors, and $\mathbf{S}$ is the source vector representing the effect of plasma-induced body forces.

Time-accurate solutions to Eq. (1) are numerically obtained by the implicit approximately factored finite-difference algorithm of Beam and Warming [34] employing Newton-like subiterations [35], which has evolved as an efficient tool for generating solutions to a wide variety of complex fluid flow problems. Second-order-accurate backward-implicit time differencing was used to obtain temporal derivatives.

The implicit segment of the algorithm incorporates second-order-accurate centered differencing for all spatial derivatives and utilizes nonlinear artificial dissipation [36] to augment stability. Efficiency is enhanced by solving this implicit portion of the factorized equations in diagonalized form [37]. Temporal accuracy, which can be degraded by the use of the diagonal form, is maintained by utilizing subiterations within a time step. This technique has been commonly invoked in order to reduce errors due to factorization, linearization, diagonalization, and explicit application of boundary conditions. It is useful for achieving temporal accuracy on overset zonal mesh systems and for a domain decomposition implementation on parallel computing platforms. Any deterioration of the solution caused by the use of artificial dissipation and by lower-order spatial resolution of implicit operators is also reduced by the procedure. Three subiterations per time step have been applied to preserve second-order temporal accuracy in the present application.

The compact difference scheme that is employed to evaluate spatial derivatives for the explicit part of the factored form of Eq. (1) is based on the pentadiagonal system of Lele [38] and is capable of attaining spectral-like resolution. This is achieved through the use of a centered implicit difference operator with a compact stencil, thereby reducing the associated discretization error. For the present computations, a fourth-order tridiagonal subset of Lele's system is utilized. The scheme has been adapted by Visbal and Gaitonde [39] as an implicit iterative time-marching technique, applicable for unsteady vortical flows. It is used in conjunction with a sixth-order low-pass Pade-type nondispersive spatial filter developed by Gaitonde et al. [40], which has been shown to be superior to the use of explicitly added artificial dissipation for maintaining both stability and accuracy on stretched curvilinear meshes [39]. The filter is sequentially applied to the solution vector in each of the three computational directions following each subiteration. A more thorough description of the governing equations and complete details of the numerical method appear in Ref. [41], but have been omitted here for brevity. Application of the subiteration process and use of the high-order filter scheme result in solutions with fourth-order spatial and second-order temporal accuracy.

The aforementioned features of the numerical algorithm are embodied in a parallel version of the time-accurate three-dimensional computer code FDL3DI [42], which has proven to be reliable for steady and unsteady fluid flow problems, including vortex breakdown [43,44], transitional wall jets [45], synthetic jet actuators [46], roughness elements [47], plasma flows [30–33], and direct numerical and large-eddy simulations of subsonic [23,48] and supersonic flowfields [49,50].

Empirical Plasma Model

Many quantitative aspects of the fundamental processes governing plasma/fluid interactions remain unknown or computationally prohibitive, particularly for transitional and turbulent flows. These circumstances have given rise to the development of a wide spectrum of models with varying degrees of sophistication that may be employed for more practical simulations. Among the simplified methods specifically focused on discharge/fluid coupling is that of Roth et al. [51,52], who associated transfer of momentum from ions to neutral particles based on the gradient of electric pressure. A more refined approach, suitable for coupling with fluid response, was an empirical model proposed by Shyy et al. [53] using separate estimates for the charge distribution and electric field. Known plasma physics parameters were linked to experimental data. This representation has been successfully employed for several previous simulations of plasma-controlled flows [30–33] and is also adopted as the primary model in the present investigation.

A schematic representation of a typical single asymmetric DBD plasma actuator is depicted in Fig. 1(*a*). The actuator consists of two electrodes that are separated by a thin dielectric insulator and mounted on the turbine blade surface. An oscillating voltage, in the kilohertz frequency range, is applied to the electrodes, developing an electric field about the actuator. When the imposed voltage is sufficiently high, the dielectric produces a barrier discharge that weakly ionizes the surrounding gas. Momentum acquired by the resulting charged particles from the electric field is transferred to the primary neutral molecules by a combination of electrodynamic body forces and poorly understood complex collisional interactions. In the numerical exploration of flow control strategies,

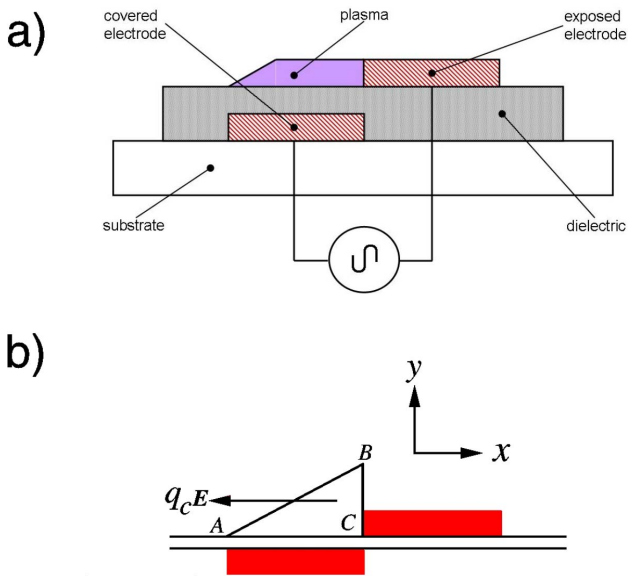

Fig. 1 Schematic representation of plasma actuator and geometry for empirical plasma-force model

the entire process may be modeled as a body force vector acting on the net fluid external to the actuator, which produces a flow velocity.

The model for the geometric extent of the plasma field generated by such an actuator is indicated in Fig. 1(*b*). The triangular region defined by Line Segments *AB*, *BC*, and *AC* constitutes the plasma boundary. Outside of this region, the electric field is not considered strong enough to ionize the air. The electric field has its maximum value on Segment *AC* and linearly varies within *ABC*. The peak value of the electric field is obtained from the applied voltage and the spacing between the electrodes. Along the Segment *AB*, the electric field diminishes to its threshold value, which was taken as 30 kV/cm [53]. The electric body force is equal to $q_c\mathbf{E}$ and provides coupling from the plasma to the fluid, resulting in the source vector $\mathbf{S}$ appearing in Eq. (1). It is assumed that this force locally acts tangential to the blade surface. Because the charge density is assumed to be constant within Region *ABC* [53], its nondimensional representation q_c is taken as unity, corresponding to the value of 1.0×10^{11} electrons/cm^3 [53]. The plasma scale parameter D_c arises from nondimensionalization of the governing equations, represents the ratio of the electrical force of the plasma to the inertial force of the fluid, and is defined as

$$D_c = \frac{\rho_c e_c E_r c}{\rho_\infty u_\infty^2} \tag{2}$$

where $\rho_c=1.0\times10^{11}$ electrons/cm^3, $e_c=1.6\times10^{-19}$ C, and E_r is a reference electric field magnitude.

Some specific details of the plasma model incorporated in the present simulations were specified corresponding to the turbine blade experiments of Huang et al. [7,9,10]. The ratio of the threshold electric field magnitude to its peak value was set to 0.043. Referring to Fig. 1(*b*), Distances *BC* and *AC* nondimensionalized by the blade chord were specified as $BC=0.0125$ and $AC=0.0250$. These values are similar to those employed in previous simulations for winglike configurations [30–32]. For the purposes of the present computations, it is assumed that the actuator is mounted flush with the turbine blade surface and does not protrude above it. Due to empiricism of the formulation, there is some ambiguity regarding the value of the scale parameter D_c. Another unresolved issue is the direction of the force imposed on the flowfield. For the empirical model, we assign a component only in either the negative x (counterflow) or positive z (spanwise) direction, approximately tangent to the blade surface. This representation is consistent with previous simulations [30–33].

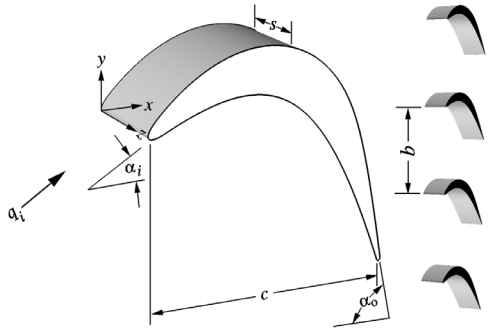

Fig. 2 Schematic representation of the turbine blade configuration

Details of the Computations

Shown in Fig. 2 is a schematic representation of the turbine blade shape, given by the Pratt & Whitney "PakB" research design, which is a Mach number scaled version of geometries typically used in low-pressure turbines [1–5]. This blade geometry has an inlet flow angle $\alpha_i=35.0$ deg and a design exit flow angle $\alpha_o=60.0$ deg. The axial chord to spacing ratio (solidity) is 0.75, resulting in an interblade spacing $b=4/3$.

Computational Meshes. To conserve computational resources, only a single turbine blade passage is considered, and periodic conditions are enforced in the vertical direction (y) to represent a single turbine stage flowfield. The computational domain surrounding the blade was described by a body-fitted mesh system, whose origin was located at the inboard leading edge of the blade (see Fig. 2). The mesh employs an *O*-grid topology and was elliptically generated using automated software [54]. Figure 3(*a*) exhibits the basic grid about the turbine blade, which was comprised of 348 points in the circumferential direction (I), 189 points in the blade-normal direction (J), and 101 points in the spanwise direction (K). Minimum spacing in the J direction occurs at the blade surface. Mesh points for $1\leqslant I\leqslant 5$ and $I_{\max-4}\leqslant I\leqslant I_{\max}$ are coincident in an overlap region at the blade leading edge so that periodic conditions in the circumferential direction may be enforced in order to complete the *O*-grid construct. In order to apply periodic conditions in the vertical direction, the streamwise (x) point locations and vertical spacing along $I_{1u}-I_{2u}$ are identical to those along $I_{1l}-I_{2l}$ for $J_{\max-4}\leqslant J\leqslant J_{\max}$.

To properly capture the correct fluid physics for these flow control simulations, the basic grid structure was modified to enhance resolution in the actuator and near-wall regions. This was done by removing points in the suction surface grid, signified by the blanked area in the *O*-grid of Fig. 3(*a*), and replacing them with an embedded refined mesh, as seen in Fig. 3(*b*). This technique is identical to that which was successfully employed by Rizzetta and Visbal [28,29,33] in similar computations. The size of the refined-mesh region was $(313\times185\times101)$ grid points in (I,J,K) respectively.

In order to facilitate application of inflow and outflow conditions to the turbine blade domain, overset grids were utilized upstream and downstream of the blade region. These are found in Fig. 3(*c*) and consisted of $(46\times61\times101)$ and $(31\times75\times101)$ mesh points in the streamwise, vertical, and spanwise directions for the upstream and downstream domains, respectively. The total number of grid points in all domains was approximately 12.0

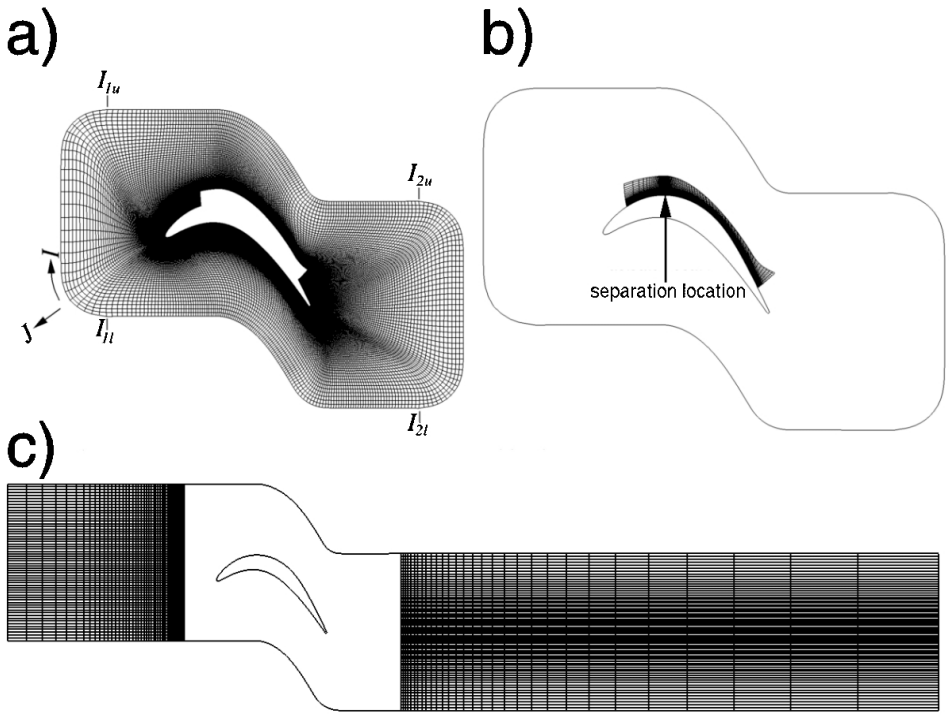

Fig. 3 Turbine blade computational mesh system

$\times 10^6$, which should provide adequate resolution for the present computations, based on the grid refinement study for the base line case of Ref. [28].

Temporal Considerations. Operationally, DBD actuators are inherently unsteady devices. Within the context of the empirical model, however, the body force imposed on the fluid is assumed to be steady, owing to the high frequency of the applied voltage (typically 5–10 kHz). These devices may also be operated in a pulsed manner as described by Corke and Post [8], thereby reducing total power consumption. The pulsed mode of operation also introduces low-frequency forcing to the flow, which may be more receptive to control, and offers the potential of improved effectiveness. For simulation of pulsed actuation, the forcing amplitude is modulated according to a prescribed duty cycle. The duty cycle is the portion of the fundamental forcing period over which the device is active, which was 50% in the present case. It should be noted that the applied forcing wave form introduces multiple harmonics of the primary frequency, as was demonstrated in Refs. [28,32]. The nondimensional forcing frequency $\mathcal{F}=7.56$ is identical to that of previous experiments [2–5] and simulations [28,29,33] with

$$\mathcal{F} = cf/u_\infty \bar{q}_i \tag{3}$$

All of the computations presented here were obtained using a time step of $\Delta t = 1.47 \times 10^{-4}$, where t is nondimensionalized by reference quantities. Based on inflow conditions, this corresponds to a time increment of approximately $\Delta t_i = 1.20 \times 10^{-4}$ and represents 1300 time steps/cycle of the pulsing frequency. Flowfields for each case were initialized from previously obtained solutions and processed for 104,000 time steps in order to remove transients and attain an equilibrium state. Final results were then evolved for an additional 104,000 time steps during which statistical information was collected. Statistics were monitored to assure that a converged sample was achieved. This duration represents approximately 12.2 characteristic time units, based on the inflow velocity, and corresponded to 80 cycles of pulsed control.

Boundary Conditions. Inflow and outflow conditions for the complete turbine blade domain were obtained in a manner consistent with subsonic internal flows, which have commonly been employed in Reynolds-averaged Navier–Stokes applications [55]. Along the upstream boundary, the total pressure, total temperature, and inlet flow angle were specified, and the velocity magnitude was obtained from the interior solution. Downstream, the exit static pressure (p_∞) was fixed, and other flow variables were extrapolated from within the domain. Because the inflow velocity develops as part of the solution, the Reynolds number based on the inflow conditions was not known a priori. A reference Mach number (M_∞) of 0.1 was selected for all computations. For the base line solution, the reference Reynolds number (Re_∞) was adjusted to match the desired inflow condition, Re. This same Reynolds number was then employed in the current simulations. When flow control was applied, however, the inflow velocity magnitude increased due to a reduction in blockage in the blade passage. Although this situation was anticipated, the reference Reynolds number was not altered. Thus, the inflow Reynolds numbers are somewhat higher than the nominal value of 25,000. This approach for the inflow and outflow boundaries was previously employed by Rizzetta and Visbal [23,28,29,33] in similar computations.

Periodic conditions were applied along the upper and lower portions of the turbine blade as previously indicated in Fig. 3(*a*). Periodic conditions were also applied along the upper and lower horizontal boundaries of the upstream and downstream domains displayed in Fig. 3(*c*). The downstream domain was intentionally severely stretched in the streamwise direction to prevent spurious reflections from the outflow boundary. This technique transfers information to high spatial wave numbers and then dissipates it by the low-pass filter [56]. Flow variables in all regions of overlapped meshes were obtained from explicit sixth-order accurate Lagrangian interpolation formulas, including the upstream and downstream domains, the turbine blade grid, and the refined-mesh region. The interpolation approach for high-order numerical solu-

Table 1 Description of cases

Actuator type	Configuration (see Fig 4)	Control direction	Actuator location	s	D_c	Plasma-force model	C_w
None [33]	NA	NA	NA	0.20	NA	NA	1.02
DBD [33]	A	Counterflow	x_a=0.34	0.20	25.0	Empirical [53]	0.19
DBD	A	Counterflow	x_a=0.34	0.20	10.0	Empirical [53]	0.32
DBD	A	Counterflow	x_a=0.34	0.20	6.25	Empirical [53]	0.27
DBD	A	Counterflow	x_a=0.34	0.20	25.0	Basic principles [61–63]	0.29
DBD	A	Counterflow	x_a=0.34	0.20	25.0	Potential [64,65]	0.51
DBD	B	Counterflow	x_a=0.24	0.20	25.0	Empirical [53]	0.14
DBD	C	Counterflow	x_a=0.34, 0.67	0.20	25.0	Empirical [53]	0.15
DBD	D	Counterflow	x_a=0.34	0.10	25.0	Empirical [53]	0.62
DBD	E	Spanwise	x_a=0.34	0.05	25.0	Empirical [53]	0.65
DBD	F	Spanwise	x_a=0.3–0.8	0.10	25.0	Empirical [53]	1.18
Jet [29]	NA	Spanwise	x_a=0.37	0.20	NA	NA	0.48

tions has been successfully applied by Sherer [57] for the simulation of fluid dynamic and acoustic problems. As previously stated, periodic conditions were invoked in the spanwise direction. On the blade surface, the no slip condition was enforced along with an isothermal wall and a fourth-order accurate representation of zero normal pressure gradient.

Domain Decomposition. For parallel processing, the previously described computational domains were decomposed into a series of subzones, which were then distributed on individual processors of a massively parallel computing platform (HP XC Opteron). Decompositions were constructed to provide an approximately equal number of grid points in every subzone, thereby balancing the computational work load among the processors. Faces at the boundaries of each subzone block were overset into adjacent domains, such that an overlap of five planes was established. Although this incurred an overhead due to redundant computation, it maintained the formal high-order accuracy of both the numerical differencing and filtering schemes. Because a vast majority of the overlapping mesh points of the respective decompositions were coincident, no further interpolation was required. Automated software [58] was used to identify donor and recipient grid points in the overlapping domains. Internode communication among the processors was established through standard message-passing interface (MPI) library routines [59], which were used to transfer information between the various subzones of the flowfield at domain boundaries. A total of 176 processors were employed for all of the computations reported here.

Overview of the Simulations

The numerical results of Rizzetta and Visbal [33] provided an initial study of single asymmetric DBD actuator flow control for a highly loaded low-pressure turbine blade. That work confirmed that effective control and a resultant increase in turbine efficiency could be achieved with a plasma force. One aspect of the study determined the magnitude of the scale parameter D_c, which is required to maintain time-mean attached flow along the blade suction surface. In addition, comparisons were made between pulsed and continuous controls, and coflowing and counterflowing orientations of the actuator. It was found that the most effective control was obtained with counterflow pulsed actuation for D_c=25.0. This value of D_c corresponds to a fairly low power requirement, easily attainable by modern plasma actuators. For comparison, the value of D_c corresponding to the experiments of Huang et al. [7,9,10], which employed less refined plasma-generating devices, was estimated to be 23.4.

All the simulations of Rizzetta and Visbal [33] utilized full-span actuation, where the spanwise extent of the computational domain s was taken as 0.2. This value of s was found to be adequate to capture the transitional flowfield in the prior investigation of Ref. [23] and is also used here for full-span actuator configurations. Based on the results of Ref. [33], only pulsed actuation is considered here, using a 50% duty cycle.

Three-dimensional simulations were carried out for nine specific cases, which are summarized in Table 1. Also provided in Table 1 are the base line (no control) and benchmark (counterflow, Configuration A, D_c=25.0) results from Ref. [33] and a vortex-generating jet case from Ref. [29], which are included for comparison. These configurations are represented in Fig. 4, where the arrows indicate the actuation direction. It can be noted in the figure that Cases A, B, C, and D represent counterflow actuation, while Cases E and F correspond to spanwise oriented actuators. From the time-mean flowfields, control effectiveness may be quantified by calculation of the integrated wake total pressure loss coefficient C_w defined as

$$C_w = \frac{1}{s(y_{\max} - y_{\min})} \int_0^s \int_{y_{\min}}^{y_{\max}} \left(\frac{P_{ti} - \bar{P}_{to}}{P_{ti} - \bar{p}_i} \right) dy dz \tag{4}$$

Equation (4) is evaluated along the upstream boundary of the downstream mesh in Fig. 3(*c*), which is located 0.67 chords downstream of the blade trailing edge. Values of C_w for each case appear in Table 1. For the benchmark case [33], the actuator was located just upstream of separation in the time-mean flowfield of the base line solution, which occurred at x=0.37. In sections to follow, results of these simulations will be presented in three groups, corresponding, respectively, to counterflow and spanwise actuation employing the empirical plasma model, and the effect of different plasma models upon the benchmark configuration. Inflow conditions and computational mesh spacings given in wall units are listed in Ref. [41].

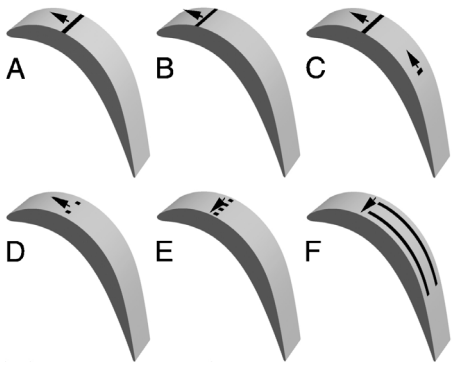

Fig. 4 Actuator configurations

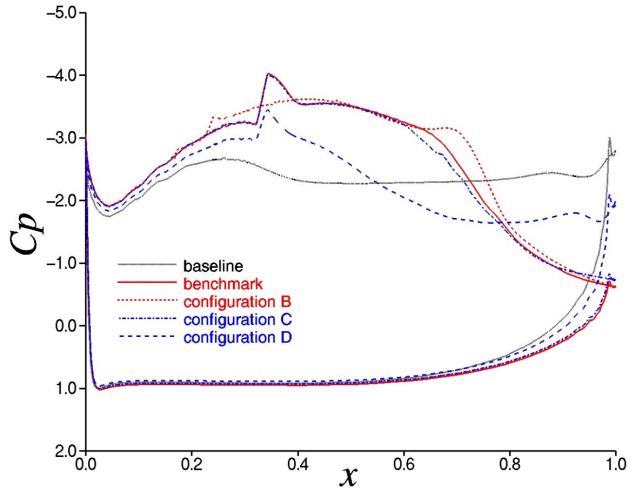

Fig. 5 Time-mean surface pressure coefficient distributions for counterflow actuation

Results for Counterflow Actuation

Counterflow actuation configurations correspond to Cases A, B, C, and D, which are seen in Fig. 4. As previously noted, the benchmark simulation incorporated full-span actuation with $x_a = 0.34$. Locating the actuator further upstream from the separation point was explored with Configuration B. It was thought that at lower Reynolds numbers, separation would move upstream. If control could be effective when placed at a more forward position, then efficiency enhancement would be maintained over a wider range of operating conditions (i.e., Reynolds numbers). With Configuration B, the full-span actuator was positioned 10% of the blade chord further upstream than its location in Configuration A such that $x_a = 0.24$.

Configuration C consists of dual actuators. In addition to a full-span actuator at the benchmark location ($x_a = 0.34$), a second finite-span actuator (array) is situated at the downstream location $x_a = 0.67$. This was done in order to help promote transition to more fully turbulent flow, and break down coherent two-dimensional structures, which formed in the benchmark simulation. The spanwise extent of the second actuator was 0.1, and its interactuator spacing was also 0.1. The use of a single array of spanwise distributed counterflow actuators, located at the benchmark position ($x_a = 0.34$), was examined with Configuration D. For this case, the spanwise extent of the actuator was 0.05 and the interactuator spacing was 0.05.

Although not the primary focus of this study, the use of extremely small levels of the plasma control force was also explored for the benchmark configuration by employing values of the scale parameter D_c, which were less than 25.0. Results for D_c equal to 10.0 and 6.25, respectively, can be found in Table 1. It is seen that even for these low values of D_c, a reduction in the wake total pressure low coefficient C_w of about 70% is possible. No other results corresponding to these solutions will be presented. Apart from these two cases, all other simulations in the investigation were carried out for $D_c = 25.0$.

Features of the Time-Mean Flowfields. Time-mean surface pressure coefficient distributions for counterflow actuation cases are presented in Fig. 5. These results were obtained along the centerline of the computational domain for each solution. The large plateau region in the base line distribution is characteristic of a massively separated flow. The dominant effect of flow control is to reduce separation of the time-mean flowfield on the blade suction surface. This reduces blockage and increases the inflow velocity, thereby decreasing pressure on the upstream portion of the suction surface, while increasing it downstream, relative to the base line case. Cases B and C effectively eliminated the plateau. This was achieved because the flow was aligned with the blade surface, and was also true for the benchmark solution. Although the finite-span case (Configuration D) reduced the extent of separation, a smaller plateau is still present. Based on the wake total pressure loss coefficient C_w, Cases B and C were slightly more effective than the benchmark arrangement (see Table 1).

Profiles of the time-mean velocity magnitude for the counterflow cases are observed in Fig. 6. These profiles were extracted along lines (n) normal to the blade surface at each x-station on the periodic spanwise boundary. Magnitudes shown in the figure have been normalized by the inflow velocity q_i. Particularly notable is increased fullness of the profiles for Cases B and C relative to the base line solution near the trailing edge ($x = 0.9$). This is not true for Case D.

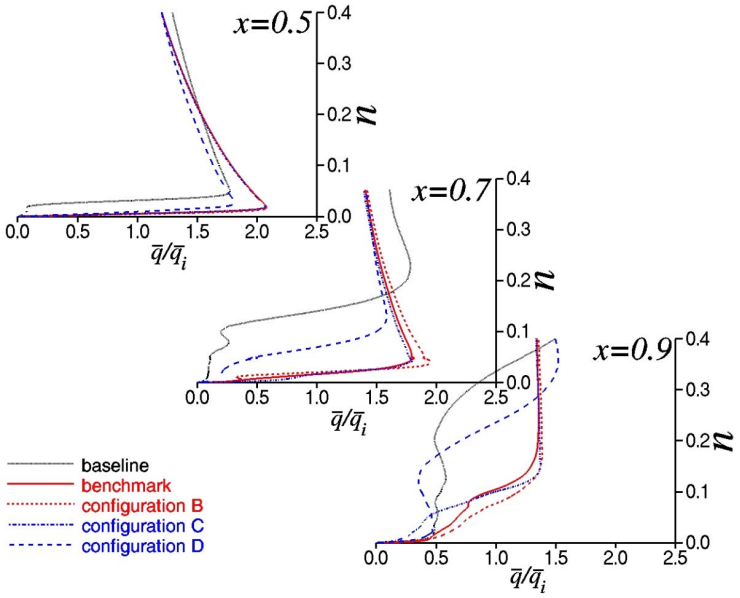

Fig. 6 Time-mean velocity magnitude profiles for counterflow actuation

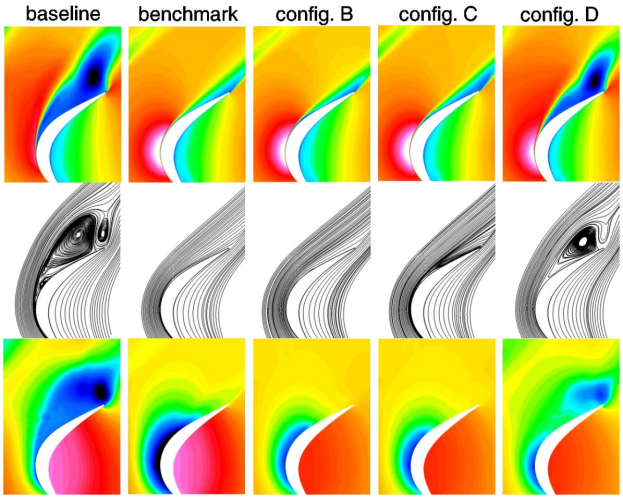

Fig. 7 Time-mean planar contours of *u* velocity, streamlines, and planar contours of C_p for counterflow actuation

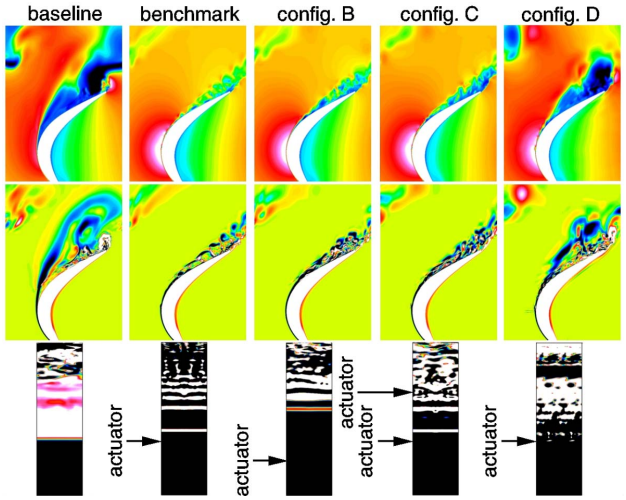

Fig. 9 Instantaneous planar contours of *u* velocity, planar contours of spanwise vorticity, and contours of spanwise vorticity on the blade surface for counterflow actuation

A composite visual comparison of the flowfields for these cases is exhibited in Fig. 7. Contours of u velocity are displayed in the top row of the figure, streamlines in the middle row, and pressure coefficient (C_p) at the bottom. Massive separation in the base line case is apparent. Results depicted here are consistent with those of the surface pressure distributions (Fig. 5). Streamlines illustrate the massively separated flow of the base line case. Body conforming time-mean flow is evident in the figure for the benchmark result and Cases B and C. Although these flows include very small regions of shallow separation, for practical purposes, they may be considered to be fully attached up to the blade trailing edge. A reduction in the separated flow region is observed for Case D. The thin wakes for Cases B and C, relative to the base line flow, are visible in the u contours. The effect of separated flow regions occurring for the base line case and Configuration D is reflected in the C_p contours.

Features of the Unsteady Flowfields. Profiles of the root-mean-square fluctuating velocity magnitude, on the spanwise periodic boundary, at several streamwise locations are found in Fig. 8. Fluctuations in the base line case evolve from unsteadiness of an unstable shear layer. In the control situations, root-mean-square velocity magnitudes also contain contributions due to pulsed actuation. As a result, the location of the maximum fluctuation generally occurs further from the blade surface in the base line solution. Although the peak fluctuating velocity magnitude for Configurations B and C and the benchmark is larger than that of the base line for $x=0.7$ and $x=0.9$, actuation reduces high fluctuating velocity in the outer portion of the profile ($n>0.25$) caused by massive separation. With Configuration D, separation has not been as effectively controlled, so that the profile at $x=0.9$ is similar to that of the base line.

A composite representation of the instantaneous flowfields for these cases appears in Fig. 9. Contours of u velocity and spanwise vorticity along the centerline plane are seen in the top and middle rows of the figure, respectively, while spanwise vorticity on the blade surface viewed from above is at the bottom. The middle row

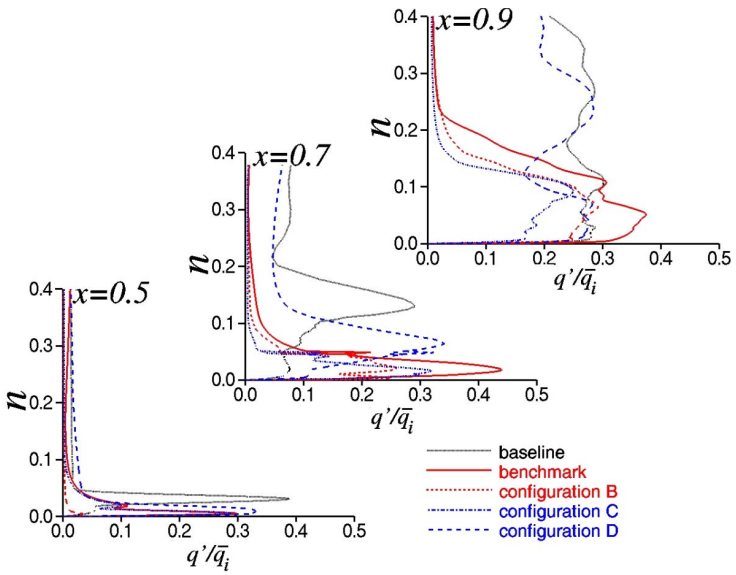

Fig. 8 Root-mean-square fluctuating velocity magnitude profiles for counterflow actuation

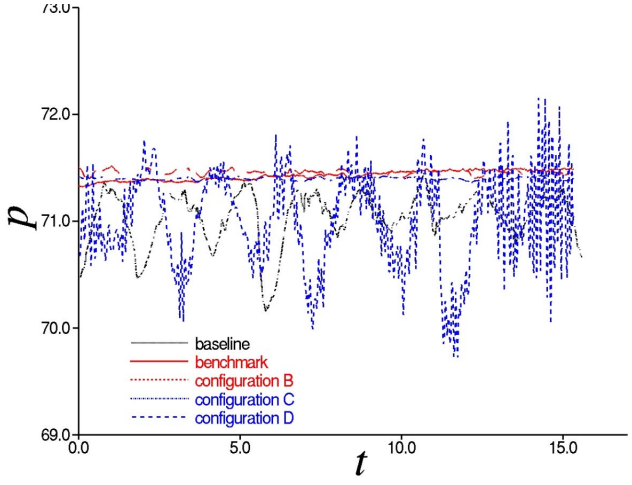

Fig. 10 Trailing edge surface pressure time history for counterflow actuation

of spanwise vorticity is particularly useful for understanding the control mechanisms. It was shown in Ref. [33] for the benchmark case that control was imposed by modifying the inherently unstable boundary layer near its separation point. The plasma actuator forced the boundary layer to roll up into small vortices just downstream of the actuator location. These vortices were shed at a frequency one-half that of the pulsed control and convected downstream at a distance from the blade surface that was not large. This greatly enhanced mixing and brought higher momentum fluid into the boundary layer, thereby maintaining time-mean attached flow and reducing wake losses. The fairly coherent vortical structures are visible in the spanwise vorticity contours (middle row) of the benchmark solution. Dark portions of the surface vorticity (bottom row) signify regions of attached flow.

For Configuration B, actuation was applied further upstream from separation than in the benchmark case and expedited transition. As a result, no coherent vortices evolved, and the flowfield was dominated by fine-scale fluid structures. Configuration C was specifically designed to eliminate fluid coherence. It was believed that coherence could promote structural fatigue and be detrimental to instrumentation and acoustic signature for turbine applications. The approach with Configuration C was to apply a second counterflow actuator downstream of the first to help break down coherent structures. In addition, the second actuator was of finite span, so as to reduce two-dimensional effects. It is noted for Configuration C in Fig. 9 that only fine-scale structures are present. Both Configurations B and C have wake total pressure loss coefficients that are slightly less than the benchmark case (see Table 1).

Configuration D considered only a single finite-span counterflow actuator at the same location as that of the benchmark case. Although some control was exerted in this situation, the actuation was not as effective as the benchmark. The arrangement failed to manipulate the boundary layer in a useful manner or to generate transition. Effectiveness arose only through enhanced mixing.

Time histories of the nondimensional trailing-edge pressure are indicated in Fig. 10. Sizable excursions in the base line case and Configuration D correspond to the shedding of large vortical structures. Because massive separation and the associated vortex shedding have been mitigated for Cases B and C and the benchmark, pressure fluctuations are greatly reduced.

Turbulent kinetic energy frequency spectra for Configuration B are displayed in Fig. 11. The data used to generate these spectra were collected at a distance of $n=0.03$ from the blade surface. This length ($n=0.03$) is approximately equal to one-half of the boundary-layer thickness of the time-mean velocity profile upstream of separation in the base line case. Near the actuator location ($x=0.5$), the discrete peaks in E_ω for the control cases correspond to harmonics of the pulsing frequency. The occurrence of this behavior is identical to that for pulsed vortex-generating jets, which was described in detail in Ref. [29]. At $x=0.7$, subharmonics of the pulsing frequency have been excited in the benchmark spectra. As was previously noted, this phenomenon was caused by the small vortices generated in the boundary layer downstream of the actuator. No subharmonics are apparent for Configuration B, as the small coherent vortical structures have been suppressed. Turbulence levels of the benchmark solution are higher than the base line at $x=0.5$ and $x=0.7$ due to energy being added to the flowfield. Peak levels of Configuration B are higher than the benchmark at these location, although the broadband content is lower. Farther downstream in the trailing-edge region ($x=0.9$), all

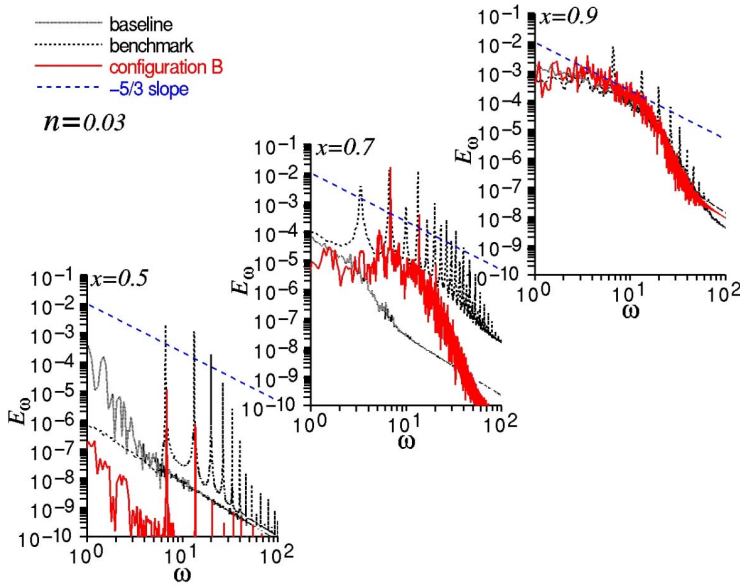

Fig. 11 Turbulent kinetic energy frequency spectra for counterflow actuation Configuration B

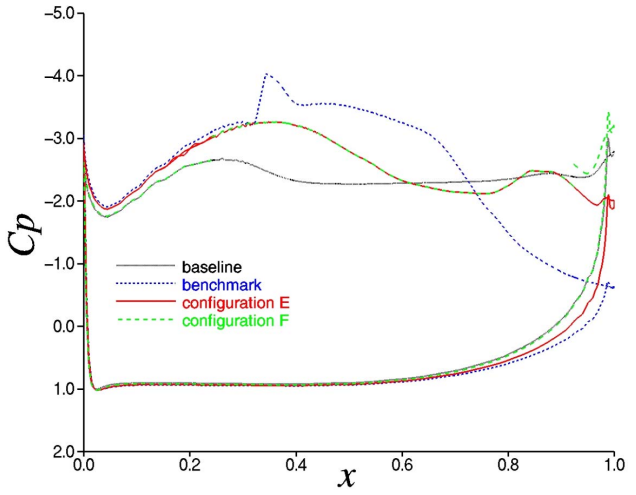

Fig. 12 Time-mean surface pressure coefficient distributions for spanwise actuation

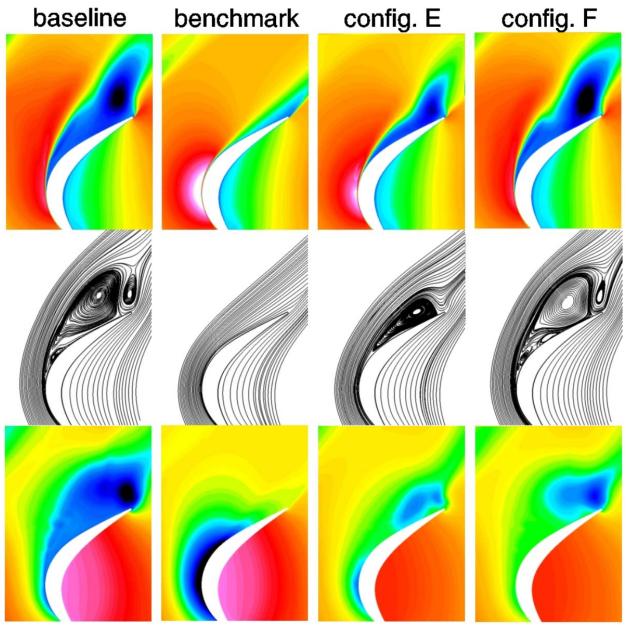

Fig. 13 Time-mean planar contours of *u* velocity, streamlines, and planar contours of C_p for spanwise actuation

respective spectra attain a similar level. Peaks associated with actuation in the benchmark case at this location are not present for Configuration B. A small inertial range in the spectra can be observed in all results. Additional details of both the time-mean and unsteady flowfields may be found in Ref. [41].

Results for Spanwise Actuation

Cases E and F represent configurations where actuators were oriented such that the plasma force was directed in the spanwise direction. This is similar to experimental [1–5] and computational [23,28,29] investigations using vortex-generating jets. Configuration E considers a distributed array of actuators, which are short in the streamwise direction. Actuators that have an axial length equal to one-half of the blade chord are represented by Configuration F. This type of actuation has been proposed to control the fully turbulent flow for a plate-mounted "hump" model [60], which is somewhat different than the transitional situation being examined here.

Time-mean surface pressure coefficient distributions for these cases are presented in Fig. 12. Some reduction in the pressure plateau is visible, but these distributions are less favorable than the benchmark result. Although some control was exerted for these configurations, they were not as effective as the benchmark case. The composite flowfield comparison for these cases is illustrated in Fig. 13. This figure is similar to Fig. 7, where *u* velocity, streamlines, and pressure coefficient are found in the top, middle, and bottom rows, respectively. Massive separation is seen to occur for Configuration F, much like the base line case. The wake loss coefficient for this configuration is actually higher than that of the base line (see Table 1). The reason for this behavior is that the spanwise-directed force, applied over a long axial extent, tended to displace the boundary layer away from the blade surface without generating appreciable mixing or promoting transition, thereby increasing blockage in the blade passage. Supplementary figures of both the time-mean and instantaneous flowfields for these configurations are provided in Ref. [41].

Effect of Alternate Plasma-Force Models

Due to its simplicity, ease of application, and low computational requirements, the empirical plasma-force model was used to explore a number of actuator configurations for the complex turbine blade flowfield. Because of some uncertainties in its formulation and implementation, however, two other plasma-force models were employed in the simulation of Configuration A, analogous to the benchmark case. These include the force distribution obtained from a computation founded on basic principles [61–63] and that derived from a potential formulation [64,65].

The basic-principles approach employs the charge density and electric field in order to provide the force distribution about the actuator. These are obtained from a two-dimensional three-species collisional plasma-sheath model, which includes the charge and momentum continuity equations. Gauss's law is invoked for the electric potential. As air chemistry for many of the important processes that occur during plasma formation is poorly understood, the working fluid was assumed to be helium. The governing equations were solved with a multiscale ionized gas flow code using a finite-element procedure to overcome the equation stiffness generated by multispecies charge-separation phenomena. More complete details of the computation are available in Refs. [61–63].

The potential force model utilizes Maxwell's equation and Gauss's law to represent the charge density in terms of the electric field potential. Boltzmann's relationship is then applied, and after some approximations are made, a single elliptic equation for the electric potential may be obtained. Boundary conditions on the actuator electrode surfaces are obtained from a lumped-element electric circuit model, accounting for the charging of the dielectric during the alternating current cycle. Both the charge density and electric field may be calculated from the potential, thus supplying the force distribution. References [64,65] furnish more details about development and application of the model.

Force distributions resulting from both the basic-principles and potential force models were averaged in time over one actuation cycle. These time-mean distributions were then modulated according to the 50% duty cycle. This same procedure was previously employed for the basic-principles model by Gaitonde et al. [66] and by Visbal et al. [32] in the plasma control of wing stall. To maintain consistency among all the approaches, the axial extents of the actuators were scaled to match that used with the empirical model. In addition, the maximum force magnitudes were also made identical to that of the empirical model. Therefore, it is primarily differences in the spatial plasma-force distributions that are being considered. Alternative techniques for scaling the plasma-force components are certainly possible [66].

Force distributions created by each of the respective models are displayed in Fig. 14. Contours of the *x* and *y* force components, and the resultant force vector are observed in vertical columns

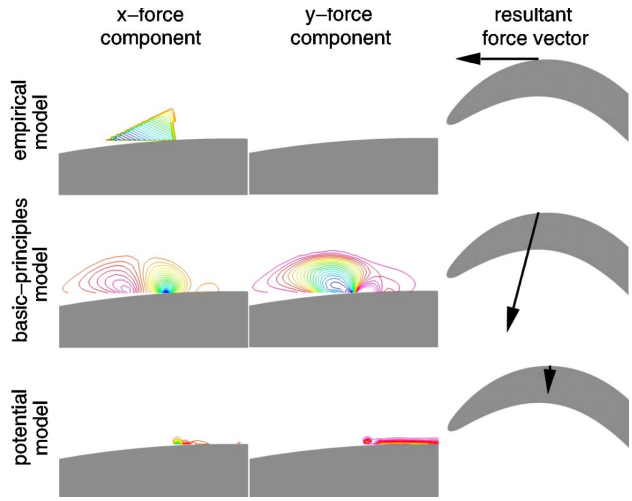

Fig. 14 Planar contours of the *x* and *y* plasma-force components, and the resultant plasma-force vector for counterflow actuation Configuration A with various plasma-force models

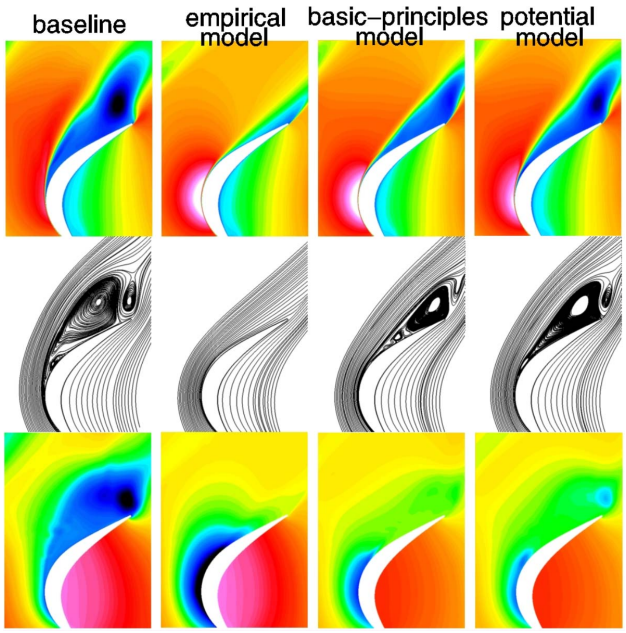

Fig. 16 Time-mean planar contours of *u* velocity, streamlines, and planar contours of C_p for counterflow actuation Configuration A with various plasma-force models

from left to right, respectively. The empirical model was assumed to have no component in the x direction. It is evident that the basic-principles model generates an appreciable force, with the majority of it vertically oriented. By comparison, a very small resultant force evolves from the potential model. The major component of this force is also in the y direction.

Features of the time-mean flowfields simulated with each of the respective plasma-force models are compared in Figs. 15 and 16. In these comparisons, the benchmark result is now referred to as the empirical-model case. Time-mean surface pressure coefficient distributions presented in Fig. 15 show that the size of the pressure plateau has been reduced with the basic-principles and potential models but not eliminated as for the empirical model. Figure 16 exhibits a reduction in the wake thickness and decrease in the recirculation region. Although not as effective as the empirical approach, the basic-principles model reduced the wake loss coefficient by over 70%. An improvement of 50% was achieved with the potential model. Once again, a more complete description of these results is contained in Ref. [41].

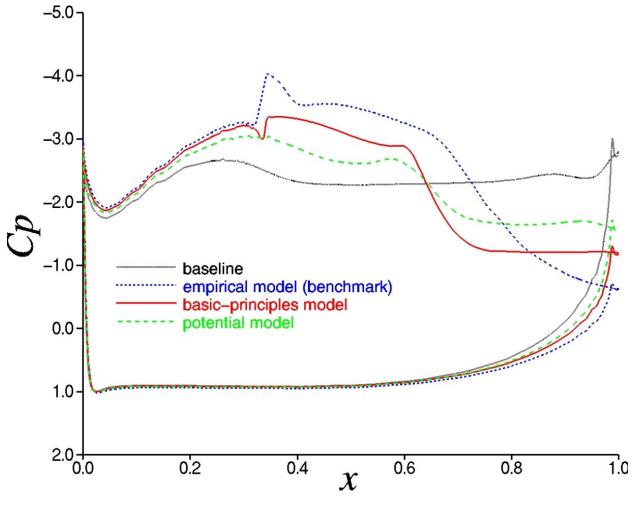

Fig. 15 Time-mean surface pressure coefficient distributions for counterflow actuation Configuration A with various plasma-force models

Summary and Conclusions

This study investigated a number of plasma-based flow control strategies for mitigating separation and reducing wake total pressure loss of a highly loaded low-pressure turbine at a chord Reynolds number of 25,000. A high-fidelity numerical scheme, with an overset grid approach, was employed in order to accurately simulate the complex transitional flowfield. Some of the aspects that were considered included the chordwise location of actuators, spanwise periodic arrays of actuators, and multiple actuators for the case of counterflow actuation. Spanwise-directed plasma-force actuation was also considered. In addition, the effect of using alternate plasma-force models in the simulation of the turbine blade flowfield was assessed.

It should be noted that these computations correspond only to an isolated linear cascade configuration. As such, they neglect any heat input from a combustor or rotational effects that would occur in a practical turbine installation. This approach, however, is identical to previous experimental [1–5] and computational [21–23,26–29,33] studies.

For counterflow actuation simulations, several items became apparent. First, the previously obtained benchmark case (Configuration A) with $D_c=25.0$ was actually a very efficient arrangement. This value of D_c is considered to be fairly low, representing power requirements easily attainable by current plasma actuators. Solutions obtained with even lower values of D_c (10.0, 6.25) were almost as effective, resulting in a reduction in the wake total pressure loss coefficient of about 70%. Second, when the actuator was located 10% of the chord upstream from separation (Configuration B), the flow rapidly transitioned and approached a fully turbulent state near the blade trailing edge. It is believed that this configuration would be useful for applications at somewhat lower Reynolds numbers. In addition, coherent structures, which formed at a subharmonic of the plasma pulsing frequency in the benchmark case, were eliminated. Third, a more rapid transition to turbulence was also achieved with the addition of a secondary array of spanwise-distributed actuators, downstream of the primary full-span actuation location (Configuration C). This configuration also eliminated quasi-two-dimensional coherent structures. Finally, use

of only a single array of spanwise-distributed actuators (Configuration D) was not as efficient in reducing wake losses.

When actuation was oriented such that the plasma force was directed spanwise, flow control was not as effective in diminishing separation. Use of an array of spanwise-distributed actuators (Configuration E) resulted in a wake loss coefficient much like that of a similar arrangement with counterflow control (Configuration D). When the array had an axial extent equal to one-half of the blade chord (Configuration F), the wake loss coefficient was actually worse than that of the base line case with no control at all. This was due to displacement of the boundary layer away from the blade surface, thereby increasing blockage in the flow passage.

Because of uncertainties in application of the empirical plasma-force model, other formulations were considered for the benchmark configuration. These included a highly sophisticated multiequation basic-principles description and a potential equation approach employing lumped-element electric circuitry. As much as possible, consistency between the various methods was maintained. The basic-principles simulation was similar, yet slightly less effective, to that of the empirical model. Due to a small force component in the axial direction, it was found that less control authority was exerted when the potential equation was used to model actuation. Previous work [33] has shown that these deficiencies could easily be overcome by raising the actuation power level, which is equivalent to increasing the value of the scale parameter D_c, within the context of the present investigation. We emphasize that the value $D_c=25.0$ is considered to be very small, so that much higher levels are easily attainable by modern plasma actuators in order to exert more control. Consideration of alternate plasma-force formulations demonstrates that the empirical model provides results that are similar to those of more elaborate formulations, and is therefore adequate for the exploration of plasma-actuation strategies in the control of complex fluid flows.

Acknowledgment

The work presented here was sponsored by the U.S. Air Force Office of Scientific Research and was monitored by R. W. Jefferies. Computational resources were supported in part by a grant of supercomputer time from the U.S. Department of Defense Major Shared Resource Center at Wright-Patterson AFB, OH. The authors wish to thank D. Gaitonde and J. Poggie for a number of helpful discussions. They are also grateful to S. Roy, T. Corke, and T. Apker for supplying force distributions used in this work.

Nomenclature

b = nondimensional interblade spacing, $4/3$
C_p = turbine blade surface pressure coefficient, $2(p-p_i)/\rho_i q_i^2$
c = turbine blade axial chord
C_w = integrated wake total pressure loss coefficient
D_c = plasma scale parameter
$\mathbf{E}$ = nondimensional electric field vector
E_ω = nondimensional turbulent kinetic energy frequency spectra
f = dimensional imposed actuator pulsing frequency, Hz
$\mathbf{F},\mathbf{G},\mathbf{H}$ = inviscid vector fluxes
$\mathbf{F}_v,\mathbf{G}_v,\mathbf{H}_v$ = viscous vector fluxes
$\mathcal{F}$ = nondimensional imposed actuator pulsing frequency, $cf/u_\infty \bar{q}_i$
I,J,K = coordinate grid indices in the circumferential, blade normal, and spanwise directions
$\mathcal{J}$ = Jacobian of the coordinate transformation
p = nondimensional static pressure
P_t = nondimensional total pressure
q = nondimensional planar velocity magnitude, $\sqrt{u^2+v^2}$
q_c = nondimensional charge density
$\mathbf{Q}$ = vector of dependent variables
Re_∞ = reference Reynolds number, $\rho_\infty q_\infty c/\mu_\infty$
Re = chord inlet Reynolds number, $\rho_i \bar{q}_i \mathrm{Re}_\infty/\mu_i$
s = nondimensional spanwise domain extent
$\mathbf{S}$ = source vector
t = nondimensional time based on the reference velocity, u_∞
u,v,w = nondimensional Cartesian velocity components in the x, y, and z directions
x,y,z = nondimensional Cartesian coordinates in the streamwise, vertical, and spanwise directions
x_a = streamwise position of actuator location
α = turbine blade flow angle
ξ,η,ζ = nondimensional body-fitted computational coordinates
ρ = nondimensional fluid density
ω = nondimensional frequency

Subscripts

i,o = inflow and outflow conditions
∞ = dimensional reference value

Superscripts

$\bar{}$ = time-mean quantity
$'$ = root-mean-square fluctuating component

References

[1] Sondergaard, R., Bons, J. P., Sucher, M., and Rivir, R. B., 2002, "Reducing Low-Pressure Turbine Stage Blade Count Using Vortex Generator Jet Separation Control," ASME Paper No. GT-2002-30602.
[2] Bons, J. P., Sondergaard, R., and Rivir, R. B., 1999, "Control of Low-Pressure Turbine Separation Using Vortex Generator Jets," AIAA Paper No. 99-0367.
[3] Bons, J. P., Sondergaard, R., and Rivir, R. B., 2001, "Turbine Separation Control Using Pulsed Vortex Generator Jets," ASME J. Turbomach., **123**(2), pp. 198–206.
[4] Bons, J. P., Sondergaard, R., and Rivir, R. B., 2002, "The Fluid Dynamics of LPT Blade Separation Control Using Pulsed Jets," ASME J. Turbomach., **124**(1), pp. 77–85.
[5] Sondergaard, R., Rivir, R. B., and Bons, J. P., 2002, "Control of Low-Pressure Turbine Separation Using Vortex Generator Jets," J. Propul. Power, **18**(4), pp. 889–895.
[6] List, J., Byerley, A. R., McLaughlin, T. E., and Dyken, R. D., 2003, "Using a Plasma Actuator to Control Laminar Separation on a Linear Cascade Turbine Blade," AIAA Paper No. 2003-1026.
[7] Huang, J., Corke, T. C., and Thomas, F. O., 2003, "Plasma Actuators for Separation Control of Low Pressure Turbine Blades," AIAA Paper No. 2003-1027.
[8] Corke, T. C., and Post, M. L., 2005, "Overview of Plasma Flow Control: Concepts, Optimization, and Applications," AIAA Paper No. 2005-0563.
[9] Huang, J., Corke, T. C., and Thomas, F. O., 2006, "Plasma Actuators for Separation Control of Low-Pressure Turbine Blades," AIAA J., **44**(1), pp. 51–57.
[10] Huang, J., Corke, T. C., and Thomas, F. O., 2006, "Unsteady Plasma Actuators for Separation Control of Low-Pressure Turbine Blades," AIAA J., **44**(7), pp. 1477–1487.
[11] Lorber, P., McCormick, D., Anderson, T., Wake, D., MacMartin, D., Pollack, M., Corke, T., and Breuer, K., 2000, "Rotorcraft Retreating Blade Stall Control," AIAA Paper No. 2000-2475.
[12] Corke, T. C., Jumper, E. J., Post, M. L., Orlov, D., and McLaughlin, T. E., 2002, "Application of Weakly-Ionized Plasmas as Wing Flow-Control Devices," AIAA Paper No. 2002-0350.
[13] Post, M. L., and Corke, T. C., 2003, "Separation Control on High Angle of Attack Airfoil Using Plasma Actuators," AIAA Paper No. 2003-1024.
[14] Post, M. L., and Corke, T. C., 2004, "Separation Control Using Plasma Actuators-Stationary and Oscillating Airfoils," AIAA Paper No. 2004-0841.
[15] Corke, T. C., He, C., and Patel, M. P., 2004, "Plasma Flaps and Slats: An Application of Weakly-Ionized Plasma Actuators," AIAA Paper No. 2004-2127.
[16] Post, M. L., and Corke, T. C., 2004, "Separation Control Using Plasma Actuators-Dynamic Stall Control on an Oscillating Airfoil," AIAA Paper No. 2004-2517.
[17] Morris, S. C., Corke, T. C., VanNess, D., Stephens, J., and Douville, T., 2005, AIAA Paper No. 2005-0782.
[18] Thomas, F. O., Kozlov, A., and Corke, T. C., 2006, "Plasma Actuators for Bluff Body Flow Control," AIAA Paper No. 2006-2845.
[19] Patel, M. P., Ng, T. T., Vasudevan, S., Corke, T. C., and He, C., 2006, "Plasma Actuators for Hingeless Aerodynamic Control of an Unmanned Air Vehicle," AIAA Paper No. 2006-3495.
[20] Raverdy, B., Mary, I., Sagaut, P., and Liamis, N., 2001, "Large-Eddy Simula-

tion of the Flow Around a Low Pressure Turbine Blade," *Direct and Large-Eddy Simulation IV* (ERCOFTAC Series Vol. 8), B. J. Guerts, R. Friedrich, and O. Metais, eds., Kluwer Academic, Dordrecht, The Netherlands, pp. 381–388.
[21] Mittal, R., Venkatasubramanian, S., and Najjar, F. M., 2001, "Large-Eddy Simulation of Flow Through a Low-Pressure Turbine Cascade," AIAA Paper No. 2001-2560.
[22] Postl, D., Gross, A., and Fasel, H. F., 2003, "Numerical Investigation of Low-Pressure Turbine Blade Separation Control," AIAA Paper No. 2003-0614.
[23] Rizzetta, D. P., and Visbal, M. R., 2003, "Numerical Investigation of Transitional Flow Through a Low-Pressure Turbine Cascade," AIAA Paper No. 2003-3587.
[24] Wissink, J. G., 2003, "DNS of Separating, Low-Reynolds Number Flow in a Turbine Cascade With Incoming Wakes," Int. J. Heat Fluid Flow, **24**(4), pp. 626–635.
[25] Kalitzin, G., Wu, X., and Durbin, P. A., 2003, "DNS of Fully Turbulent Flow in a LPT Passage," Int. J. Heat Fluid Flow, **24**(4), pp. 636–644.
[26] Postl, D., Gross, A., and Fasel, H. F., 2004, "Numerical Investigation of Active Flow Control for Low-Pressure Turbine Blade Separation," AIAA Paper No. 2004–750.
[27] Gross, A., and Fasel, H. F., 2004, "Active Control of Separation for Low-Pressure Turbine Blades," AIAA Paper No. 2004-2203.
[28] Rizzetta, D. P., and Visbal, M. R., 2004, "Numerical Simulation of Separation Control for a Highly-Loaded Low-Pressure Turbine," AIAA J., **43**(9), pp. 1958–1967.
[29] Rizzetta, D. P., and Visbal, M. R., 2006, "Numerical Study of Active Flow Control for a Transitional Highly-Loaded Low-Pressure Turbine," ASME J. Fluids Eng., **128**(5), pp. 956–967.
[30] Gaitonde, D. V., Visbal, M. R., and Roy, S., 2005, "Control of Flow Past a Wing Section With Plasma-Based Body Forces," AIAA Paper No. 2005-5302.
[31] Visbal, M. R., and Gaitonde, D. V., 2005, "Control of Vortical Flows Using Simulated Plasma Actuators," AIAA Paper No. 2006-0505.
[32] Visbal, M. R., Gaitonde, D. V., and Roy, S., 2006, "Control of Transitional and Turbulent Flows Using Plasma-Based Actuators," AIAA Paper No. 2006-3230.
[33] Rizzetta, D. P., and Visbal, M. R., 2007, "Numerical Investigation of Plasma-Based Flow Control for a Transitional Highly-Loaded," AIAA Paper No. 2007-938.
[34] Beam, R., and Warming, R., 1978, "An Implicit Factored Scheme for the Compressible Navier-Stokes Equations," AIAA J., **16**(4), pp. 393–402.
[35] Gordnier, R. E., and Visbal, M. R., 1993, "Numerical Simulation of Delta-Wing Roll," AIAA Paper No. 93-0554.
[36] Jameson, A., Schmidt, W., and Turkel, E., 1981, "Numerical Solutions of the Euler Equations by Finite Volume Methods Using Runge-Kutta Time Stepping Schemes," AIAA Paper No. 81-1259.
[37] Pulliam, T. H., and Chaussee, D. S., 1981, "A Diagonal Form of an Implicit Approximate-Factorization Algorithm," J. Comput. Phys., **39**(2), pp. 347–363.
[38] Lele, S. A., 1992, "Compact Finite Difference Schemes With Spectral-Like Resolution," J. Comput. Phys., **103**(2), pp. 16–42.
[39] Visbal, M. R., and Gaitonde, D. V., 1999, "High-Order-Accurate Methods for Complex Unsteady Subsonic Flows," AIAA J., **37**(10), pp. 1231–1239.
[40] Gaitonde, D., Shang, J. S., and Young, J. L., 1997, "Practical Aspects of High-Order Accurate Finite-Volume Schemes for Electromagnetics," AIAA Paper No. 97-0363.
[41] Rizzetta, D. P., and Visbal, M. R., 2007, "Simulation of Plasma-Based Flow-Control Strategies for Transitional Highly Loaded Low-Pressure Turbines," AIAA Paper No. 2007-4216.
[42] Gaitonde, D., and Visbal, M. R., 1998, "High-Order Schemes for Navier-Stokes Equations: Algorithm and Implementation into FDL3DI," Air Force Research Laboratory, Technical Report No. AFRL-VA-WP-TR-1998–3060.
[43] Gordnier, R. E., 1995, "Computation of Delta-Wing Roll Maneuvers," J. Aircr., **32**(3), pp. 486–492.
[44] Visbal, M. R., 1993, "Computational Study of Vortex Breakdown on a Pitching Delta Wing," AIAA Paper No. 93-2974.
[45] Visbal, M., Gaitonde, D., and Gogineni, S., 1998, "Direct Numerical Simulation of a Forced Transitional Plane Wall Jet," AIAA Paper No. 98-2643.
[46] Rizzetta, D. P., Visbal, M. R., and Stanek, M. J., 1999, "Numerical Investigation of Synthetic-Jet Flowfields," AIAA J., **37**(8), pp. 919–927.
[47] Rizzetta, D. P., and Visbal, M. R., 2006, "Direct Numerical Simulation of Flow Past an Array of Distributed Roughness Elements," AIAA Paper No. 2006-3527.
[48] Rizzetta, D. P., Visbal, M. R., and Blaisdell, G. A., 2003, "A Time-Implicit High-Order Compact Differencing and Filtering Scheme for Large-Eddy Simulation," Int. J. Numer. Methods Fluids, **42**(6), pp. 665–693.
[49] Rizzetta, D. P., and Visbal, M. R., 2002, "Application of Large-Eddy Simulation to Supersonic Compression Ramps," AIAA J., **40**(8), pp. 1574–1581.
[50] Rizzetta, D. P., and Visbal, M. R., 2003, "Large-Eddy Simulation of Supersonic Cavity Flowfields Including Flow Control," AIAA J., **41**(8), pp. 452–1462.
[51] Roth, J. R., 2003, "Aerodynamic Flow Acceleration Using Paraelectric and Peristaltic Electrohydrodynamic Effects of a One Atmosphere Uniform Glow Discharge Plasma," Phys. Plasmas, **10**(5), pp. 2117–2128.
[52] Roth, J. R., Sin, H., and Madham, R. C. M., 2003, "Flow Re-Attachment and Acceleration by Paraelectric and Peristaltic Electrohydrodynamic (EHD) Effects," AIAA Paper No. 2003-0531.
[53] Shyy, W., Jayaraman, B., and Anderson, A., 2002, "Modeling of Glow Discharge-Induced Fluid Dynamics," J. Appl. Phys., **92**(11), pp. 6434–6443.
[54] Steinbrenner, J. P., Chawner, J. P., and Fouts, C. L., 1991, "The GRIDGEN 3D Multiple Block Grid Generation System, Volume II: User's Manual," Wright Research and Development Center, Technical Report No. WRDC-TR-90–3022.
[55] Gruber, B., and Carstens, V., 2001, "The Impact of Viscous Effects on the Aerodynamic Damping of Vibrating Transonic Compressor Blades: A Numerical Study," ASME J. Turbomach., **123**(2), pp. 409–417.
[56] Visbal, M. R., and Gaitonde, D. V., 2001, "Very High-Order Spatially Implicit Schemes for Computational Acoustics on Curvilinear Meshes," J. Comput. Acoust., **9**(4), pp. 1259–1286.
[57] Sherer, S. E., 2003, "Further Analysis of High-Order Overset Grid Method With Applications," AIAA Paper No. 2003-3839.
[58] Suhs, N. E., Rogers, S. E., and Dietz, W. E., 2003, "PEGASUS 5: An Automated Preprocessor for Overset-Grid Computational Fluid Dynamics," AIAA J., **41**(6), pp. 1037–1045.
[59] Message Passing Interface Forum, 1994, "MPI: A Message-Passing Interface Standard," Computer Science Department, Technical Report No. CS-94–230.
[60] He, C., and Corke, T. C., 2007, "Numerical and Experimental Analysis of Plasma Flow Control Over a Hump Model," AIAA Paper No. 2007-935.
[61] Balagangadhar, D., and Roy, S., 2001, "Design Sensitivity Analysis and Optimization of Steady Fluid-Thermal Systems," Comput. Methods Appl. Mech. Eng., **190**(42), pp. 5465–5479.
[62] Roy, S., and Pandey, B. P., 2003, "Development of a Finite Element-Based Hall-Thruster Model," J. Propul. Power, **19**(5), pp. 964–971.
[63] Roy, S., Singh, K. P., Kumar, H., Gaitonde, D. V., and Visbal, M., 2006, "Effective Discharge Dynamics for Plasma Actuators," AIAA Paper No. 2006-374.
[64] Enloe, C. L., McLaughlin, T. E., VanDyken, R. D., Kachner, K. D., Jumper, E. J., and Corke, T. C., 2004, "Mechanism and Responses of a Single Dielectric Barrier Plasma Actuator: Geometric Effects," AIAA J., **42**(3), pp. 595–604.
[65] Orlov, D. M., and Corke, T. C., 2005, "Numerical Simulation of Aerodynamic Plasma Actuator Effects," AIAA Paper No. 2005-1083.
[66] Gaitonde, D. V., Visbal, M. R., and Roy, S., 2006, "A Coupled Approach for Plasma-Based Flow Control Simulation of Wing Sections," AIAA Paper No. 2006-1205.

Friction Factor Measurements in an Equally Spaced Triangular Array of Circular Tubes

Peter Vassallo[1]
e-mail: vassall@kapl.gov

Paul Symolon

Lockheed Martin Corporation,
Schenectady, NY 12301

Friction factor data for adiabatic cross flow of water in a staggered tube array were obtained over a Reynolds number range (based on hydraulic diameter and gap velocity) of about 10,000–250,000. The tubes were 12.7 mm (0.5 in.) *outer diameter in a uniformly spaced triangular arrangement with a pitch-to-diameter ratio of 1.5. The friction factor was compared to several literature correlations and was found to be best matched by the Idelchik correlation. Other correlations were found to significantly vary from the test data. Based on the test data, a new correlation is proposed for this tube bundle geometry, which covers the entire Reynolds number range tested.*
[DOI: 10.1115/1.2903817]

Keywords: friction factor, tube bundle, pressure drop, staggered array

Introduction

Pressure drop across a tube bank is one of the primary design considerations for shell and tube heat exchangers. The pressure drop is a function, among other things, of tube arrangement and packing as well as system flow rate. Friction factor correlations have been used for many years to determine the pressure loss based on relevant design parameters. These correlations offer a means of assessing the pressure losses quickly without the need for expensive and time consuming computational methods.

A summary of early work is provided by Chilton and Generaux [1]. In this paper, a general equation for friction factor, based on tube gap spacing and gap velocity, was developed by fitting a curve to eight data sets. Later, Gunter and Shaw [2] considered a broader set of data and concluded that the data best collapsed using an equivalent hydraulic diameter as well as transverse and longitudinal pitch-to-diameter ratios. Friction factors for bare tubes of diameters between 0.5 mm and 127 mm were included, with transverse and longitudinal pitches ranging from 1.25 to 5 diameters.

Perhaps, the most widely referenced correlation is that provided by Zukauskas [3]. This correlation, in graphical form, has been reprinted in numerous heat transfer and heat exchanger design manuals [4,5]. The correlation is plotted as a function of pitch and spacing as well as Reynolds number based on gap velocity and tube diameter. It covers a wide range of Reynolds number from 10 to 1,000,000. Another useful, well regarded resource for pressure losses in a variety of geometries is provided by Idelchik [6]. Here, a method for obtaining friction factor in staggered tube arrays is provided based on gap velocity, tube diameter, and numerous geometric factors.

The tube configuration currently being considered is made up of an equally spaced, staggered triangular array with tube OD =12.7 mm. Several methods, including those described above, were used to determine friction factor for this geometry, and a large spread was observed for the Reynolds number range of interest (i.e., between 10,000 and 250,000). The data of Kays and London [7], which most closely matched our test configuration, although limited to Reynolds numbers less than 23,000, indicated a relatively low friction factor, nearly half that of Chilton–Generaux. The predictions of Gunter–Shaw, Zukauskas, and Idelchik lay in between each successively giving decreasing values of friction factor. As a result of the spread of these predictions and the lack of high Reynolds number data, a test was performed to obtain more specific data for the desired tube geometry.

Calculation of Tube Bundle Geometric Parameters

Figure 1 illustrates the nomenclature associated with modeling pressure drop in a triangular tube array.

A single unit cell of the rod array (the cross hatched region in Fig. 1) can be analyzed to derive the volume porosity and hydraulic diameter. For uniformly spaced triangular rod arrays ($S=(\sqrt{3}/2)P$),

$$\gamma_v = \frac{\text{fluid volume}}{\text{total volume}} = 1 - \frac{\pi}{2\sqrt{3}}\left(\frac{D}{P}\right)^2 \tag{1}$$

$$D_v = \frac{4 \times \text{fluid volume}}{\text{wetted area}} = \left[\frac{2\sqrt{3}}{\pi}\left(\frac{P}{D}\right)^2 - 1\right]D \tag{2}$$

For a triangular array with $D=12.7$ mm and $P/D=1.5$, Eq. (1) gives $\gamma_v=0.597$ and Eq. (2) gives $D_v=18.8$ mm. These values are derived for a large tube array free of wall effects. If the walls of the test section are included in the wetted area calculation, the volume porosity is unchanged and the volumetric hydraulic diameter decreases 9% to 17.3 mm. However, while the wetted area contributes to the hydraulic diameter, it is believed to have an insignificant effect on the pressure drop because cross-flow resistance is dominated by the form drag of the tubes. Therefore, the infinite bundle hydraulic diameter of 18.8 mm has been used in the data reduction calculations.

Experimental Description

Test Section. A sketch of the test section is shown in Fig. 2. The test section consisted of a stainless steel rectangular duct, 30.48 cm (12 in.) ×11.43 cm (4.5 in.) in cross section and 182.88 cm (72 in.) in length. The test section was horizontally oriented, with the tubes parallel to the floor. The test section included a flow straightener at the inlet, consisting of a perforated plate followed by a bundle of 9.5 mm (3/8 in.) OD thin walled tubes. The test section contained 60 rows of tubes with six tubes

[1]Corresponding author.

Contributed by the Fluids Engineering Division of ASME for publication in the JOURNAL OF FLUIDS ENGINEERING. Manuscript received September 4, 2007; final manuscript received October 10, 2007; published online April 4, 2008. Assoc. Editor: Phillip M. Ligrani. Paper presented at the ASME Turbo Expo 2004: Land, Sea and Air (GT2004), Vienna, Austria, June 14–17, 2004.

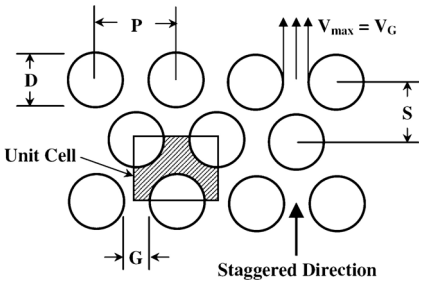

Fig. 1 Schematic of triangular tube array

per row, arranged in a triangular pitch. The surface of the tubes was nominally smooth. The rows alternate between a row with five full tubes with two half tubes welded to the wall and a row with six full tubes so that the flow area in each row is one-third of the inlet flow area. Pressure tap locations are shown in Fig. 2; the taps were flush to the sidewall of the test assembly. An acrylic window was included in the test section for future visualization or laser measurements.

Instrumentation. Calibrated differential Rosemount transducers were used to measure the pressure drop with an uncertainty of $\pm 1\%$ of reading or ± 0.01 psi, whichever was greater. Care was taken to thoroughly bleed the transducers so that no air bubbles were present. Measurements taken at zero flow confirmed that no measurement bias due to trapped air was present (i.e., the data indicated <0.01 psi at zero flow).

A Venturi flow device calibrated for tube bundle $\mathrm{Re} > 10{,}000$ was used to measure the flow rate with an uncertainty of $\pm 1\%$. The primary Venturi used to take the flow rate data was checked with a second in-line Venturi and the two measurements agreed to within 1% for the applicable range of the second Venturi (i.e., $\mathrm{Re} > 100{,}000$). Standard Type-K thermocouples were used to measure the water temperature (within $\pm 1.1°\mathrm{C}$).

As a check of the pressure data accuracy, the ten bundle incremental pressure drops were added together and compared to the total plenum to plenum ΔP_{3-13}. The difference was at most a 2% error for the lowest flow tested. For higher flows where pressure drops are greater, the difference was generally within two-tenths of a percent.

Experimental Method for Obtaining Friction Factor. For convenience in making comparisons, the incremental pressure drops were converted to loss factors by dividing the pressure drop by the dynamic head:

$$K = \frac{\Delta P}{\frac{1}{2}\rho V^2} \tag{3}$$

For the dynamic head, we used either the average velocity in the tube gaps (V_G) if the ΔP was in the bundle or the average velocity in the unrodded part of the duct ($0.333 V_G$) if the ΔP was across the perforated plate or flow straightener.

For comparison purposes, the loss factor is plotted versus position in the test section in Fig. 3. All the data taken (i.e., at different flows and temperatures) are plotted to show the overall trends as well as the mean results. For Tap 3 to Tap 4, the pressure drop is higher because the flow must be accelerated (by a factor of 3) from the open duct velocity to the gap velocity. Conversely, for Tap 12 to Tap 13, the flow decelerates by the same amount, causing a pressure recovery and a smaller loss factor.

It is also observed in Fig. 3 that, for the incremental pressure drops within the bundle, the loss factor from tap 11 to tap 12 is greater than the other seven bundle incremental loss factors by 5% (on the average). This may have been due to a flow perturbation at the window, or possibly a defect in Tap 11 or 12, such as a burr. For this reason, the friction factor was based on the sum of the pressure drops from Tap 4 to Tap 11 rather than from Tap 4 to Tap 12. The Darcy friction factor is therefore defined as

$$f = \frac{2\Delta P_{4-11}}{\rho (Q/A_G)^2} \frac{D_v}{L_{4-11}} \tag{4}$$

Experimental Uncertainty in the Friction Factor. By propagating errors through Eq. (4), the error in friction factor can be expressed in terms of the error in the measured parameters. Neglecting density uncertainty and uncertainty in the length between pressure taps,

$$\frac{\varepsilon_f}{f} = \sqrt{\left[\frac{\varepsilon_{\Delta P}}{\Delta P}\right]^2 + 4\left\{\left[\frac{\varepsilon_Q}{Q}\right]^2 + \left[\frac{\varepsilon_A}{A_{\mathrm{gap}}}\right]^2\right\} + \left[\frac{\varepsilon_{D_v}}{D_v}\right]^2} \tag{5}$$

The uncertainty for the pressure drop and flow rate measurements within the calibrated range of the primary Venturi (i.e., $\mathrm{Re} > 11{,}000$) was $\pm 1\%$. The effect on the flow area of a rod being at an off nominal position was studied and showed that a 0.127 mm error in rod the position resulted in less than a tenth of a percent change in the gap flow area. From test section design tolerances, the uncertainties in the flow area and hydraulic diameter were estimated to be $\pm 1\%$. Using these values in Eq. (5), the uncertainty in friction factor is $\pm 3.2\%$. A similar propagation of errors on Reynolds number yields

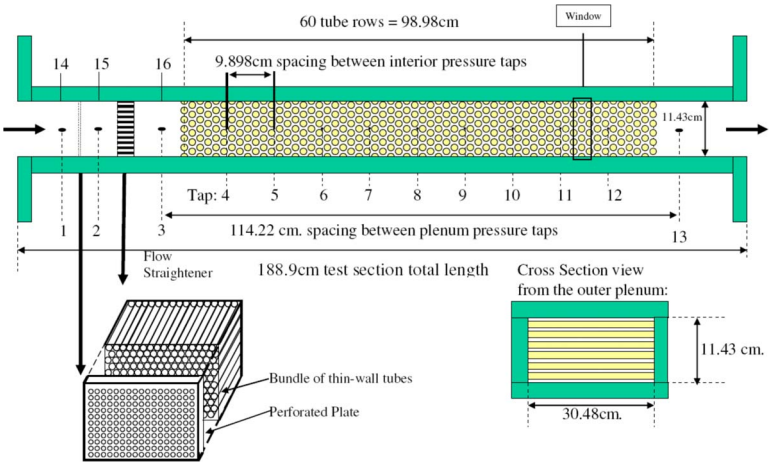

Fig. 2 Test section schematic (not to scale)

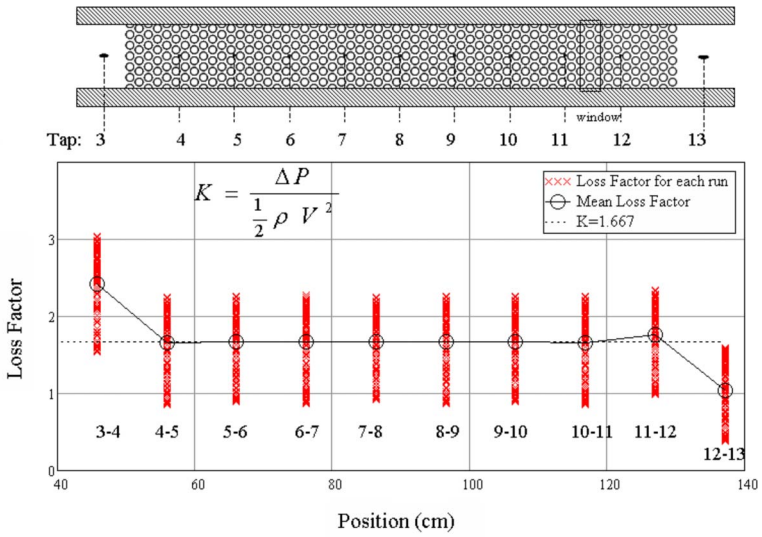

Fig. 3 Loss factors versus position in the test section

$$\frac{\varepsilon_{\mathrm{Re}}}{\mathrm{Re}} = \sqrt{\left[\frac{\varepsilon_Q}{Q}\right]^2 + \left[\frac{\varepsilon_A}{A_{\mathrm{gap}}}\right]^2 + \left[\frac{\varepsilon_{D_v}}{D_v}\right]^2 + \left[\frac{\varepsilon_v}{v}\right]^2} \tag{6}$$

Based on the uncertainty in loop temperature ($\pm 1.1\,^\circ$C), the uncertainty in viscosity is $\pm 3\%$ for the range of loop temperatures studied. The overall uncertainty in Reynolds number is therefore $\pm 3.5\%$.

Results and Discussion

The friction factor data (119 points in total) are plotted versus Reynolds number in Fig. 4 with the error bars determined from Eqs. (5) and (6). Temperatures were varied from 10°C to 45°C to extend the range of Reynolds number and to confirm that no temperature sensitivities existed. The scatter in the data is seen to be within the specified measurement uncertainty.

Also included in Fig. 4 are predictions from other sources to provide context for the present data. The points for Zukauskas [3] and Kays and London [7] were directly taken from the graphs provided in those references. The Zukauskas method matched the current tube geometry, while the Kays and London data closely matched it ($P/D=1.5$ and $S/D=1.25$). The correlations for Idelchik, Chilton–Generaux, and Gunter–Shaw are summarized as follows.

Idelchik Method. For $3\times 10^3 < \mathrm{Re}_D < 10^5$,

$$f_I = K\mathrm{Re}_D^{-0.27}N \tag{7}$$

$$\bar{S} = \frac{(P-D)}{((\sqrt{0.25P^2+S^2})-D)} = 1 \tag{8}$$

For $P/D \geq 1.44$ and $0.1 < \bar{S} < 1.7$,

$$K = 3.2 + 0.66(1.7-\bar{S})^{1.5} = 3.59 \tag{9}$$

$$f = f_I\frac{D_v}{L} \tag{10}$$

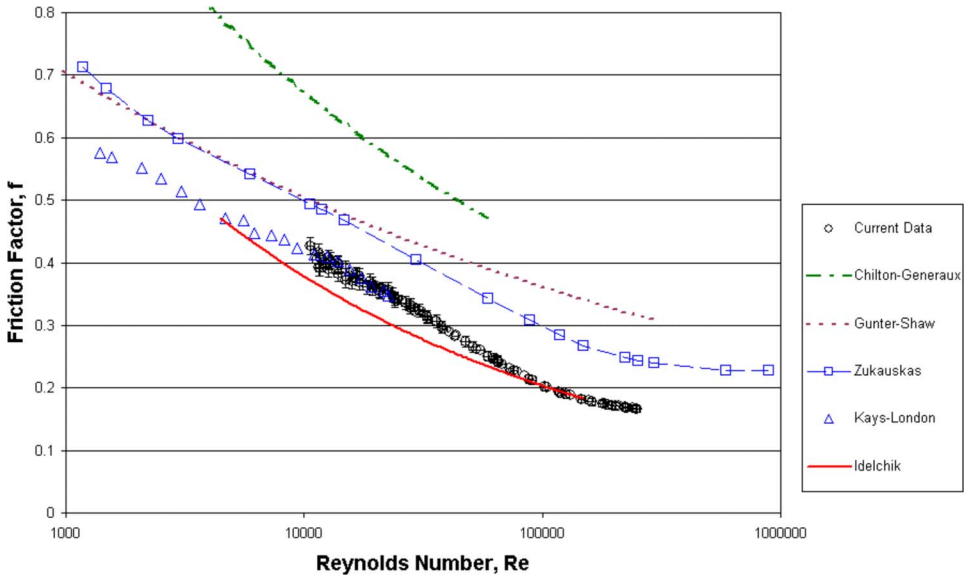

Fig. 4 Cross-flow friction factor data versus other sources

Table 1 Calculated pressure drop in the test section described in Fig. 2 for two cases: with and without tubes. The temperature was taken as 20°C; with tubes: $L/D_v=5.27$, $A=0.0116$ m^2; without tubes: $L/D_H=0.6$, $A=0.035$ m^2.

Q	With tubes				Without tubes				
(m^3/s)	Re	f	V (m/s)	ΔP (kPa)	Re	f	V (m/s)	ΔP (Pa)	ΔP_{ratio}
0.006	10,500	0.423	0.56	0.35	30,568	0.024	0.19	0.25	1417
0.031	50,000	0.273	2.66	5.09	145,560	0.017	0.88	3.96	1284
0.062	100,000	0.211	5.32	15.76	291,120	0.015	1.76	13.62	1158
0.154	250,000	0.164	13.30	76.53	727,799	0.013	4.41	72.87	1050

$$\mathrm{Re} = \mathrm{Re}_D \frac{D_v}{D} \tag{11}$$

Chilton and Generaux Method. For $50 < \mathrm{Re}_G < 2\times 10^4$,

$$f_{C-G} = 3\mathrm{Re}_G^{-0.2} N \tag{12}$$

$$f = f_{C-G}\frac{D_v}{L} \tag{13}$$

$$\mathrm{Re} = \mathrm{Re}_G \frac{D_v}{G} \tag{14}$$

Note that the correlation was based on the data for $1.25 < P/D < 5$.

Gunter–Shaw Method. For isothermal flow in an equally spaced triangular tube array and $5\times 10^2 < \mathrm{Re}_v < 3\times 10^5$,

$$f = 1.92\mathrm{Re}_v^{-0.145}\left(\frac{D_v}{P}\right)^{0.4} \tag{15}$$

As seen in Fig. 4, the data are best matched overall by Idelchik, especially for $\mathrm{Re} > 80{,}000$. For $\mathrm{Re} < 80{,}000$, the data slightly depart from Idelchik and exhibit a curvature similar to Zukauskas. The Kays and London data are in excellent agreement within the range $10{,}000 < \mathrm{Re} < 23{,}000$ and Chilton–Generaux is noticeably higher. Except for Chilton–Generaux, which has no explicit sensitivity to pitch or spacing ratios, it is unclear why such variation exists. As far as the data are concerned, differences in working fluid, errors in density or viscosity, flow-pressure measurement errors, unknown wall effects, variations in tube pitch and/or spacing, limited number of tube rows, and uncertainties in surface roughness are possible culprits, all of which make it difficult to obtain universal correlations. It does appear that for most accurate results, testing in the particular geometry of interest is recommended. Based on this, a new correlation was developed for our data as follows:

$$f = \begin{cases} \dfrac{3.6862}{\mathrm{Re}_v^{0.2337}} & \text{if } \mathrm{Re}_v < 27{,}582 \\ 0.1527 + 0.818\left[1 - \left(\dfrac{\mathrm{Re}_v}{10^6}\right)^{0.3532}\right]^{4.4974} & \text{if } 27{,}582 \leq \mathrm{Re}_v \leq 10^6 \\ 0.1527 & \text{if } \mathrm{Re}_v > 10^6 \end{cases} \tag{16}$$

Note that the significant digits in the correlation are necessary to maintain a continuous function. Also, note that the traditional power law relationship between f and Re accurately matches the data up to Re of about 30,000 (where fitting yields $f = 3.6862/\mathrm{Re}^{0.2337}$). At higher Re, the alternative equation shown above was required to obtain a good fit.

This fit matches the data to within ±5% (effectively the uncertainty of the data), and the rms error in f is 0.00393. In practice, Eq. (16) is valid for Reynolds numbers ranging from 10,000 to 250,000, where the data were taken. The use of the correlation outside the data range should take into consideration additional uncertainty. However, based on the trends observed in the Zukauskus correlation (which is based on air data up to a million Re), the correlation may be extrapolated up to a million Reynolds number. For Re greater than a million, a constant value of $f = 0.1527$ is assumed, based on similar high Re trends in the Zukauskus correlation and the present data.

As a sensitivity study, the pressure drop across the tube bundle was calculated using the friction factors from Eq. (16) and compared to the pressure drop for the hypothetical case with the tubes removed and flow held constant. The results are presented in Table 1 for a wide range of Reynolds number, indicating a ΔP ratio between 1000 and 1400. Thus, even though the tube bundle friction factor is only an order of magnitude higher than the standard duct friction factor, the effective viscous blockage of the tubes contributes to an overall pressure drop that is three orders of magnitude higher.

Conclusions

Experiments have been carried out to determine the friction factor for cross flow in an equally spaced triangular tube array with $P/D = 1.5$. These data extend the Reynolds number range of previous data taken by Kays and London in a similar tube geometry by a factor of 10 (up to $\mathrm{Re} = 250{,}000$). In the overlap region between data sets ($10{,}000 < \mathrm{Re} < 22{,}500$), excellent agreement was noted. However, there is a wide variation in prediction of pressure drop in this geometry when employing available correlations, that is, nearly a factor of 2 in friction factor. The Idelchik correlation best matched the data for $\mathrm{Re} > 80{,}000$, while the Zukauskas method best matched the shape of the data between $10{,}000 < \mathrm{Re} < 250{,}000$. A new correlation was presented, which matches the data to within ±5% over the full Reynolds number range. Since there are numerous factors that impact the overall friction factor, particularly tube spacing and surface roughness,

future testing in a variety of tube configurations may allow for construction of a more accurate, general correlation that covers a wider range of tube geometries.

Acknowledgment

The authors are grateful to Randy Odell and Charles Zarnofsky for their aid in designing and assembling the test hardware.

Nomenclature

- A = cross flow area, m^2
- A_G = flow area in gap between tubes, m^2
- D = tube outside diameter (mm)
- D_v = tube bundle hydraulic diameter, defined volumetrically (mm)
- f = darcy friction factor, based on D_v
- G = gap spacing between tubes (mm)
- N = number of tube rows between ΔP taps
- P = distance between tubes centers (pitch, mm)
- Q = volumetric flow rate (m^3/s)
- Re = Reynolds number, based on gap velocity and hydraulic diameter
- Re_D = Reynolds number, based on gap velocity and tube diameter
- Re_G = Reynolds number, based on gap velocity and gap spacing
- S = row to row spacing between tubes (in.)
- V_G = average velocity in the gaps between tubes (m/s)
- ρ = density (kg/m^3)
- μ = dynamic viscosity (kg/s m)
- ν = kinematic viscosity (m^2/s)
- ΔP = pressure drop (Pa)
- γ_v = volume porosity

References

[1] Chilton, T. H., and Generaux, R. P., 1933, "Pressure Drops Across Banks of Tubes," Trans. Am. Inst. Chem. Eng., **29**, pp. 161–173.

[2] Gunter, A. Y., and Shaw, W. A., 1945, "A General Correlation of Friction Factors of Various Types of Surfaces in Cross Flow," Trans. ASME, **67**, pp. 643–660.

[3] Zukauskas, A., 1987, "Heat Transfer From Tubes in Cross Flow," Adv. Heat Transfer, **18**, pp. 87–159.

[4] Zukauskus, A., and Ulinskas, R., 1983, "Banks of Plain and Finned Tubes," *Heat Exchanger Design Handbook*, Hemisphere, New York, Sec. 2.2.4.

[5] Incropera, F. P., and DeWitt, D. P., 1981, *Fundamentals of Heat Transfer*, Wiley, New York.

[6] Idelchik, I. E., 1986, *Handbook of Hydraulic Resistance*, 2nd ed., Hemisphere, New York.

[7] Kays, W. M., and London, A. L., 1964, *Compact Heat Exchangers*, 2nd ed., McGraw-Hill, New York.

Changkun Chen
Department of Mechanical Science and Bioengineering,
Graduate School of Engineering Science,
Osaka University,
1-3 Machikaneyama, Toyonaka,
Osaka 560-8531, Japan
e-mail: chenchangkun@mbox.me.es.osaka-u.ac.jp

Christophe Nicolet
Laboratory for Hydraulic Machines (LMH-IMHEF),
École Polytechnique Fédérale de Lausanne (EPFL),
Avenue de Cour 33bis,
CH-1007 Lausanne, Switzerland
e-mail: christophe.nicolet@epfl.ch

Koichi Yonezawa
Department of Mechanical Science and Bioengineering,
Graduate School of Engineering Science,
Osaka University,
1-3 Machikaneyama, Toyonaka,
Osaka 560-8531, Japan
e-mail: yonezawa@me.es.osaka-u.ac.jp

Mohamed Farhat
e-mail: mohamed.farhat@epfl.ch

Francois Avellan
e-mail: francois.avellan@epfl.ch

Laboratory for Hydraulic Machines (LMH-IMHEF),
École Polytechnique Fédérale de Lausanne (EPFL),
Avenue de Cour 33bis,
CH-1007 Lausanne, Switzerland

Yoshinobu Tsujimoto
Department of Mechanical Science and Bioengineering,
Graduate School of Engineering Science,
Osaka University,
1-3 Machikaneyama, Toyonaka,
Osaka 560-8531, Japan
e-mail: tujimoto@me.es.osaka-u.ac.jp

One-Dimensional Analysis of Full Load Draft Tube Surge

One-dimensional stability analysis of a hydraulic system composed of a penstock, a runner, and a draft tube was carried out to determine the cause of the full load draft tube surge. It is assumed that the cavity volume at the runner exit is a function of the pressure at the vortex core evaluated from the instantaneous local pressure at the runner exit and an additional pressure decrease due to the centrifugal force on the swirling flow. It was found that the diffuser effect of the draft tube has a destabilizing effect over all flow rates, while the swirl effects stabilize/destabilize the system at larger/smaller flow rates than the swirl-free flow rate. Explanations of the destabilizing mechanism are given for the diffuser and swirl flow effects. [DOI: 10.1115/1.2903475]

1 Introduction

Securing stable operation is one of the most important issues in hydraulic power generation systems. At part load, a draft tube surge occurs when the frequency of the vortex rope whirl agrees with the resonant frequency of the hydraulic system [1–4]. It is also known that a surge can occur even at full load [5] and the cause is still not clear. Koutnik and Pulpitel [6] simulated the full load surge by representing the effect of the cavitation in the draft tube by using cavitation compliance $C=-\partial V_c/\partial p_D$ and mass flow gain factor $\chi=-\partial V_c/\partial Q_D$, where V_c is the volume of the cavity and p_D and Q_D are the pressure and flow rate downstream of the cavity. It was shown that the instability occurs when the absolute value of the negative mass flow gain factor is larger than a certain value, which depends on the value of the cavitation compliance and system head losses. This model was combined with the numerical analysis software SIMSEN to analyze the full load surge observed in a real plant [7].

Although Refs. [6,7] show that a full load surge can be successfully simulated by using an appropriate value of the mass flow gain factor, the flow mechanism determining the value of the mass flow gain factor is not clear yet. The present study is intended to

Contributed by the Fluids Engineering Division of ASME for publication in the JOURNAL OF FLUIDS ENGINEERING. Manuscript received September 27, 2007; final manuscript received January 15, 2008; published online April 14, 2008. Assoc. Editor: Steven Ceccio.

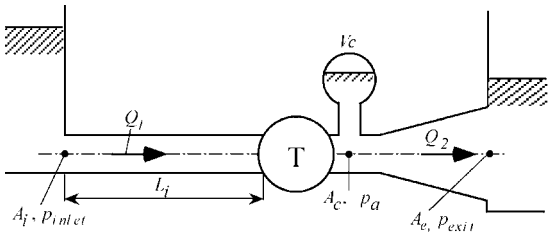

Fig. 1 Hydraulic system for the analysis

clarify the diffuser effect of the draft tube and the effects of swirl in the downstream of the runner on the hydraulic instabilities in power generation plants.

2 Analytical Model

We consider a system composed of an inlet pipe of length L_i and area A_i, a turbine runner, and a draft tube with the inlet and exit areas A_c and A_e, respectively, as shown in Fig. 1. It is assumed that a cavity of volume V_c appears downstream of the turbine and upstream of the draft tube. Then, from continuity, the following relation exists between upstream and downstream flow rates Q_1 and Q_2:

$$Q_2 - Q_1 = dV_c/dt \tag{1}$$

Under constant runner speed and guide vane opening, we can represent the runner by a resistance with a constant loss coefficient ζ_T, which depends on the guide vane opening. If we assume the incompressible flow, the following equation can be obtained from the unsteady version of Bernoulli's equation applied to the upstream pipe:

$$p_{\text{inlet}} = p_a + \rho\frac{L_i}{A_i}\frac{dQ_1}{dt} + \rho\frac{\zeta_T}{2A_i^2}Q_1^2 \tag{2}$$

where p_{inlet} is the pressure at the pipe inlet and p_a is the pressure at the runner discharge. The loss in the pipe can be included in ζ_T. By applying the unsteady version of Bernoulli's equation to the draft tube, we obtain

$$p_a = p_{\text{exit}} + \rho\frac{L_e}{A_e}\frac{dQ_2}{dt} + \rho\frac{\zeta_2 - D}{2A_e^2}Q_2^2 \tag{3}$$

where $L_e = \int (A_e/A(s))ds$ is the effective length of the draft tube, A_e is the exit area of the draft tube, $D = (A_e/A_c)^2 - 1$ is the diffusion factor, A_c is the inlet area of the draft tube, and ζ_2 is the loss coefficient of the draft tube. For simplicity, ζ_2 is assumed to be constant although it may depend on the swirl of the discharge flow [8].

At off-design operating point, the discharge flow from the runner swirls and a vortex is formed. If the pressure p_c at the vortex center is lower than the vapor pressure, a cavity will appear. The volume of the cavity can be considered to be a function of the core pressure p_c,

$$V_c = V_c(p_c) \tag{4}$$

Due to the centrifugal force on the swirling flow, the core pressure p_c is lower than the ambient pressure p_a and can be expressed as

$$p_c = p_a - \rho\alpha c_{\theta 2}^2 \tag{5}$$

Here, $c_{\theta 2}$ is a representative swirl velocity and α is a pressure coefficient for the swirl effects. If we assume a Rankine combined vortex with the core radius a and the outer radius R, α is determined to be $\alpha = (R/a)^2 - 1/2$, with $c_{\theta 2}$ evaluated at the outer radius R, although the real flow from the runner is much more complicated [8].

From the velocity triangle at the runner discharge, we obtain

$$c_{\theta 2} = c_{m2}\cot\beta_2 - U_2 = \frac{Q_1}{S}\cot\beta_2 - U_2 \tag{6}$$

where c_{m2} is the meridional velocity at the runner exit, β_2 is the runner exit vane angle, S is the runner exit area, and U_2 is the runner exit peripheral speed.

By putting Eqs. (3) and (6) in Eq. (5), we obtain

$$p_c = p_{\text{exit}} + \rho\frac{L_e}{A_e}\frac{dQ_2}{dt} + \rho\frac{\zeta_2 - D}{2A_e^2}Q_2^2 - \rho\alpha\left(\frac{\cot\beta_2}{S}Q_1 - U_2\right)^2 \tag{7}$$

We define the cavitation compliance C by

$$C = -dV_c/dp_c \tag{8}$$

Then, the continuity equation (1) can be expressed as

$$\begin{aligned} Q_2 - Q_1 = dV_c/dt &= (dV_c/dp_c)(dp_c/dt) = -C(dp_c/dt) \\ &= -\rho C\frac{L_e}{A_e}\frac{d^2Q_2}{dt^2} + \rho C\frac{D-\zeta_2}{A_e^2}Q_2\frac{dQ_2}{dt} \\ &\quad + 2\rho C\alpha\frac{\cot\beta_2}{S}\left(\frac{\cot\beta_2}{S}Q_1 - U_2\right)\frac{dQ_1}{dt} \end{aligned} \tag{9}$$

The second term with dQ_2/dt represents the diffuser effect corresponding to the mass flow gain factor. If the discharge flow Q_2 is increased, the ambient pressure p_a is decreased if the diffuser effect D is larger than the loss ζ_2, resulting in an increase in cavity volume. The third term with dQ_1/dt represents the effect of swirl. This term may also be called the "mass flow gain factor" but this term is associated with the upstream flow Q_1. At flow rates higher than design ($Q_1 > U_2 S\tan\beta_2$), the tangential velocity $c_{\theta 2}$ and the cavity volume increase as the upstream flow rate Q_1 is increased. The opposite result is obtained at a smaller flow rate.

By putting Eq. (3) in Eq. (2), we obtain

$$p_{\text{inlet}} = p_{\text{exit}} + \rho\frac{L_e}{A_e}\frac{dQ_2}{dt} + \rho\frac{\zeta_2 - D}{2A_e^2}Q_2^2 + \rho\frac{L_i}{A_i}\frac{dQ_1}{dt} + \rho\frac{\zeta_T}{2A_i^2}Q_1^2 \tag{10}$$

Equations (9) and (10) are the fundamental equations in determining $Q_1(t)$ and $Q_2(t)$. For stability analysis, we assume $Q_1 = \bar{Q}_1 + \tilde{Q}_1(t)$, $Q_1 = \bar{Q}_2 + \tilde{Q}_2(t)$ and $\bar{Q}_1 \gg \tilde{Q}_1(t)$, $\bar{Q}_2 \gg \tilde{Q}_2(t)$. By assuming $\bar{Q}_1 = \bar{Q}_2 = \bar{Q}$, the unsteady parts of Eqs. (10) and (9) can be expressed as

$$0 = \rho\frac{L_e}{A_e}\frac{d\tilde{Q}_2}{dt} + \rho\frac{\zeta_2 - D}{A_e^2}\bar{Q}\tilde{Q}_2 + \rho\frac{L_i}{A_i}\frac{d\tilde{Q}_1}{dt} + \rho\frac{\zeta_T}{A_i^2}\bar{Q}\tilde{Q}_1 \tag{11}$$

$$\begin{aligned} \tilde{Q}_2 - \tilde{Q}_1 &= -\rho C\frac{L_e}{A_e}\frac{d^2\tilde{Q}_2}{dt^2} + \rho C\frac{D-\zeta_2}{A_e^2}\bar{Q}\frac{d\tilde{Q}_2}{dt} \\ &\quad + 2\rho C\alpha\frac{\cot\beta_2}{S}\left(\frac{\cot\beta_2}{S}\bar{Q} - U_2\right)\frac{d\tilde{Q}_1}{dt} \end{aligned} \tag{12}$$

Here, we assume $\tilde{Q}_1 = \tilde{Q}_{1,0}e^{j\omega t}$, $\tilde{Q}_2 = \tilde{Q}_{2,0}e^{j\omega t}$, where j is an imaginary unit and we consider that the real parts of complex quantities have physical meanings. If we put these expressions in Eqs. (11) and (12), we obtain a set of homogeneous linear equations in terms of $\tilde{Q}_{1,0}$ and $\tilde{Q}_{2,0}$. The characteristic equation is obtained by setting the determinant of the coefficient matrix of the linear equations to zero:

$$-\left(\frac{\rho L_i}{A_i}\frac{\rho L_e}{A_e}C\right)(j\omega)^3-\left[\frac{\rho\zeta_T}{A_i^2}\bar{Q}\frac{\rho L_e C}{A_e}-\frac{\rho L_i}{A_i}\frac{\rho C}{A_e^2}(D-\zeta_2)\bar{Q}+2\rho C\alpha\frac{\cot\beta_2}{S}\left(\frac{\cot\beta_2}{S}\bar{Q}-U_2\right)\frac{\rho L_e}{A_e}\right](j\omega)^2+\left[-\frac{\rho L_e}{A_e}-\frac{\rho L_i}{A_i}+\frac{\rho\zeta_T}{A_i^2}\frac{\rho C}{A_e^2}(D-\zeta_2)\bar{Q}^2-2\rho C\alpha\frac{\cot\beta_2}{S}\left(\frac{\cot\beta_2}{S}\bar{Q}-U_2\right)\frac{\rho(\zeta_2-D)}{A_e^2}\bar{Q}\right](j\omega)+\left[-\frac{\rho(\zeta_2-D)}{A_e^2}\bar{Q}-\frac{\rho\zeta_T}{A_i^2}\bar{Q}\right]=0 \tag{13}$$

Equation (13) is a third order equation in terms of $j\omega$ with real coefficients. From the characteristic equation (13), we can determine the complex frequency $\omega=\omega_R+j\omega_I$. The expression $e^{j\omega t}=e^{j\omega_R t}\cdot e^{-\omega_I t}$ shows that the real part ω_R gives the frequency and the imaginary part ω_I gives the damping rate.

By taking the complex conjugate of Eq. (13), we can show that if $\omega_1=\omega_{1R}+j\omega_{1I}$ is a solution of Eq. (13), then $\omega_2=-\omega_{1R}+j\omega_{1I}$ is another solution. The solutions ω_1 and ω_2 are practically the same solutions with the same frequency ω_{1R} and the common damping ω_{1I}. This also requires that the real part of the third solution be zero ($\omega_{3R}=0$). So, the solutions can be expressed as $\omega_1=\omega_{1R}+j\omega_{1I}$, $\omega_2=-\omega_{1R}+j\omega_{1I}$, and $\omega_3=j\omega_{3I}$.

Since Eq. (13) is a third order equation in terms of $j\omega$ with real coefficients, Hurwitz's criterion can be applied to obtain the stability condition:

$$\left[\frac{\zeta_T}{A_i^2}\bar{Q}\frac{L_e}{A_e}-\frac{L_i}{A_i}\frac{D-\zeta_2}{A_e^2}\bar{Q}+2\alpha\frac{\cot\beta_2}{S}\left(\frac{\cot\beta_2}{S}\bar{Q}-U_2\right)\frac{L_e}{A_e}\right]\times\left[\frac{L_e}{A_e}+\frac{L_i}{A_i}-\frac{\zeta_T}{A_i^2}\frac{\rho C}{A_e^2}(D-\zeta_2)\bar{Q}^2-2\rho C\alpha\frac{\cot\beta_2}{S}\left(\frac{\cot\beta_2}{S}\bar{Q}-U_2\right)\frac{(D-\zeta_2)}{A_e^2}\bar{Q}\right]>\frac{L_i}{A_i}\frac{L_e}{A_e}\left[\frac{\zeta_2-D}{A_e^2}+\frac{\zeta_T}{A_i^2}\right]\bar{Q} \tag{14}$$

Equation (14) can be used to determine the stable/unstable flow rate regions. However, the equation is rather complicated and we discuss the stability mainly based on the direct solution of the characteristic equation (13).

3 Causes of Instability

3.1 Diffuser Effect of the Draft Tube. Equation (12) can be written as

$$\rho C\frac{L_e}{A_e}\frac{d^2\tilde{Q}_2}{dt^2}+\rho C\frac{\zeta_2-D}{A_e^2}\bar{Q}\frac{d\tilde{Q}_2}{dt}+\tilde{Q}_2=\tilde{Q}_1+2\rho C\alpha\frac{\cot\beta_2}{S}\left(\frac{\cot\beta_2}{S}\bar{Q}-U_2\right)\frac{d\tilde{Q}_1}{dt} \tag{15}$$

If we consider the case of $\tilde{Q}_1=0$, negative damping occurs when

$$D>\zeta_2 \tag{16}$$

This is caused by the diffuser effect of the draft tube. The frequency is given by

$$\omega_e=\sqrt{\frac{A_e}{\rho L_e C}} \tag{17}$$

This mechanism can be explained as follows. We consider the case when Q_2 is increased. From Eq. (3), p_a will decrease if $D>\zeta_2$ due to the diffuser effect, and the cavity volume V_c is increased. Then, Eq. (1) shows that Q_2 is increased further if Q_1 is kept constant. This positive feedback is the cause of the instability due to the diffuser effect.

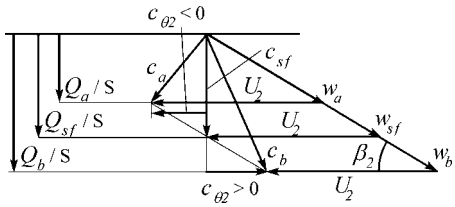

Fig. 2 Velocity triangle at the runner exit for three flow rates

3.2 Swirl Effect. We differentiate Eq. (11) with t and represent $d^2\tilde{Q}_2/dt^2$ with other terms. By putting it into Eq. (12), we obtain the following equation:

$$\rho C\frac{L_i}{A_i}\frac{d^2\tilde{Q}_1}{dt^2}+\left[\rho C\frac{\zeta_T}{A_i^2}\bar{Q}+2\rho C\alpha\frac{\cot\beta_2}{S}\left(\frac{\cot\beta_2}{S}\bar{Q}-U_2\right)\right]\frac{d\tilde{Q}_1}{dt}+\tilde{Q}_1=\tilde{Q}_2 \tag{18}$$

Here, we consider the case with $\tilde{Q}_2=0$. The first term of the multiplier on $d\tilde{Q}_1/dt$ shows the damping caused by the resistance of the runner. The second term representing the effect of swirl becomes negative or positive depending on the value of tangential velocity $c_{\theta 2}=c_{m2}\cot\beta_2-U_2=(\bar{Q}/S)\cot\beta_2-U_2$. The tangential velocity becomes zero at the flow rate $Q_{sf}=SU_2\tan\beta_2$ and this is called the swirl-free flow rate. At a flow rate smaller than the swirl-free flow rate Q_{sf}, the swirl causes instability by reducing the damping coefficient. At a larger flow rate than the swirl-free flow rate, the swirl enhances damping. These effects can be explained as follows.

The velocity triangle at the runner exit is shown in Fig. 2 for three flow rates Q_a, Q_{sf}, and Q_b. At smaller flow rate Q_a, the absolute value of the tangential velocity will decrease if the flow rate Q_a is increased. Then, the pressure in the vortex core will increase and the cavity volume is decreased. The continuity equation (1) shows that the inlet flow rate Q_a is increased further. This positive feedback is the cause of the instability. At larger flow rate Q_b the tangential velocity increases if the flow rate is increased. Then, the core pressure is decreased and the cavity volume is increased. This results in the decrease in the upstream flow rate Q_1. This negative feedback is the cause of the stabilizing effect at a higher flow rate.

3.3 Energy Balance. We consider the displacement work of the cavitation region,

$$E=\int p_a(Q_2-Q_1)dt=\int p_aQ_2dt-\int p_aQ_1dt=E_2-E_1 \tag{19}$$

under a steady oscillation condition. The pressure p_a near the cavitation region can be evaluated from Eq. (2) or (3). Here, we separate each quantity p_a into steady $\bar{p}_a$ and unsteady $\tilde{p}_{a0}e^{j\omega t}$ components and assume $\tilde{p}_{a0}\ll\bar{p}_a$. We put $Q_1=\bar{Q}_1+\tilde{Q}_{10}e^{j\omega t}$ in Eq. (2) and obtain

$$\bar{p}_a=p_{\text{inlet}}-\rho\frac{\zeta_T}{2A_i^2}\bar{Q}^2 \tag{20}$$

$$\tilde{p}_a=-\rho\frac{L_i}{A_i}j\omega\tilde{Q}_1-\rho\frac{\zeta_T}{A_i^2}\bar{Q}_1\tilde{Q}_1 \tag{21}$$

and Eq. (3) leads to

$$\bar{p}_a=p_{\text{exit}}+\rho\frac{\zeta_2-D}{2A_e^2}\bar{Q}_2^2 \tag{22}$$

$$\tilde{p}_a = \rho\frac{L_e}{A_e}j\omega\tilde{Q}_2 + \rho\frac{\zeta_2 - D}{A_e^2}\bar{Q}_2\tilde{Q}_2 \tag{23}$$

First, we consider the upstream energy transfer within a period T,

$$E_1 = \int_0^T p_a Q_1 dt = \int_0^T (\bar{p}_a + \tilde{p}_a)(\bar{Q}_1 + \tilde{Q}_1)dt = \bar{p}_a\bar{Q}_1 T + \int_0^T \tilde{p}_a\tilde{Q}_1 dt$$

$$= \bar{E}_1 + \tilde{E}_1 \tag{24}$$

In the same way,

$$E_2 = \int_0^T p_a Q_2 dt = \bar{p}_a\bar{Q}_2 T + \int_0^T \tilde{p}_a\tilde{Q}_2 dt = \bar{E}_2 + \tilde{E}_2 \tag{25}$$

We consider the unsteady displacement work $\tilde{E}_1$ and $\tilde{E}_2$.

Using expression (21), we obtain the upstream work $\tilde{E}_1$ as follows:

$$\tilde{E}_1 = \int_0^T \tilde{p}_a\tilde{Q}_1 dt = -\rho\frac{L_i}{A_i}\int_0^T (j\omega\tilde{Q}_1)\tilde{Q}_1 dt - \rho\frac{\zeta_T}{A_i^2}\bar{Q}_1\int_0^T \tilde{Q}_1\tilde{Q}_1 dt$$

$$= -\rho\frac{\zeta_T}{A_i^2}\bar{Q}_1|\tilde{Q}_{10}|^2\frac{\pi}{\omega} \tag{26}$$

By using Eq. (23), we obtain

$$\tilde{E}_2 = \rho\frac{\zeta_2 - D}{A_e^2}\bar{Q}_2|\tilde{Q}_{20}|^2\frac{\pi}{\omega} \tag{27}$$

So,

$$\tilde{E} = \tilde{E}_2 - \tilde{E}_1 = \rho\bar{Q}\frac{\pi}{\omega}\left(\frac{\zeta_2 - D}{A_e^2}|\tilde{Q}_{20}|^2 + \frac{\zeta_T}{A_i^2}|\tilde{Q}_{10}|^2\right) \tag{28}$$

This means that the displacement work is dissipated by the upstream and downstream resistances.

The above discussions are based on the dynamics of the upstream and downstream flow channels. Equations (21) and (23) do not include the dynamics of cavitation. To clarify the contribution of cavitation, we use the continuity equation under cavitation, Eq. (12),

$$\tilde{Q}_2 - \tilde{Q}_1 = -\rho C\frac{L_e}{A_e}\frac{d^2\tilde{Q}_2}{dt^2} + \rho C\frac{D - \zeta_2}{A_e^2}\bar{Q}\frac{d\tilde{Q}_2}{dt}$$

$$+ 2\rho C\alpha\frac{\cot\beta_2}{S}\left(\frac{\cot\beta_2}{S}\bar{Q} - U_2\right)\frac{d\tilde{Q}_1}{dt} \tag{29}$$

By appropriately using Eqs. (21) and (23), we obtain

$$\tilde{E} = \int_0^T \tilde{p}_a(\tilde{Q}_2 - \tilde{Q}_1)dt = -\rho\frac{L_i}{A_i}2\rho C\alpha\frac{\cot\beta_2}{S}\left(\frac{\cot\beta_2}{S}\bar{Q}_1\right.$$

$$\left. - U_2\right)\omega^2\frac{\pi}{\omega}|\tilde{Q}_{10}|^2 \tag{30}$$

By equating Eqs. (28) and (30), we obtain

$$\rho\bar{Q}\frac{\pi}{\omega}\left(\frac{\zeta_2 - D}{A_e^2}|\tilde{Q}_{20}|^2 + \frac{\zeta_T}{A_i^2}|\tilde{Q}_{10}|^2\right)$$

$$= -\rho\frac{L_i}{A_i}2\rho C\alpha\frac{\cot\beta_2}{S}\left(\frac{\cot\beta_2}{S}\bar{Q} - U_2\right)\omega^2\frac{\pi}{\omega}|\tilde{Q}_{10}|^2 \tag{31}$$

Equation (31) shows the following.

(1) The displacement work by the cavity due to swirl shown by the right hand side should be dissipated by the resistance in the upstream and downstream.

Table 1 Solutions of characteristic equations for the standard case

Third order equation, Eq. (13)	
$\omega_{1,2} = \pm 13.14 - 5.17j$	$\tilde{Q}_{1,0}/\tilde{Q}_{2,0} = -0.0217 \mp 0.018j$
$\omega_3 = 0 + 1.88j$	$\tilde{Q}_{1,0}/\tilde{Q}_{2,0} = -0.303 \mp 0j$
Second order equation, Eq. (15)	
$\omega_{1,2} = \pm 12.33 - 2.34j$	$\tilde{Q}_{1,0}/\tilde{Q}_{2,0} = -0.0228 \mp 0.015j$

(2) With $D = \zeta_2$, steady oscillation is possible only for $\bar{Q}_1 < SU_2\tan\beta_2$.
(3) With $\alpha = 0$, steady oscillation is possible only for $D = \zeta_2 + A_e^2/A_i^2|\tilde{Q}_{10}/\tilde{Q}_{20}|^2\zeta_T$.
(4) The cavity provides energy only through the swirl flow effects. With the diffuser effects, the energy is provided by the diffuser and the cavity does not contribute to the energy supply. The cavity is needed only for constituting a vibration system.

5 Numerical Results

The values of the parameters used for sample calculations are given in the nomenclature. These values are determined by considering a test facility at EPFL and used for sample calculations as standard values except for the parameters specified for each case. The value of the loss coefficient ζ_T representing the effect of the runner was determined by assuming that the applied head H equals the loss head $(\zeta_T/2g)(\bar{Q}/A_i)^2$ across the runner. The value of the cavitation compliance C was determined so that the frequency given by Eq. (17) becomes 0.16 times the rotational frequency of the impeller, f_n.

The swirl-free flow rate Q_{sf}, which gives no swirl at the runner exit, is calculated to be

$$Q_{sf} = SU_2\tan\beta_2 = 0.618\ \mathrm{m^3/s}$$

5.1 Mode of Oscillation. The ratio of the amplitudes of the flow rate fluctuation in the upstream and downstream can be determined from Eq. (11) to be

$$\frac{\tilde{Q}_{1,0}}{\tilde{Q}_{2,0}} = -\left[\frac{\rho(\zeta_2 - D)}{A_e^2}\bar{Q} + \frac{\rho L_e}{A_e}j\omega\right]\Bigg/\left[\frac{\rho\zeta_T}{A_i^2}\bar{Q} + \frac{\rho L_i}{A_i}j\omega\right] \tag{32}$$

Since $(\zeta_2 - D)/A_e^2 \ll \zeta_T/A_i^2$ and $L_e \ll L_i$, inlet flow rate fluctuation $\tilde{Q}_1$ is much smaller than the outlet flow rate fluctuation $\tilde{Q}_2$. In this case, Eq. (15) with $\tilde{Q}_1 = 0$ is expected to give a good approximation.

Table 1 shows the result for the standard case. Third order equation shows the results from Eq. (13) and second order equation shows the results from Eq. (15) with $\tilde{Q}_1 = 0$. The third order equation has solutions ω_1 and ω_2 with the same imaginary part, and positive and negative real parts with the same absolute value. The real part of ω_3 is zero and the imaginary part is positive, suggesting an exponentially decaying mode. This shows that the third order characteristic equation (13) gives substantially only one oscillatory mode. As expected, $|\tilde{Q}_{1,0}/\tilde{Q}_{2,0}|$ is much smaller than 1 for ω_1 and ω_2. The second order equation (15) also gives the solutions ω_1 and ω_2 with positive and negative real parts with the same absolute value. We discuss about the absolute value of the real part of ω_1 and ω_2 as the frequency and the common imaginary part of ω_1 and ω_2 as the damping rate. The difference of the values of ω_1 and ω_2 from the second and third equations is not as small as expected from the small value of $|\tilde{Q}_{1,0}/\tilde{Q}_{2,0}|$. This

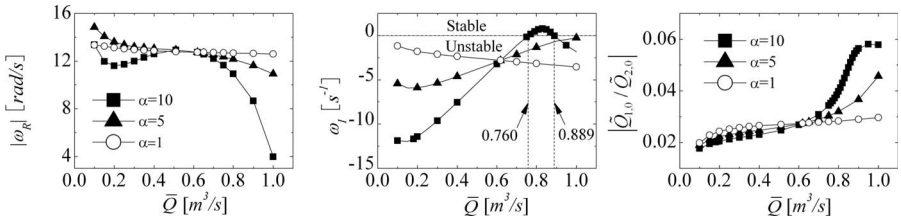

Fig. 3 Effects of mean flow rate $\bar{Q}$ under standard conditions

shows that the swirl has a significant effect even if the upstream flow rate fluctuation is small, perhaps caused by larger values of $\cot\beta_2=3.17$ and $\alpha=10$.

5.2 Effects of Mean Flow Rate and Contributions of Diffuser and Swirl Effects. A large effect of mean flow rate $\bar{Q}$ on the instability is expected from the discussion in the last section. So, the effect of flow rate is examined from the numerical results from Eq. (13). Here, the head is assumed to be constant and the mean flow rate $\bar{Q}$ is changed by changing the value of ζ_T. Figure 3 shows the results with three values of the pressure coefficient of swirl α. With the standard value $\alpha=10$, the instability occurs for $\bar{Q}<0.760$ m^3/s or $\bar{Q}>0.889$ m^3/s, which includes the standard flow rate $Q_s=0.51$ m^3/s and the swirl-free flow rate $Q_{sf}=0.618$ m^3/s. For $\bar{Q}<0.76$ m^3/s, the value of $|\tilde{Q}_{1,0}/\tilde{Q}_{2,0}|$ is smaller but it increases significantly for $\bar{Q}>0.889$ m^3/s. With smaller values of $\alpha=5$ and $\alpha=1$, ω_I is negative for all flow rates $\bar{Q}$ shown. To understand this result, diffuser effects and the swirl effects are examined independently.

First, calculations were made with $\alpha=0$ to examine the diffuser effects and the results are shown in Fig. 4 with various values of the diffusion factor D. $D_{stand}=27.7$ is the standard value of the diffusion factor. We should note that small but positive damping $\omega_I>0$ is obtained for the case of $D-\zeta_2=0$. This shows that the diffuser effect represented by D is the cause of the instability. For $D=D_{stand}$ and $D=0.5D_{stand}$, the instability occurs for all flow rates and the amplifying rate $-\omega_I$ increases with the flow rate and the value of the diffusion factor D. This is expected from the damping term in Eq. (15).

Second, the effect of swirl is examined by setting $D-\zeta_2=0$ and the results with several values of swirl pressure coefficient α are shown in Fig. 5. Equation (18) with $\tilde{Q}_2=0$ suggests that the upstream resonant frequency $\omega_i=\sqrt{A_i/\rho L_i C}=2.13$ rad/s. However, the frequency is closer to the downstream resonant frequency $\omega_e=\sqrt{A_e/\rho L_e C}=12.56$ rad/s of Eq. (17).

The critical flow rate at which the damping coefficient on $d\tilde{Q}_1/dt$ in Eq. (18) becomes zero is obtained to be $\bar{Q}=0.569$ m^3/s. However, the critical flow rate with $\omega_I=0$ shown in Fig. 5 is closer to the swirl-free flow rate $Q_{sf}=0.618$ m^3/s irrespective of the value of α. The damping rate ω_I is nearly proportional to the value of α. For the case of $D-\zeta_2=0$, Hurwitz's criterion (14) reduces to

$$\bar{Q}>\frac{2\alpha U_2\cot\beta_2/S}{\dfrac{\zeta_T}{A_i^2}+2\alpha\left(\dfrac{\cot\beta_2}{S}\right)^2-\left(\dfrac{\zeta_T}{A_i^2}\dfrac{L_i}{A_i}\right)\Big/\left(\dfrac{L_e}{A_e}+\dfrac{L_i}{A_i}\right)} \tag{33}$$

For the present case with $L_i/A_i \gg L_e/A_e$, the third term in the denominator on the right hand side almost cancels the first term and Eq. (20) can be approximated by

$$\bar{Q}>\frac{2\alpha U_2\cot\beta_2/S}{2\alpha(\cot\beta_2/S)^2}=SU_2\tan\beta_2=Q_{sf} \tag{34}$$

These results show that in real cases with $L_i/A_i \gg L_e/A_e$, the swirl effect causes the instability at smaller flow rates than the swirl-free flow rate irrespective of the larger loss coefficient ζ_T of the runner. This result is in good agreement with Dorfler's study [9], which indicates that the self-excited surge can also occur at a low flow rate. The amplitude of the upstream flow rate fluctuation is much smaller and the frequency is closer to the downstream resonant frequency ω_e.

If we consider the case with $D-\zeta_2=0$ and $\zeta_T=0$, the characteristic equation (13) is reduced to

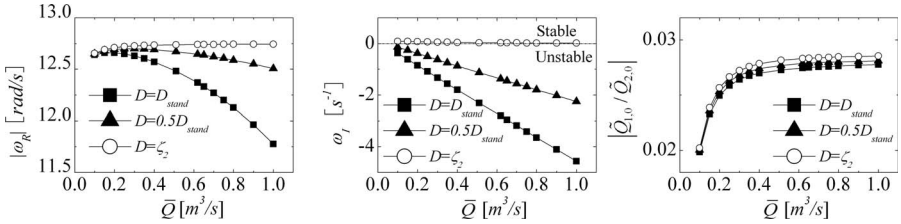

Fig. 4 Effects of diffusion factor D under $\alpha=0$

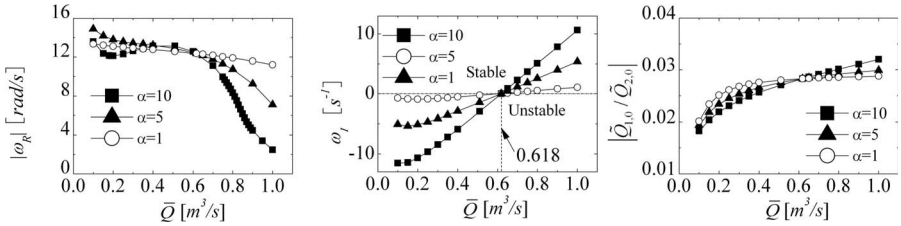

Fig. 5 Effects of pressure coefficient of swirl α under $D-\zeta_2=0$

$$-\left(\frac{\rho L_i}{A_i}\frac{\rho L_e}{A_e}C\right)\omega^2+j\left[\frac{2\rho C\alpha\cot\beta_2}{S}\left(\frac{\cot\beta_2}{S}\bar{Q}-U_2\right)\frac{\rho L_e}{A_e}\right]\omega+\left[\frac{\rho L_e}{A_e}+\frac{\rho L_i}{A_i}\right]=0 \quad (35)$$

This equation shows that the damping is caused by the swirl effects and the resonant frequency is given by

$$\omega_r=\sqrt{\frac{L_e/A_e+L_i/A_i}{\rho C(L_i/A_i)(L_e/A_e)}} \quad (36)$$

We obtain the downstream resonance with $\omega_r=\omega_e=\sqrt{A_e/\rho CL_e}$ for $L_i/A_i \gg L_e/A_e$ and the upstream resonance with $\omega_r=\omega_i=\sqrt{A_i/\rho CL_i}$ for $L_i/A_i \ll L_e/A_e$. This shows that the swirl effect can cause both upstream and downstream flow oscillations although the upstream flow rate fluctuation is essential in the positive feedback loop of the instability through the swirl.

In order to discuss about the combined effects of the diffusion and the swirl, we compare the results shown in Figs. 3–5. The similarity of the plots of ω_R in Figs. 3 and 5 shows that the swirl has the most significant effects on the frequency ω_R under standard conditions. The comparison of the plots of ω_I shows that ω_I for the standard case in Fig. 3 approximately equals the sum of those in Fig. 4 with $D=D_{\text{stand}}$ and in Fig. 5 except for the case of $\alpha=10$ with a larger value of $\bar{Q}$. The examination of $|\tilde{Q}_{1,0}/\tilde{Q}_{2,0}|$ in each figure shows that the value is generally small but relatively larger values are obtained at larger values of $\bar{Q}$ with $\alpha=10$ for the general case shown in Fig. 3. This and the behavior of ω_I in Fig. 3 for the case of $\alpha=10$ with larger value of $\bar{Q}$ are considered to be a result of the combined effects of diffusion and swirl.

6 Conclusion

It was found that the diffuser effect of the draft tube destabilizes the hydraulic system over the entire flow range. The swirl flow from the runner stabilizes/destabilizes the system above/below the swirl-free flow rates. In both cases, the frequency of oscillation is determined from the compliance of the cavitation and the inertial length of the draft tube. For general cases with larger penstock length and runner resistance, the amplitude of the flow rate fluctuation is much larger in the downstream of the runner as compared to that in the upstream. The analysis can be applied not only to the full load surge but also to the part load surge, which has been considered to be a forced oscillation due to the vortex rope whirl.

Further research is needed to correlate these findings with experimental observations in real hydropower systems. Various simplifying assumptions have been made in this study. For the application to a real system, we need to take into account the flow compressibility effects in the penstock. For lower frequency oscillations, we may need to take into account the changes in the runner speed and guide vane opening. Swirl in the draft tube may mitigate the flow separation and thus reduce the value of draft tube resistance ζ_2 [8]. At a higher mean flow rate than design, this effect might destabilize the system, and the stability would be enhanced at lower flow than design. These effects should be clarified in future study.

Acknowledgments

The authors would like to express their sincere gratitude to Professor Michihiro Nishi at Kyusyu Institute of Technology, Mr. Hiroshi Kato of DMW Corporation, and Professor Takashi Kubota of South China University of Technology for their fruitful discussions.

Nomenclature

Standard Value

$A_c=0.125\ \text{m}^2$ = draft tube inlet area
$A_i=0.22\ \text{m}^2$ = inlet pipe area
$A_e=0.67\ \text{m}^2$ = draft tube exit area
$C=97.2\times10^{-7}\ \text{m}^4\ \text{s}^2/\text{kg}$ = cavitation compliance
c_2 = runner exit absolute velocity
c_{m2} = runner exit meridional velocity
$c_{\theta 2}$ = runner exit tangential velocity
$D=(A_e/A_c)^2-\text{I}=27.7$ = diffusion factor of draft tube
$d=0.4\ \text{m}$ = runner exit diameter
$f_n=12.5\ \text{Hz}$ = rotational speed
$H=14.8\ \text{m}$ = head
$L_e=4.36\ \text{m}$ = effective length of draft tube
$L_i=50\ \text{m}$ = inlet pipe length
p = pressure
$Q=0.51\ \text{m}^3/\text{s}$ = flow rate
$Q_{\text{sf}}=0.618\ \text{m}^3/\text{s}$ = swirl-free flow rate
$\bar{Q}$ = steady part of flow rate
$\tilde{Q}$ = unsteady part of flow rate
$S=0.125\ \text{m}^2$ = runner exit area
$U_2=15.7\ \text{m/s}$ = runner exit circumferential velocity
V_c = volume of cavity
$\alpha=10$ = pressure coefficient of swirl
$\beta_2=17.5\ \text{deg}$ = runner exit blade angle
$\rho=1000\ \text{kg/m}^3$ = fluid density
$\omega=\omega_R+j\omega_I$ = complex frequency
$\zeta_2=0.207$ = loss coefficient of draft tube
$\zeta_T=54.2$ = runner resistance

References

[1] Jacob, T., and Prenat, J.-E., 1996, "Francis Turbine Surge: Discussion and Data Base," *Proceedings of the 18th IAHR Symposium*, Valencia, Spain.
[2] Nishi, M., 1984, "Surging Characteristics of Conical and Elbow Type Draft Tubes," *Proceedings of the 12th IAHR Symposium on Hydraulic Machinery and System*, Stirling, U.K., pp. 272–283.
[3] Nishi, M., Matsunaga, S., Kubota, T., and Senoo, Y., 1982, "Flow Regimes in an Elbow-Type Draft Tube," *Proceedings of the 11th IAHR Symposium on Hydraulic Machinery and System*, Amsterdam, Netherlands, Paper No. 38, pp. 1–13.
[4] Nishi, M., Wang, X., Okamoto, M., and Matsunaga, S., 1994, "Further Investigation on the Pressure Fluctuations Caused by Cavitated Vortex Rope in an Elbow Draft Tube," *Cavitation and Gas Fluid Flow Machinery and Devices, ASME*, pp. 63–70.
[5] Prenat, J.-E., and Jacob, T., 1986, "Investigating the Behavior at High Load of a Francis Turbine Model," *Proceedings of the 13th IAHR Symposium*, Montreal, Canada.
[6] Koutnik, J., and Pulpitel, L., 1996, "Modeling of the Francis Turbine Full-Load Surge," *Modeling, Testing and Monitoring for Hydro Power Plants*, Lausanne, Switzerland.
[7] Koutnik, J., Nicolet, C. A., Schoul, G., and Avellan, F., 2006, "Overload Surge Event in a Pumped Storage Power Plant," *Proceedings of the 23rd IAHR Symposium*, Yokohama, Japan, Paper No. 135.
[8] Susan-Resiga, R., Ciocan, G. D., Anton, I., and Avellan, F., 2006, "Analysis of the Swirling Flow Downstream a Francis Turbine Runner," ASME J. Fluids Eng., **128**, pp. 177–189.
[9] Dorfler, P. K., 1985, "Francis Turbine Surge Prediction and Prevention," *Proceedings of the Waterpower '85*, pp. 952–961.

Study of Oscillating Flow of Viscoelastic Fluid With the Fractional Maxwell Model

Jiu-hong Jia[1]
Dr.
e-mail: jhjia@sjtu.edu.cn

Hong-xing Hua

State Key Laboratory of Vibration, Shock and Noise,
Shanghai Jiaotong University,
Shanghai 200240, China

The oscillating flow of the viscoelastic fluid in cylindrical pipes has been applied in many fields, such as industries of petroleum, chemistry, and bioengineering. It is studied using the fractional derivative Maxwell model in this paper. The exact solution is obtained utilizing a simpler and more reasonable technique. According to this velocity solution, the time-velocity profile of one kind of viscoelastic fluid is analyzed. From analysis, it is found that the flow behaves like the Newton fluid when the oscillating frequency is low, and the flow reversal occurs when the oscillating frequency is high. Moreover, two series approximations for the velocity are obtained and analyzed for different model parameters. In one series approximation, the velocity is parabolic in profile, while in the other series approximation, the velocity presents three characteristics: (1) it is independent of radius and at the centerline is smaller than that of steady Poiseuille flow, (2) the phase lags about 90 deg *with respect to the imposed pressure gradient, and (3) the Richardson annular effect is found near the wall.* [DOI: 10.1115/1.2903517]

Keywords: Fractional derivative Maxwell model, viscoelastic fluid, oscillating flow, pipe flow, Richardson annular effect

1 Introduction

The oscillating flow of the viscoelastic fluid in cylindrical pipes has been applied in many fields, such as industries of petroleum, chemistry, and bioengineering. Using Maxwell model, the problem has been discussed by several authors [1–3]. However, it is difficult to suggest a model, which can exhibit all properties of viscoelastic fluid. For this reason, many models have been proposed and most of them are empirical or semiempirical. Recently, fractional calculus has encountered much success in the description of viscoelasticity [4–9]. Using the Riemann–Liouville fractional calculus operators to replace the time derivative of the integer order of the Maxwell model, the fractional derivative Maxwell model is obtained. This generalization allows one to define precisely noninteger order derivatives for different materials. Moreover, experimental research has illustrated that a better agreement of the experimental data could be achieved with the fractional Maxwell model than the ordinary Maxwell model [4,5].

Because of the advantages above mentioned, Tan [10] studied four unsteady flows of a viscoelastic fluid with the fractional derivative Maxwell model between two infinite parallel plates. Hayat [11] discussed three types of unidirectional flows induced by general periodic oscillations of a plate using the fractional derivative Maxwell model. Yin [12] solved the oscillating flow of a viscoelastic fluid in a pipe with the fractional derivative Maxwell model. Qi [13] calculated the unsteady flow of the viscoelastic fluid in a channel.

The purpose of this paper is to study the oscillating flow of the viscoelastic fluid in an infinite pipe using the fractional derivative Maxwell model. The exact solution of the flow is obtained. This solution has been obtained by Yin [12] using the Laplace transform and the inverse Laplace transform, but it is complicated. In this paper, it is solved using a simpler and clearer technique. Subsequently, two series approximations for the velocity of oscillating flow are calculated and analyzed. Some new physical phenomena are found for the viscoelastic fluid oscillating flow.

2 Governing Equation

A transient one-directional oscillating Poiseuille flow of an incompressible viscoelastic fluid in a tube with the radius of R under a periodic pressure gradient is studied. The well-known fractional derivative Maxwell model that can describe the above viscoelastic fluid can be written as Eq. (1). Further and detailed information could be referred to Refs. [10–14].

$$\sigma + \lambda^{\alpha}\frac{\partial^{\alpha}\sigma}{\partial t^{\alpha}} = G\lambda^{\beta}\frac{\partial^{\beta}\varepsilon}{\partial t^{\beta}} \tag{1}$$

where σ is the shear stress, and ε is the rate of shear straining. $\lambda=\mu/G$ is the relaxation time, in which G is the shear modulus, $G\neq 0$, and μ is the viscosity constant. α and β are, respectively, the stress derivative and the strain derivative, and the span of their values is between zero and unity. Moreover, the condition $\alpha\leqslant\beta$ should be satisfied owing to the thermodynamics consistency [14]. When $\alpha=\beta=1$, it can be simplified as the Maxwell model.

Because the oscillating flow in a pipe is symmetrical, the velocity has only z directional component in the cylindrical coordinate system (r,θ,z), i.e.,

$$\mathbf{u} = u_z(r,t)\mathbf{e}_z \tag{2}$$

where z is the coordinate along the centerline of the pipe, r is the radial distance from the centerline, and $\mathbf{e}_z$ is the unit vector in the z direction. Moreover, only the σ_{rz} component of the stress tensor is nonzero. So Eq. (1) can be written as

$$\sigma_{rz}(t) + \lambda^{\alpha}\frac{\partial^{\alpha}\sigma_{rz}(t)}{\partial t^{\alpha}} = G\lambda^{\beta}\frac{\partial^{\beta-1}}{\partial t^{\beta-1}}\frac{\partial u_z}{\partial r} \tag{3}$$

and the momentum equation in the absence of body force is

$$\rho\frac{\partial u_z}{\partial t} = -\frac{\partial p}{\partial z} + \frac{\partial \sigma_{rz}}{\partial r} + \frac{1}{r}\sigma_{rz} \tag{4}$$

where ρ is the density of the viscoelastic fluid. No-slip boundary condition is

[1]Corresponding author.

Contributed by the Fluids Engineering Division of ASME for publication in the JOURNAL OF FLUIDS ENGINEERING. Manuscript received May 20, 2007; final manuscript received October 25, 2007; published online April 1, 2008. Assoc. Editor: Dimitris Drikakis.

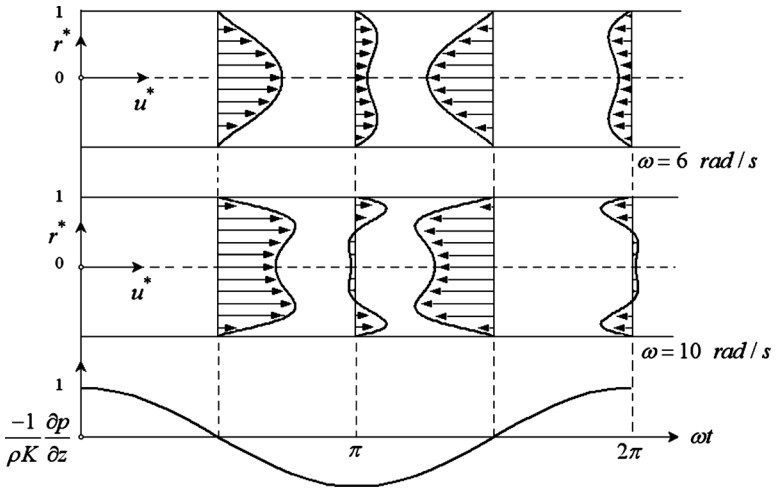

Fig. 1 Velocity distribution of an oscillating pipe flow at different instants within one period

$$u_z(R,t) = 0 \tag{5}$$

Eliminating σ_{rz} in Eqs. (3) and (4), the governing equation for u_z is obtained as follows:

$$\rho\frac{\partial u_z}{\partial t} + \frac{\partial p}{\partial z} + \lambda^\alpha \frac{d^\alpha}{dt^\alpha}\left(\rho\frac{\partial u_z}{\partial t} + \frac{\partial p}{\partial z}\right) = G\lambda^\beta \frac{d^{\beta-1}}{dt^{\beta-1}}\left(\frac{\partial^2 u_z}{\partial r^2} + \frac{1}{r}\frac{\partial u_z}{\partial r}\right) \tag{6}$$

3 Exact Solution of the Oscillating Pipe Flow

For the oscillating flow, the pressure gradient can be assumed as

$$\frac{\partial p}{\partial z} = -\rho K \exp(i\omega t) \tag{7}$$

where ρ, K, and ω are constants. The velocity can be assumed as

$$u_z(r,t) = \nu(r)\exp(i\omega t) \tag{8}$$

Substituting Eqs. (7) and (8) into Eq. (6) gives

$$r^2\frac{\partial^2 \nu}{\partial r^2} + r\frac{\partial \nu}{\partial r} - \frac{(1+(i\lambda\omega)^\alpha)r^2}{\upsilon\lambda(i\lambda\omega)^{\beta-2}}\left(\nu - \frac{K}{i\omega}\right) = 0 \tag{9}$$

where $\upsilon = \mu/\rho$.

Two function transforms are introduced as

$$w(r) = \nu(r) - K/i\omega \tag{10}$$

$$r' = \xi r \tag{11}$$

where

$$\xi^2 = -(1+(i\lambda\omega)^\alpha)/\upsilon\lambda(i\lambda\omega)^{\beta-2} = -\frac{1+|\lambda\omega|^\alpha\left(\cos\frac{\alpha\pi}{2} + i\ \text{sign}\ \omega \sin\frac{\alpha\pi}{2}\right)}{\upsilon\lambda|\lambda\omega|^{\beta-2}\left(\cos\frac{(\beta-2)\pi}{2} + i\ \text{sign}\ \omega \sin\frac{(\beta-2)\pi}{2}\right)} \tag{12}$$

According to Eqs. (10) and (11), by making the transformation of variables to Eqs. (5) and (9), respectively, the corresponding no-slip condition becomes

$$w(R') = -K/i\omega \tag{13}$$

and the governing equation becomes

$$(r')^2\frac{\partial^2 w}{\partial (r')^2} + r'\frac{\partial w}{\partial r'} + (r')^2 w = 0 \tag{14}$$

Equation (14) is the standard zeroth order Bessel function equation. So the value of the velocity can be easily obtained from Eqs. (10), (13), and (14), shown as

$$\nu(r) = \frac{K}{i\omega}\left(1 - \frac{J_0(\xi r)}{J_0(\xi R)}\right) \tag{15}$$

Substituting Eq. (15) into Eq. (8), the velocity solution of the oscillating pipe flow can be solved as

$$u_z(r,t) = u(r,t) = \frac{K}{i\omega}\left(1 - \frac{J_0(\xi r)}{J_0(\xi R)}\right)\exp(i\omega t) \tag{16}$$

In order to show some time-velocity profiles in the pipe, a viscoelastic silicone gel fluid with the density of $\rho = 930\ \text{kg/m}^3$ is chosen. The parameters in the constitutive equation of the silicone gel are $\alpha = 0.565$, $\lambda = 0.0922$, $\beta = 1$, and $\mu = 1930$ [4]. The velocity profile of the oscillating pipe flow for two frequencies, $\omega = 6$ rad/s and $\omega = 10$ rad/s, is shown in Fig. 1 at different instants during one period of oscillation. It should be noted that the flow behaves like Newton fluids when $\omega = 6$ rad/s [15], and the flow reversal occurs in the case $\omega = 10$ rad/s.

4 Results and Discussion

The solution is neat in form but very difficult to be evaluated numerically. Following what Uchida [16] did about the velocity solution of the oscillating pipe flow of the Newtonian fluids, the velocity can be expressed as the series approximations to be analyzed numerically.

In order to facilitate calculation of the velocity series approximations, several dimensionless parameters are introduced as

$$r^* = \frac{r}{R}, \quad \omega^* = \frac{\omega R^2}{\upsilon}, \quad u^* = \frac{u}{u_{\max}} \tag{17}$$

where $u_{\max} = \rho K R^2/4\mu$ is the velocity at the centerline of the steady Poiseuille flow when the pressure gradient is $-\rho K$.

Substituting the above dimensionless parameters into Eq. (16) yields the dimensionless velocity

$$u^*(r^*,t) = \frac{4}{i\omega^*}\left(1 - \frac{J_0(i\varpi r^*)}{J_0(i\varpi)}\right)\exp(i\omega t) \tag{18}$$

where

$$\varpi^2 = \frac{(1+(i\lambda\omega)^\alpha)R^2}{\upsilon\lambda(i\lambda\omega)^{\beta-2}} = \frac{R_e}{W_e}\frac{(1+(i\lambda\omega)^\alpha)}{(i\lambda\omega)^{\beta-2}}$$

$$= \frac{R_e}{W_e}\frac{1+|\lambda\omega|^\alpha\left(\cos\frac{\alpha\pi}{2}+i\,\mathrm{sign}(\lambda\omega)\sin\frac{\alpha\pi}{2}\right)}{|\lambda\omega|^{\beta-2}\left(\cos\frac{(\beta-2)\pi}{2}+i\,\mathrm{sign}(\lambda\omega)\sin\frac{(\beta-2)\pi}{2}\right)}$$

in which R_e and W_e are, respectively, the Reynolds and Weissenberg numbers.

The series approximations of the velocity can be divided into the following two expressions.

When $|\varpi|<4$,

$$u^*(r^*,t) = \frac{4\varpi^2}{i\omega^*}(1-(r^*)^2)e^{i\omega t} \tag{19}$$

When $|\varpi|>4$,

$$u^*(r^*,t) = \frac{4}{i\omega^*}\left[1-\frac{1}{\sqrt{r^*}}e^{-\varpi(1-r^*)}\right]e^{i\omega t} \tag{20}$$

Because the imaginary part of the velocity does not have real meaning, only the real part of the velocity is analyzed in this paper. The real part of Eq. (19) gives

$$u^*(r,t) = 4(1-(r^*)^2)|\lambda\omega|^{1-\beta}\left[\sin(\omega t)\left(\cos\left(\frac{\beta-2}{2}\pi\right)+|\lambda\omega|^\alpha\cos\left(\frac{\alpha-\beta+2}{2}\pi\right)\right)-\cos(\omega t)\mathrm{sign}(\lambda\omega)\times\left(\sin\left(\frac{\beta-2}{2}\pi\right)-|\lambda\omega|^\alpha\sin\left(\frac{\alpha-\beta+2}{2}\pi\right)\right)\right] \tag{21}$$

The real part of Eq. (20) is

$$u^*(r^*,t) = \frac{4}{\omega^*}\left[\sin\omega t-\frac{1}{\sqrt{r^*}}e^{-\sqrt{\tilde{r}}(1-r^*)\cos\theta/2}\sin\left(\omega t-\sqrt{\tilde{r}}(1-r^*)\sin\frac{\theta}{2}\right)\right] \tag{22}$$

where

$$\tilde{r}e^{i\theta} = \varpi^2 = (1+(i\lambda\omega)^\alpha)R^2/\upsilon\lambda(i\lambda\omega)^{\beta-2}, \quad (-\pi/2\leqslant\theta\leqslant\pi/2) \tag{23}$$

For small $|\varpi|$, the velocity distribution is parabolic. The effect of elasticity here is equivalent to an increased viscous effect. For large $|\varpi|$ and consequently for large $\sqrt{\tilde{r}}$, the second term of Eq. (22) decreases as the distance from the wall increases. Moreover, far from the wall $u^*(r^*,t)=4/\omega^*\sin(\omega t)$ is independent of the distance from the wall and the phase of which lags about a quarter of a period with respect to the imposed pressure gradient. However, there is a high-speed region near the wall, the investigation is given as follows.

The mean squared velocity over 1 cycle is defined as

$$\overline{u^2(r,t)} = \frac{\omega}{2\pi}\int_0^{2\pi/\omega}[u(r,t)]^2dt \tag{24}$$

The time squared average velocity is obtained as

$$\frac{\overline{u^2(r^*,t)}}{K^2/2\omega^2} = 1-\frac{2}{\sqrt{r^*}}e^{-C}\cos C+\frac{e^{-2C}}{r^*} \tag{25}$$

where $C=\sqrt{\tilde{r}}(1-r^*)\cos/\theta 2$, and $\overline{u_\infty^2}=K^2/(2\omega)^2$ is time average of the velocity at large distance from the wall.

When $\tilde{r}=\omega^*$ and $\theta=\pi/2$, Eq. (25) becomes

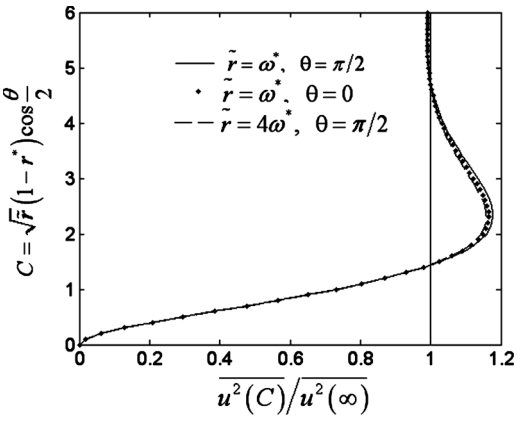

Fig. 2 Richardson annular effect (overshoot) of the velocity nearby the wall of the pipe in the oscillating pipe flow of a viscoelastic fluid with the fractional derivative Maxwell model

$$\frac{\overline{u(r^*,t)^2}}{K^2/2\omega^2} = 1-\frac{2}{\sqrt{r^*}}e^{-C'}\cos C'+\frac{1}{r^*}e^{-2C'} \tag{26}$$

where $C'=(1-r^*)\sqrt{\omega^*/2}$. This is the special case of Eq. (25) and is the expression of the time squared average velocity of viscous fluid oscillating flow in a pipe [17].

Following the work of Ref. [17], the distributions of Eq. (25) with three sets of $|\varpi|$ are shown in Fig. 2. The first set is just the same with theirs in Ref. [17]. The others are chosen at random on the condition that Eq. (26) is satisfied. The three curves are nearly alike. Judging as the way in Ref. [17], there is an overshoot in each of the velocity near the wall, which occurs when $\cos C+\sin C\approx e^{-C}$, or $C\approx 2.284$. Where and when the high-velocity region happens is independent of r^* and θ, namely, there is no dependence on $|\varpi|$, so the Richardson annular effect [18] will happen to fractional derivative Maxwell viscoelastic fluids.

5 Conclusions

The oscillating flow of viscoelastic fluids in an infinite pipe using the fractional derivative Maxwell model is studied. The governing equation is derived and the exact solution is obtained. The time-velocity profiles of the silicon gel are analyzed. The analysis results show that the flow behaves like the Newton fluid for small oscillating frequencies, and the flow reversal occurs for high oscillating frequencies. With different model parameters, two series approximations for the velocity are obtained. The analyses of the series approximations present the following characteristics.

When $|\varpi|<4$, the velocity is parabolic and not in phase with the imposed pressure gradient. When $|\varpi|>4$, the phase angle of the velocity far from the wall of the pipe is shifted by 90 deg and the velocity at the centerline is smaller than that of steady Poiseuille flow. Furthermore, the Richardson annular effect of the velocity near the wall of the pipe is found.

Acknowledgment

The author is grateful for the support from the National Natural Science Foundation of China (Nos. 05131/1046 and 1010503020203).

References

[1] Gorla, R. S. R., 1981, "Unsteady Thermal Boundary Layer Flow of a Non-Newtonian Fluid Over a Flat Plate," Int. J. Eng. Sci., **19**, pp. 1391–1399.

[2] Rahaman, K. D. and Ramkissoon, H., 1995, "Unsteady Axial Viscoelastic Pipe Flows," J. Non-Newtonian Fluid Mech., **57**, pp. 27–28.

[3] Andrienko, Yu. A., Siginer, D. A., and Yanovsky, Yu. G., 2000, "Resonance Behavior of Viscoelastic Fluids in Poiseuille Flow and Application to Flow Enhancement," Int. J. Non-Linear Mech., **35**, pp. 9–102.

[4] Makris, N., 1991, "Theoretical and Experimental Investigation of Viscous

Dampers in Applications of Seismic and Vibration Isolation [D]," State University of New York at Buffalo, Buffalo, N.Y.
[5] Dao, Y. S., and Ti, Q. J., 1998, "Study on the Constitutive Equation With Fractional Derivative for the Viscoelastic Fluids—Modified Jeffreys Model and Its Application," Rheol. Acta, **37**, pp. 512–517.
[6] Palade, L. I., Attane, P., Huilgol, R. R., and Mena, B., 1999, "Anomalous Stability Behavior of a Properly Invariant Constitutive Equation Which Generalises Fractional Derivative Models," Int. J. Eng. Sci., **37**, pp. 315–329.
[7] Rossikhin, Y. A., and Shitikova, M. V., 2001, "A New Method for Solving Dynamic Problems of Fractional Derivative Viscoelasticity," Int. J. Eng. Sci., **39**, pp. 149–176.
[8] Hernández-Jiménez, A., Hernández-Santiago, J., Macias-García, A., and Sánchez-González, J., 2002, "Relaxation Modulus in PMMA and PTFE Fitting by Fractional Derivative Maxwell Model," Polym. Test., **21**, pp. 325–331.
[9] Kulish, V. V., and Lage, J. L., 2002, "Application of Fractional Calculus to Fluid Mechanics, Journal of Fluids Engineering," ASME Trans. J. Fluids Eng., **124**, pp. 803–806.
[10] Tan, W., Pan, W., and Xu, M., 2003, "A Note on Unsteady Flows of a Viscoelastic Fluid With the Fractional Derivative Maxwell Model Between Two Parallel Plates," Int. J. Non-Linear Mech., **38**, pp. 645–650.
[11] Hayat, T., Nadeem, S., and Asghar, S., 2004, "Periodic Unidirectional Flows of a Viscoelastic Fluid With the Fractional Derivative Maxwell Model," Appl. Math. Comput., **151**, pp. 153–161.
[12] Yin, Y. B., and Zhu, K. Q., 2006, "Oscillating Flow of a Viscoelastic Fluid in a Pipe With the Fractional Derivative Maxwell Model," Appl. Math. Comput., **173**, pp. 231–242.
[13] Qi, H. T. and Xu, M. Y., 2007, "Unsteady Flow of Viscoelastic Fluid With Fractional Maxwell Model in a Channel," Mech. Res. Commun., **34**, pp. 210–212.
[14] Jia, J. H., Shen, X. Y., and Hua, H. X., 2007, "Viscoelastic Behavior Analysis and Application of Fractional Derivative Maxwell Model," J. Vib. Control, **13**, pp. 385–401.
[15] Schlichting, H., 2000, *Boundary-Layer Theory*, Springer, New York.
[16] Uchida, S. Z., 1956, "The Pulsating Viscous Flow Superposed on the Steady Laminar Motion of Imcompressible Fluid in a Circular Pipe," Z. Angew. Math. Phys., **7**, pp. 197–204.
[17] White, F. M., 1974, *Viscous Fluid Flow*, McGraw-Hill, New York.
[18] Richardson, E. G., and Tyler, E., 1929, "The Transverse Velocity Gradient Near the Mouth of Pipes in Which an Alternating Or Continuous Flow of Air Is Established," Proc. Phys. Soc., **42**, pp. 1–15.

Alternate Scales for Turbulent Boundary Layer on Transitional Rough Walls: Universal Log Laws

Noor Afzal
Department of Mechanical Engineering,
Aligarh University,
Aligarh 202002, India
e-mail: noor.afzal@yahoo.com

The present work deals with four new alternate transitional surface roughness scales for description of the turbulent boundary layer. The nondimensional roughness scale ϕ is associated with the transitional roughness wall inner variable $\zeta=Z_+/\phi$, the roughness friction Reynolds number $R_\phi=R_\tau/\phi$, and the roughness Reynolds number $\mathrm{Re}_\phi=\mathrm{Re}/\phi$. The two layer theory for turbulent boundary layers in the variables, mentioned above, is presented by method of matched asymptotic expansions for large Reynolds numbers. The matching in the overlap region is carried out by the Izakson–Millikan–Kolmogorov hypothesis, which gives the velocity profiles and skin friction universal log laws, explicitly independent of surface roughness, having the same constants as the smooth wall case. In these alternate variables, just above the wall roughness level, the mean velocity and Reynolds stresses are universal and do not depend on surface roughness. The extensive experimental data provide very good support to our universal relations. There is no universality of scalings in traditional variables and different expressions are needed for inflectional type roughness, monotonic Colebrook–Moody roughness, k-type roughness, d-type roughness, etc. In traditional variables, the velocity profile and skin friction predictions for the inflectional roughness, k-type roughness, and d-type roughness are supported well by the extensive experimental data. The pressure gradient effect from the matching conditions in the overlap region leads to the universal composite laws, which for weaker pressure gradients yields log laws and for strong adverse pressure gradients provides the half-power laws for universal velocity profiles and in traditional variables the additive terms in the two situations depend on the wall roughness.
[DOI: 10.1115/1.2844583]

1 Introduction

The rough wall flows are of great importance, but they are much more poorly understood than flows over smooth walls. The technological importance of rough wall bounded turbulent flows is well known. In many situations, a turbulent flow develops over surfaces that are hydrodynamically rough for some portion of their length. The major impact of wall roughness is to perturb the wall layer, which, in general, leads to an increase in wall shear stress. The increase in wall shear stress is almost invariably accompanied by an increase in the wall heat and mass transfer rate.

Millikan [1] was first to propose the two layer asymptotic theory. For transitional rough and fully smooth pipes in the wall region, he adopted the smooth wall variable Z_+ and for fully rough pipes, he used the inner wall variable Z/h. Millikan proposed the log law, where the prefactor is the Karman constant (a universal number) and the additive term depends on wall roughness and represents a shift of the velocity profile in the overlap region. Furthermore, for fully rough walls, the additive intercept also has a universal value that differs from the fully smooth wall value. Clauser [2] and Hama [3] simplified the matter and represented the rough wall by defining a roughness function ΔU_+, as an additional term to smooth wall log law, that arises from the transitional rough wall region as given below $\Delta U_+=(u/u_\tau)_S-(u/u_\tau)$, where suffix S refers to the fully smooth wall. The shift in the overlap region remains the same as estimated at the edge of turbulent boundary layer ($y=\delta$, $u=U_c$) as $\Delta U_+=(U_c/u_\tau)_S-(U_c/u_\tau)=(2/C_f)_S^{1/2}-(2/C_f)^{1/2}$, where $C_f=2\tau_w/\rho U_c^2$ is the local skin friction coefficient. The experiments for determination of the roughness function ΔU_+ have been described in Flack et al. [4] and Connelly et al. [5]. The roughness function ΔU_+ is a useful descriptor of the surface roughness effects on mean velocity distribution in the inner region. It physically represents the roughness dominated shift in the velocity profile from the log law of a smooth wall. For $\Delta U_+>0$, the shift is downward due to the increase of the drag and for $\Delta U_+<0$, the shift is upward due to the reduction of the drag of the rough surface (Abe et al. [6]). The roughness function ΔU_+, such as friction velocity u_τ, is a characteristic of the hydraulic wall roughness subjected to the oncoming fluid stream. The roughness function ΔU_+ data for various types of roughness may be found in Schlichting [7], Ligrani and Moffat [8], Bandyopadhyay [9], Raupach et al. [10], Patel [11], Piquet [12], Jimenez [13], Leonardi et al. [14], Afzal and Seena [15], Djendi et al. [16], Mochizuki et al. [17], Afzal [18], and Schultz and Flack [19].

The normal coordinate is $Z=y+\epsilon_r$, where ϵ_r is the origin of the normal coordinate on the rough surface, caused by irregular protrusions of the hydraulic roughness of height h. It is a particular level between the protrusion bases and heads, which automatically satisfies the constraints $0<\epsilon_r<h$ and $\epsilon_r=0$ for smooth surface. Clauser [2] proposed a method of determining the effective surface roughness origin ϵ_r and skin friction u_τ. The methods used for determination of the wall shear stress on the rough surfaces are not ideal. The modified Clauser chart method assumes that the log law is valid for rough wall boundary layers and requires the solution of additional degrees of freedom (the wall offset and the roughness function ΔU_+). Krogstad et al. [20] modified this procedure by including the wake region in the determination of the wall shear stress. Although this method allows for more points in the boundary layer to be used in determining the wall shear stress, it assumes both the existence of the log law and the functional

Contributed by the Fluids Engineering Division of ASME for publication in the JOURNAL OF FLUIDS ENGINEERING. Manuscript received March 30, 2007; final manuscript received November 2, 2007; published online April 1, 2008. Assoc. Editor: Philip M. Ligrani.

form of the law of the wake for rough wall flows. The method also simultaneously determines C_f and ΔU_+. Acharya et al. [21] observed that simultaneous selection of these parameters can yield an improved statistical fit of the data but may, in some cases, give an increase error in C_f. Using the total stress method on rough wall boundary layers has its own shortcomings. This method relies on a plateau in the Reynolds shear stress profile, which is often not clearly defined in the roughness sublayer, and has fairly high measurement uncertainty in this region (Schultz and Flack [19,22]).

The theories of the transitionally rough wall turbulent boundary layer are based on the inner layer fully smooth wall variable $Z_+ = Zu_\tau/\nu$ or the fully rough wall variable Z/h (Schlichting [7], Raupach et al. [10], Patel [11], Piquet [12], and Jimenez [13]). There is no universality of scalings in traditional variables and different expressions are needed for various types of roughness, as suggested, for example, with inflectional type roughness, monotonic Colebrook [23]—Moody [24] roughness, *k*-type/*d*-type roughness, etc., are predicted in present work. The alternative scale is connected with traditional roughness function. This alternate scale provides the wall roughness effects in the new inner wall length scale $\zeta = Z_+/\phi$, which has opened the avenues of new parameters, such as roughness friction Reynolds number and roughness Reynolds numbers. These new parameters provide universal velocity profile and universal friction factor relations that are explicitly independent of wall roughness. It also helps to yield the traditional relations and also provides insight into the roughness scale ϕ formaulation for inflectionl type roughness as well as *k*-type and *d*-type roughness. On the other hand, the traditional study of rough wall is based on fully smooth wall inner scale Z_+, where the effect of the wall roughness shows a shift of the velocity profile log law by an amount equal to the roughness function over the fully smooth wall layer log law.

The present work deals with an alternate new transitional surface roughness scale ϕ for a turbulent boundary layer, in terms of the transitional roughness inner variable $\zeta = Z_+/\phi$ and the roughness friction Reynolds number R_ϕ, where the velocity and Reynolds stresses are explicity independent of transitional wall roughness. The two layer theory for a turbulent boundary layer based on new alternate variables has been presented at large Reynolds numbers by method on matched asymptotic expansions. In the overlap region, the matching by the Izakson–Millikan–Kolmogorov hypothesis [25] for velocity profiles and friction factor gives log laws that are universal explicitly independent of wall roughness, which implicitly involve nondimensional roughness scale ϕ. The extensive experimental data provide good support to the universal log laws for the velocity profile and the friction factor on transitional rough wall boundary layers. The effects of the pressure gradient on the matching conditions in the overlap region lead to the composite laws, described in Appendix A. For weaker pressure gradient, the matching provides the log laws and for strong adverse pressure gradient the matching yields the half-power laws, where the additive constant in both situations in the inner layer depends on the wall roughness.

2 Analysis of Turbulent Boundary Layer

The boundary layer equations for incompressible two-dimensional mean turbulent flow subjected to pressure gradient, in standard notation (Schlichting [7]), are

$$\frac{\partial u}{\partial x} + \frac{\partial v}{\partial y} = 0 \tag{1}$$

$$u\frac{\partial u}{\partial x} + v\frac{\partial u}{\partial y} = -\frac{1}{\rho}\frac{dp}{dx} + \nu\frac{\partial^2 u}{\partial y^2} + \frac{1}{\rho}\frac{\partial \tau}{\partial y} \tag{2}$$

The boundary conditions are $y=0$, $u=v=\tau=0$, and $y/\delta \to \infty$, $u \to U_c(x)$, $\tau \to 0$. Here u and v are the velocity components in x streamwise and y the normal directions. $\tau = -\rho\langle u'v'\rangle$ is the appropriate Reynolds shear stress, $p'(x) = -\rho U_c dU_c/dx$ is the streamwise pressure gradient, $U_c(x)$ is the velocity at the edge of the turbulent boundary layer of thickness δ, ν is the molecular kinematic viscosity, and ρ is the fluid density.

The present work defines the roughness velocity u_ϕ and roughness coordinate y_ϕ, in terms of axial velocity u at normal distance y, as $y_\phi = y/\phi$ and $u_\phi = u/\phi$, where ϕ is the nondimensional roughness scale defined later, such that all mean relative motions and energy-containing components of the turbulent motion do not depend on surface roughness. The appropriate inner variables are

$$\zeta = \frac{Zu_{\tau\phi}}{\nu} = \frac{Z_+}{\phi}, \quad Z_+ = \frac{Zu_\tau}{\nu}, \quad Z = y + \epsilon_r \tag{3}$$

where $u_+ = u_\phi/u_{\tau\phi} = u/u_\tau$ and $u_{\tau\phi} = u_\tau/\phi$. Here, ϵ_r is the virtual origin located below the top of the roughness element, $u_\tau = (\tau_w/\rho)^{1/2}$ is the friction velocity, and τ_w is the skin friction. The roughness friction Reynolds number R_ϕ and roughness Reynolds number Re_ϕ are

$$R_\phi = \frac{\delta u_{\tau\phi}}{\nu} = \frac{R_\tau}{\phi}, \quad \mathrm{Re}_\phi = \frac{\delta U_{c\phi}}{\nu} = \frac{\mathrm{Re}}{\phi} \tag{4}$$

where $R_\tau = \delta u_\tau/\nu$ and $\mathrm{Re} = \delta U_c/\nu$. The two Reynolds numbers are connected by the relation $R_\phi = \mathrm{Re}_\phi(C_f/2)^{1/2}$ and $C_f = 2(u_\tau/U_c)^2$, where C_f is the skin friction coefficient. The transitional rough wall experimental data analyzed here show that the nondimensional roughness scale ϕ may be connected to traditional nondimensional roughness function ΔU_+ by relation

$$\Delta U_+ = \frac{1}{k}\ln\phi, \quad \phi = \exp(k\Delta U_+) \tag{5}$$

The traditional approach to turbulent shear flow of a rough wall is based on the roughness function ΔU_+, which represents the shift of the velocity profile on a rough wall over the smooth wall value (based on fully smooth wall coordinate y_+). In the present work, effects on roughness are introduced by defining a nondimensional wall variable $\zeta = Z_+/\phi$, such that the theory is explicitly independent of transitional surface roughness. The velocity profile data in the alternate wall variable ζ and the friction factor data in the alternate parameter $\mathrm{Re}_\phi = \mathrm{Re}/\phi$, the roughness Reynolds number, show universality, as the results do not explicitly depend on surface transitional roughness. The nondimensional roughness scale ϕ for the inflectional type roughness is predicted here which turns out to be a simple expression. It leads to an expression for the frictional resistance (in the case of inflectional rough surface boundary layer in the present work). The inflectional roughness in a fully developed turbulent pipe flow has been considered by Afzal and Seena [16]. The well known Moody diagram described the frictional resistance for monotonic roughness by Colebrook [23] and Moody [24], where the present work deals with such a diagram for the inflectional roughness (Nikuradse [25]). The overall description of turbulent shear flow has been in terms of two separate length scales (inner wall and outer nonlinear wake) at large Reynolds numbers. The appropriate parameter R_ϕ is the roughness friction Reynolds number.

2.1 Inner Wall Layer. The inner region scales (ν and $u_{\tau\phi}$) give the inner length scale $\nu/u_{\tau\phi}$ in the inner limit ζ fixed for $R_\phi \to \infty$. The velocity and Reynolds stress in the inner variables are

$$u = \phi^2 u_{\tau\phi} u_i(\zeta, R_\phi), \quad \tau = \rho\phi^2 u_{\tau\phi}^2 \tau_+(\zeta, R_\phi), \quad \zeta = \frac{Zu_{\tau\phi}}{\nu} \tag{6}$$

The momentum equation (2) in the inner rough wall layer becomes

$$\frac{\partial u_i}{\partial \zeta} + \tau_+ = 1 + K_\phi \zeta + O(\epsilon R_\phi)^{-1}, \quad K_\phi = \frac{\nu p'}{\phi^2 \rho u_\phi^3} \tag{7}$$

where K_ϕ represents the nondimensional pressure gradient parameter

2.2 Outer Layer. The outer layer length scale δ and the outer limit are $Y=Z/\delta$ fixed for $R_\phi \to \infty$. The velocity and Reynolds stress in the outer layer variables are

$$Y = \frac{Z}{\delta}, \quad X = \int L^{-1} dx, \quad \frac{\delta}{L} = \epsilon^2 \tag{8}$$

$$u = U_c F(X,Y), \quad F = \frac{\partial f}{\partial Y}, \quad \tau = \rho u_\tau^2 T(X,Y) \tag{9}$$

Here, δ is the outer boundary layer thickness and L is the scale of flow variations in the x direction. Equations (1) and (2) in outer layer become

$$\frac{1}{\chi}(1-\beta)T' + ff'' + \beta(1-f'^2) + X(1-\beta)(f''f_X - f'f'_X) = -\frac{(1-\beta)}{\chi R_\tau} f''' \tag{10}$$

subjected to the boundary conditions at the edge of the boundary layer

$$f'(X,\infty) = 1, \quad T(X,\infty) = 0 \tag{11}$$

The dash denotes differentiation with respect to the normal coordinate Y and suffix X denotes the differentiation with respect to coordinate X along the surface. The pressure gradient parameter β and the boundary layer growth parameter χ are

$$\beta = \frac{m}{1+m}, \tag{12a}$$

$$m = \frac{\delta}{U_c}\frac{dU_c}{d\delta}, \tag{12b}$$

$$\chi = \frac{\delta_X}{\delta} \tag{12c}$$

The outer asymptotic expansions are

$$f = f_o(X,Y) + \epsilon f_1(X,Y) + o(\epsilon) \tag{13}$$

$$F = F_o(X,Y) + \epsilon F_1(X,Y) + o(\epsilon) \tag{14}$$

$$T = T_o(X,Y) + \epsilon T_1(X,Y) + o(\epsilon) \tag{15}$$

The outer equation (10) and boundary conditions (11), in view of the asymptotic expansions (13)–(15), give the first and second order outer layer equations,

$$(1-\beta)\chi^{-1}T'_o + f_o f''_o - \beta(1-f'^2_o) + X(1-\beta)(f''_o f_{oX} - f'_o f'_{oX}) = 0 \tag{16}$$

$$(1-\beta)\chi^{-1}T'_1 + f_o f''_1 - 2\beta f'_o f'_1 + f''_o f_1 + X(1-\beta)(f''_o f_{1X} - f'_1 f'_{oX} + f''_1 f_{oX} - f'_o f'_{1X}) = 0 \tag{17}$$

subjected to the boundary conditions $f'_0(X,\infty)-1=T_0(X,\infty)=0$ and $f'_1(X,\infty)=T_1(X,\infty)=0$. The lowest order, outer layer equation (16) corresponds to that of a nonlinear wake, which for a constant eddy viscosity closure model of outer layer has been analyzed in Appendix B. These outer layer open equations have been inviscid, which fail to satisfy the no slip boundary condition. Consequently, an inner wall layer containing the viscous term is needed.

2.3 Matching. These relations provide the matching functional equations, as we are dealing with open equations of mean turbulent shear flow without any closure, following Afzal and Narasimha [26], by Izakson–Millikan–Kolmogorov (IMK) hypothesis: Between the viscous and the energetic scales in any turbulent flow exists an overlap domain over which the solutions characterizing the flow in the two corresponding limits must match as the Reynolds number approaches infinity. The resemblance of the IMK hypothesis to conventional matching associated with closed equations seems peculiar to turbulence theory. For sufficiently large Reynolds numbers, there exists an overlap domain where the inner and outer layer solutions must match. The matching of inner and outer layer velocities in the overlap region, for large Reynolds numbers, requires

$$\phi u_i(X,\zeta) = U_{c+} F_0(X,Y) - F_1(X,Y) \tag{18}$$

where $U_{c+}(R_\phi)=U_c/u_\tau$ for $\zeta \to \infty$, $Y \to 0$ for $R_\phi \to \infty$. This is an open functional equation connecting four unknown functions. The relation (18) provides the matching functional equations, as we are dealing with open equations of mean turbulent shear flow without any closure, by IMK hypothesis (Afzal and Narasimha [26]). The resemblance of the IMK hypothesis to conventional matching associated with closed equations seems peculiar to turbulence theory. For sufficiently large Reynolds numbers, there exists an overlap domain where the inner and outer layer solutions must match. For $R_\phi \to \infty$, the function $U_{+\infty} \to \infty$ and the relations (18) require that the inner velocity distribution $u_i(X,\zeta)$ should be unbounded for large ζ. Note that this matching would be impossible if $u_i(X,\zeta)$ was bounded as $\zeta \to \infty$. The open functional equation possesses a partial solution, and differentiating it with respect to y, and using the relation (18), we get

$$\zeta \frac{\partial u_+}{\partial \zeta} = U_{c+} Y \frac{\partial F_0}{\partial Y} - Y \frac{\partial F_1}{\partial Y} \tag{19}$$

as $\zeta \to \infty$ and $Y \to 0$. For large Reynolds numbers $R_\phi \to \infty$, the function $U_{\infty+} \to \infty$ and the matching of the leading order term in Eq. (19) demands

$$Y \frac{\partial F_0}{\partial Y} = o(\epsilon), \quad Y \to 0 \tag{20}$$

where $\epsilon = u_\tau / U_c$. Equation (20) permits the simplest solution

$$\frac{\partial F_0}{\partial Y} = \text{finite} \quad \text{at } Y = 0 \tag{21}$$

along with the wall slip velocity $F_0(X,0)=b_S$, where constant b_S depends on pressure gradient. This implies that nonlinear outer layer solution $F_0(X,Y)$ admits the similarity analysis, described in Appendix B, and wall slip velocity $U_S=b_S U_c$ is finite. Furthermore, Eq. (21) permits other solutions also, which have not been considered here. In view of these arguments, the matching relations (18) and (19) become

$$u_+(X,\zeta) = U_{S+} - F_1(X,Y) \tag{22}$$

$$\zeta \frac{\partial u_+}{\partial \zeta} = -Y \frac{\partial F_1}{\partial Y} \tag{23}$$

where $U_{S+}=U_S/u_\tau$ as $\zeta \to \infty$ and $Y \to 0$ for $R_\phi \to \infty$. The integration of relation (23) gives the velocity profile log laws, in the overlap region of the inner and outer regions. In law of the rough wall,

$$\frac{u}{u_\tau} = \frac{1}{k} \ln \zeta + B \tag{24}$$

In outer local velocity defect law,

$$\frac{U_S - u}{u_\tau} = -\frac{1}{k} \ln Y + D_S \tag{25}$$

In skin friction log law,

$$\frac{U_S}{u_\tau} = \frac{1}{k}\ln R_\phi + B + D_S \tag{26}$$

The lowest order outer layer flow is governed by a nonlinear wake equation (16), which under the outer boundary condition and matching condition with inner layer has been in equilibrium as described Appendix B of present work and Afzal [27,28]. Furthermore, under constant eddy viscosity closure model, we get traditional Falkner–Skan equation (B1) subjected to the certain boundary conditions (B2a,b,c) that provide a finite slip velocity U_S on the surface as a function of the pressure gradient. For a shallow wake $U_S=U_c$, implying $F_0(Y)=1$, $b_S=1$, and $D_S=D$ and the composite solution may be expressed as

$$\frac{u}{u_\tau} = \frac{1}{k}\ln\zeta + B + \frac{\Pi}{k}W(Y) \tag{27}$$

$$\frac{U_c-u}{u_\tau} = -\frac{1}{k}\ln Y + \frac{\Pi}{k}[W(1)-W(Y)] \tag{28}$$

$$\frac{U_c}{u_\tau} = \frac{1}{k}\ln R_\phi + B + D \tag{29}$$

Here, $D=W(1)\Pi/k$, Π is the wake parameter, and $W(Y)$ is the wake function of Coles [29], defined by the relation (28), subjected to the boundary conditions $W(0)=0$ and $W(1)=1$ or 2 as desired. The skin friction relation (29) may also be expressed as

$$\sqrt{\frac{2}{C_f}} = \frac{1}{k}\ln\left(\mathrm{Re}_\phi\sqrt{\frac{C_f}{2}}\right) + B + D \tag{30}$$

The effects of the pressure gradient on the matching conditions in the overlap region lead to universal composite laws, described in the Appendix. For weaker pressure gradient, the matching provides the relations (A10) and (A11), for strong adverse pressure gradient the matching yields the half-power laws for velocity profile (A12) and (A13) in universal variables, and in traditional variables the intercepts in two situations depend on the wall roughness.

3 Reduction to Traditional Picture With Shallow Outer Wake Layer

The universal velocity profile (27), with the help of expressions (5), is expressed in traditional smooth wall variable Z_+ and roughness function ΔU_+ as

$$\frac{u}{u_\tau} = \frac{1}{k}\ln Z_+ + B - \Delta U_+ + \frac{\Pi}{k}W(Y) \tag{31}$$

Likewise, the skin friction relation (29) yields

$$\frac{U_c}{u_\tau} = \frac{1}{k}\ln R_\tau + B - \Delta U_+ + \frac{\Pi}{k}W(1) \tag{32}$$

The velocity profile (31) may also be expressed as

$$\frac{u}{u_\tau} = \frac{1}{k}\ln Z_+ + B_t + \frac{\Pi}{k}W(Y), \tag{33a}$$

$$\Delta U_+ = B - B_t \tag{33b}$$

In terms of rough wall variables, the velocity profile (33a) and (33b) becomes

$$\frac{u}{u_\tau} = \frac{1}{k}\ln\frac{Z}{h} + B_T + \frac{\Pi}{k}W(Y), \quad B_t + \frac{1}{k}\ln h_+ = B_T \tag{34}$$

Here, B and B_T are intercepts of log laws in fully smooth wall and transitional rough wall flows. The roughness function ΔU_+ and roughness scale ϕ from above relations yield

$$\Delta U_+ = \frac{1}{k}\ln h_+ + B - B_T \tag{35}$$

$$\phi = \exp(k\Delta U_+) = h_+\exp[k(B-B_T)] \tag{36}$$

For fully smooth hydraulic wall, h_+ is sufficiently small (say, less than about 5 for sand roughness); the flow is hydraulically smooth, where $B=5.5$. For fully rough hydraulic wall, h_+ sufficiently large (say, more than about 70 for sand roughness); the flow is fully rough where $B_F=8.5$.

The law of rough wall (31) and skin friction law (32) may alternately be expressed in terms of meteorological variables as given below:

$$\frac{u}{u_\tau} = \frac{1}{k}\ln\frac{Z}{Z_0} + \frac{\Pi}{k}W(Y) \tag{37}$$

$$\frac{U_c}{u_\tau} = \frac{1}{k}\ln\frac{Z_0}{\delta} + D \tag{38}$$

Here, Z_{0+} is the roughness length, where effective wall may be regarded displaced inward from actual wall by an amount Z_0. It is connected with roughness scale by the relation $Z_{0+}=\phi\exp(-kB)$.

4 Roughness Scale ϕ and Roughness Length Z_{0+}

4.1 Monotonic Roughness. In commercial monotonic roughness, Colebrook [23] fortuitously proposed that roughness scale ϕ is simply the sum of fully smooth wall $\phi=1$ and fully rough wall $\phi=\chi h_+$, where $\chi=\exp[k(B-B_F)]$. Adopting $B=5$ for fully smooth wall and $B_F=8.5$ for fully rough wall yields $\chi=0.306$. The composite function [23] is $\phi=1+\chi h_+$.

4.2 Inflectional Roughness. The inflectional roughness of Nikuradse [25] has been analyzed by Loselevich and Pilipenko (see Cebeci [30]) to suggest the following correlation:

$$\Delta U_+ = (B - 8.5 + k^{-1}\ln h_+)\sin[0.4258(\ln h_+ - 0.811)] = \frac{1}{k}\ln\phi \tag{39}$$

for $2.25 \leqslant h_+ < 90$ with $B=5.2$ and $k=0.42$.

In the present work, the roughness scale ϕ for the inflectional roughness of Nikuradse [25] from modification of the Colebrook monotonic relation, by introducing an exponential function that approaches unity for $h_+\to\infty$, is stated below:

$$\phi = 1 + \chi h_+\exp\left(-\frac{j}{h_+}\right) \tag{40}$$

$$\Delta U_+ = \frac{1}{k}\ln\left[1 + \chi h_+\exp\left(-\frac{j}{h_+}\right)\right] \tag{41}$$

The roughness length Z_{0+} is connected with the roughness scale by the relation

$$Z_{0+} = \left[1 + \chi h_+\exp\left(-\frac{j}{h_+}\right)\right]\exp(-kB) \tag{42}$$

The log law constants B_T and B_t based on the roughness function (41) become

$$B_T = B - \frac{1}{k}\ln\left[\frac{1}{h_+} + \chi\exp\left(-\frac{j}{h_+}\right)\right] \tag{43}$$

$$B_t = B - \frac{1}{k}\ln\left[1 + \chi h_+\exp\left(-\frac{j}{h_+}\right)\right] \tag{44}$$

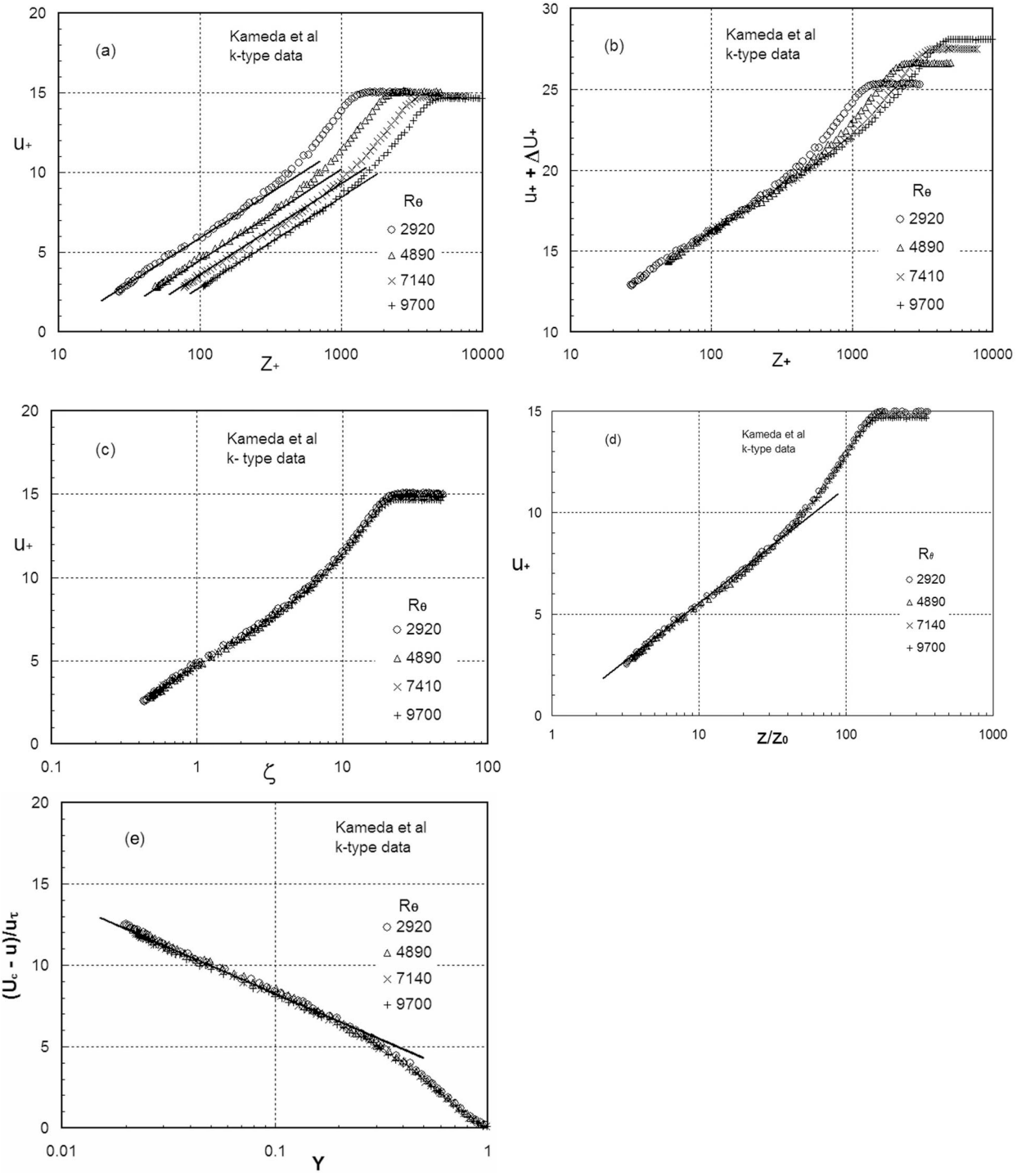

Fig. 1 The velocity distribution on *k*-type roughness from data of Kameda et al. [32] in semilog plots: (*a*) Inner smooth wall variables (u_+, Z_+). (*b*) Velocity profile shifted by the roughness function $u_+ + \Delta U_+$ against smooth wall variable Z_+. (*c*) Our universal variables for inner transitional rough wall (u_+, ζ). (*d*) Alternate universal inner rough wall variables $(u_+, Z/Z_0)$. (*e*) Outer velocity defect variables $((U_c - u)/u_\tau, Y)$.

respectively, and are the intercepts of the wall log laws for fully smooth and fully rough walls. The velocity profile log law (27) and the skin friction log law (29) become

$$\frac{u}{u_\tau} = \frac{1}{k}\ln\left\{Z_+ \Big/ \left[1 + \chi h_+ \exp\left(-\frac{j}{h_+}\right)\right]\right\} + B + \frac{\Pi}{k}W(Y) \tag{45}$$

$$\frac{U_c}{u_\tau} = \frac{1}{k}\ln\left\{R_\tau \Big/ \left[1 + \chi h_+ \exp\left(-\frac{j}{h_+}\right)\right]\right\} + B + \frac{\Pi}{k}W(1) \tag{46}$$

The skin friction log law (46) may also be expressed as

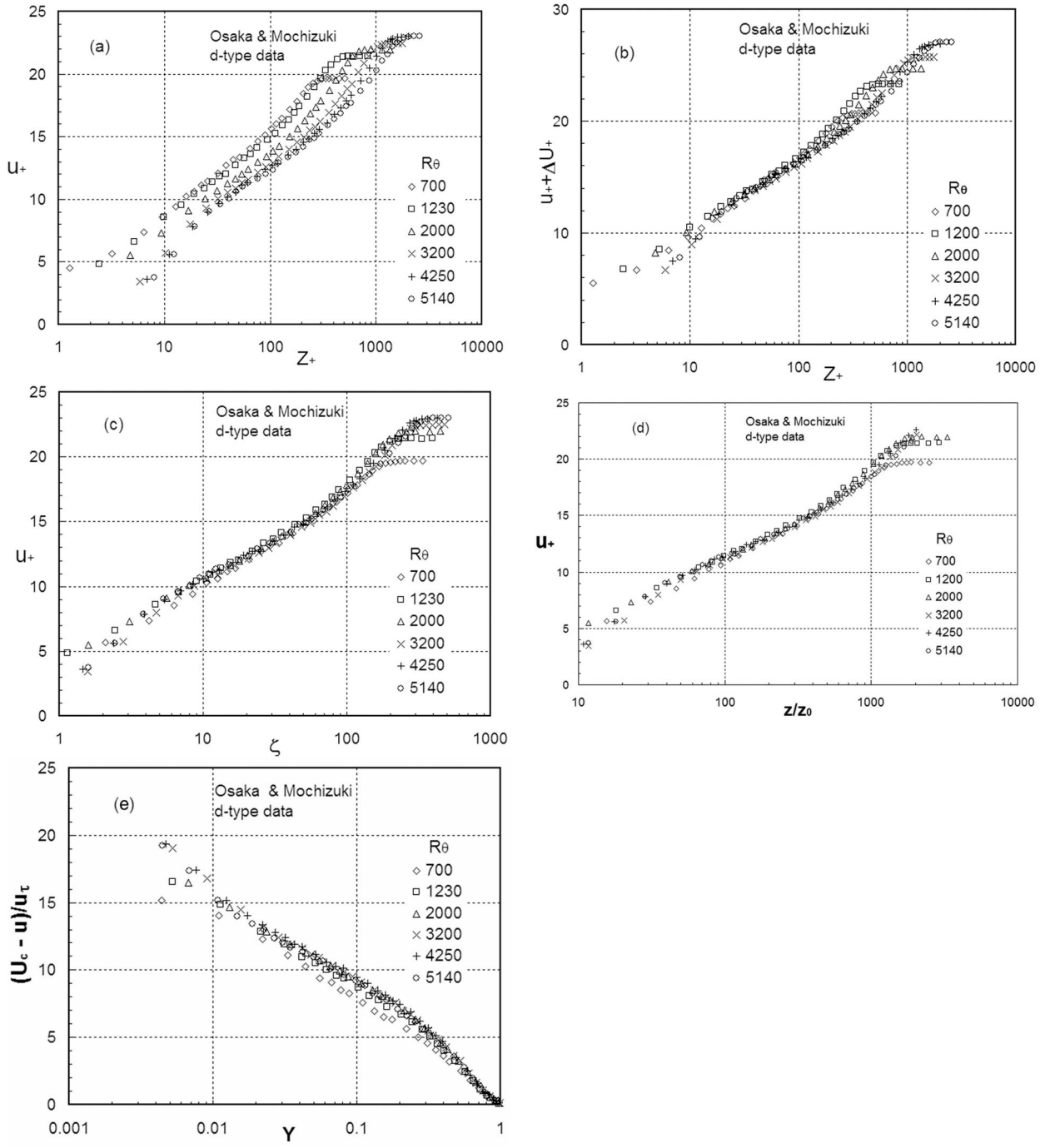

Fig. 2 The log law velocity distribution on d-type roughness from data of Osaka and Mochizuki [31] in semilog plots: (*a*) Inner smooth wall variables (u_+, Z_+). (*b*) Velocity profile shifted by the roughness function $u_+ + \Delta U_+$ against smooth wall variable Z_+. (*c*) Our universal variables for inner transitional rough wall (u_+, ζ). (*d*) Alternate universal inner rough wall variables $(u_+, Z/Z_0)$. (*e*) Outer velocity defect variables $((U_c - u)/u_\tau, Y)$.

$$\frac{U_c}{u_\tau} = -\frac{1}{k}\ln\left[\frac{1}{R_\tau}\exp[-k(B+D)] + \frac{h}{\delta}\exp(-k(B_F+D)) \times \exp\left(-\frac{j}{h_+}\right)\right] \tag{47}$$

The skin friction coefficient C_f in terms of the friction Reynolds number $R_\tau = u_\tau \delta/\nu$ becomes

$$\sqrt{\frac{2}{C_f}} = -\frac{1}{k}\ln\left[\exp[-k(B+D)]\left\{\frac{1}{R_\tau} + \chi\frac{h}{\delta}\exp\left(-\frac{j}{R_\tau}\frac{\delta}{h}\right)\right\}\right] \tag{48}$$

The relation (48) in terms of the Reynolds number $\mathrm{Re} = U_c\delta/\nu$ becomes

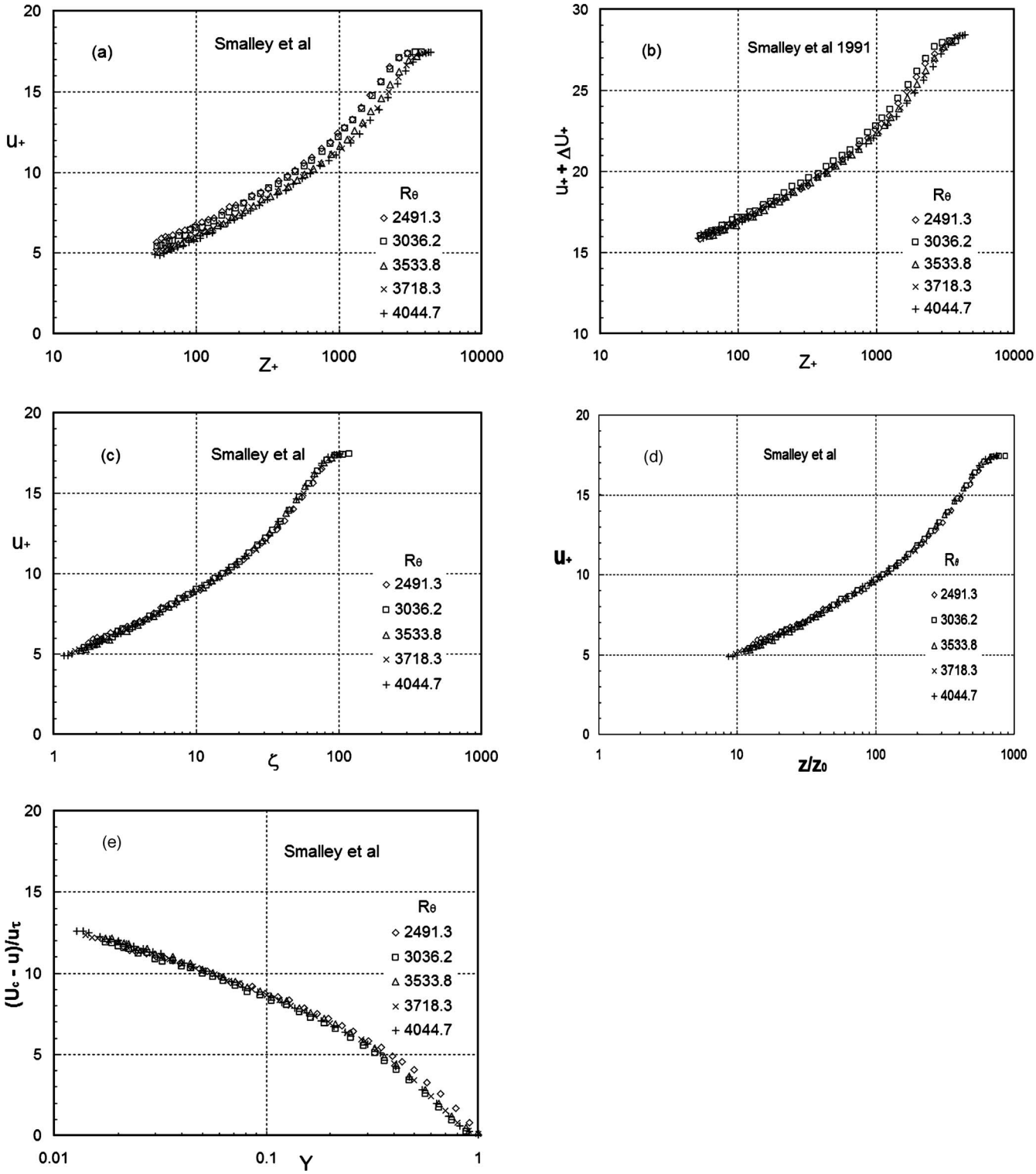

Fig. 3 The log law velocity distribution due to rod roughness data of Smalley et al. [34] in semilog plots: (*a*) Inner smooth wall variables (u_+, Z_+). (*b*) Velocity profile shifted by the roughness function $u_+ + \Delta U_+$ against smooth wall variable Z_+. (*c*) Our universal variables for inner transitional rough wall (u_+, ζ). (*d*) Alternate universal inner rough wall variables $(u_+, Z/Z_0)$. (*e*) Outer velocity defect variables $((U_c - u)/u_\tau, Y)$.

$$\sqrt{\frac{2}{C_f}} = -\frac{1}{k}\ln\left[\exp[-k(B+D)]\left\{\frac{1}{\mathrm{Re}}\sqrt{\frac{2}{C_f}} + \chi\frac{h}{\delta}\exp\left(-\frac{j}{\mathrm{Re}}\sqrt{\frac{2}{C_f}}\frac{\delta}{h}\right)\right\}\right] \tag{49}$$

For present predictions for inflectional roughness, fit to the data required $j=11$ and for Colebrook monotonic roughness $j=0$.

4.3 *k*-Type and *d*-Type Surface Roughness. The data of Osaka and Mochizuki [31] for *d*-type roughness, Kameda et al. [32] for *k*-type roughness, Antonia and Krogstad [33] for rod roughness, and Smalley et al. [34] for rod roughness, as shown later, are predicted by the following simple relations:

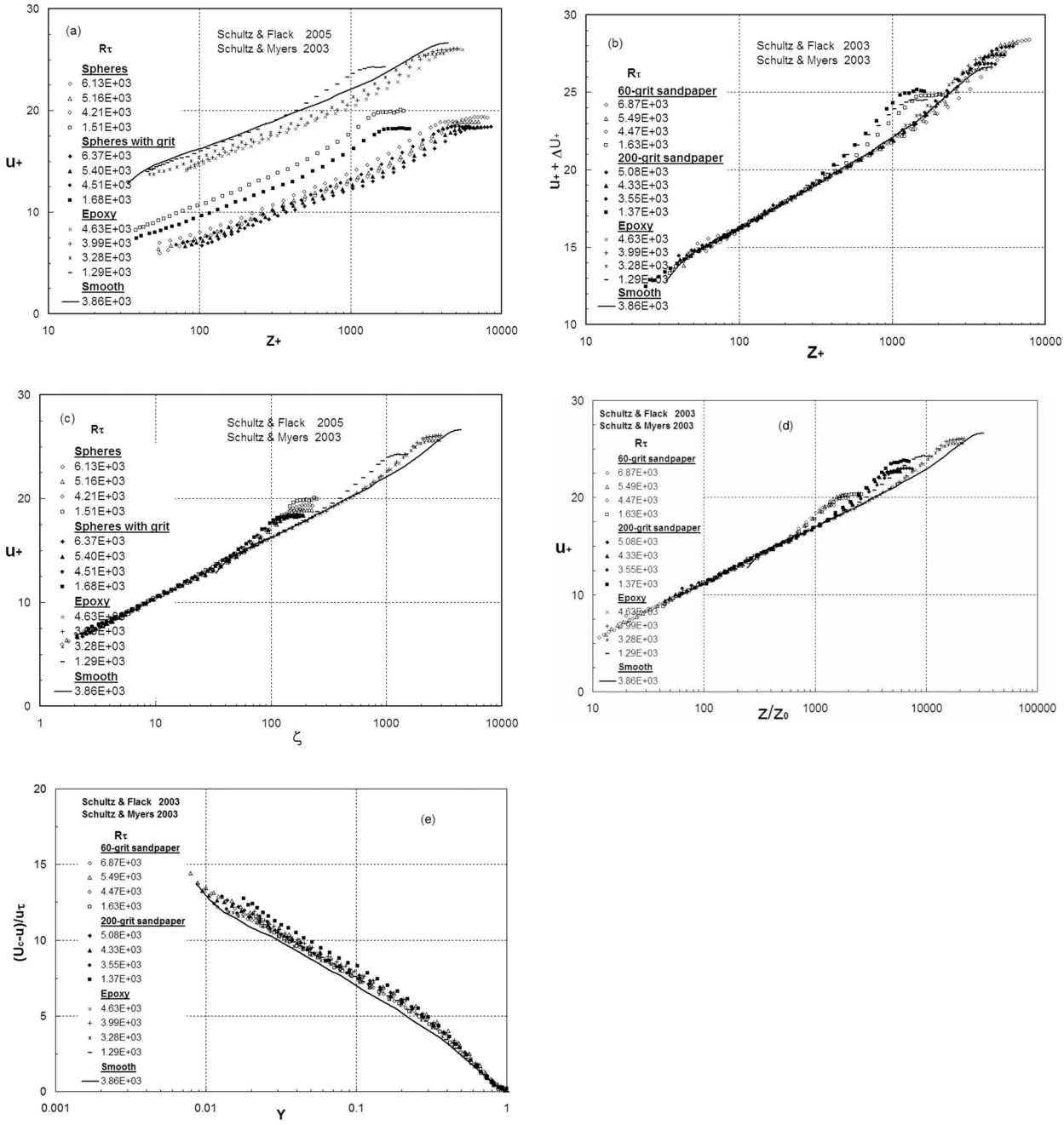

Fig. 4 The log law velocity distribution on 60- and 220-grid sand grain data of Schultz and Flack [36] and epoxy roughness data of Schultz and Myers [35] in semilog plots: (*a*) Inner smooth wall variables (u_+, Z_+). (*b*) Velocity profile shifted by the roughness function $u_+ + \Delta U_+$ against smooth wall variable Z_+. (*c*) Our universal variables for inner transitional rough wall (u_+, ζ). (*d*) Alternate universal inner rough wall variables $(u_+, Z/Z_0)$. (*e*) Outer velocity defect variables $((U_c - u)/u_\tau, Y)$.

$$\phi = h_+, \quad \Delta U_+ = \frac{1}{k} \ln h_+ \tag{50}$$

for k-type and d-type roughness. The constants B_T and B_t from relation (49) yield

$$B_t = B_T - \frac{1}{k} \ln h_+, \quad B_T = B \tag{51}$$

The skin friction (29) for k-type and d-type roughness becomes

$$\sqrt{\frac{2}{C_f}} = \frac{1}{k} \ln\left(\frac{\delta}{h}\right) + B + D \tag{52}$$

5 Results and Discussion

The velocity profile (27) and the skin friction (29) are universal log laws, valid for any kind of roughness. The inner and outer layers in the overlap region give log laws, whose slope k and additive terms B and D are universal numbers, independent of surface roughness. The inner roughness variable ζ and roughness friction Reynolds number R_ϕ implicitly depend on the surface roughness scale ϕ. The types of roughness commonly considered may be the sand grain roughness, the commercial technical roughness, the k-type roughness, and the d-type roughness in the engineering applications along with wide variety of the atmospheric

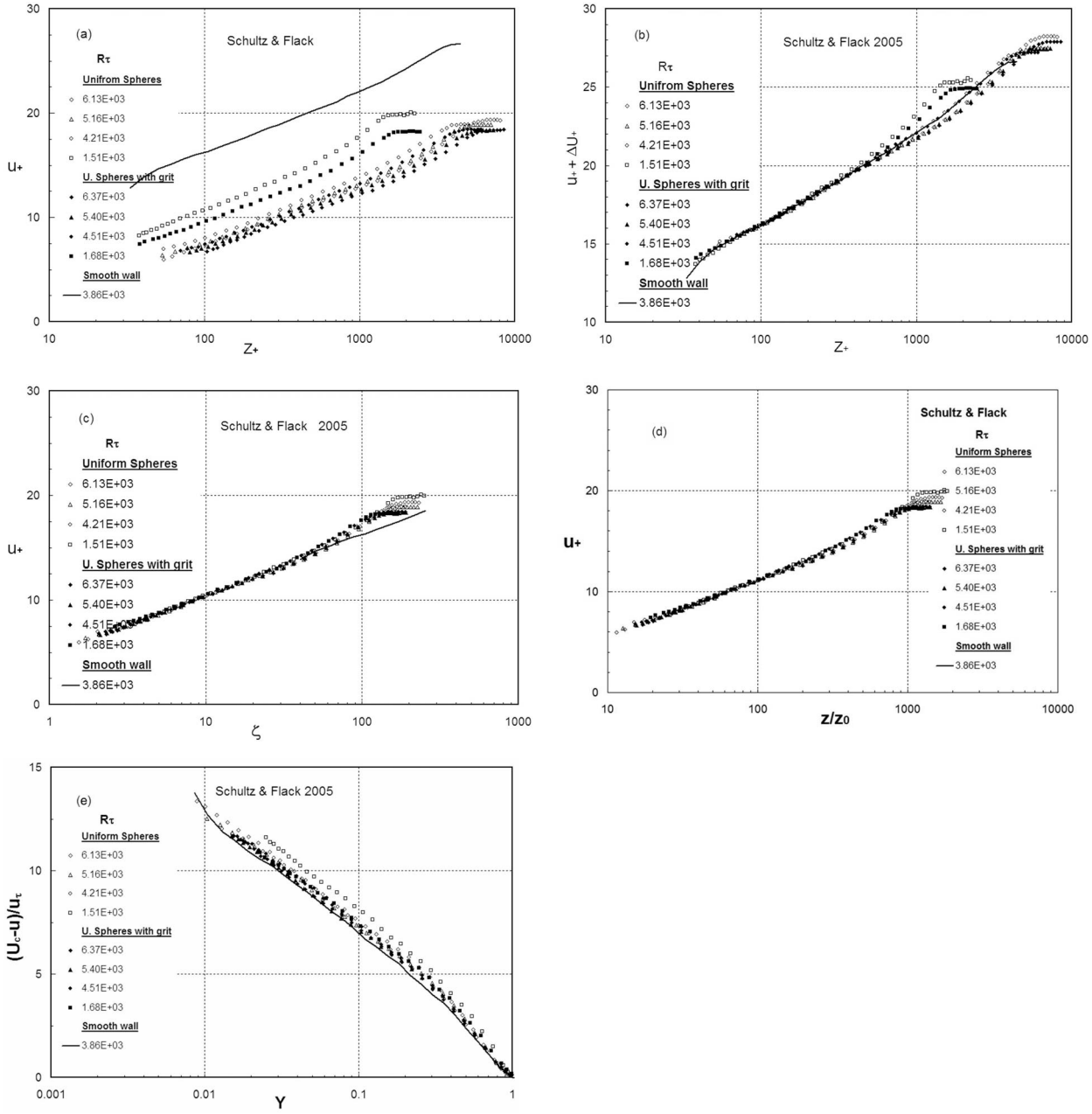

Fig. 5 The log law velocity distribution on uniform spheres and uniform spheres with grit data of Schultz and Flack [22] in semilog plots: (*a*) Inner smooth wall variables (u_+, Z_+). (*b*) Velocity profile shifted by the roughness function $u_+ + \Delta U_+$ against smooth wall variable Z_+. (*c*) Our universal variables for inner transitional rough wall (u_+, ζ). (*d*) Alternate universal inner rough wall variables $(u_+, Z/Z_0)$. (*e*) Outer velocity defect variables $((U_c - u)/u_\tau, Y)$.

surfaces. The experimental data from various sources (Osaka and Mochizuki [31], Kameda et al. [32], Antonia and Krogstad [33], Smalley et al. [34], Schultz and Myers [35], Schultz and Flack [22,36], and Rahman and Webster [37]) for zero pressure gradient have been considered.

The velocity profile from data of Kameda et al. [32] for *k*-type roughness are shown in Figs. 1(*a*)–1(*d*). In traditional smooth wall variables (u_+, Z_+), the velocity profile data are shown in Fig. 1(*a*), which in the overlap region may be represented by lines that shift their locations with change of roughness parameter h_+ or δ/h. The velocity distribution shifted by roughness function $u_+ + \Delta U_+$ versus, smooth wall variable Z_+ is shown in Fig. 1(*b*) on log-log plot, which is the Clauser–Hama type similarity and does not depend on wall roughness. In the transitional rough wall variables (u_+, ζ), the velocity profile data, shown in Fig. 1(*c*), are universal relation (24), where all data collapse on this single line, irrespective of roughness scale h_+ or δ/h. In the outer layer shallow defect variables $(U_{e+} - u_+, Y)$, the velocity profiles also collapse on line (35), shown in Fig. 1(*d*), and do not depend on wall roughness. Present work as well as that of Schultz and Flack [19,22] and Connelly et al. [5] support the Townsend [38] similarity hypothesis in the outer layer, which states that the turbulence outside of the roughness sublayer, a layer extending out approximately five roughness heights from the wall, is independent of the surface condition at sufficiently high Reynolds numbers. The velocity distribution data of Osaka and Mochizuki [31] for *d*-type roughness are shown in Figs. 2(*a*)–2(*e*), and the data of Smalley et al. [34] in Figs. 3(*a*)–3(*e*). The velocity distribution data of Schultz and Myers

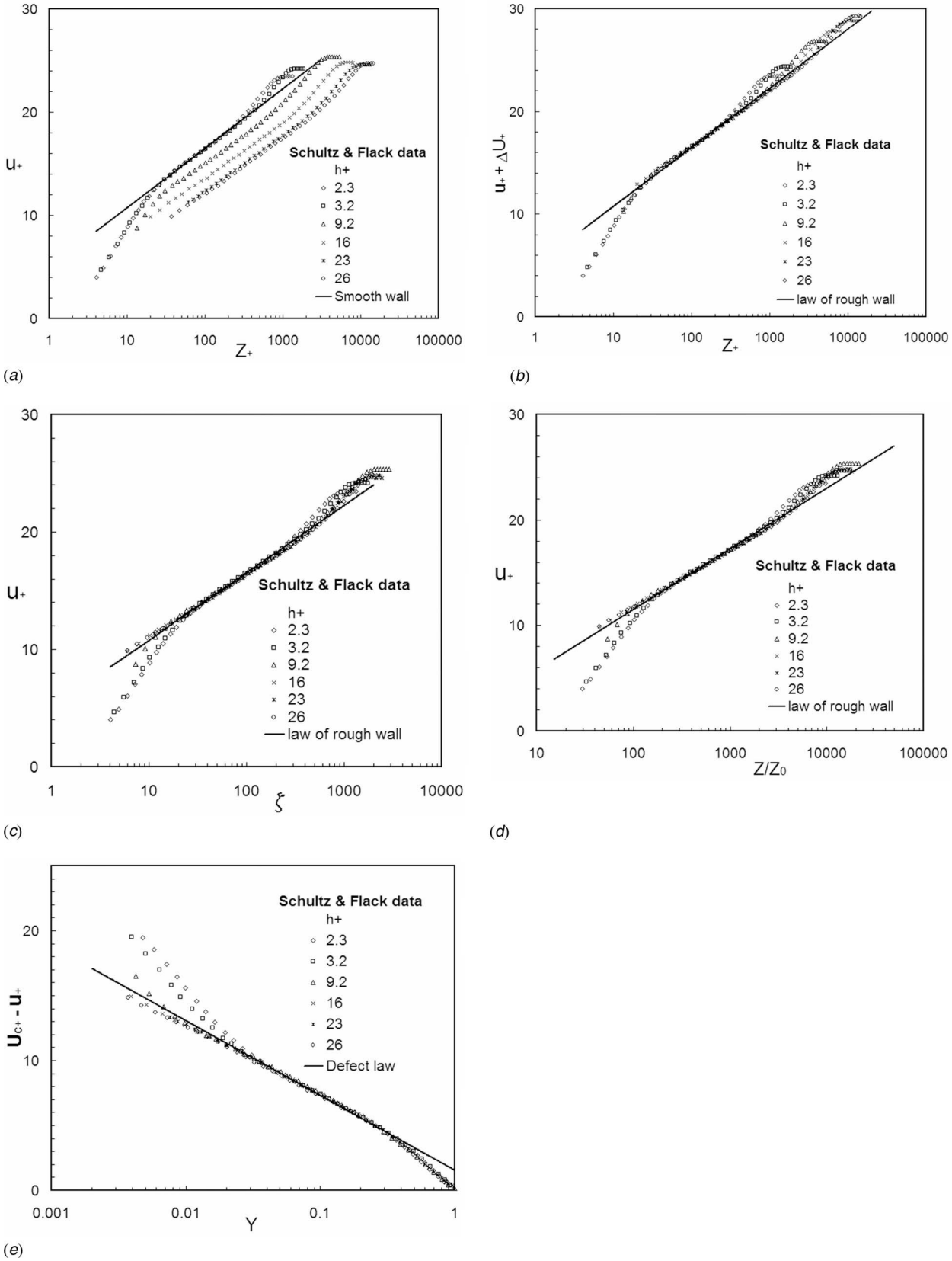

Fig. 6 The log law velocity distribution on machine honed surface roughness data of Schultz and Flack [19] in semilog plots: (*a*) Inner smooth wall variables (u_+, Z_+). (*b*) Velocity profile shifted by the roughness function $u_+ + \Delta U_+$ against smooth wall variable Z_+. (*c*) Our universal variables for inner transitional rough wall (u_+, ζ). (*d*) Alternate universal inner rough wall variables $(u_+, Z/Z_0)$. (*e*) Outer velocity defect variables $((U_c - u)/u_\tau, Y)$.

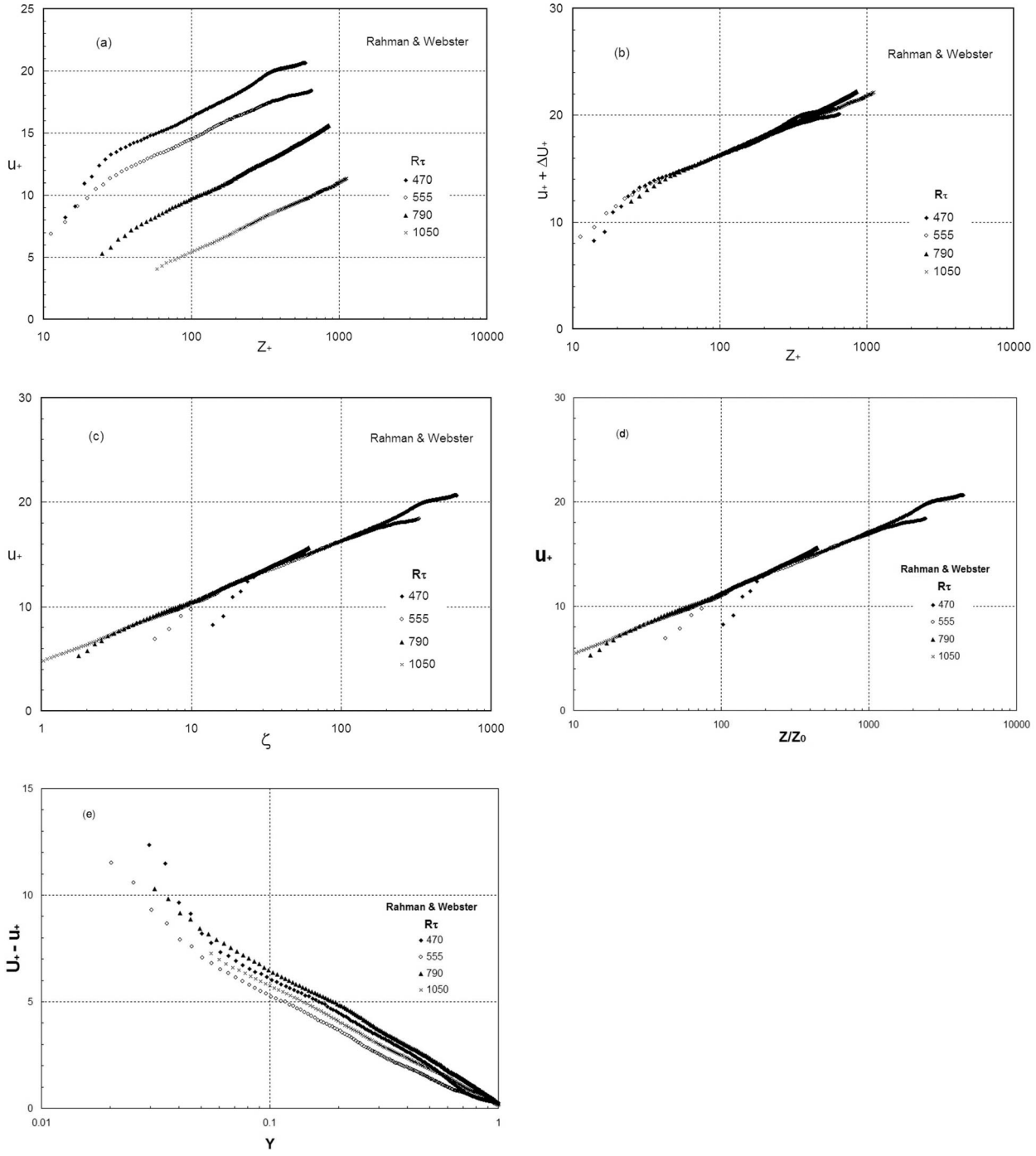

Fig. 7 The log law velocity distribution on river bed roughness from data of Rahman and Webster [37] in semilog plots: (*a*) Inner smooth wall variables (u_+, Z_+). (*b*) Velocity profile shifted by the roughness function $u_+ + \Delta U_+$ against smooth wall variable Z_+. (*c*) Our universal variables for inner transitional rough wall (u_+, ζ). (*d*) Alternate universal inner rough wall variables $(u_+, Z/Z_0)$. (*e*) Outer velocity defect variables $((U_c - u)/u_\tau, Y)$.

[35], and Schultz and Flack [36] are shown in Figs. 4(*a*)–4(*e*), the data of Schultz and Flack [22] in Figs. 5(*a*)–5(*e*), the machine honed surface roughness data of Schultz and Flake [19] in Figs. 6(*a*)–6(*e*), and data of Rahman and Webster [37] in Figs. 7(*a*)–7(*e*). The velocity distribution data in Figs. 2–7 marked *a* are in traditional smooth wall variables (u_+, Z_+), *b* are in Clauser–Hama variables $(u_+ + \Delta U_+, Z_+)$, *c* are in transitional rough wall variables (u_+, ζ), *d* are in alternate rough wall variables $(u_+, Z/Z_o)$, and *e* are in traditional outer variables $(U_{e+} - u_+, Y)$ and are analogous to Figs. 1(*a*)–1(*e*). No additional comment is needed.

The data of the roughness function ΔU_+ with roughness variable h_+ are shown in Fig. 8(*a*). The present prediction (38) for inflectional type roughness and Colebrook [23] monotonic roughness are also shown in the same figure for appreciation of commercial technical roughness effects. The data marked Schultz & Flack 1, Schultz & Flack 2, and Schultz & Myers [35] compare well with sand grain roughness prediction (38). The data of Osaka and Mochizuki [31] for *d*-type roughness, Kameda et al. [32] for *k*-type roughness, and Smalley et al. [34] may be described by the following simple predictions (47)–(49). The roughness potential ϕ

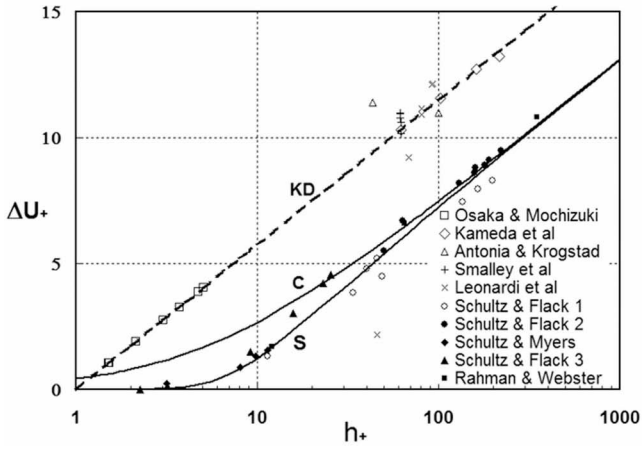

(*a*)

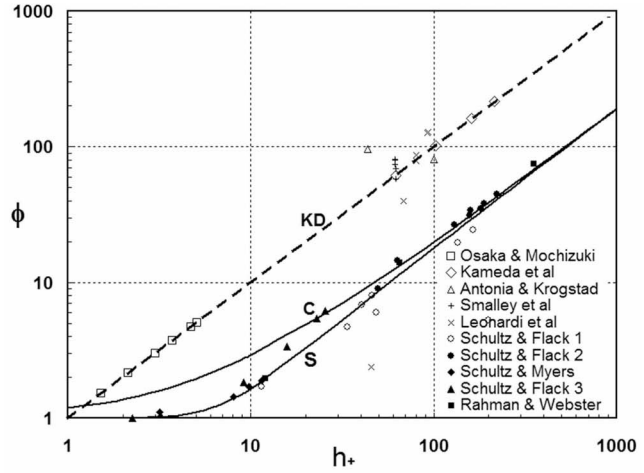

(*b*)

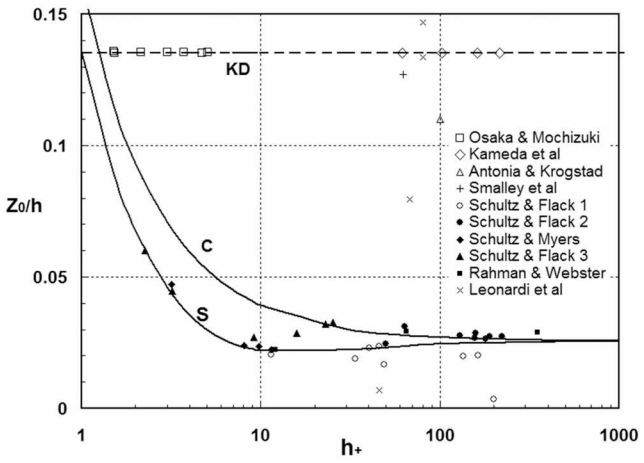

(*c*)

Fig. 8 Comparison of the roughness scales data with present predictions. (*a*) The roughness function ΔU_+ against wall roughness parameter h_+ for various values of δ/h. (*b*) Roughness scale ϕ against wall roughness parameter h_+ for various values of δ/h. (*c*) Roughness scale Z_0/h against wall roughness parameter h_+ for various values of δ/h. The lines marked *S* is the inflectional roughness ($j=11$) and marked *C* is for Colebrook monotonic roughness ($j=0$) from predictions Eq. (40) for roughness scale ϕ, Eq. (41) for roughness function ΔU_+, and Eq. (42) for roughness length Z_{0+}. Line marked *KD* is the prediction (51) for *k*-type and *d*-type roughnesses.

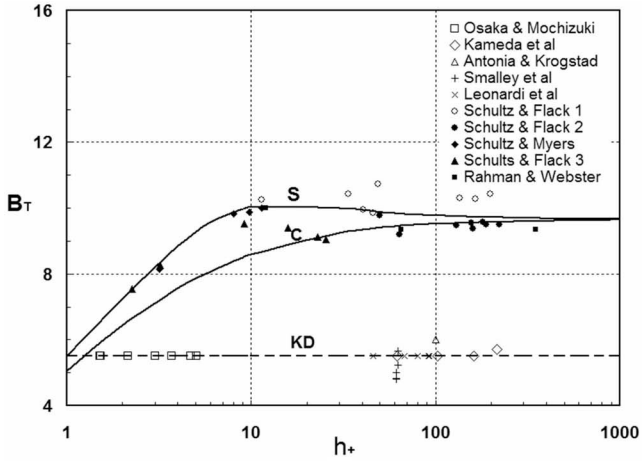

(*a*)

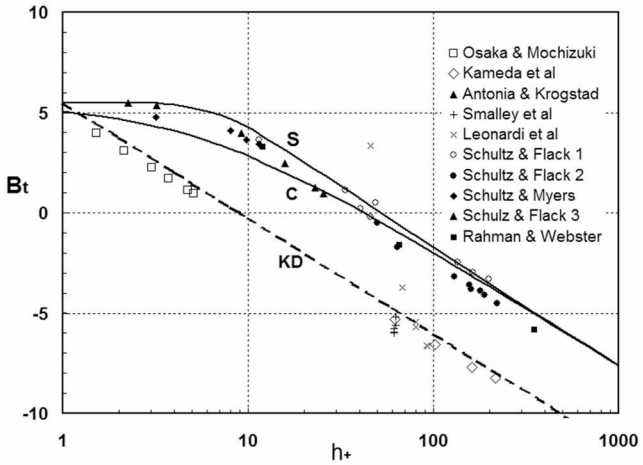

(*b*)

Fig. 9 The log law intercept B_T and B_t for boundary layer data for various values of h_+ and δ/h. Prediction lines line marked *S* are for sand grain roughness and marked *C* is for Colebrook commercial roughness. Line marked *KD* is the prediction for *k*-type and *d*-type roughnesses.

with roughness variable h_+ data is shown in Fig. 8(*b*). The present prediction (41) for the inflectional roughness ($j=11$) and Colebrook monotonic roughness ($j=0$) are also shown in the same figure. The data of Schultz and Flack [22] marked as Schultz & Flack 1 and Schultz and Flack [36] marked as Schultz & Flack 2 and Schultz & Myers [35] compare well with prediction (48) for inflectional type roughness. The data of Osaka and Mochizuki [31] for *k*-type roughness, Kameda et al. [32] for *d*-type roughness, and Smalley et al. [34] may be described by the following simple predictions $\phi=h_+$. The surface roughness Z_o/h with roughness variable h_+ data is shown in Fig. 8(*c*) along with our prediction for inflectional type roughness and Colebrook [23] monotonic roughness.

The predicted relation (43) for the additive constant B_T for inflectional roughness, shown in Fig. 9(*a*), compares well with the data of Antonia and Krogstad [30] for mesh type roughness, Schultz and Flack [36] for sand paper roughness, Schultz and Flack [22] for uniform spheres and uniform spheres with grit type roughness, and Schultz and Myers [35] for epoxy wall roughness. Furthermore, the additive constant B_t shown in Fig. 9(*b*) also compares well with the prediction (44) for inflectional roughness with data of Schultz and Flack [19,22,36]. The predictions (43) and (44) for B_T and B_t compare well with the data of Osaka and

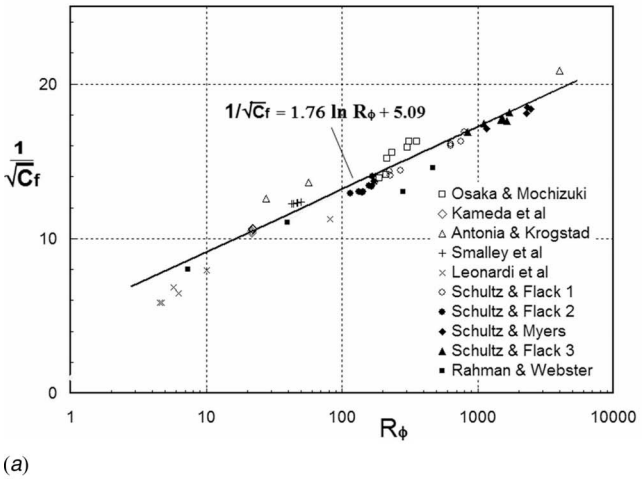

(*a*)

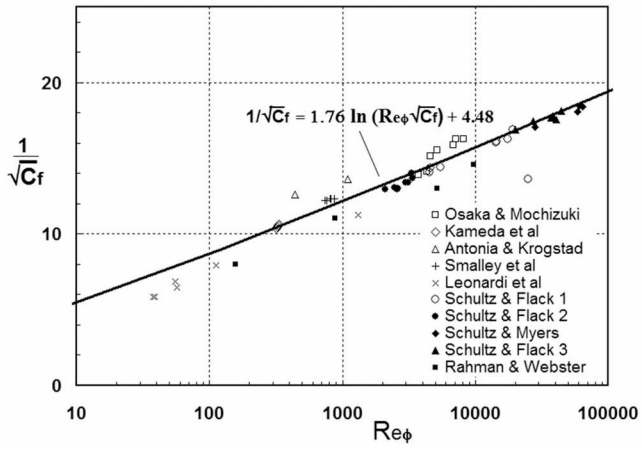

(*b*)

Fig. 10 Comparison of universal skin friction C_f predictions and experimental data for turbulent flow boundary layer on transitional rough walls. (*a*) Skin friction coefficient C_f against roughness Reynolds number $R_\phi = R_\tau/\phi$ data and universal prediction (53), $1/\sqrt{C_f} = 1.76 \ln R_\phi + 5.09$. (*b*) Skin friction coefficient C_f against roughness Reynolds number $\mathrm{Re}_\phi = \mathrm{Re}/\phi$ data and universal prediction (54), $1/\sqrt{C_f} = 1.76 \ln(\mathrm{Re}_\phi \sqrt{C_f}) + 4.48$.

Mochizuki [31] for *d*-type roughness, Kameda et al. [32] for *k*-type roughness, and Antonia and Krogstad [33], Smalley et al. [34], and Leonardi et al. [14] for rod roughness.

In fact, the friction factor predictions (39) and (40) are universal relations, explicitly independent of surface roughness. The skin friction, in alternate variables (C_f, Re_ϕ) shown in Fig. 10(*a*), also collapses on a single universal line predicted by relation (39). Likewise, the friction factor in alternate transitional roughness variables (C_f, Re_ϕ) from roughness data is shown in Fig. 10(*b*), which collapses on a single line predicted by relation (30). The data for various types of roughness, in transitional wall roughness, provide good support to universal skin friction, and the log laws (29) or (30) become

$$\frac{1}{\sqrt{C_f}} = 1.76 \ln R_\phi + 5.09 \tag{53}$$

$$\frac{1}{\sqrt{C_f}} = 1.76 \ln(\mathrm{Re}_\phi \sqrt{C_f}) + 4.48 \tag{54}$$

The relations (53) and (54) demand $(B+D)/\sqrt{2} = 5.09$, which imply $B = 5$ and $D = 2.2$. The universal skin friction log laws (53) and (54) are expressed in terms of traditional Reynolds numbers as

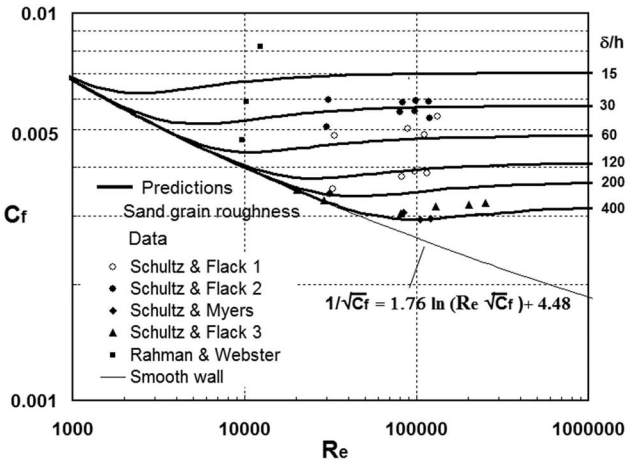

Fig. 11 Comparison of the skin friction C_f versus traditional Reynolds number Re prediction (55) for $\delta/h = 15$, 30, 60, 120, 200, and 400 with experimental data for inflectional wall roughness

$$\frac{1}{\sqrt{C_f}} = 1.76 \ln\left[\frac{1}{R_\tau} + 0.306 \frac{h}{\delta} \exp\left(-\frac{j}{R_\tau} \frac{\delta}{h}\right)\right] + 5.09 \tag{55}$$

$$\frac{1}{\sqrt{C_f}} = 1.76 \ln\left[\frac{1}{\mathrm{Re}\sqrt{C_f}} + 0.216 \frac{h}{\delta} \exp\left(-\frac{1.414 j}{\mathrm{Re}\sqrt{C_f}} \frac{\delta}{h}\right)\right] + 4.48 \tag{56}$$

For the data of Antonia and Krogstad [33] for mesh roughness, Schultz and Flack [19] for machine honed surface roughness, Schultz and Meyers [35] for epoxy roughness, Schultz and Flack [36] for sand paper roughness, Schultz and Flack [22] for uniform sphere and uniform spheres with grit and Rahman and Webster [37] for river bed roughness, the skin friction is shown in Fig. 11 against Re the Reynolds number. These data are compared with the predictions (53) and (54) with $j = 11$ for the inflectional type roughness of Nikuradse, for various values of roughness parameter $\delta/h = 15$, 30, 60, 120, 200, and 400. For each value of δ/h, the prediction represents a line that for large R_τ approaches to fully rough wall limit and for small R_τ it merges with smooth wall skin friction law. For the data of Osaka and Mochizuki [31] for *k*-type roughness, Kameda et al. [32] for *d*-type roughness, Antonia and Krogstad [33] for rod roughness, Smalley et al. [34] for rod roughness, and Leonardi et al. [14], the skin friction is shown in Fig. 12 against Re the Reynolds number. These data are compared with the prediction (58) for *k*-type and *d*-type roughness for various values of roughness parameter $\delta/h = 20$, 50, 100, 200, and 400 as well as smooth walls. For each value of the roughness parameter δ/h, the prediction approaches to fully rough wall limiting value for R_τ and smooth wall skin friction law for small R_τ. The prediction shown in Figs. 11 and 12 compares well with data for various values of the wall roughness parameter δ/h.

6 Conclusions

The alternate new nondimensional roughness scale ϕ, transitional inner coordinate $\zeta = Z_+/\phi$, new parameters $R_\phi = R_\tau/\phi$, the roughness friction Reynolds number, and $\mathrm{Re}_\phi = \mathrm{Re}/\phi$, the roughness Reynolds number, have been proposed. Here, $\phi = k^{-1} \ln \Delta U_+$ is roughness scale connected with traditional roughness function ΔU_+.

The alternative scale is connected with traditional roughness function, which provides the wall roughness effects in the new inner wall variable $\zeta = Z_+/\phi$, which has opened the avenues of new parameters such as roughness friction Reynolds number and roughness Reynolds numbers. These new parameters provide uni-

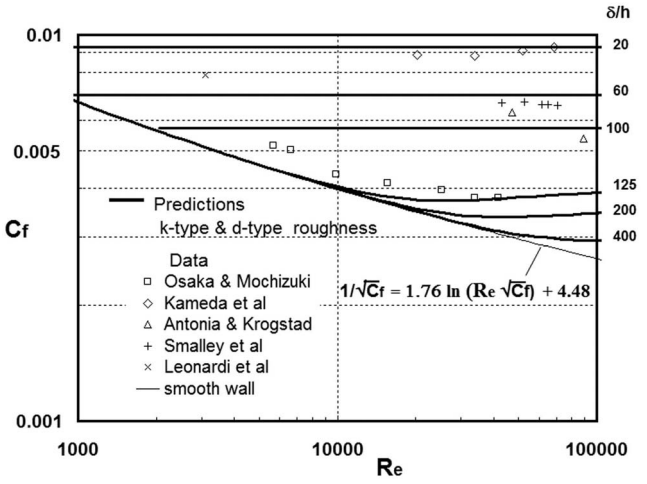

Fig. 12 Comparison of the skin friction C_f versus traditional Reynolds number Re with prediction (52) for $\delta/h=20$, 60, 100, 125, 200, and 400 with experimental data for *k*-type and *d*-type wall roughnesses

versal velocity profile and universal friction factor relations that are explicitly independent of wall roughness. It also helps to yield the traditional relations and also provides insight into the roughness scale ϕ formulation for inflectionl type roughness as well as *k*-type and *d*-type roughness. On the other hand, the traditional study of rough wall is based on fully smooth wall inner scale Z_+, where effect of the wall roughness shows a shift of the velocity profile log law by an amount equal to roughness function over the fully smooth wall layer log law.

In the alternate rough wall variables, the velocity profile u_+ versus inner transitional roughness variable $\zeta=Z_+/\phi$, the skin friction C_f versus inner transitional roughness Reynolds number $\mathrm{Re}_\phi=\mathrm{Re}/\phi$ are universal, explicitly independent of wall roughness but implicitly involving the roughness scale ϕ. The extensive experimental data for transitional wall roughness provide very good support to present theory of universal velocity profile in the inner layer and the skin friction. The outer velocity profiles (28) are also universal, which supports Townsend's similarity hypothesis.

The present deals with transitional inner wall variable $\zeta=Z_+/\phi$, for a given roughness level ϕ, leading to universal laws, explicity independent of transitional wall roughness. On the other hand, traditional rough wall theories are based either on fully smooth inner layer variable $Z_+=Zu_\tau/\nu$ or fully rough wall inner variable Z/h and the results depend on type of roughness function ΔU_+ or roughness scale ϕ.

The roughness scale ϕ prediction of inflectional roughness compares well with the data of Schultz and Flack [22,36]. The data of Osaka and Mochizuki [31] for *d*-type roughness, Kameda et al. [32] for *k*-type roughness, and Antonia and Krogstad [33] and Smalley et al. [34] for rod roughness compare well with the *k*-type and *d*-type roughness prediction $\phi=h_+$. The traditional log laws intercept B_T and B_t for the appropriate roughness scale also compare well with the corresponding data.

There is no universality of scalings in traditional variables and different expressions are needed for various types of roughness, as suggested, for example, with inflectional type roughness, monotonic Colebrook–Moody roughness, *k*-type/*d*-type roughness, etc. are predicted. In traditional variables, the skin frictions are predicted for inflectional roughness and *k*-type/*d*-type roughness. The experimental data provide good support to the predictions of the skin friction in terms of traditional log law for inflectional roughness as well as *k*-type and *d*-type roughness.

The effects of the pressure gradient on the matching conditions in the overlap region (described in Appendix A) lead to the composite laws. For weaker pressure gradient, the matching yields the relations (A10) and (A11) and for strong adverse pressure gradient the matching yields the half-power laws for velocity profile (A12) and (A13), whose intercept in inner layer depends on transitional wall roughness.

Acknowledgment

N.A. is thankful to the All India Council of Technical Education, New Delhi for the support of this work.

Appendix A: Pressure Gradient Effects From Matching in the Overlap Region for a Transitional Rough Surface

The matching of velocity u and Reynolds shear stress τ demand $u_{i,o}=u_{o,i}$ and $\tau_{i,o}=\tau_{o,i}$, where suffix (i,o) means the outer limit of inner solution and suffix (o,i) means the inner limit of outer solution. The matching of the nondimensional mixing length parameter

$$\left(\frac{y}{\sqrt{\tau}}\frac{\partial u}{\partial y}\right)_{i,o}=\left(\frac{y}{\sqrt{\tau}}\frac{\partial u}{\partial y}\right)_{o,i} \tag{A1}$$

is also of significance. The inner limit (ζ fixed, $R_\phi\to\infty$) of outer expansions is the outer limit (Y fixed, $R_\phi\to\infty$) of inner expansion. The matching condition (A1), expressed in terms of outer and inner expansions, yield

$$\frac{\zeta}{\sqrt{\tau_+}}\frac{\partial u_+}{\partial \zeta}=\epsilon^{-1}\frac{Y}{\sqrt{T}}\frac{\partial F_0}{\partial Y}-\frac{Y}{\sqrt{T}}\frac{\partial F_1}{\partial Y} \tag{A2}$$

as $\zeta\to\infty$ and $Y\to 0$ for $R_\phi\to\infty$ and the perturbation parameter is $\epsilon=u_\tau/U_c$. The matching of the inner equation (3) for Reynolds shear stress τ_+ at large ζ with the outer equation (15) for Reynolds shear stress T yields

$$\tau_+=1+K_\phi\zeta \tag{A3a}$$

$$T=1+\lambda Y \tag{A3b}$$

Based on relations (A2) and (A3a,b), the nondimensional matching condition yields

$$\frac{\zeta}{\sqrt{1+K_\phi\zeta}}\frac{\partial u_+}{\partial \zeta}=\epsilon^{-1}\frac{Y}{\sqrt{1+\lambda Y}}\frac{\partial F_o}{\partial Y}-\frac{Y}{\sqrt{1+\lambda Y}}\frac{\partial F_1}{\partial Y} \tag{A4}$$

As $R_\phi\to\infty$, $\epsilon\to 0$, the matching of leading order term demands

$$\frac{Y}{\sqrt{1+\lambda Y}}\frac{\partial F_0}{\partial Y}\to 0 \quad \text{as } Y\to 0 \tag{A5}$$

and the next order terms become

$$\frac{\zeta}{\sqrt{1+K_\phi\zeta}}\frac{\partial u_+}{\partial \zeta}=-\frac{Y}{\sqrt{1+\lambda Y}}\frac{\partial F_1}{\partial Y} \tag{A6}$$

Integration of each side of Eq. (A6) leads to matching conditions for tangential velocity as

$$\frac{u}{u_\tau}=\frac{A}{2}\ln\zeta+A\left[-\ln\frac{\sqrt{1+K_\phi\zeta}+1}{2}+\sqrt{1+K_\phi\zeta}-1\right]+B \tag{A7}$$

$$\frac{U_S-u}{u_\tau}=-\frac{A}{2}\ln Y-A\left[-\ln\frac{\sqrt{1+\lambda Y}+1}{2}+\sqrt{1+\lambda Y}-1\right]+D_S \tag{A8}$$

$$\frac{U_S}{u_\tau} = \frac{A}{2}\ln R_\phi + B + D_S \tag{A9}$$

Here, $b = U_S/U_\infty = F_0(x,0)$ is the slip velocity at the wall and $A = 2/k$. For a fully smooth wall, the relation (A7) was first proposed by Townsend [38] and Afzal [27].

For weak pressure gradients $K_\phi \to 0$ and $\lambda \to 0$, the relations (A7) and (A8) may be expanded in the powers of ζ and Y, respectively, where the effect of pressure gradient appears as algebraic terms as given below:

$$k\frac{u}{u_\tau} = \ln\zeta + kB + \frac{1}{2}K_\phi\zeta - \frac{1}{16}K_\phi^2\zeta^2 + \cdots \tag{A10}$$

$$k\frac{U_S - u}{u_\tau} = -\ln Y + kD_S - \frac{1}{2}\lambda Y + \frac{1}{16}\lambda^2 Y^2 + \cdots \tag{A11}$$

For strong adverse pressure gradients $K_\phi \to \infty$ and $\lambda \to \infty$, the relations (A7) and (A8) may be expressed as half-power laws

$$\frac{u}{u_\tau} = A\sqrt{K_\phi\zeta} + C + \frac{A}{2}\left[-(K_\phi\zeta)^{-1/2} + \frac{1}{12}(K_\phi\zeta)^{-3/2} + \cdots\right] \tag{A12}$$

$$\frac{U_S - u}{u_\tau} = -A\sqrt{\lambda Y} + E + \frac{A}{2}\left[(\lambda Y)^{-1/2} - \frac{1}{12}(\lambda Y)^{-3/2} + \cdots\right] \tag{A13}$$

$$C = -\frac{A}{2}\ln K_\phi + A(\ln 2 - 1) + B \tag{A14}$$

$$E = \frac{A}{2}\ln\lambda + A(-\ln 2 + 1) + D_S \tag{A15}$$

The inner half-power laws (A12) and (A13) may also be expressed as

$$\frac{u}{u_p} = A\sqrt{y_p} + C_p + \frac{A}{2}\left[-\Lambda R_p(y_p)^{-1/2} + \frac{1}{12}(\Lambda R_p)^2(y_p)^{-3/2} + \cdots\right] \tag{A16}$$

$$C_p = (\Lambda R_p)^{1/2}\left[-\frac{A}{2}\ln K_\phi + A(\ln 2 - 1) + B\right] \tag{A17}$$

$$\frac{U_S - u}{u_\delta} = -A\sqrt{Y} + E_p + \frac{A}{2}\left[\Lambda Y^{-1/2} - \frac{1}{12}\Lambda^2 Y^{-3/2} + \cdots\right] \tag{A18}$$

$$E_p = \Lambda^{1/2}\left[-\frac{A}{2}\ln\Lambda + A(-\ln 2 + 1) + D_S\right] \tag{A19}$$

Based on pressure scales, the inner variable is $y_p = yu_p/\nu$, inner velocity scale is $u_p = (\nu p'/\rho)^{1/3}$, the outer velocity scale is $u_\delta = (\delta p'/\rho)^{1/2}$ and the nondimensional parameters are $\Lambda = \tau_w/(\delta p')$ and $R_p = u_p\delta/\nu$. For a transitional rough surface, near separation, the inner half-power law (A16) becomes

$$\frac{u}{u_p} = A\sqrt{y_p} + C_p \tag{A20}$$

The outer half-power law (A18) becomes

$$\frac{U_S - u}{u_\delta} = -A\sqrt{Y} + E_p \tag{A21}$$

The additive constant C_p in the inner layer half-power law (A20) depends on wall roughness potential ϕ or the roughness function ΔU_+ as

$$C_p = (\Lambda R_p)^{1/2}\left[\frac{A}{2}\ln\left(\frac{(\Lambda R_p)^{3/2}}{\phi}\right) + A(\ln 2 - 1) + B\right] \tag{A22}$$

$$C_p = (\Lambda R_p)^{1/2}\left[\frac{A}{2}\ln(\Lambda R_p)^{3/2} + A(\ln 2 - 1) + B - \Delta U_+\right] \tag{A23}$$

The outer layer does not depend on wall roughness and supports the Townsend [38] hypothesis. The turbulent boundary layer on a fully smooth surface ($\phi = 1$, $\Delta U_+ = 0$) with negligible wall shear stress, in the neighborhood of separation, was considered by Stratford [39] and outer layer self-preserving nonlinear outer flow by Townsend [40]. Furthermore, using dimensional arguments for large adverse pressure gradient, the half-power law for velocity distribution was proposed by Stratford [39], and the self-preserving nonlinear outer flow was patched with by Townsend [40], which was later matched asymptotically by Afzal [41] in the terminology of the method of matched asymptotic expansions. The shallow outer wake layer ($U_S \equiv U_c$) under very strong adverse pressure gradient was adopted by Kader and Yaglom [42] to get the half-power law for the outer velocity profile, which is not valid in the neighborhood of the separation domain (Afzal [41,43]). From turbulent boundary layer experimental data, the half-power law constants A versus Λ, C_p versus ΛR_p, and E_p versus Λ on a fully smooth surface ($\phi = 1$, $\Delta U_+ = 0$) are also shown in Afzal [43], under strong adverse pressure gradient with negligible wall shear stress, in the neighborhood of separation. It is shown that the data power law slope A versus Λ data would not be inconsistent with $A = 2/k$, where $k = 0.4$ is the universal value of the Karman constant.

Appendix B: Nonlinear Outer Wake Layer With Eddy Viscosity Model

The present work dealt with the open equations of turbulent motion, up to a point beyond which it is not possible to proceed any further without a closure hypothesis. Consequently, in outer layer the Clauser's constant eddy viscosity model has been adopted for lowest order outer Eq. (16) subjected to the boundary conditions $f_0'(X,\infty) - 1 = T_0(X,\infty) = 0$ and the matching conditions $\tau \to \tau_w$ demanding $T_0(X,0) = 1$. The eddy viscosity hypothesis $\tau = \nu_\tau \partial u/\partial y$ in outer layer where $\alpha_c = \nu_\tau/U_e\delta^*$ being Clauser constant, $\delta = \alpha_c a_1(x - x_o)$ and $(1+m)a_1 = \delta^*/\delta$ and the outer layer has been in equilibrium, $f_0(X,Y) = f(Y)$ subjected to the power law velocity $U_e \propto \delta^n$ at the edge of the boundary layer, give

$$f''' + ff'' + \beta(1 - f'^2) = 0 \tag{B1}$$

$$f(0) = 0, \tag{B2a}$$

$$f''(0)\int_o^\infty (1 - f')dY = \frac{\epsilon^2}{\alpha_c}, \tag{B2b}$$

$$f'(\infty) = 1 \tag{B2c}$$

The Falkner–Skan equation (B1) with the pressure gradient parameter $\beta = m/(1+m)$ is subjected to the boundary conditions of prescribed wall shear stress (B2b). The solution to these equations predict the outer slip velocity $f'(0) = b_S$ as a function of the parameter ϵ^2/α_c. For $\epsilon \to 0$, the wake- and jetlike solutions are described in Afzal [27,28,41]. The zero slip velocity ($f'(0) = b_S = 0$) with $f''(0) = 0$ implies a point of vanishing skin friction and the solution of the Falkner–Skan equations (B1) and (B2) predicts $\beta = -0.198838$ and $m = -0.0.165858$. Furthermore, the outer flow is a shallow wake ($U_S = U_c$), and the lowest order outer solution becomes $f'(Y) = 1$ and $b_S = 1$.

References

[1] Millikan, C. B., 1938, "A Critical Discussion of Turbulent Flows in Channels and Circular Tubes," *Proceedings of Fifth International Congress on Applied Mechanics*, Cambridge, 1938, J. P. den Hartog and H. Peters, eds., Wiley, New York/Chapman and Hall, London, pp. 386–392.

[2] Clauser, F. H., 1954, "Turbulent Boundary Layers in Adverse Pressure Gradients," J. Aeronaut. Sci., **21**, pp. 91–108.

[3] Hama, F. R., 1954, "Boundary Layer Characteristics for Smooth and Rough Surface," Soc. Nav. Archit. Mar. Eng., Trans., **62**, pp. 333–358.

[4] Flack, K. A., Schultz, M. P., and Shapiro, T. A., 2005, "Experimental Support for Townsend's Reynolds Number Similarity Hypothesis on Rough Walls," Phys. Fluids, **17**, p. 035102.

[5] Connelly, J. S., Schultz, M. P., and Flack, K. A., 2006, "Velocity-Defect Scaling for Turbulent Boundary Layers With a Range of Relative Roughness," Exp. Fluids, **40**, pp. 188–195.

[6] Abe, K., Matsumoto, A., Munakata, H., and Tani, I., 1990, "Drag Reduction by Sand Grain Roughness," *Structure of Turbulence and Drag Reduction*, A. Gyr, ed., Springer, Berlin, pp. 341–348.

[7] Schlichting, H., 1968, *Boundary Layer Theory*, Mc-Graw Hill, New York.

[8] Ligrani, P. M., and Moffat, R. J., 1986, "Structure of Transitionally Rough and Fully Rough Turbulent Boundary Layers," J. Fluid Mech., **162**, pp. 69–98.

[9] Bandyopadhyay, P. R., 1987, "Rough Wall Turbulent Boundary Layer in the Transition Regime," J. Fluid Mech., **180**, pp. 231–266.

[10] Raupach, M. R., Antonia, R. A., and Rajagopalan, S., 1991, "Rough-Wall Turbulent Boundary Layer," Adv. Appl. Mech., **44**, pp. 1–25.

[11] Patel, V. C., 1998, "Perspective: Flow at High Reynolds Number and Over Rough Surfaces: Achilles Heel of CFD," ASME J. Fluids Eng., **120**, pp. 434–444.

[12] Piquet, J., 1999, *Turbulent Flow*, Springer-Verlag, Berlin.

[13] Jimenez, J., 2004, "Turbulent Flow Over Rough Walls," Annu. Rev. Fluid Mech., **36**, pp. 173–196.

[14] Leonardi, S., Orlandi, P., Smalley, R. J., Djenidi, L., and Antonia, R. A., 2003, "Direct Numerical Simulation of Turbulent Channel Flow with Transverse Square Bars on One Wall," J. Fluid Mech., **491**, pp. 229–238.

[15] Afzal, N., and Seena, A., 2007, "Alternate Scales for Turbulent Flow in Transitional Rough Pipes: Universal Log Laws," ASME J. Fluids Eng., **129**, pp. 80–90.

[16] Djendi, L., Elavarasan, R., and Antonia, R. A., 1999, "The Turbulent Boundary Layer Over Transverse Square Cavities," J. Fluid Mech., **395**, pp. 271–294.

[17] Mochizuki, S., Kameda, T., and Osaka, H., 2006, "Self-Preservation of a Turbulent Boundary Layer Over d-type Roughness," J. Fluid Sci. Technol., **1**, pp. 24–35.

[18] Afzal, N., 2006, "Turbulent Boundary Layers on Transitional Rough Surfaces: New Approach to Universal Scaling," *36th AIAA Fluid Dynamics Conference Meeting and Exhibit*, Jun. 5–8 San Francisco, Ca, Paper No. AIAA-2006-2886.

[19] Schultz, M. P., and Flack, K. A., 2007, "The Rough-wall Turbulent Boundary Layer From the Hydraulically Smooth to the Fully Rough Regime," J. Fluid Mech., **580**, pp. 381–496.

[20] Krogstad, P-A., Antonia, R. A., and Browne, L. W. B., 1992, "Comparison Between Rough and Smooth-Wall Turbulent Boundary Layers," J. Fluid Mech., **245**, pp. 599–617.

[21] Acharya, M., Bornstein, J., and Escudier, M. P., 1986, "Turbulent Boundary Layers on Rough Surfaces," Exp. Fluids, **4**, pp. 33–47.

[22] Schultz, M. P., and Flack, K. A., 2005, "Outer Layer Similarity in Fully Rough Wall Turbulent Boundary Layers," Exp. Fluids, **38**, pp. 328–340.

[23] Colebrook, C. F., 1939, "Turbulent Flow in Pipes with Particular Reference to the Transition Region Between the Smooth and Rough Pipe Laws," Journal of Institution of Civil Engineers, London, **11**, pp. 133–156.

[24] Moody, L. F., 1944, "Friction Factors for Pipe Flow," Trans. ASME, **66**, p. 671684.

[25] Nikuradse, J., 1933, "Laws of Flow in Rough Pipe," VDI, Forschungsheft N-361, English Translation NACA TM 1292.

[26] Afzal, N., and Narasimha, R., 1976, "Axisymmetric Turbulent Boundary Layers Along a Circular Cylinder With Constant Pressure," J. Fluid Mech., **74**, pp. 113–129.

[27] Afzal, N., 1996, "Wake Layer in Turbulent Boundary Layer with Pressure Gradient: A New Approach," *Invited Lecture in Asymptotic Methods for Turbulent Shear Flows at High Reynolds Numbers*, K. Gersten, ed., Kluwer Academic, Dordrecht, pp. 95–118.

[28] Afzal, N., 2007, "Power Law Velocity Profile in the Turbulent Boundary Layer on Transitional Rough Surfaces," ASME J. Fluids Eng., **129**(8), pp. 1083–1100.

[29] Coles, D., 1956, "The Law of the Wake in the Turbulent Boundary Layer," J. Fluid Mech., **1**, pp. 191–226.

[30] Cebeci, T., 2004, *Analysis of Turbulent Flows*, Elsevier, New York.

[31] Osaka, H., and Mochizuki, S., 1991, "On Turbulence Structure of the Boundary Layer on d-type Rough Wall," *Experimental Heat Transfer, Fluid Mechanics and Thermodynamics*, Keffler Shah and Ganic, eds., Elsevier Science, pp. 412–422.

[32] Kameda, T., Osaka, H., and Mochizuki, S., 1998, "Mean Flow Quantities for the Turbulent Boundary Layer over a k-type Rough Wall," *13 Adust. Fluid Mechanics Conference*, Monash University, Melbourne, pp. 357–360.

[33] Antonia, R. A., and Krogstad, P. A., 2001, "Turbulence Structure in Boundary Layer over Different Types of Surface Roughness," Fluid Dyn. Res., **28**, pp. 139–157.

[34] Smalley, R. J., Antonia, R. A., and Djenidi, L., 2001, "Self Preservation of Rough-Wall Turbulent Boundary Layers," Eur. J. Mech. B/Fluids, **20**, pp. 591–602.

[35] Schultz, M. P., and Myers, A., 2003, "Comparison of Three Roughness Function Determination Methods," Exp. Fluids, **35**(4), pp. 372–379.

[36] Schultz, M. P., and Flack, K. A., 2003, "Turbulent Boundary Layers over Surfaces Smoothed by Sanding," ASME J. Fluids Eng., **125**, pp. 863–870.

[37] Rahman, S., and Webster, D. R., 2005, "The Effects of Bed Roughness on the Scaler Fluctuations of Turbulent Boundary Layer," Exp. Fluids, **38**, pp. 372–384.

[38] Townsend, A. A., 1976, *The Structure of Turbulent Shear Flow*. 2nd ed., Cambridge University Press, Cambridge.

[39] Stratford, B. S., 1959, "The Prediction of Separation of the Turbulent Boundary Layers," J. Fluid Mech., **5**, pp. 1–35.

[40] Townsend, A. A., 1960, "The Development of Turbulent Boundary Layers with Negligible Wall Stress," J. Fluid Mech., **8**, pp. 143–155.

[41] Afzal, N., 1983, "Analysis of a Turbulent Boundary Layer Subjected to a Strong Adverse Pressure Gradient," Int. J. Eng. Sci., **21**, pp. 563–576.

[42] Kader, B. A., and Yaglom, A. M., 1978, "Similarity Treatment of Moving Equilibrium Turbulent Boundary Layers in Adverse Pressure Gradients," J. Fluid Mech., **89**, pp. 305–342.

[43] Afzal, N., 2008, "Turbulent Boundary Layer with Negligible Wall Stress," ASME J. Fluids Eng., **130**, to be published.

Near Surface Velocity Distributions for Intermittent Separation of Turbulent Boundary Layers

V. A. Sandborn
Colorado State University,
Fort Collins, CO 80523

At the location of intermittent turbulent boundary layer separation a finite positive mean surface shear stress still exists. It is demonstrated that viscous coordinates and a mixing length turbulent model may still be used at the location of intermittent separation. The large scale turbulent mixing in the separation region appears to require the universal mixing constant, K, increases with Reynolds number. Once true zero-mean-surface-shear-stress separation occurs, the mixing length model for the turbulent flow near the surface is no longer valid and a constant eddy viscosity is indicated. [DOI: 10.1115/1.2903818]

Introduction

The concept that turbulent boundary layer separation can be viewed as a transition process was proposed by Sandborn and Kline [1]. This model identified a region of *intermittent separation*, which was the location associated with the adverse affects of separation. The point where the *mean surface shear stress* is equal to *zero* is downstream of the intermittent separation location. Sandborn and Liu [2] experimentally demonstrated experimentally the relation between the intermittent and the zero-mean-shear-stress separations.

A detailed description of the physics of intermittent separation is lacking. The model of Sandborn and Kline associated intermittent separation with the location where viscous affects on the mean velocity distribution could be neglected. A simple velocity defect-power law distribution led to the correlation of the profile shape factors at intermittent separation. Although intermittent separation was associated with absents of viscous effects, it was evident that the surface shear stress, while small, was not zero. The measurements of Simpson, et al. [3,4] confirmed the existence of a finite surface shear at the location of intermittent separation. The measurements of Sandborn and Liu [2] indicated flow reversal of the order of 30% at intermittent separation for small Reynolds numbers; while the laser measurements of Simpson, et al. [4], at moderate Reynolds numbers, indicate 20% reversal. Sandborn and Liu assumed that 50% reversal corresponded to the zero-mean-surface-shear-stress separation. Obviously, the mean surface shear stress will depend not only on the percent reversal, but also on the magnitude of the forward and reverse flows. While a need exists to better specify wall functions and/or boundary conditions related to the intermittent separation, it should be noted that the work of Stratford [5] and more recent studies (e.g., Castillo et al. [6]), using a zero-surface-shear-stress boundary condition, were able to predict the occurrence of intermittent separation. The present study examines the flow near the surface in the separation region using boundary conditions compatible with the model for intermittent separation.

Intermittent Separation

It is well established that the turbulent boundary layer velocity distributions, near the surface, in zero and moderate pressure gradients, are similar (*law of the wall*) when nondimensionalized by the wall parameters, $U_\tau = \sqrt{\overline{\tau_w}/\rho}$ and $y^* \equiv yU_\tau/\nu$, where $\overline{\tau_w}$ is the mean surface shear stress and ρ and ν are the fluid density and kinematic viscosity, respectively. Obviously, for $\overline{\tau_w}=0$, these coordinates are not usable. However, for the flow up to intermittent separation a finite value of $\overline{\tau_w}$ exists, suggesting the wall parameters may still be of value.

The laser velocimeter data of Simpson, et al. [4] demonstrate that the near wall velocity distributions deviate systematically from the law of the wall as the flow proceeds into the separation-transition region, Fig. 1. The values of U_τ used for Fig. 1 were determined from surface-heat-transfer sensors which agreed with the empirical Ludwieg–Tillmann skin friction relation. While the accuracy of the measured surface shear stress near separation may be limited (listed as $\pm 12\%$ [4]), the uncertainty of $\overline{\tau_w}$ was not likely to be of the order of four times smaller, which would be required to agree with the law of the wall. It appeared that the near surface velocities reported by Simpson, et al. start to deviate from the law of the wall approximately at the location where the first indications of flow reversal ($\approx 1\%$ reversal) were observed.

Van Driest [7] demonstrated that the log-law velocity distribution found for the zero pressure gradient turbulent boundary layers could be obtained using the archaic mixing length model for the turbulence near the surface. The separation-transition region velocity distribution might also be modeled similar to the upstream boundary layer flow.

Integration of the x-direction equation of motion close to the surface leads to a relation of the form (where the Reynolds stress, $\rho\overline{uv}$, is related to the velocity gradient)

$$\tau_w + y\frac{\partial p}{\partial x} = f\left(\frac{\partial U}{\partial y}\right) \tag{1}$$

where p is the static pressure and U is the local velocity. The function,f, is modeled, Van Driest [7], using the mixing length; and for the case of no viscous damping,

$$f = \mu\frac{\partial U}{\partial y} + \rho K^2 y^2\left(\frac{\partial U}{\partial y}\right)^2 \tag{2}$$

The function,f, could be viewed as a special series expansion of the local velocity gradient. K is identified as the *universal mixing constant*. Van Driest solved Eqs. (1) and (2) for the case $\partial p/\partial x = 0$. For $\partial p/\partial x$ not equal to zero the solution of Eqs. (1) and (2) in nondimensional form is

Contributed by the Fluids Engineering Division of ASME for publication in the JOURNAL OF FLUIDS ENGINEERING. Manuscript received February 24, 2005; final manuscript received October 11, 2007; published online April 9, 2008. Review conducted by Joseph Katz.

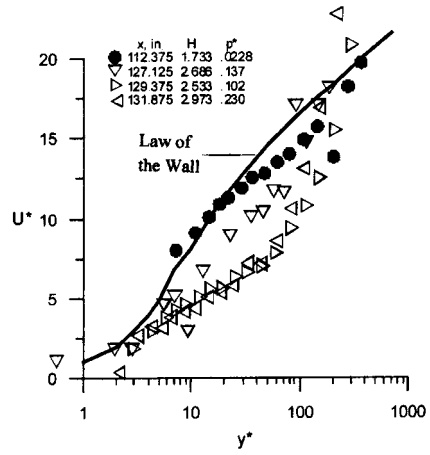

Fig. 1 Velocity distributions upstream and in the separation region. Data of Simpson et al. [4] (uncertainty: U=0.2 f/s, y =0.002 in.).

$$U^* = \int_0^{y^*} \frac{2(1+y^*p^*)dy^*}{1+\sqrt{1+4K^2y^{*2}(1+y^*p^*)}} \tag{3}$$

where $U^*=U/U_\tau$ and $p^*=(\nu/U_\tau^3)(1/\rho)(\partial p/\partial x)$. (Note that only the positive value of the square root, shown in Eq. (3), appears of interest.)

The present derivation requires that $\partial p/\partial x$ is not a variable with y in the region of interest. Experimentally, it has been shown that the pressure varies with y-distance near the surface [2]; however, the x- and y-momentum equations are found to be nearly independent.

Stratford's separation analysis sets $\overline{\tau_w}=0$ and uses only the second term in Eq. (2) for f to arrive at the prediction that $U\propto\sqrt{y}$. Schlichting and Gersten [8] presented a *dimensional analysis* leading to $U\propto\sqrt{y}$ for vanishing wall shear stress.

Equation (3) indicates that the values of U^* will increase as p^* increases for fixed values of K and y^*. Although K is identified as the universal mixing constant in the literature, its value appears to vary from less than 0.4 to greater than 0.6 for the nonseparating flows. For the separating flows the large scale structure of the outer flow dominates the distributions [9]; thus, K might be expected to increase in the separation region.

Figure 2(*a*) compares the laser measurements of Simpson et al. [4] at x=129.375 (R_θ=19,089, p^*=0.102, and K=0.7) and 131.875 in. (R_θ=16,188, p*0.230, and K=0.8) (intermittent separation was indicated at x=130 in.) with Eq. (3).

Also shown in Fig. 2(*a*) is an empirical curve fit to the measurements

$$U^* = 0.763\sqrt{y^*} + 2.04 \tag{4}$$

This type of relation, which was employed by Stratford, is a reasonable representation of the velocity distribution for y^* in the range of 10–100. However, Eq. (3) offers an improved prediction of the velocity distribution close to the surface.

Figure 2(*b*) shows measurements reported by Simpson et al. [3], which required a value of K between 1 and 1.5 for comparison with Eq. (3). Also shown in Fig. 2(*b*) is a set of measurements of Simpson, et al. [4] taken at a location downstream of the intermittent separation, which indicates a value of K of the order of 4. Obviously, the need to have a variable K demonstrates the lack of similarity for the flow near the surface in the separation region. The need for the large values of K may also indicate the change of the turbulent process from a mixing length to an eddy viscosity type characteristic.

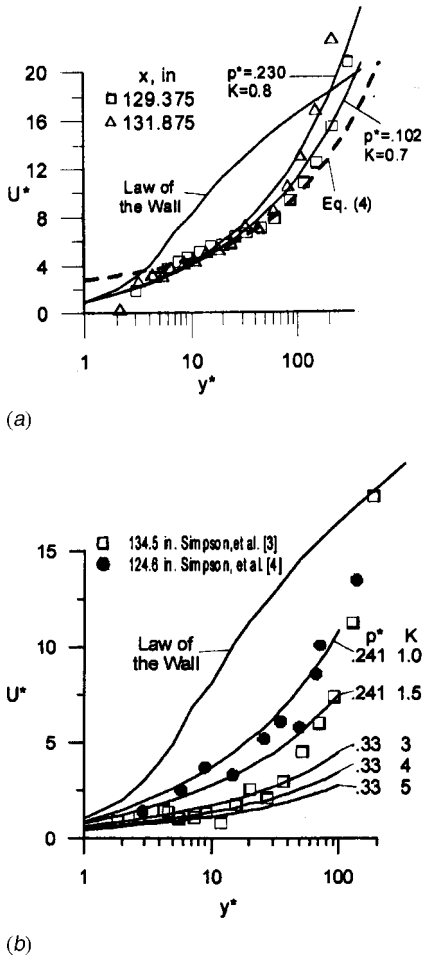

Fig. 2 Comparison of intermittent separation profiles with the predictions of Eq. (3). (*a*) Data of Simpson et al. [4]. (*b*) Data of Simpson et al. [3] and downstream data of Simpson et al. [4].

To evaluate the affect of low Reynolds number, (R_θ=1100 and 1880), intermittent separation, a set of measurements using a TSI fiber-optics-laser velocimeter, was made in a small (8.9 $\times$16.5 cm^2) expanding duct [10]. The velocimeter fiber optics probe, with a focal length of 120 mm, was mounted on a traverse external to the duct. The traverse could be set within $\pm$0.02 mm, although the location of the measuring volume with respect to the surface was limited to 0.05 mm. The laser output was evaluated directly from the TSI Colorburst software (FINE), where values of the mean velocities were determined by summing the individual time realizations of the velocity. While the velocities were recorded to four significant figures, the accuracy was limited by the bias corrections discussed below.

Since the fluctuations in velocity in the intermittent separation region were many times the mean values, biasing errors for the computed mean velocity will occur, as discussed by McLaughin and Tiederman [11]. The biasing was due to more high velocity tracer particle realizations being sampled than low velocity particle. McLaughtin and Tiederman gave a one dimensional correction for biasing as

$$P_{\text{corr}}(U) = \frac{U_m}{U} P_{\text{bias}}(U) \tag{5}$$

Where $P(U)$ is the probability of the velocity, U, and U_m is the correct mean value. The analysis of McLaughlin and Tiederman did not foresee the use of Eq. (5) for the separation cases, where the velocity can be positive or negative, as well as zero. As a first

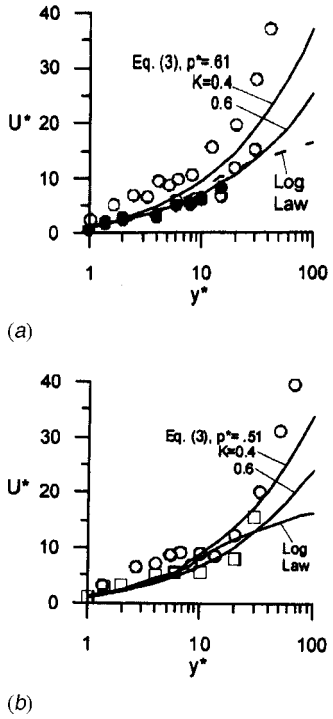

Fig. 3 Velocity near the surface at intermittent separation in the duct. (○) Measured; (□ and ●) bias corrections, Eq. (5). (*a*) R_θ=1110. (*b*) R_θ=1880.

approximation Eq. (5) was applied for $|U|>U_m$, with no correction for the probability between $\pm U_m$. An iteration process was employed to determine U_m.

The values of U_m, with and without bias corrections, are shown in Fig. 3. The bias corrections were as great as 60% for the data very close to the surface, so the comparison with the predictions of Eq. (3) is a first approximation. The actual comparison of Eq. (3), shown in Fig. 3, for $K=0.4-0.6$ might be viewed as a check on the bias correction.

There is a marked difference in the near wall velocity distributions between the present low Reynolds numbers, R_θ=1100 and 1880, and the moderate values, R_θ=15,000–20,000. The values of p^* decrease with increasing Reynolds number, Fig. 4, which lead to the differences in the velocity distributions. The high Reynolds number data plotted in Fig. 4 were those reported by Schubauer and Klebanoff [12] and Sandborn [13]. The relatively small variation of p^* for $R_\theta>20{,}000$ is consistent with the similarity findings at high Reynolds numbers [6].

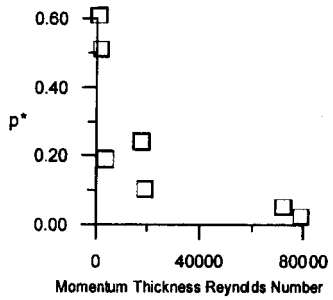

Fig. 4 Variation of the non dimensional pressure gradient with Reynolds number

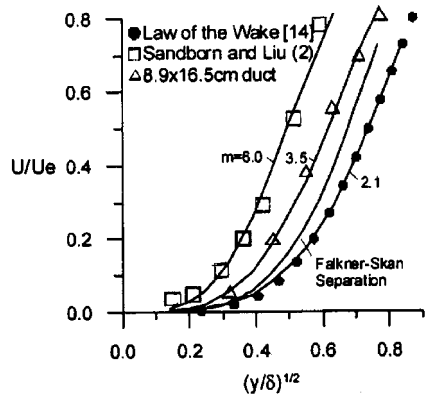

Fig. 5 Zero-mean-surface-shear-stress separation velocity profiles. $U/U_e=1+(1-y/\delta)^m[m\ln(1-y/\delta)-1]$.

Zero-Mean-Surface-Shear-Stress Separation

Since the major adverse affects associated with boundary layer separation occur at the intermittent separation location, the *zero-mean-surface-shear-stress separation* is mainly of academic interest. While many studies have use $\overline{\tau}_w=0$ as a boundary condition, the predictions always relate back to the intermittent separation flows. The early pitot tube and hot wire measurements of Sandborn and Liu [2] examined the velocity distribution at the point where the flow was reversed 50% of the time. The velocity distribution was found to be nearly the same as that for laminar separation. The measurements indicated that near the $\overline{\tau}_w=0$ separation location, the mean velocity is responding as if the flow has a *constant eddy viscosity*.

Measured velocity distributions at the location $\overline{\tau}_w=0$ are rarely reported. A near wall velocity distribution for flow with 50% reversal measured in the 8.9×16.5 cm^2 duct is plotted versus $\sqrt{y/\delta}$, Fig. 5. The 50% time reversal profile of Sandborn and Liu [2] and Coles' [14] tabulated *law of the wake* (separation) velocity distribution are also shown in Fig. 5. The *laminar* separation profile for the similarity flow of Falkner–Skan is also shown in Fig. 5 [15], together with empirical laminar separation profiles [16]. No region of velocity proportional to the square root of distance is evident for either the theoretical, empirical, tabulated, or measured profiles. Thus, it is evident that the mixing length model and the Stratford type analysis do not apply when the point of *true* $\overline{\tau}_w=0$ occurs in turbulent boundary layers.

Conclusions

It is found that once the turbulent boundary layer begins the transition process to separated flow the velocity distributions deviates from the logarithmic law of the wall. Employing Van Driest's mixing length model to the pressure gradient flow, and allowing the universal mixing constant, K, to take values from 0.4 to 1 or greater, it was possible to obtain a reasonable approximation for the near wall velocity distributions at intermittent separation. The value of K was found to increase as the Reynolds number increased. The large scale turbulent mixing becomes more pronounced with increasing Reynolds number.

Stratford's analysis predicts that the velocity distribution varies as the square root of distance near the surface. The square root variation may be a reasonable approximation for the *intermittent* separation profiles over a limited distance from the surface. However, the measured velocity profiles at the location of zero-mean-surface-shear-stress separation do not indicate a square root variation with distance. The zero-shear separation velocity variation agrees with a model of constant eddy viscosity rather than that of a mixing length.

References

[1] Sandborn, V. A., and Kline, S. J., 1961, "Flow Models in Boundary Layer Stall Inception," J. Basic Eng., **83**(3), pp. 317–327.

[2] Sandborn, V. A., and Liu, C. Y., 1968, "On Turbulent Boundary Layer Separation," J. Fluid Mech., **23**(2), pp. 293–301.

[3] Simpson, R. L., Strickland, J. H., and Barr, P. W., 1974, "Laser and Hot Film Anemometer Measurements in a Separating Turbulent Boundary Layer," Report No. WT-3, NTIS AD-A001115, Thermal and Fluid Science Center, Southern Methodist University.

[4] Simpson, R. L., Chew, Y. T., and Shivaprasad, B. G., 1980, "Measurements of a Separating Boundary Layer," Project SQUID, Report No. SMU-4-Pu, NTIS AD-Ao9525213.

[5] Stratford, B. S., 1959, "An Experimental Flow With Zero Skin Friction Throughout Its Region of Pressure Rise," J. Fluid Mech., **5**(1), pp. 17–35.

[6] Castillo, L., Wang, X., and George, W. K., 2004, "Separation Criterion for Turbulent Boundary Layer Via Similarity Analysis," J. Fluids Eng., **126**(3), pp. 297–304.

[7] Van Driest, E. R., 1956, "On Turbulent Flow Near a Wall," J. Aeronaut. Sci., **23**(11), pp. 1007–1011.

[8] Schlichting, H., and Gersten, K., 2000, *Boundary Layer Theory*, 8th ed., Springer, New York, p. 545.

[9] Simpson, R. L., 1989 "Turbulent Boundary Layer Separation," Annu. Rev. Fluid Mech., **21**, pp. 205–234.

[10] Sandborn, V. A., 2002, "Surface-Shear-Stress Pulses in Adverse-Pressure-Gradient Turbulent Boundary Layers," AIAA J., **40**(1), pp. 177–179.

[11] McLaughlin, D. K., and Tiederman, W. G., 1973, "Biasing Correction for Individual Realization of Laser Anemometer Measurements in Turbulent Flow," Phys. Fluids **16**(12), pp. 2082–2088.

[12] Schubauer, G. B., and Klebanoff, P. S., 1951, "Investigation of Separation of the Turbulent Boundary Layer," NACA Report No. 1030.

[13] Sandborn, V. A., 2003, "Reynolds-Number Correlations for Separation of Turbulent Boundary Layers" AIAA J., **41**(4), pp. 744–747.

[14] Coles, D., 1956, "The Law of the Wake in the Turbulent Boundary Layer," J. Fluid Mech., **1**, pp. 191–226.

[15] Smith, A. M. O., 1954, "Improved Solutions of the Falkner and Skan Boundary Layer Equation," Sherman Fairchild Fund Paper No. FF-10, Institute of the Aeronautical Sciences.

[16] Sandborn, V. A., 1959, "Equation for the Mean Velocity Distribution of Boundary Layers," NASA Memorandom 2-5-59E.

Optimal Performance and Geometry of Supersonic Ejector

N. I. I. Hewedy

Mofreh H. Hamed[1]
e-mail: mofrehhh@yahoo.com

F. Sh. Abou-Taleb

Tarek A. Ghonim
e-mail: tarek_ghonim@yahoo.com

Mechanical Power Engineering Department,
Faculty of Engineering,
Menoufiya University,
Egypt

The optimum geometries of the ejectors, which give maximum efficiency, are numerically predicted and experimentally measured. The numerical investigation is based on flow equations governing turbulent, compressible, two-dimensional, steady, time averaged, and boundary layer equations. These equations are iteratively solved using finite-difference method under the conditions of different flow regimes, which can be divided into several distinctive regions where the methods for estimating the mixing length are different for each flow region. The first region depicts the wall boundary layer, jet shear layer, and secondary and primary potential flows. The second one contains a single region of developing flow. A simple ejector with convergent-divergent primary nozzle was fabricated and experimentally tested. The present theoretical and experimental results are well compared with published data. The results obtained are used to correlate the optimum ejector geometry, pressure ratio, and ejector optimum efficiency as functions of the operation parameters and ejector area ratio. The resultant correlations help us to select the optimum ejector geometry and its corresponding maximum efficiency for particular operating conditions. [DOI: 10.1115/1.2903742]

Keywords: supersonic flow, two-dimensional flow, optimum ejector geometry, ejector area ratio, maximum ejector efficiency

1 Introduction

For many years, ejectors utilizing readily available fluids have been employed in industry to economically produce vacuums and pump secondary fluids. Figure 1 presents a view of typical ejector and its principal components. As shown, two streams of differing momentum are mixed in a duct where the higher momentum stream (primary fluid) sucks the lower momentum (secondary fluid) via entrainment. Ejector efficiency and its performance are based on the ability of the adjacent streams to adequately mix and exchange momentum.

Many studies were directed toward understanding of the flow phenomena and performance of ejectors. Donald and Robert [1] carried out an experimental and theoretical investigation at supersonic and subsonic Mach numbers of auxiliary inlets supplying secondary air flow to ejector exhaust nozzle. The tests were extensively conducted on two ejector configurations over a wide range of primary nozzle pressure ratios at Mach numbers of 0.64, 1.5, 1.8, and 2.0. Fabri and Paulon [2] experimentally and theoretically studied supersonic air-air ejectors. The theoretical analysis was based on one-dimensional flow and the experimental study was conducted on a constant-area mixing ejector. The effects of different parameters, such as length of the mixer, terminating diffuser length, cross section of the mixer, and primary flow Mach number, were theoretically studied. Kirti et al. [3] numerically studied the turbulent mixing in the initial region of heterogeneous axisymmetric coaxial confined jets. A binary isothermal system of nonreacting gases is considered. Results were obtained for four different jet configurations for which the experimental data were available. A formulation was presented for the eddy viscosity and the eddy diffusivity that adequately describes the confined turbulent mixing of heterogeneous streams in the initial region. Abou-Taleb [4] experimentally and analytically studied the effect of geometric parameters on the performance of ejectors. Approximate formulas for calculating pressure ratio and optimum entrainment ratio as well as the optimum design conditions were derived. Dutton and Carroll [5] developed a one-dimensional constant-area flow model for solving a large class of supersonic ejector optimization problems. Design curves for common case of adiabatic primary and secondary gases of equal molecular weight and stagnation temperature were also presented and discussed. Raman and Taghavi [6] provided a detailed experimental evaluation of a rectangular, multielement, supersonic jet mixer-ejector nozzle. Information on the mixing, pumping, ejector wall pressure distribution characteristics of four simple, multi-element, jet mixer-ejector configurations was presented. The obtained results showed that the ejector configuration that produced the maximum entrainment ratio also exhibited the lowest wall pressures in the inlet region and maximum thrust augmentation. Guillaume and Judge [7] presented a unique means of increasing the efficiency of a jet pump by elliptical nozzles on jets instead of round jets. At high flow rates, the jet pump using the elliptical jets was shown to have an efficiency that was approximately a factor of 6 greater than the pump using the round jets. Szabo [8] studied analytically the influence of the material quality of the primary gas jets on the final vacuum created by a supersonic gas ejector. Examined ejectors showed that their geometry greatly depended on the quality changes of the operating primary gas due to the temperature and pressure changes. Kandakure et al. [9] developed a numerical model to understand the hydrodynamic characteristics with reference to ejector geometry and the effects of operating conditions on the ejector performance. Karambirov and Chebaevskii [10] described a method of choosing an ejector geometry for given operating conditions. Generalized dimensionless characteristics of ejectors were given for averaged loss coefficients. They explored the possibility of decreasing the coefficients of heat loss by improving the profile for the delivery of passive fluids to an ejector pump (use of stepped diffuser). Yong et al. [11] numerically and experimentally studied the development of a large-entrainment-ratio axisymmetric supersonic ejector for microbutane combustor. Operation conditions as well as geometric parameters of the ejector were systematically changed and their effects on volume-flow-rate ratio were investigated in a series of experiments where butane was mostly simulated by air. From the review, it is clear that the performance of air ejectors mainly depends on the geometric

[1]Presently at Kafrelsheikh University.

Contributed by the Fluids Engineering Division of ASME for publication in the JOURNAL OF FLUIDS ENGINERING. Manuscript received December 31, 2006; final manuscript received October 4, 2007; published online April 16, 2008. Review conducted by Phillip M. Ligrani.

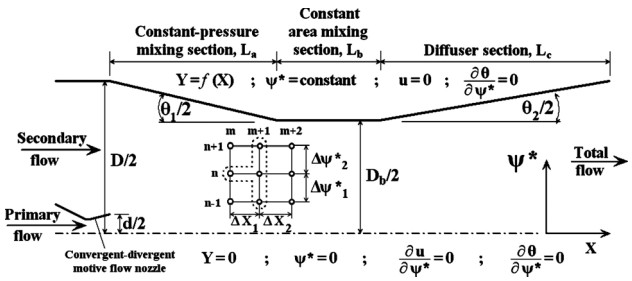

Fig. 1 Ejector geometry, boundary conditions, and computational grid

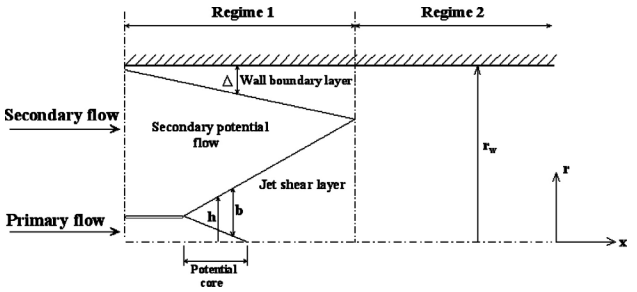

Fig. 3 Flow regions

and operational parameters. Most of past publications did not concern with overall efficiency enhancement by optimization of the geometric parameters and choosing of the operating conditions in order to give the maximum overall ejector efficiency. The primary motivation behind this work is to fulfill the following: (1) development and validation of a 2D mathematical model to predict the performance of supersonic ejectors, (2) selecting the optimum geometry of an ejector in order to optimize its performance, and (3) relating the geometric and operational parameters by both numerically based correlations and design charts deduced from the theoretical investigation in order to obtain optimum ejector design (maximum efficiency) for a wide range of operational parameters.

2 Experimental Setup

The experimental installation is schematized in Fig. 2. Compressor of sufficient capacity is used to ensure the continuous operation of the ejector. Compressed air (at a maximum pressure of about 8 bars and an ambient stagnation temperature) is filtered to remove large particles, such as dust and compressed oil droplets. The compressed air is then directed toward an air reservoir, which is connected to the entrance of the primary flow nozzle of the ejector. A pressure control valve is used to adjust the primary flow stagnation pressure P_{o1}. The entrained air flow is taken from the surrounding atmosphere. The entrained mass flow rate can be regulated by means of a valve located at the entrance of the aspiration tube.

Apparatuses installed on the primary and secondary air circuits to measure the stagnation pressures and mass flow rates are also shown in Fig. 2. Pressure taps distributed along the ejector were used to measure wall static pressure distributions.

In the tested ejector as illustrated in Fig. 1, the exit diameter of the primary flow nozzle is 6.2 mm (inner), the dimensionless constant pressure mixing section length (L_a/D_b), constant-area mixing section length (L_b/D_b), diffuser section length (L_c/D_b), and area ratio (A_r) are 4.08, 4.46, 8.9, and 17.38, respectively, while the total angles of the constant pressure mixing section and the diffuser section, θ_1 and θ_2, are 5.4 deg and 2.7 deg, respectively. The uncertainty for all the measuring devices is found to be in the range of 0.05–6.45%.

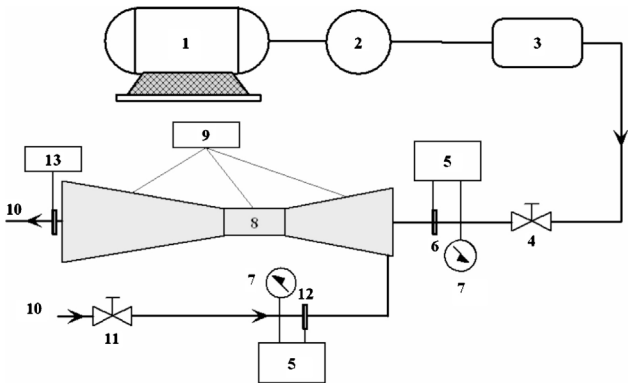

Fig. 2 Experimental setup

3 Mathematical Model

The flow through the ejector is modeled based on the governing flow equations under the assumptions reported in Ref. [15].

3.1 Governing Equations. For axisymmetric flow, the system of equations governing turbulent, compressible, steady, time-averaged, and boundary layer flows can be written in terms of stream function, ψ using the proposed transformation by Krause [12,15] as follows.

In continuity equation,

$$\frac{\partial \bar{\rho}\bar{u}}{\partial x} + \frac{1}{r}\frac{\partial(\bar{\rho}\bar{v}r)}{\partial r} = 0 \tag{1}$$

In momentum equation,

$$\bar{u}\frac{\partial \bar{u}}{\partial x} = -\frac{1}{\bar{\rho}}\frac{d\bar{p}}{dx} + \frac{\bar{u}}{2\psi}\frac{\partial}{\partial \psi}\left[\frac{\bar{\mu}\bar{\rho}\bar{u}r^2}{2\psi}\frac{\partial \bar{u}}{\partial \psi} - \overline{u'(\rho v)'}r\right] \tag{2}$$

In energy equation,

$$\bar{u}\bar{c}_p\frac{\partial \bar{T}}{\partial x} = \frac{\bar{u}}{\bar{\rho}}\frac{d\bar{p}}{dx} + \frac{\bar{u}}{2\psi}\frac{\partial}{\partial \psi}\left[\frac{\bar{k}\bar{\rho}\bar{u}r^2}{2\psi}\frac{\partial \bar{T}}{\partial \psi} - \bar{c}_p\overline{T'(\rho v)'}r\right] + \frac{\Phi}{\bar{\rho}} \tag{3}$$

where

$$\Phi = \left(\frac{\bar{\rho}\bar{u}r}{2\psi}\frac{\partial \bar{u}}{\partial \psi}\right)^2 - \overline{u'(\rho v)'}\left(\frac{\bar{\rho}\bar{u}r}{2\psi}\frac{\partial \bar{u}}{\partial \psi}\right)$$

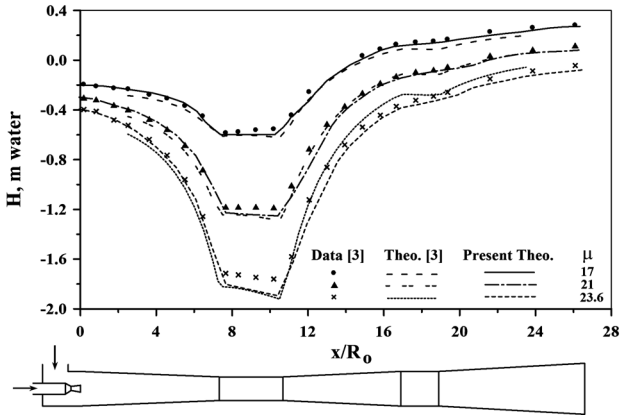

Fig. 4 Comparison between predicted wall static pressure distributions and published theoretical and experimental data [3] for different entrainment ratios (P_{O1}=24 bars, T_{O1}=706 K)

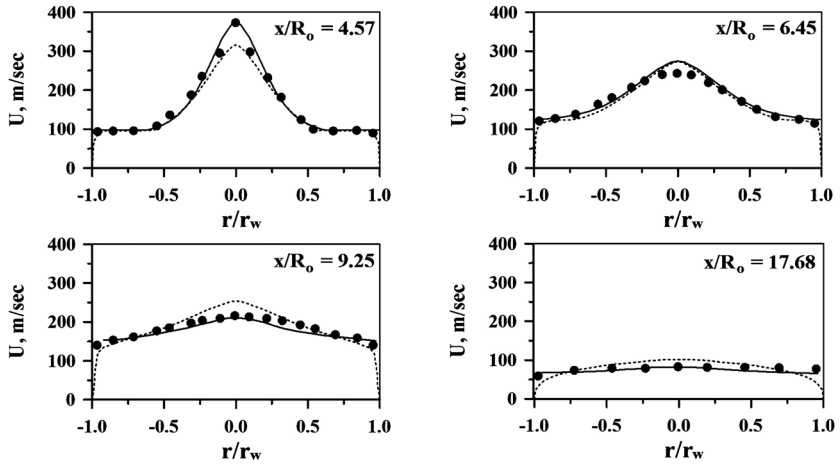

Fig. 5 Comparison between predicted radial variation of axial velocity and published theoretical and experimental data [3] at four axial locations (P_{O1}=24 bars, T_{O1}=706 K, and μ=21)

$$\frac{\partial \psi^2}{\partial y} = \bar{\rho}\bar{u}r, \quad \frac{\partial \psi^2}{\partial x} = \bar{\rho}\bar{v}r$$

Using the eddy viscosity model, the "turbulent shear stress" and "turbulent heat transfer" are defined by

$$\tau_T = \bar{\rho}\varepsilon\frac{\partial \bar{u}}{\partial r} = -\overline{u'(\rho v)'} = \frac{\bar{\rho}^2\bar{u}r\varepsilon}{2\psi}\frac{\partial \bar{u}}{\partial \psi} \tag{4}$$

$$q_T = \bar{\rho}\bar{c}_p\varepsilon_H\frac{\partial \bar{T}}{\partial r} = -\bar{c}_p\overline{(\rho v)'T'} = \frac{\bar{\rho}^2\bar{u}r}{2\psi}\bar{c}_p\varepsilon_H\frac{\partial \bar{T}}{\partial \psi} \tag{5}$$

where ε is termed the "eddy momentum diffusivity" and ε_H is the "eddy thermal diffusivity."

After substitution from Eqs. (4) and (5), Eqs. (2) and (3) can be expressed in a dimensionless form and regrouping in X-ψ^* coordinates [15] as

$$u\frac{\partial u}{\partial X} = -\frac{1}{2\rho^*}\frac{dp}{dX} + \frac{u}{2\psi^*}\frac{\partial}{\partial \psi^*}\left[S\frac{\partial u}{\partial \psi^*}\right] \tag{6}$$

$$uc_p^*\frac{\partial \theta}{\partial X} = \frac{C_L}{2\rho^*}u\frac{dp}{dX} + \frac{C_L uS}{2\psi^*}\left(\frac{\partial u}{\partial \psi^*}\right)^2 + \frac{u}{2\psi^*}\frac{\partial}{\partial \psi^*}\left(Q\frac{\partial \theta}{\partial \psi^*}\right) \tag{7}$$

where

$$C_L = \frac{(\gamma-1)M_1^2}{\frac{T_{wr}}{T_1} - 1}$$

$$Q = \left(\frac{\mu^*}{P_{r1}} + \frac{E\rho^*}{P_{rt}}\right)\frac{Y^2\rho^* u}{2\psi^*}$$

$$S = \left(\frac{\mu^* + E\rho^*}{2\psi^*}\right)Y^2\rho^* u$$

3.2 Turbulent Shear Stress and Heat Transfer. The well-known Prandtl assumption for the turbulent shear stress and heat transfer is

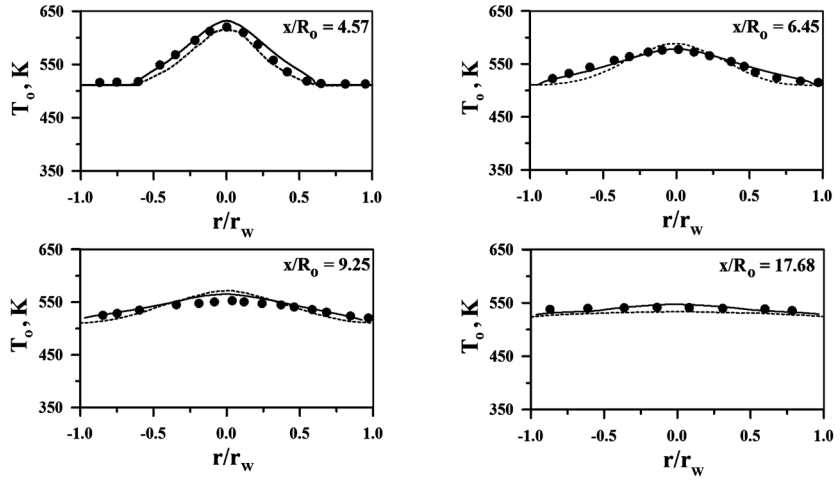

Fig. 6 Comparison between predicted radial variation of stagnation temperature and published theoretical and experimental data [3] at four axial locations (P_{O1}=24 bars, T_{O1}=706 K, and μ=21)

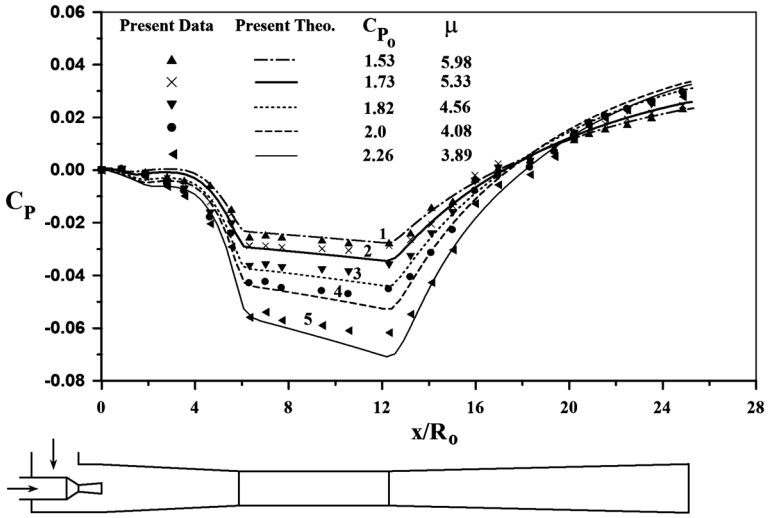

Fig. 7 Comparison between predicted wall static pressure coefficient distributions and experimental data at different inflow conditions

$$\varepsilon = l_m^2 \frac{\partial \bar{u}}{\partial r} \tag{8}$$

In a dimensionless form and X-ψ^* coordinates, Eq. (8) becomes

$$E = \frac{u\rho^* Y}{2\psi^*} L_m^2 \left| \frac{\partial u}{\partial \psi^*} \right|$$

For specifying the approximate relationship between the mixing length and the mean flow variables, confined jet mixing, as reported in Ref. [13], can be split into several distinctive regions, as shown in Fig. 3. The first region is called Regime 1, which contains the wall boundary layer, and jet shear layer, and secondary and primary potential flow regions, while the second one is called Regime 2, which contains a single region of developing flow. The methods of estimating mixing length are different in each flow region. In the jet shear layer, the mixing length is assumed to be dependent only on the shear layer width [14]. The definitions of the wall boundary layer thickness and shear layer thickness were based on the value of r at which the local velocity was 0.99 of the external stream velocity and taken as depicted in Ref. [15].

3.3 Finite-Difference Equations. The general form of differential equations (6) and (7) in finite-differencing form according to grid lines shown in Fig. 1 is

$$A_{n-1}\beta_{m+1,n} + B_{n-1}\beta_{m+1,n+1} + C_{n-1}\beta_{m+1,n-1} = D_{n-1} \tag{9}$$

where β is the generalized dependent variable representing u and θ for the conservation of momentum and energy, respectively. While A, B, C, and D are the source terms taken as depicted in Ref. [15].

3.4 Boundary Conditions. At the inlet, the air velocity profile is assumed to be uniform. At outlet, the gradient of flow variables in the flow direction is set to zero. Along the axis of symmetry, the following boundary conditions were used:

$$Y = 0, \quad \psi^* = 0, \quad \frac{\partial u}{\partial \psi^*} = 0, \quad \frac{\partial \theta}{\partial \psi^*} = 0$$

The wall boundary conditions are

$$Y = f(X) \quad \text{(known wall geometry)}, \quad \psi^* = \text{const}, \quad u = 0$$

$$\frac{\partial \theta}{\partial \psi^*} = 0$$

3.5 Solution Procedure and Convergence. The system of equations (9) has been solved using an implicit finite-difference scheme based on the arrangement shown in Fig. 1. The solution procedure and convergence are realized by the algorithm depicted in Ref. [15].

3.6 Model Validation. A test for the present model is carried out for a typical case of air-air ejector. So the model has been tested and validated against the published experimental and analytical results of Ref. [3]. These comparisons are presented in Figs. 4–6 under the same conditions of motive stagnation pressure and temperature, P_{o1} and T_{o1}, for the tested ejector. It is evident from Fig. 4 that the present predicted wall static pressure distributions and experimental one [3] are in closer agreement compared to analytical results of Ref. [3], while Figs. 5 and 6, show the present predicted, experimental, and theoretical velocity and temperature profiles at four axial locations of Ref. [3]. The comparison shows acceptable agreement. However, the experimental and theoretical velocity and temperature profiles of Ref. [3] are in closer agreement than the present predicted and experimental of Ref. [3], which may be due to the empirical input of the velocity and temperature profiles at each flow section into the analytical model presented in Ref. [3], while the present model depends only on the assumed initial conditions.

To more validate the present model, the model has been compared to the present experimental results, as shown in Fig. 7, for wall static pressure coefficient distributions at five different values of motive stagnation pressure coefficient. The comparison is in a reasonable agreement.

4 Optimum Ejector Design

The objective of optimum ejector design is to achieve a maximum efficiency through the following procedures.

(1) A random value of an area ratio is chosen.
(2) Operational parameters μ, λ, and C_{p_o} in order to avoid shocks, separation, and secondary flow recirculation are selected.
(3) Minimum optimum dimensionless ejector lengths (L_a/D_b, L_b/D_b, and L_c/D_b) are selected in order to minimize the overall ejector weight and to maximize the overall ejector efficiency.
(4) For each optimum ejector design, there are certain values of the operational parameters, which give the maximum effi-

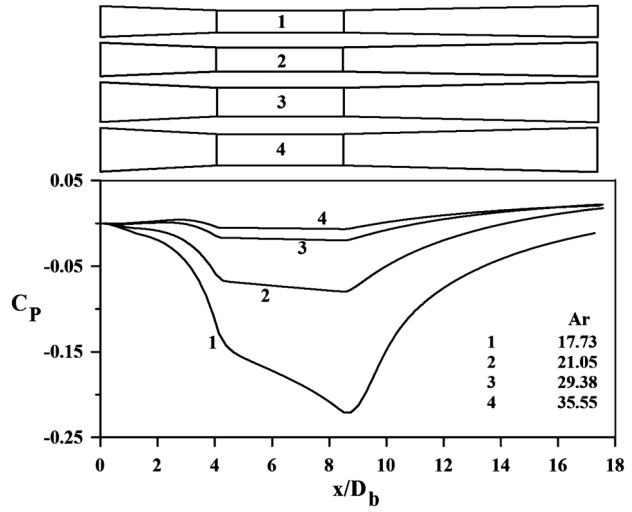

Fig. 8 Effect of area ratio on static pressure coefficient distributions along the ejector geometry (μ=6, C_{p_o}=1.76, λ=1)

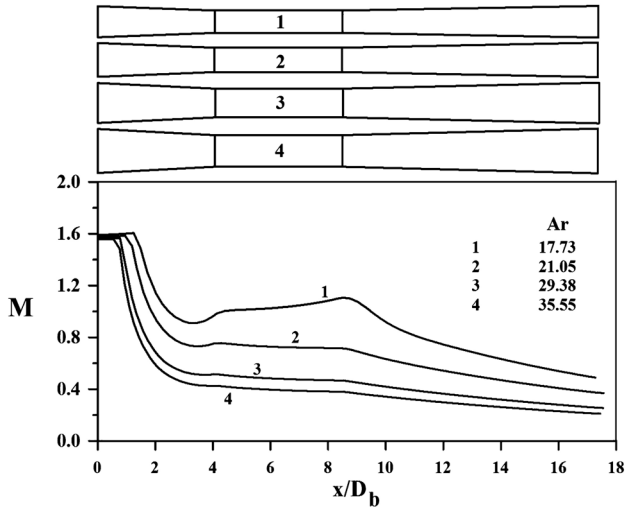

Fig. 9 Effect of area ratio on centerline Mach number distributions along the ejector geometry (μ=6, C_{p_o}=1.76, λ=1)

ciency. The optimum dimensionless lengths are correlated as functions of the ejector area ratio and the operating parameters. Both the optimum ejector lengths together with the optimum operational parameters are interpreted in optimum characteristic curves.

4.1 Optimum-Constant-Pressure Mixing Section Length (L_a/D_b). Mixing of supersonic primary flow with the subsonic secondary flow leads to an abrupt pressure rise, which leads to possible regions of recirculation or separation, which are undesirable in optimum designs. A convergent section results in a higher velocity of the secondary flow (leading to its acceleration), which is accompanied by a decrease in the static pressure that equalizes, to some extent, the abrupt pressure rise due to the mixing leading to an overall constant pressure mixing. After several trials, the optimum-constant pressure mixing length is found to be the length at the end of which the flow becomes no longer supersonic.

4.2 Optimum-Constant-Area Mixing Section Length (L_b/D_b). After selection of the optimum-constant-pressure mixing section length, both streams of flow are allowed to completely mix in a constant-area mixing section. The optimum length of the constant-area mixing section is the length at the end of which fully developed flow is accomplished.

4.3 Optimum Diffuser Section Length (L_c/D_b). The optimum length of diffuser section is selected to recover the pressure until a certain back pressure. In all calculations in the present study, an atmospheric back pressure is chosen.

5 Results and Discussion

5.1 Effect of Area Ratio, A_r. Ejector area ratio is considered as the main geometric parameter in designing an ejector for a particular operation. The ejector area ratio (A_r) is defined as the ratio between the area of the constant-area mixing section and the exit area of the primary flow nozzle. The inner exit primary flow diameter is kept constant at 6.2 mm, while the constant-area mixing section is varied in order to investigate the effect of A_r, on ejector performance. Increasing the area ratio increases the secondary flow inlet area (where θ_1 and θ_2 are constants). A larger secondary flow area results in a smaller velocity, smaller Mach number, and consequently a larger static pressure. The effect of area ratio on the static pressure coefficient and centerline flow Mach number at four different area ratios is shown in Figs. 8 and 9. From the figures, it is clear that A_r, has a positive effect on the static pressure coefficient and a negative effect on the centerline Mach number. The effect of area ratio on the ejector efficiency (η) and the pressure ratio (ϕ) at different operating conditions is shown in Fig. 10.

Figure 10(a) shows the effect of area ratio on the ejector efficiency and pressure ratio at four different mass ratios. At a certain value of area ratio, ejector efficiency is increased as the mass ratio increases while for a given mass ratio, ejector efficiency is firstly increased due to the increase in the area ratio, which increases the static temperature of the secondary flow. However, the ejector efficiency is then decreased due to the increase in total energy loss represented in the exit stagnation pressure, P_{oe}. Figure 10(b) shows the effect of area ratio on the ejector efficiency and pressure ratio at six different temperature ratios. For a given value of area ratio, efficiency is increased as the temperature ratio decreases because of a decrease in the primary flow static temperature. While for a given value of temperature ratio, the ejector efficiency is firstly increased due to an increase in the static temperature of the secondary flow but it is then decreased due to the increase in the frictional losses associated with decreasing exit stagnation pressure, P_{oe}. Figure 10(c) represents the effect of area ratio on the ejector efficiency and pressure ratio at four different stagnation pressure coefficients. At a certain area ratio, a lower stagnation pressure coefficient leads to efficiency enhancement due to the power saving represented in a lower primary flow stagnation pressure. While at a certain value of C_{p_o}, efficiency is firstly increased due to an increase in the secondary flow static temperature T_2 and it is then decreased due to a decrease in exit stagnation pressure at ejector exit.

5.2 Optimum Characteristic Curves. To obtain the optimum characteristic curves through the previously mentioned optimization procedures, five values of area ratios A_r, are selected 9.78, 17.38, 39.11, 108.65, and 278.14. For each area ratio, the operational parameters λ, μ, and C_{p_o} are chosen by systematic trial together with the optimum ejector dimensionless lengths L_a/D_b, L_b/D_b, and L_c/D_b.

The five previously mentioned area ratios are separately investigated to develop correlations relating ejector maximum efficiency, pressure ratio, and ejector optimum dimensionless lengths to area ratio and operational parameters. The area ratio under investigation is kept constant and the operational parameters λ, μ, and C_{p_o} are systematically varied one by one while keeping the others as constants. The maximum efficiency is selected with its pressure ratio and the ejector optimum dimensionless lengths and

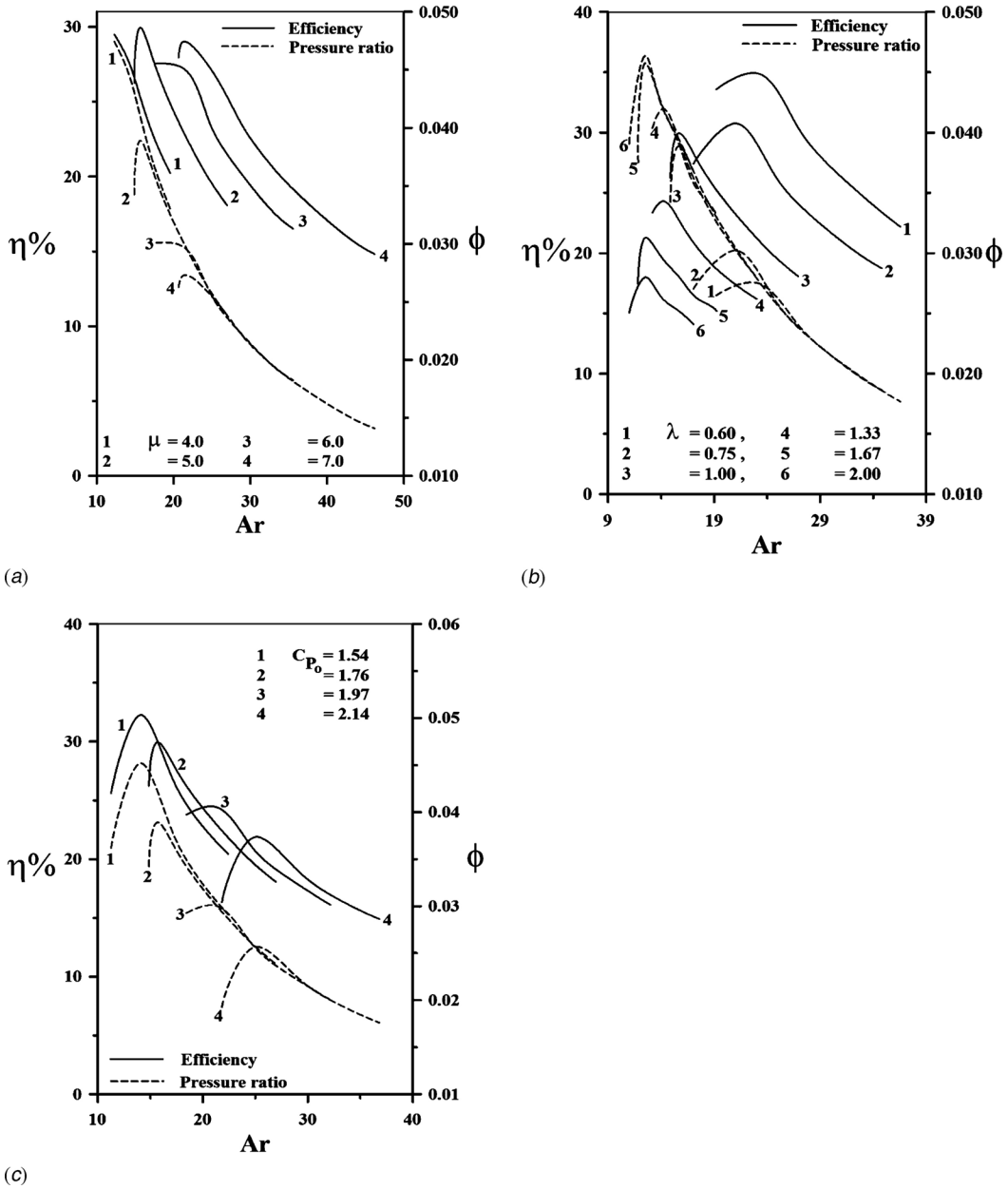

Fig. 10 Effect of area ratio on ejector efficiency and pressure ratio for different inflow conditions: (*a*) Effect of mass ratio (C_{p_o}=1.76, λ=1.0); (*b*) effect of temperature ratio (C_{p_o}=1.76, μ=5); (*c*) effect of stagnation pressure coefficient (μ=5, λ=1.0)

so on. The obtained results are used in developing numerical formulas relating all the parameters under study. The obtained correlations for air-driven air ejectors with $\theta_1 = 5.4$ deg and $\theta_2 = 2.7$ deg are in the following forms:

$$\frac{L_a}{D_b} = \frac{6.605 C_{p_0}^{2.193} \mu^{0.595}}{\lambda^{0.507} A_r^{1.115}} \tag{10}$$

$$\frac{L_a + L_c}{D_b} = \frac{8.787 C_{P_0}^{2.071} \mu^{1.509}}{\lambda^{0.693} A_r^{1.303}} \tag{11}$$

$$\frac{L_T}{D_b} = \frac{8.545 C_{P_0}^{0.827} \mu^{0.837}}{\lambda^{0.496} A_r^{0.572}} \tag{12}$$

$$\phi = \frac{1.048 \lambda^{0.13}}{C_{P_0}^{0.498} \mu^{0.393} A_r^{0.662}} \tag{13}$$

$$\eta = \frac{132.81 \mu^{0.439}}{C_{P_0}^{0.0938} \lambda^{0.77} A_r^{0.587}} \tag{14}$$

A comparison between the numerical results and the values obtained by the deduced formulas is represented in Fig. 11. The comparison shows an acceptable agreement. The formulas are validated for an area ratio of $9.78 \le A_r \le 278.14$, a mass ratio of $2 \le \mu \le 51$, a temperature ratio of $1 \le \lambda \le 4$, and with a stagnation pressure coefficient of $1.28 \le C_{p_o} \le 4.10$.

Figure 12 illustrates the optimum characteristic curves for ejector selection under maximum efficiency at five different area ra-

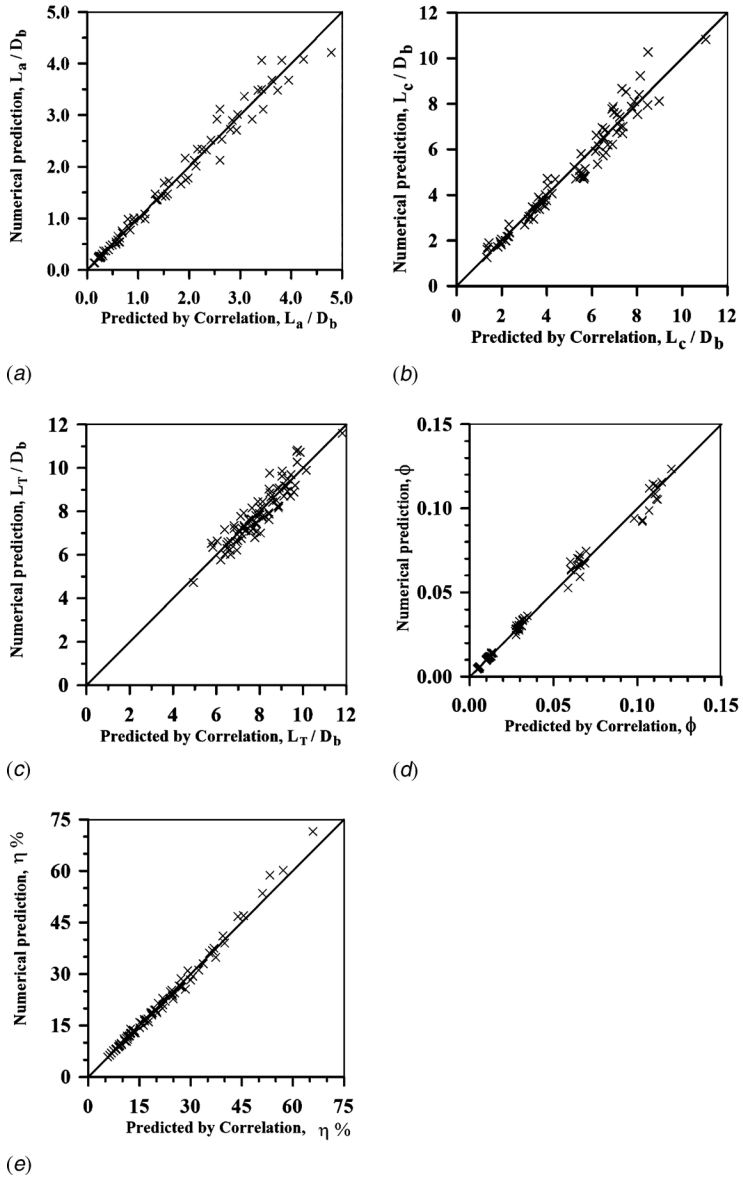

Fig. 11 Comparison between numerical prediction and values predicted by correlations (10)–(14)

tios. Intermediate values of temperature ratios can be obtained by interpolation.

Figure 13 represents the optimum characteristic curves of a certain ejector at four different temperature ratios in order to operate at maximum efficiency. The formulas obtained are then used to determine the optimum lengths of the ejector. For example, from Fig. 13(*a*), if it is required to operate with a mass ratio of $\mu=8$ for an isothermal ejector ($\lambda=1$), then the optimum stagnation pressure coefficient should be 1.28, which gives an optimum efficiency of 36% and a pressure ratio of 0.03 at an area ratio of 39.11. However, the efficiency and pressure ratio would be about 46.5% and 0.045, respectively, if a square root of an area ratio is chosen by interpolation to be about 5.6 ($A_r=31.36$). Then the optimum ejector dimensionless lengths could be obtained from the formulas as functions of μ, λ, A_r, and C_{p_o}. To validate the performed optimization, three optimized geometries, the dimensions of which can be obtained from correlations (10)–(12) with an area ratio of 17.38, are selected from the optimum design charts and the correlations, fabricated and experimentally tested. The obtained results are compared to that theoretically predicted and also to that obtained from the correlations. The comparison shown in Fig. 13(*a*) shows a reasonable agreement.

6 Conclusions

The present study is concerned with numerical and experimental investigation of supersonic primary flow and subsonic secondary flow air-air ejectors. A general method of calculating two-dimensional mixing of compressible jet in variable-area ducts has been developed and validated against previously published theoretical and experimental data. The choice of an eddy diffusivity model for momentum and heat transfer is effective. Formulas for ejector optimum (maximum efficiency) design are obtained by fitting the numerical results and relating the ejector operational parameters to the ejector optimum geometric dimensionless

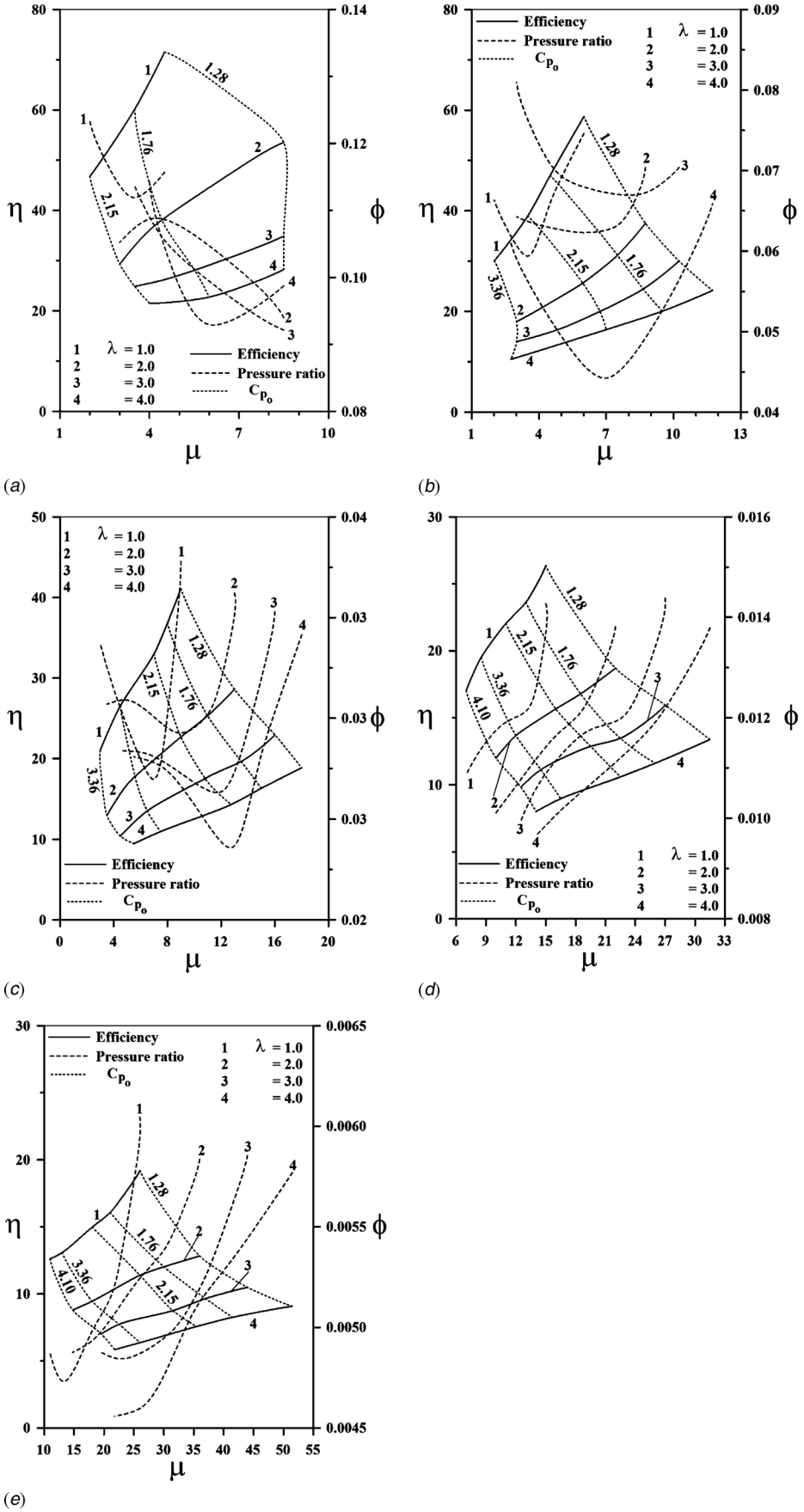

Fig. 12 Optimum characteristic curves for ejector performance at five different area ratios: (*a*) $\sqrt{A_r}$=3.13; (*b*) $\sqrt{A_r}$=4.17; (*c*) $\sqrt{A_r}$=6.25; (*d*) $\sqrt{A_r}$=10.42; (*e*) $\sqrt{A_r}$=16.68

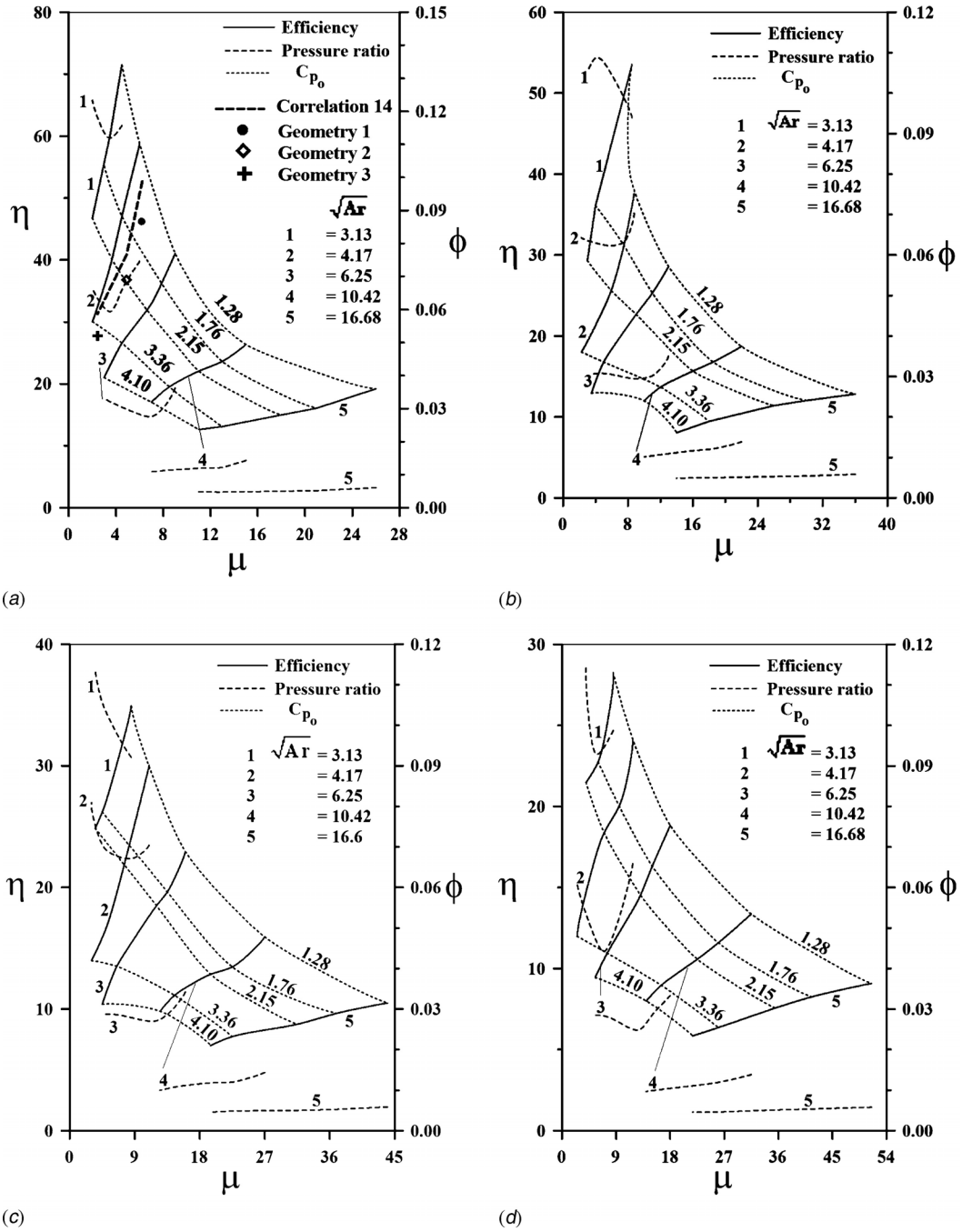

Fig. 13 Optimum characteristic curves for ejector performance at four different temperature ratios: (*a*) λ=1; (*b*) λ=2; (*c*) λ=3; (*d*) λ=4

parameters, pressure ratio, and optimum efficiency. In order to optimize the ejector operation, maximum efficiency, for a particular operating conditions, it is strongly recommended to combine both geometric and operational parameters.

Nomenclature

A_{n-1} = coefficient in the finite-difference equation (9)
A_r = area ratio $(D_b/d)^2$
b = local jet shear layer width
B_{n-1} = coefficient in the finite-difference equation (9)
$\bar{c}_p$ = time-averaged specific heat at constant pressure
c_p^* = dimensionless specific heat, $\bar{c}_p/c_{p1}$
c_{p1} = specific heat at nozzle exit plane
C_L = Eckert number, $(\gamma-1)M_1^2/T_{\mathrm{wr}}/T_1-1$
C_{n-1} = coefficient in the finite-difference equation (9)
C_p = wall static pressure coefficient, $P_i-P_1/0.5\rho_1 u_1^2$
C_{p_o} = primary flow stagnation pressure coefficient, $P_{o1}-P_{\mathrm{ref}}/0.5\rho_1 U_1^2$
d = internal exit diameter of the primary flow nozzle
D = diameter of the constant pressure mixing section at the nozzle exit plane
D_b = diameter of the constant-area mixing section
D_{n-1} = coefficient in the finite-difference equation (9)

E = dimensionless eddy viscosity, ε/ν_1
H = wall static pressure head
h = distance from shear layer outer edge to the jet centerline
$\bar{k}$ = time-averaged thermal conductivity
k_1 = thermal conductivity of primary flow at nozzle exit plane
l_m = mixing length
L_m = dimensionless mixing length
m^o = mass flow rate
M = Mach number
M_1 = primary flow Mach number at nozzle exit plane, $U_1/(\gamma RT_1)^{1/2}$
$\bar{p}$ = time-averaged static pressure
p = dimensionless pressure, $\bar{p}/0.5\rho_1 U_1^2$
P = wall static pressure
P_o = stagnation pressure
P_{ref} = reference atmospheric pressure
Pr_t = turbulent Prandtl number, $\varepsilon/\varepsilon_H$
Pr_1 = Prandtl number, $\mu_1 c_{p1}/k_1$
Q = dimensionless parameter in Eq. (7)
q_T = turbulent heat transfer, $\overline{(\rho v)'T'}$
S = dimensionless parameter in Eqs. (6) and (7)
T = local static temperature
$\bar{T}$ = time-averaged temperature
T' = instantaneous fluctuating temperature
T_o = stagnation temperature
T_{wr} = wall reference temperature
$\bar{u}$ = time-averaged velocity in x direction
u' = instantaneous fluctuating axial velocity component
U = local axial velocity in x direction
u = dimensionless velocity in x direction, $\bar{u}/U_1$
$\bar{v}$ = time-averaged flow velocity in r direction
v' = instantaneous fluctuating radial velocity component
x = space coordinate in the axial direction
X = dimensionless space coordinate, $U_1 x/\nu_1$
ΔX = step size in x direction
r = space coordinate in the radial direction
Y = dimensionless space coordinate in the radial direction, $U_1 r/\nu_1$
V = volume flow rate
η = ejector efficiency $=(V_2/V_1)(P_{oe}-P_{o2})/(P_{o1}-P_{oe})=\mu(T_2/T_1)\phi/(1-\phi)$
ϕ = pressure ratio, $P_{oe}-P_{o2}/P_{o1}-P_{o2}$
λ = stagnation temperature ratio, T_{o1}/T_{o2}
ψ = stream function
ψ^* = dimensionless stream function, $\psi^{*2}=\psi^2 u_1/\rho_1 v_1^2$ (for axisymmetric flow)
ρ = fluid density
$\bar{\rho}$ = time-averaged fluid density
ρ^* = dimensionless fluid density, $\bar{\rho}/\rho_1$
μ = mass ratio, m_1^o/m_2^o
$\bar{\mu}$ = time-averaged absolute viscosity
μ^* = dimensionless absolute viscosity, $\bar{\mu}/\mu_1$
μ_1 = primary flow viscosity at nozzle exit plane
τ = local shear stress
τ_T = turbulent shear stress, $\overline{(\rho v)'u'}$
ε = eddy momentum diffusivity
ε_H = eddy thermal diffusivity
θ = dimensionless temperature, $\bar{T}-T_1/T_{wr}-T_1$
θ_1 = total angle of constant pressure mixing section
θ_2 = total angle of diffuser section
ν = kinematic viscosity
δ = local wall boundary layer thickness
Δ = dimensional boundary layer thickness, $u_1\delta/\nu_1$

Subscripts

1 = primary stream condition at nozzle exit plane
2 = secondary stream condition at nozzle exit plane
e = mixing section exit condition
i = an integer number denoting the pressure tap number or location of pressure
w = wall condition

References

[1] Donald, P. H., and Robert, W. C., 1956, "Investigation at Supersonic and Subsonic Mach Numbers of Auxiliary Inlets Supplying Secondary Air Flow to Ejector Exhaust Nozzles," NACA RM E55J12a.
[2] Fabri, J., and Paulon, J., 1958, "Theory and Experiments on Supersonic Air-to-Air Ejectors," NACA TM-1410.
[3] Kirti, N. G., Torda, T. P., and Zalman, L., 1970, "Turbulent Mixing in the Initial Region of Heterogeneous Axisymmetric Coaxial Confined Jets," NASA CR-1615.
[4] Abou-Taleb, F. A., 1986, "Effect of Geometric Parameters on the Performance of Ejectors," M.Sc. thesis, Department of Mechanical Engineering, Menoufia University, Egypt.
[5] Dutton, J. C., and Carroll, B. F., 1986, "Optimal Supersonic Ejector Design," ASME J. Fluids Eng., **108**, pp. 414–420.
[6] Raman, G., and Taghavi, R., 1997, "Aeroacoustic Characteristics of a Rectangular Multi-Element Supersonic Jet Mixer-Ejector Nozzle," J. Sound Vib., **207**(2), pp. 227–247.
[7] Guillaume, D. W., and Judge, T. A., 1999, "Improving the Efficiency of a Jet Pump Using an Elliptical Nozzle," Rev. Sci. Instrum., **70**(12), pp. 4727–4729.
[8] Szabo, S., 2001, "Influence of the Material Quality of Primary Gas Jets on the Final Vacuum Created by a Supersonic Gas Ejector," Computational Applied Mechanics, **2**(1), pp. 131–144.
[9] Kandakure, M. T., Gaikar, V. G., and Patwardhan, A. W., 2005, "Hydrodynamic Aspects of Ejectors," Chem. Eng. Sci., **60**, pp. 6391–6402.
[10] Karambirov, S. N., and Chebaevskii, V. F., 2005, "Possibilities of Improving Ejector Pump Characteristics," Chemical Petroleum Engineering, **41**(1–2), pp. 75–80.
[11] Yong, F., Yuji, S., and Nobuhide, K., 2006, "Development of a Large-Entrainment-Ratio Axisymmetric Supersonic Ejector for Micro Butane Combustor," J. Micromech. Microeng., **16**, pp. S211–S219.
[12] Krause, E., 1972, "Numerical Treatment of Boundary-Layer and Navier–Stokes Equations," *VKI Lecture Series, Numerical Methods in Fluid Mechanics*, Feb. 7–11.
[13] Hedges, K. R., and Hill, P. G., 1974, "Compressible Flow Ejectors," ASME Trans. J. Fluids Eng., **96**, pp. 272–281.
[14] Schlichting, H., 1968, *Boundary Layer Theory*, McGraw-Hill Book, Inc., New York.
[15] Hewedy, N. I. I., Hamed, M. H., Abou-Taleb, F. Sh., and Ghonim, T. A., 2007, "Numerical and Experimental Investigation of Compressible Flow Ejectors," Minoufiya Engineering Research Journal, **30**(1), pp. 53–66.

A. L. Kastengren[1]
e-mail: akastengren@anl.gov

C. F. Powell

Center for Transportation Research,
Argonne National Laboratory,
Argonne, IL 60439

T. Riedel
Diesel Systems-Commercial Vehicles/
Engineering Systems Application,
Robert Bosch, GmbH,
Stuttgart 70049, Germany

S.-K. Cheong

K.-S. Im

X. Liu

Y. J. Wang

J. Wang

Advanced Photon Source,
Argonne National Laboratory,
Argonne, IL 60439

Nozzle Geometry and Injection Duration Effects on Diesel Sprays Measured by X-Ray Radiography

X-ray radiography was used to measure the behavior of four fuel sprays from a light-duty common-rail diesel injector. The sprays were at 250 bar *injection pressure and* 1 bar *ambient pressure. Injection durations of* 400 μs *and* 1000 μs *were tested, as were axial single-hole nozzles with hydroground and nonhydroground geometries. The X-ray data provide quantitative measurements of the internal mass distribution of the spray, including near the injector orifice. Such measurements are not possible with optical diagnostics. The* 400 μs *sprays from the hydroground and nonhydroground nozzles appear qualitatively similar. The* 1000 μs *spray from the nonhydroground nozzle has a relatively consistent moderate width, while that from the hydroground nozzle is quite wide before transitioning into a narrow jet. The positions of the leading- and trailing-edges of the spray have also been determined, as has the amount of fuel residing in a concentrated structure near the leading edge of the spray.* [DOI: 10.1115/1.2903516]

Introduction

Diesel engines represent a large and important class of engines in transportation applications. Their high thermal efficiency compared to spark-ignited engines makes them an attractive option for decreasing fossil fuel usage. One of the most critical aspects of combustion in diesel engines is the spray used to introduce fuel into the engine cylinder. The character of this spray greatly affects the emissions and overall efficiency of the engine [1], and has thus been the subject of intense research in recent years. Both the injection pressure and injection timing are important parameters of interest. Injection pressure can be used to regulate the amount of fuel delivered to the engine, which determines the output power of the engine. A strategy that has been developed in recent years to decrease diesel engine combustion noise is pilot injection, in which a short-duration injection is used to introduce a small quantity of fuel into the engine cylinder prior to the long-duration main injection event. Pilot injection has also been shown to reduce peak cylinder pressure [1,2]. The transient behavior of the injector while the needle is opening is more important for the short injections used for pilot injection. Thus, data regarding the behavior of both long-duration and short-duration sprays are needed.

Due to the importance of fuel sprays to engine performance, they have been an area of active experimental and computational research [3,4]. Many techniques exist to examine spray behavior, ranging from mechanical measurement techniques, such as patternators [5] and piezoelectric force transducers [4,6], to conventional optical measurements, such as shadowgraph and schlieren imaging [7–10]. More recently, laser-based diagnostics, such as Mie scattering imaging [10,11], laser-induced fluorescence [12], and exciplex fluorescence [13], have also been used to examine sprays. The most commonly measured quantities are the speed at which the leading edge of the spray advances (penetration speed) and the overall spreading angle of the spray (cone angle).

Traditional measurement techniques, however, suffer from severe limitations [14]. Mechanical measurement techniques inevitably perturb the spray flow field. Optical measurements are limited because the surfaces of droplets scatter light. In regions with a high density of fuel droplets, such as near the fuel injector orifice, this scattering becomes so pronounced that scant light penetrates the spray. This lack of light transmission obscures the internal spray structure in shadowgraph and schlieren images. In laser-based techniques, this attenuation causes nonuniform illumination of the spray [12]. Moreover, the light scattered or emitted from dense regions of the spray has a high likelihood of encountering other droplets and, in turn, being scattered. These multiple scattering effects make it difficult to quantitatively measure the spray structure, particularly in areas of high droplet density. Thus, little is known about the structure of fuel sprays in regions of high droplet density, such as near the injector orifice. Recently, the technique of ballistic imaging has been developed to attempt to overcome these multiple scattering effects [15]. While this technique can provide images of the unsteady structure of the spray, it does not provide quantitative data regarding the fuel distribution.

In recent years, X-ray radiography has been adapted to examine the internal mass distribution of diesel sprays [16–19]. Radiography has been used to examine the behavior of both diesel [15–18] and gasoline [19] sprays in a quantitative, time-resolved fashion. The radiography technique provides detailed information regarding the mass distribution of these sprays, which is unobtainable with optical techniques.

[1]Corresponding author.

Contributed by the Fluids Engineering Division of ASME for publication in the JOURNAL OF FLUIDS ENGINEERING. Manuscript received May 23, 2007; final manuscript received October 31, 2007; published online April 4, 2008. Assoc. Editor: Theodore Heindel.

In this paper, X-ray radiography was used to measure the internal mass distribution of sprays from a diesel injector for different injection durations and orifice geometries. The mass distributions of the sprays are described, as are the differences between injections using different durations and nozzle geometries. The movement of the leading and trailing edges of the sprays is shown as a function of time. The behavior of the cone angle of the sprays is examined, as is the fraction of the total spray mass residing near the spray leading edge. Similar measurements have been attempted in past X-ray radiography spray measurements by the authors [15]. However, these measurements were limited to short-duration injections and small regions near the injector. The current measurements cover a much larger field of view. Moreover, the current study probes the behavior of long-duration sprays, which are more representative of main injection event sprays.

Experimental Method

Radiography Technique. X-ray radiography is based on a simple application of linear absorption. Unlike visible light, X-radiation is not significantly scattered from the surface of fuel droplets. The dominant interaction of X-rays with the spray is absorption. A narrow beam of X-rays illuminates the spray, and the absorption of this beam is used to find the quantity of fuel in the path of the beam. If $I(0,\lambda,t)$ is the X-ray intensity incident on the spray at time t and $I(\ell,\lambda,t)$ is the X-ray intensity after passing though the spray, the following equation applies:

$$I(\ell,\lambda,t) = I(0,\lambda,t)e^{-\varepsilon(\lambda)\ell(t)} \tag{1}$$

In this equation, ε is the absorption coefficient of the fuel in the spray (with units of length^{-1}) and ℓ is the path length of fuel in the beam. In general, the absorption coefficient depends strongly on the X-ray wavelength λ. However, spectral X-ray detectors suitable for the absorption measurements needed in ultrafast radiography are not currently available. This dependence of absorption coefficient on wavelength would make it difficult to quantitatively reconstruct the path length from a measurement of X-ray intensity if the X-ray beam were polychromatic. This difficulty is overcome by using a monochromatic X-ray source, which simplifies the above equation and allows quantitative measurements to be made more easily. Using the density of the fuel (ρ), the path length can be converted into a projected density (M), in units of mass per unit area in the beam. This projected density is derived using the following formula:

$$M(t) = \frac{\rho}{\varepsilon}\ln\left(\frac{I(z=\ell,t=0)}{I(z=\ell,t)}\right) \tag{2}$$

The resulting data from X-ray radiography give a quantitative measure of the spray's projected density along the beam path as a function of time. These data provide an important complement to traditional optical spray measurements. X-ray radiography data can show the internal mass distribution of fuel sprays with good time and spatial resolution, especially in high-density regions of the spray. These are precisely the data that are unobtainable with optical techniques. Moreover, the quantitative nature of these data allows for more sophisticated analyses than have been previously used with optical measurements.

There are some important drawbacks to the radiography technique, however. Since the data are path length integrated, variations in the spray structure along the X-ray beam cannot be measured. Moreover, the data are ensemble averaged. Thus, unsteady, transient structures cannot be measured. The technique fundamentally measures features of the spray which are persistent shot to shot. Strong absorption of the X-ray beam can also limit the accuracy of the technique, with the lower transmitted intensity leading to a lower signal-to-noise ratio. In the current study, the minimum transmission is approximately 0.40 (with a corresponding path length of approximately 300 μm), which is still within the range for which the linear absorption technique is applicable. A more detailed discussion of the experimental method can be found elsewhere [20].

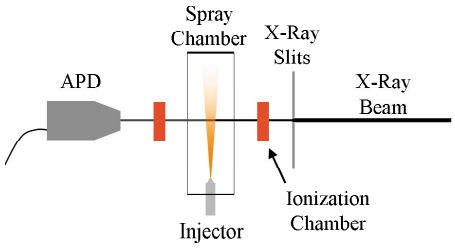

Fig. 1 Experimental layout

Two axial single-hole injection nozzles were used in this study. One has undergone very little hydrogrinding, leaving a sharp entrance to the nozzle; the ratio of nozzle entrance rounding to nozzle radius (r/R) is 0.4. The length-to-diameter ratio of this nozzle is 4.7. The other nozzle has undergone extensive (24%) hydrogrinding, resulting in a well-rounded entrance ($r/R=2.0$). The nozzle diameter of the nonhydroground nozzle is 208 μm, which is slightly larger than the hydroground nozzle (183 μm). This difference was intentional; the nozzles were designed to have approximately the same steady-state flow rate. Since the sharp entrance to the nonhydroground nozzle results in a reduced discharge coefficient, its diameter must be larger [21]. The size of these orifices is comparable to that of nozzles used in operational diesel injectors.

Four test conditions were examined in this study. Two commanded injection durations, 400 μs and 1000 μs, were used. The 400 μs duration was intended to simulate a pilot injection; the total injected quantity for these events is less than 400 μg/stroke. The 1000 μs duration allowed the spray to reach steady state. All combinations of injection duration and nozzle geometry were tested, yielding four unique injection events.

The X-ray beam used to probe the spray was produced at the 1-BM beamline at the Advanced Photon Source, a synchrotron X-ray source at Argonne National Laboratory. The X-ray beam was monochromatic, with a photon energy of 8 keV. A series of X-ray optics was used to create a tightly focused, monochromatic beam. Vertical and horizontal X-ray slits were then used to limit the beam size. The full width at half maximum (FWHM) size of the beam was 200×30 μm^2 for the short-duration spray from the hydroground nozzle and 145×12 μm^2 for the other three sprays. The time-averaged beam intensity was monitored nonintrusively using ionization chambers. The beam was directed through the spray, and a fraction of the beam was absorbed by the fuel. The transmitted X-ray beam illuminated an EG&G avalanche photodiode (APD) detector whose output is proportional to the beam intensity; the time constant of the detector is less than 5 ns. The voltage signal from the photodiode was recorded every 1 ns for a duration of 1–2 ms using a Yokogawa DL7480 500 MHz digital oscilloscope. The layout of the experimental equipment is shown schematically in Fig. 1.

The spray was created with a Bosch common-rail light-duty diesel injection system. In this system, high-pressure fuel is maintained at relatively constant pressure in a reservoir (common rail) that feeds the injector. Electrical current activates an internal hydraulic circuit in the injector, which causes the injector needle to lift, allowing fuel to exit the injector. The current is supplied to the injector in two stages. An initial burst of current (18 A), referred to as the breaking current, is supplied at the beginning of the injection to aid in opening the injector, followed by a lower current (12 A) to hold the injector open. For the 400 μs injection with the hydroground nozzle, the breaking current was applied for 250 μs, while for the other injections, the breaking current was

Table 1 Fuel properties at 30°C

Density, kg/m^3	865.4
Viscosity, m^2/s	3.32×10^{-6}
Surface tension, N/m	25.9×10^{-3}
X-ray absorption coefficient, m^2/kg	3.02 ± 0.04, 400 μs, hydroground 3.11 ± 0.04, all others

applied for 150 μs. Because of this difference in the current signal to the injector, care must be used in comparing the short-duration spray from the hydroground nozzle to the other sprays.

The injection pressure used in these sprays is 250 bars. This represents a low pressure compared to that of some modern common-rail systems, which can achieve pressures of more than 2000 bars. The injection pressure was chosen to limit the penetration speed of the spray leading edge. For the short-duration sprays, the spray event ends before the spray's leading edge reaches the edge of the measurement domain, allowing the leading and trailing edges of the spray to be measured at the same time after the start of injection. Moreover, this modest pressure is similar to that used at idle conditions in some diesel engine applications.

The spray was contained in an enclosed chamber with X-ray transparent windows. The ambient gas in the chamber was N_2 at 1 atm pressure and room temperature. Measurements at higher ambient pressure and injection pressure values over limited fields of view have been performed in the past [18]; further such measurements are ongoing. While the current ambient condition is far from the conditions in an engine cylinder during a fuel injection event, the design of the X-ray transparent windows has not sufficiently progressed to allow for large windows capable of withstanding high pressure. The larger field of view of the current experiments allows the far-field behavior of all of the sprays to be examined in detail. Moreover, a large field of view is needed to examine the evolution of the entire spray plume after the end of injection for the short-duration sprays. It should be noted that the current measurements have been performed under nonvaporizing conditions; the results may not be generally applicable to vaporizing sprays.

A purge flow of 1 L/min of N_2 gas was used to remove stray fuel droplets and vapor from the chamber without inducing large velocities in the ambient gas. The fuel used in these injections was Viscor 1487, a calibration fluid with physical and chemical properties similar to diesel fuel. A cerium-based fuel additive was added to the fuel in a ratio of 9:1 to enhance the contrast of the X-ray data, yielding a final cerium concentration of approximately 4% by mass.

The radiography technique measures the transmission of X-rays through the spray. To convert the transmission to projected mass, the absorption coefficient must be determined. The absorption coefficient of the fuel depends on the chemical identity of the fuel and the fuel density, and so it is constant throughout the experiment to a good approximation. The absorption coefficient is determined by a static measurement using the X-ray transmission through a capillary tube. Fuel properties, including the X-ray absorption coefficient, are given in Table 1.

The APD provides a path length-integrated measure of the fuel quantity for one beam path through the spray. The injector was moved in a raster pattern to study the spatial distribution of the spray. Data were taken at approximately 2500 individual locations in the flow field. The measurement grid for one of the sprays examined in this study is shown in Fig. 2. In this work, the x-coordinate represents the distance from the injector nozzle exit along the injector axis. The y-coordinate is the distance from the injector axis in a direction perpendicular to both the injector axis and the X-ray beam; the line-of-sight radiography data naturally map onto the x-y plane. As shown in Fig. 2, the data were measured in discrete transverse slices; the spacing between different

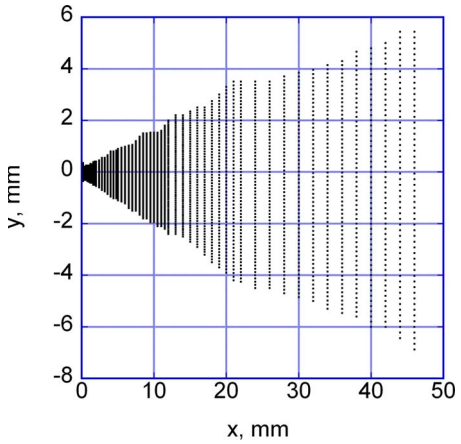

Fig. 2 Measurement locations for the long-duration spray from the hydroground nozzle

slices ranged from 0.2 mm near the orifice to 2 mm far downstream. For each slice, 25–55 measurement points were equally spaced in the y direction to measure the full transverse extent of the spray with good resolution of its structure. The spacing between data points in the y direction ranged from 30 μm near the orifice to 250 μm far downstream. To reduce the noise in the data, which is mainly caused by electronic noise in the detector readout and detector photon shot noise, the X-ray data at each measurement location are an ensemble average of 64 spray events. Recent single-shot radiography measurements near the spray orifice of similar diesel sprays have shown that shot-to-shot variations in the projected mass in the spray are quite small [22]. Thus, the ensemble-averaged results presented in this paper, including penetration speed and cone angle, appear to accurately represent the spray distribution on a single-shot basis as well.

Several steps are necessary to extract the projected density of the fuel from the APD signal. The x-ray source gives a series of 24 X-ray pulses spaced approximately 155 ns apart in a pattern, which repeats every 3.68 μs. To reduce the noise in the data, the 24 X-ray intensity peak values for each synchrotron orbit are binned together. Thus, the time step in the processed data is 3.68 μs.

The beam intensity values are in arbitrary units. To normalize these data, a measure of the beam intensity without absorption by the spray is needed. To obtain this measure, the X-ray intensity was averaged for the time period before the spray emerged from the orifice (55–75 μs). This x-ray intensity is used to normalize the data for all subsequent time steps. Next, the data are corrected for the slightly nonlinear response of the APD. This yields a final value for the transmission of the X-ray beam through the spray, which is converted to projected density using Eq. (2). This procedure is followed for each location in the measurement grid.

Experimental Uncertainty. Major contributions to the experimental uncertainty are the measurements of the spray transmission, the measurement position in the spray flow field, the absorption coefficient, and time. The standard deviation of the spray transmission is approximately 0.0025. The x and y positions of the measurements are repeatable to within ±20 μm and ±5 μm, respectively. The uncertainty in the absorption coefficient is approximately 1.5%. The time measurement is repeatable to within 1 ns throughout the data record. The accuracy of the time measurement is within 0.1%. At low mass levels, this yields a standard deviation in the projected mass of approximately 0.8 μg/mm^2. At the highest projection mass regions, where the absorption is the greatest, the standard deviation of the projected mass is 6.0 μg/mm^2.

Table 2 Measured delay between commanded and apparent SOI

Spray event	Delay, μs
400 μs, hydroground	486 ± 4
400 μs, nonhydroground	451
1000 μs, hydroground	429
1000 μs, nonhydroground	477

Results

All of the subsequent data are referenced to the time of the apparent start of injection (SOI), which is defined as the time step when fuel is first detected outside the injector orifice. Table 2 shows the time delay measured between the commanded SOI and the apparent SOI. Note that for the short-duration sprays, the current to the injector had ended before any fuel exited the injector orifice.

The X-ray data provide a unique way to visualize the ensemble-averaged spray behavior as a function of time. Figures 3–5 show the evolution of the two short-duration sprays studied in this work. Early in the spray events, a narrow jet of high-density fluid exits the nozzle. The highest projected density is near the nozzle, with a relatively sharp drop in projected density near the spray leading edge. As the sprays from both nozzles proceed further, their form is a thin jet of fluid terminated by a concentrated structure near the leading edge, as shown in Fig. 4. This structure is more easily seen in the spray from the hydroground nozzle. Previous X-ray measurements of diesel sprays at higher ambient density and injection pressure values have also shown leading-edge structures [16,18], though the structures seem to be enhanced by the current experimental conditions. After the injector closes, the trailing jets quickly dissipate, while the leading-edge structures persist, as shown in Fig. 5. The leading-edge structure appears to contain the vast majority of the mass of the spray and grows in size, becoming more dilute as it progresses downstream, especially for the hydroground nozzle spray.

The major difference between the two sprays is that the spray from the hydroground nozzle appears to develop more quickly than the spray from the nonhydroground nozzle, as shown by both the penetration of the leading edge of the spray and the overall shape of the spray. The authors hypothesize that this condition is caused largely by the difference in the breaking current timing used in these injection events; such effects are not seen in the long-duration sprays in Fig. 6, in which the same breaking current was used for both cases. It appears that the longer application of the breaking current allowed the injector to open faster and to a larger degree for the spray from the hydroground nozzle than the spray from the nonhydroground nozzle.

Figure 6–8 show the projected mass density distributions of the long-duration injections from both nozzles. The initial behavior of the sprays from both of these nozzles is very similar to the behavior of the short-duration sprays; for example, compare the appearance of Figs. 4 and 6, noting the difference in the scales of the shading. A major difference is that the jet of fluid connecting the leading-edge structure to the nozzle is denser for the long-duration sprays, as the injector remains open throughout the times shown in Figs. 6–8.

The leading-edge structure eventually penetrates past the down-

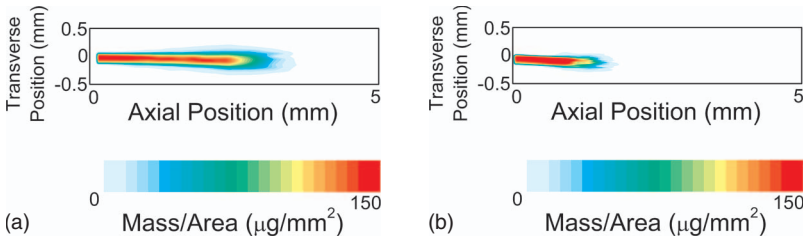

Fig. 3 Projected density for short-duration injections 77 μs after SOI; (*a*) Hydroground Nozzle (*b*) Nonhydroground Nozzle

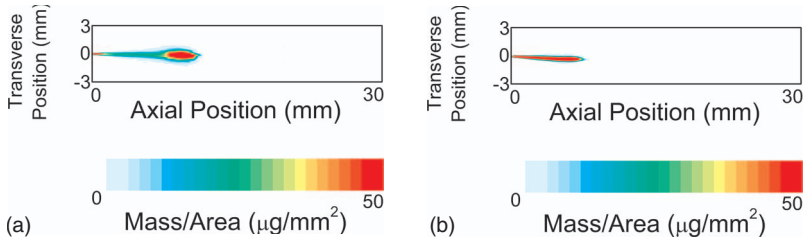

Fig. 4 Projected density for short-duration injections 206 μs after SOI; (*a*) Hydroground Nozzle (*b*) Nonhydroground Nozzle

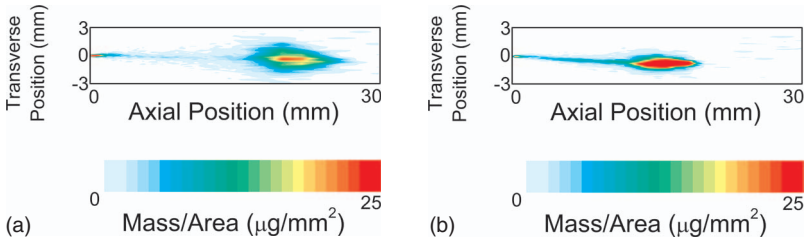

Fig. 5 Projected density for short-duration injections 365 μs after SOI; (*a*) Hydroground Nozzle (*b*) Nonhydroground Nozzle

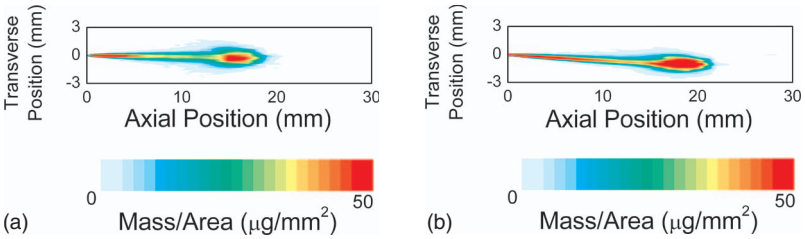

Fig. 6 Projected density for long-duration injections 328 μs after SOI; (*a*) Hydroground Nozzle (*b*) Nonhydroground Nozzle

stream edge of the measurement domain, resulting in what at first appears to be the steady-state jet behavior in Fig. 7. However, approximately 700 μs after SOI, the appearance of the spray from the hydroground nozzle changes dramatically. The wide spray shown in Fig. 7 transitions into a very narrow jet of fluid, as shown in Fig. 8; this appears to be the true steady-state behavior of the spray. No such transition is apparent in the spray from the nonhydroground nozzle. These behaviors match the results of previous studies of short-duration injections with these nozzles at 1000 bar injection pressure [16]. The nature of this transition is discussed further later in this paper.

The distribution in projected density across each measurement slice can be examined to better quantify the behavior of the spray. As Fig. 9(*b*) shows, a Gaussian curve fits the data well at most measurement positions. This agreement is not unexpected, since in a fully developed turbulent jet, one expects the concentration distribution of the jet fluid to be Gaussian [23]. A notable exception is near the injector, where the measured distribution is flatter than a Gaussian curve, as shown in Fig. 9(*a*). This behavior has been seen in previous X-ray radiography measurements of diesel sprays at various injection pressures [16], and suggests that a core of fluid near the liquid density might be present very near the nozzle. Gaussian fits were made to all of the transverse distributions to aid in further analysis of the sprays.

A consequence of the Gaussian distribution of fuel across the spray is that it is inherently difficult to define a boundary of the spray, especially for $x > 2$ mm. The mass distribution appears to smoothly decrease from a peak on the spray axis to zero far from the axis. This is in stark contrast to optical spray measurements, for which a sharp gradient in light intensity is evident at the spray periphery. This highlights the differing capacities of the radiography and optical measurement techniques. Radiography focuses on the high-density core region, whereas optical techniques focus on the periphery of the spray. As such, care must be taken in comparing the radiography results to optical measurements.

The width of the Gaussian fits can be used as a quantitative measure of the width of the sprays. Figure 10 shows the FWHM of the Gaussian fits as a function of x (axial distance from the nozzle, see Fig. 2) for the long-duration sprays at four times. The slope of these plots represents the definition of the full cone angle of the sprays used in this work. By using FWHM as the definition of the spray width, if one assumes that the sprays are axisymmetric and that the mass distribution is Gaussian, it can be shown that half of the spray mass is contained within this cone angle. It should be noted that this definition of cone angle is fundamentally different than cone angle based on visible light spray images, and thus should not be expected to yield the same results.

Early in the spray event (445 μs after SOI), the spreading rate of the spray is largely linear for both sprays. The spray is particularly wide near the leading edge of the spray, which corresponds to the leading-edge structure. At this time, the spray from the hydroground nozzle is substantially wider than the spray from the nonhydroground nozzle. However, at 644 μs after SOI, the spray from the hydroground nozzle has begun to undergo the transition seen in Figs. 7 and 8. While the spray is quite wide far downstream of the nozzle, the cone angle near the nozzle is now similar to the spray from the nonhydroground nozzle. This narrowing continues and propagates downstream. At 1068 μs after SOI (see also Fig. 8), the transition is complete. The spray from the hydro-

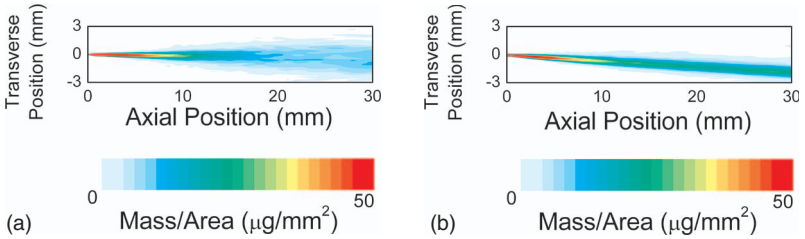

Fig. 7 Projected density for long-duration injections 641 μs after SOI; (*a*) Hydroground Nozzle (*b*) Nonhydroground Nozzle

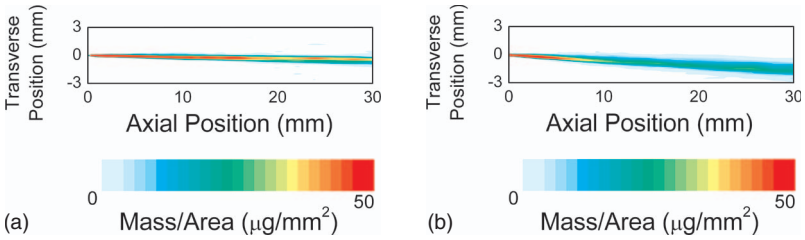

Fig. 8 Projected density for long-duration injections 1068 μs after SOI; (*a*) Hydroground Nozzle (*b*) Nonhydroground Nozzle

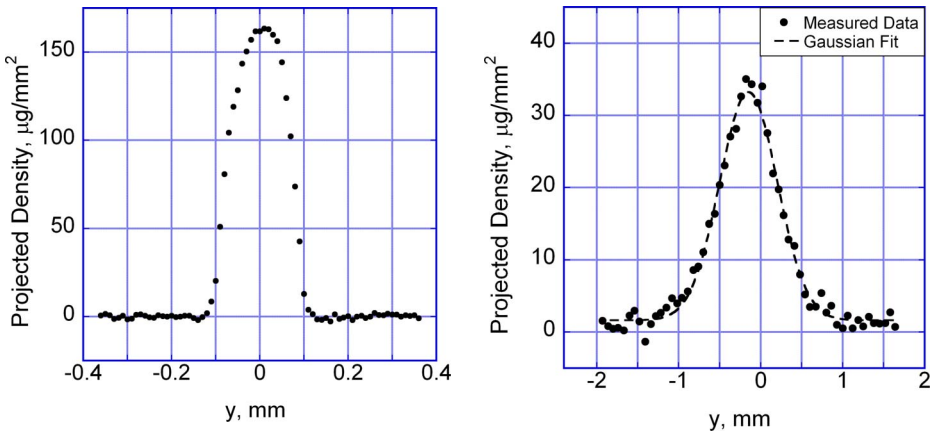

Fig. 9 Example distributions of the projected density across the spray (in the *y* direction) from the hydroground nozzle 328 μs after SOI at axial distances from the nozzle of (*a*) *x*=0.2 mm and (*b*) *x*=10.0 mm

ground nozzle is quite narrow, while the spray from the nonhydroground nozzle is virtually unchanged from its behavior 661 μs after SOI. As the spray event ends, the cone angle of the spray from the hydroground nozzle suddenly becomes wide once again, while for the nonhydroground nozzle, it becomes only slightly wider. This transitional behavior in sprays from the hydroground nozzle has been seen in short-duration injections at 1000 bar injection pressure as well [16], though the transition was not as dramatic as in the present data. Given that the previous study cited used a different injection duration and a different injection pressure, such differences are not surprising.

By performing a linear fit to the data in Fig. 10, the full cone angle of the sprays can be quantified. These data are shown in Fig. 11. A line is fitted to the Gaussian FWHM versus *x* curves, such as those shown in Fig. 10, and the slope of the line is used to calculate the full cone angle. The *x* range across which the fits were

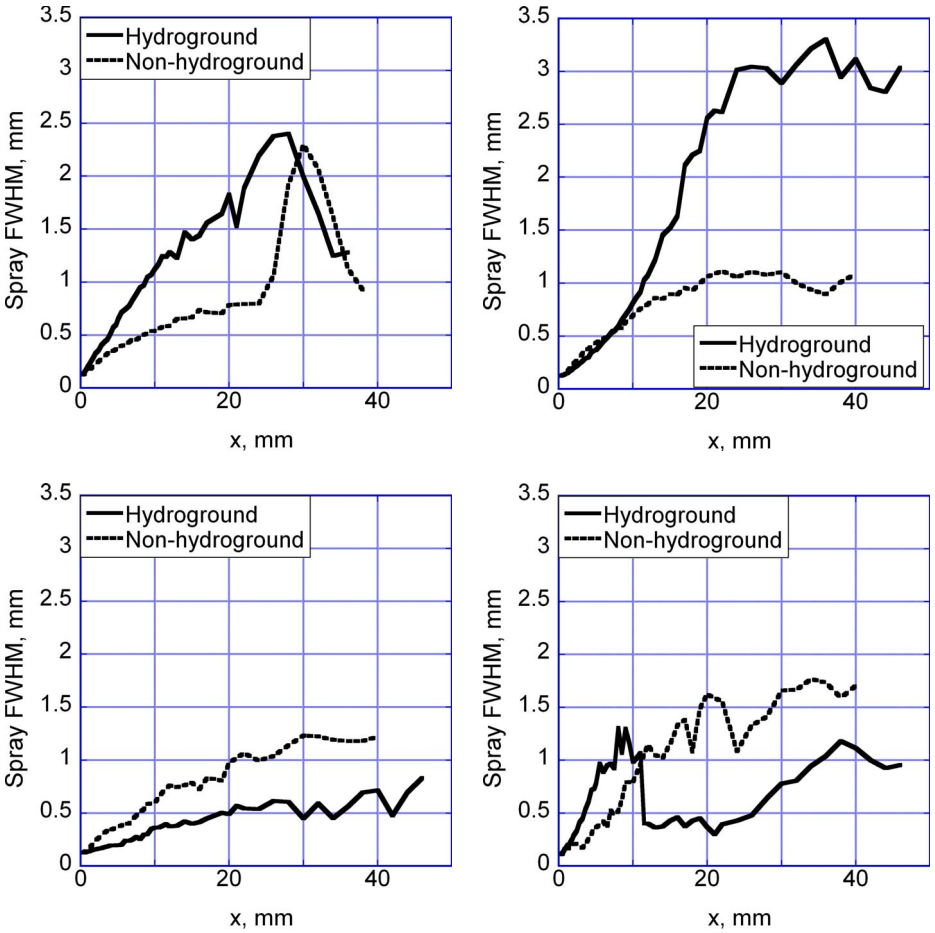

Fig. 10 FWHM of long-duration sprays, as determined by Gaussian fits, at selected times after SOI. Lines connecting the data are guides for the eye.

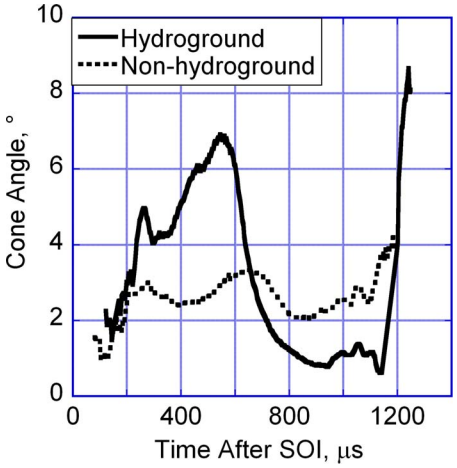

Fig. 11 Cone angle of the long-duration sprays versus time after SOI. Lines connecting the data are guides for the eye.

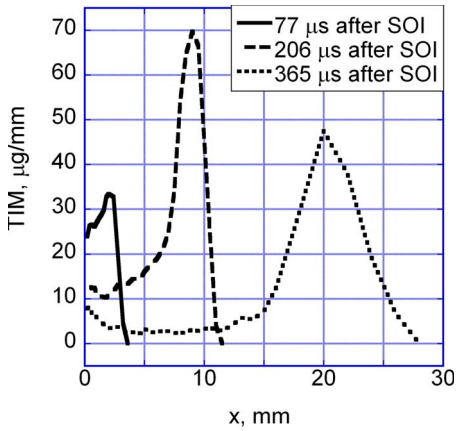

Fig. 12 TIM for the short-duration spray from the nonhydroground nozzle at selected times after SOI. Lines connecting the data are guides for the eye.

performed, was restricted to the region from 0.2 mm to 10 mm from the nozzle to ensure that the relationship between FWHM and x would be reasonably linear at most time steps. Thus, the cone angle values shown in Fig. 11 represent a near-nozzle cone angle.

Figure 11 demonstrates several points worthy of note. First, the cone angles of these sprays are much smaller than the typical values seen in optical measurements of diesel sprays, which are typically on the order of 20 deg [7,24]. This trend has been seen in past measurements of diesel sprays using X-ray radiography [16]. Since the distribution of mass across the spray is a smooth Gaussian curve, the use of FWHM as the threshold to define the cone angle is, while quantitative, arbitrary. Indeed, if one used a smaller threshold (resulting in a wider width), a larger cone angle would result. In order to achieve cone angle values comparable to those found in optical measurements, the threshold must be set at a very low projected density level (i.e., far from the center of the Gaussian distributions). This indicates that optical measurements of the cone angle measure the very periphery of the spray mass distribution.

It should be noted that the cone angle is determined optically by thresholding images of the spray. As mentioned previously, the contrast in optical spray images tends to be quite high, so the spray boundary is well defined with such a technique. Since the contrast in spray images depends on droplet size, the mass distribution in the spray, multiple scattering effects, camera gain, and the exact value of the threshold used, it is unclear what projected density level would correspond to the optical cone angle. This is a further demonstration that care must be taken in comparing optical and radiographic spray measurements.

Figure 11 also allows the extent of the narrowing of the spray distribution for the hydroground nozzle spray to be quantified. The cone angle of the spray from the hydroground nozzle decreases by a factor of nearly 5 between 475 μs and 1068 μs after SOI. This is a much more dramatic change in cone angle than is typically seen in optical measurements of diesel spray cone angle versus time [7]. The authors believe that there are two possible explanations for this dramatic change in behavior. First, the needle of the injector throttles the fuel flow in the early stages of the spray event, which is expected to create turbulence in the nozzle sac. Such turbulence will disturb the fuel jet leaving the orifice, promoting early spray breakup and a wide cone angle. As the nozzle becomes more fully open and the throttling-induced turbulence lessens, such effects should decrease. For the hydroground nozzle, with its smooth nozzle contour, this should result in a smooth flow through the nozzle, promoting a delay in the breakup of the spray and a narrower fuel jet. The sharper nozzle inlet to the nonhydroground nozzle will lead to a greater level of cavitation and turbulence than is seen in the hydroground nozzle; the flow in the orifice would be expected to be perturbed even when the needle is at full lift, which would explain why no transition occurs for this nozzle. This hypothesis also explains why the cone angle increases at the end of injection; the needle once again begins to throttle the fuel flow, and the added disturbance of the fuel flow promotes early breakup and a wider cone angle.

An alternative explanation is that the hydroground nozzle may have undergone a hydraulic flip process, whereby a gaseous sheath forms around the fuel flow in the injector orifice, allowing a largely undisturbed jet to flow from the injector. This behavior has been seen in previous experiments using axial injector nozzles [25]. However, the decreased cavitation caused by the rounded contours of the hydroground nozzle would not be expected to favor hydraulic flip, which requires a great deal of cavitation to initiate. Thus, the authors believe that throttling effects inside the injector are the most likely cause for this transition.

The spray angle for both nozzles is largest at the end of the injection event. This increase in the cone angle at the end of the injection event is well known in the literature from optical measurements. In optical measurements, the cone angle increases at the end of the injection event by approximately 20–30% [7]. The change is much more dramatic for the X-ray radiography measurements. The cone angle increases by 36% for the nonhydroground nozzle and by a factor of approximately 6 for the hydroground nozzle between 1068 μs and 1215 μs after SOI. It seems that the spray periphery, which defines the optical cone angle, does not necessarily reflect changes in the mass distribution in the core of the spray with great fidelity.

The area under the Gaussian fits provides another useful analysis tool. This area represents the integral of the projected density in a slice across the spray and will be referred to as the "transverse integrated mass" (TIM), in units of μg/mm. It gives a measure of the amount of fuel per millimeter along the spray axis at particular axial location.

Figure 12 shows the TIM at the same times as in Figs. 3–5 for the short-duration spray from the nonhydroground nozzle; the plots for the hydroground nozzle are qualitatively similar. These plots illustrate the distribution of fuel in the axial direction at a given time after SOI. While only three plots are shown, the plots for various times smoothly transition between the shapes shown in Fig. 12. Early in the spray, the fuel is distributed within the first 4 mm from the nozzle. The maximum TIM is located about 3 mm from the nozzle, near the spray leading edge. The peak in the TIM represents the concentrated structure seen near the leading edge of the spray.

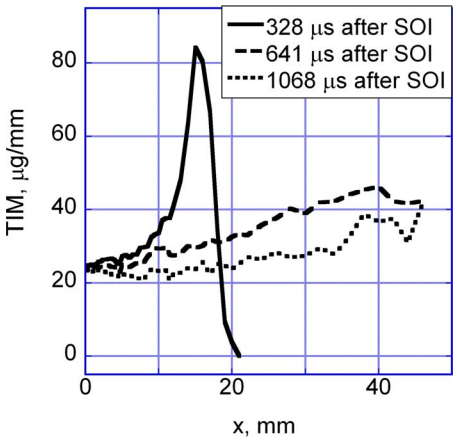

Fig. 13 TIM for the long-duration spray from the hydroground nozzle at selected times after SOI. Lines connecting the data are guides for the eye.

From shortly after SOI to approximately 150 μs after SOI, the qualitative shape of the TIM plot is quite similar to the plot for 77 μs after SOI shown in Fig. 12. The TIM value at the nozzle remains relatively constant as time progresses, the TIM smoothly increases from this value to a peak value near the spray leading edge, and the TIM sharply decreases at the spray leading edge. The peak value of the TIM increases markedly with time, indicating that mass accumulates in the leading-edge structure as the spray progresses. After approximately 150 μs after SOI, the TIM near the nozzle rapidly decreases with time, indicating that the injector is closing. The plots of TIM versus x evolve to take the form shown at 206 μs after SOI. At later times, the leading-edge structure begins to dissipate, as seen at 365 μs after SOI. The TIM values upstream also decrease as the spray dissipates.

The behavior of the TIM is somewhat different for the long-duration sprays, as shown in Fig. 13 for the spray from the hydroground nozzle. (The behavior of the TIM for the nonhydroground nozzle is similar.) In the initial stages of the spray, the TIM plot is very similar to what is seen in the short-duration sprays. After the leading-edge structure leaves the measurement domain, the TIM is largely linear with a slight positive slope. This behavior seems reasonable, since in a steady, fully developed jet, the axial flow rate is uniform in the x direction. Since the jet fluid decelerates as it moves downstream, the TIM must increase to maintain the uniform axial flow rate. The TIM values after the transition of the spray from wide to narrow are lower than those before the transition. In addition, the plot becomes flatter, which suggests that the axial velocity of the jet as a function of axial location may be more uniform after the transition.

A traditional measure of spray behavior is the speed at which the leading edge of the spray penetrates into the ambient gas. Figure 14(a) shows the position of the leading edge of the spray as a function of time after SOI for all four sprays. The spray leading edge is defined as being located at a slice once the TIM for that slice reaches 10% of the peak value for that slice. While this threshold is somewhat arbitrary, it matches the visual appearance of the projected density distributions in Figs. 3–8 quite well, and the rate at which the TIM rises as a function of time near the leading edge is so steep that the penetration versus time values are insensitive to the precise value of the threshold. To obtain the penetration speed, a fourth-order polynomial has been fitted to these data and differentiated analytically. The fits to the penetration data are generally quite accurate; the standard deviation of the residuals of the fit is approximately 0.12 mm. Except near the ends of the data record, the standard deviation in the derived penetration speed estimate is less than 5 m/s. The results are shown in Fig. 14(b). Several trends are evident in this plot. The penetration speed increases as the spray moves downstream for all cases early in the injection event. For the long-duration sprays, the spray from the nonhydroground nozzle penetrates considerably faster than the spray from the hydroground nozzle early in the spray. However, the penetration speed for both of these sprays shows the same trend subsequent to 200 μs after SOI. The higher penetration speed early in the injection event for the nonhydroground nozzle is consistent with other analysis, which shows that the injection velocity for the nonhydroground nozzle is somewhat greater than that for the hydroground nozzle early in the injection event [26].

The short-duration spray from the nonhydroground nozzle penetrates considerably slower than either of the long-duration sprays early in the spray. The short-duration spray from the hydroground nozzle, however, penetrates nearly as quickly as the long-duration spray from the nonhydroground nozzle early in the spray, with a penetration speed of roughly 100 m/s at 400 μs after SOI. The authors hypothesize that the longer breaking current duration for this injection caused the injector to open more quickly and fully than for the spray from the nonhydroground nozzle. A more rapid opening of the injector should lead to an increased pressure at the nozzle inlet, resulting in increased injection velocity, and thus a faster penetration speed. Indeed, further analysis shows significant differences in the injection velocity behavior for the two short-duration sprays which are consistent with this hypothesis [26].

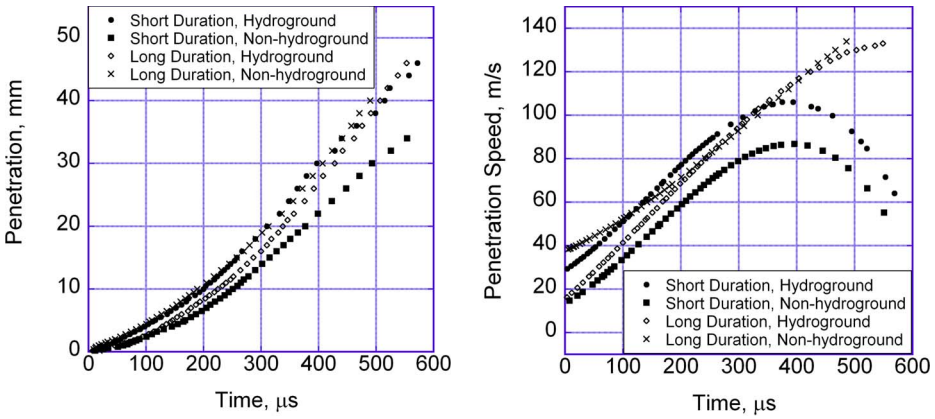

(a) (b)

Fig. 14 Spray leading-edge penetration: (a) spray leading-edge position versus time; (b) spray leading-edge speed vesus time

For both short-duration sprays, the penetration speed reaches a peak value around 400 μs after SOI and thereafter begins to decrease. This behavior follows the authors' expectations, since late in the spray event, the injectors are closed. Unlike the long-duration sprays, these short-duration sprays are no longer supplied with high-momentum fuel. As the spray loses momentum to the ambient gas, it is expected to slow down. The penetration speeds in this study are significantly lower than the penetration speeds seen in previous radiography studies of sprays at 500 bar injection pressure [18]. This is also expected, since lower injection pressure results in a lower penetration speed.

It should be noted that the current spray penetration data show increasing spray leading-edge velocity as the spray moves downstream. This is at odds with previous penetration correlations in the literature [7,11], which show constant penetration speed up to a characteristic penetration length, after which the penetration speed decreases. There are two reasons for this discrepancy. First, traditional correlations ignore the finite time required for the injector to open. Indeed, close examination of Figs. 11 and 16 of Ref. [7] show acceleration of the spray leading edge near the SOI. These effects are especially pronounced in the current study; several hundred microseconds are required for the injection velocity to approach the steady-state value [26]. Given that the injection velocity slowly increases, it is expected that the leading-edge speed would also accelerate. Moreover, according to the accepted spray correlations, the decelerating effects of the ambient gas are not felt across much of the spray domain in the current measurements. If one uses the accepted parameterization given in Ref. [7] and assumes typical values for the optical spray cone angle (20 deg) and flow diameter (183 μm for the hydroground nozzle), the characteristic penetration length is 44 mm, which is near the downstream end of the measurement domain for all of the sprays. Thus, without the injector opening effects described above, one would expect linear penetration versus time curves. When the injector opening effects are included, it is not surprising that the penetration speed accelerates for the long-duration sprays, even though this result is contrary to the accepted correlations.

A unique capability of the X-ray measurements is the ability to track not only the leading edge of the spray but also the trailing edge. Tracking the trailing edge is more difficult, however, because the trailing edge is much more diffuse than the leading edge. A direct method to find the time at which the trailing edge passes through a particular slice is to examine the projected density versus time on the spray axis and fit an appropriate function to the decline in the projected density due to the trailing edge. This method, termed edge detection in this work, has been used in previous X-ray radiographic spray measurements [18]. There are some disadvantages to this method, however. Changes in the cone angle will cause the projected density seen at a point on the spray axis to change even if the TIM for the slice remains constant. Also, the orientation of the spray axis can shift during the spray event, making it difficult to define the point whose projected density versus time data should be used to define the trailing edge.

An alternative technique to determine the trailing-edge speed uses the TIM. For each axial slice, the time-averaged TIM is calculated using all times for which a significant amount of fuel can be found in that slice. The trailing edge is considered to arrive at a particular slice when the TIM for that location decreases below 50% of the slice's time-averaged TIM. The technique is more easily automated than the edge-detection method and is insensitive to shifts in the spray axis or cone angle. Figure 15 shows a comparison between these two methods for the long-duration sprays. The plot shows that the results using the TIM-based method are smoother. While there is a time shift between the trailing-edge times found with the two methods, the slopes of the curves using the two methods are quite similar, indicating that both methods yield similar trailing-edge speeds. Given the advantages of smoothness, insensitivity to changes in the spray targeting and cone angle, and the ease of automation, for the remainder of this paper the trailing-edge speed is calculated using the TIM-based method.

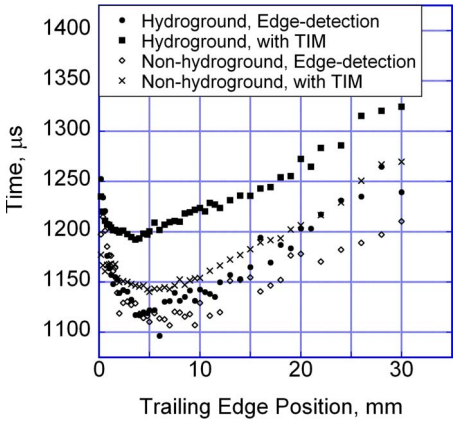

Fig. 15 Comparison of edge-detection and TIM-based methods for locating trailing edge for the long-duration sprays

Figure 16 shows the trailing-edge results for all four spray events. As the injector closes, the region close to the nozzle contains a great deal of slowly moving fluid, as seen in other experiments [27]. This makes the definition and detection of the trailing edge of the spray problematic in this region, so the data for $x < 10$ mm is omitted. The signal-to-noise ratio is also quite low near the downstream edge of the measurement domain, so data for $x > 30$ mm are also omitted.

To find the average speed of the trailing edge, linear fits have been performed for the region 10 mm $\leq x \leq$ 30 mm to determine the trailing-edge speed for all four sprays; the results of this analysis are shown in Table 3. Both of the short-duration injections show similar trailing-edge speeds of roughly 40 m/s near the end of the measurement grid, which is significantly slower than the penetration speed. The trailing edge moves at around 170 m/s in the long-duration injections, which is significantly faster than the

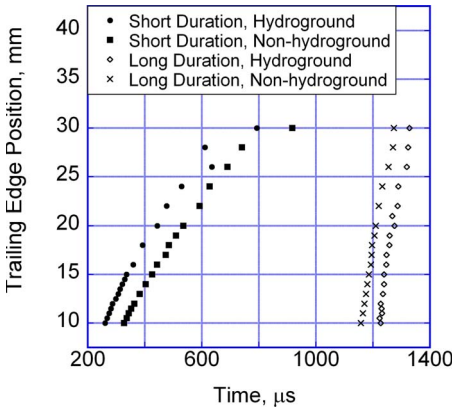

Fig. 16 Trailing-edge position versus time

Table 3 Trailing-edge speed

	Trailing-edge speed, m/s	
Spray duration	Hydroground	Nonhydroground
400 μs	41 ± 4	38 ± 4
1000 μs	176 ± 18	169 ± 11

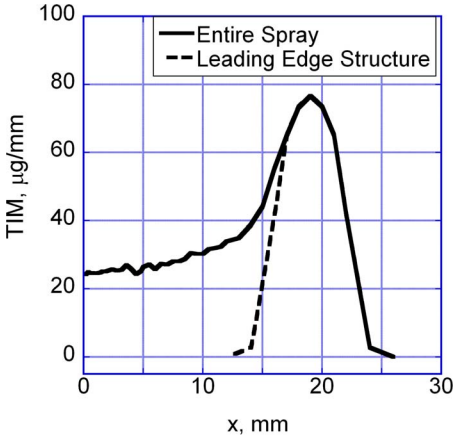

Fig. 17 Method for spray partitioning

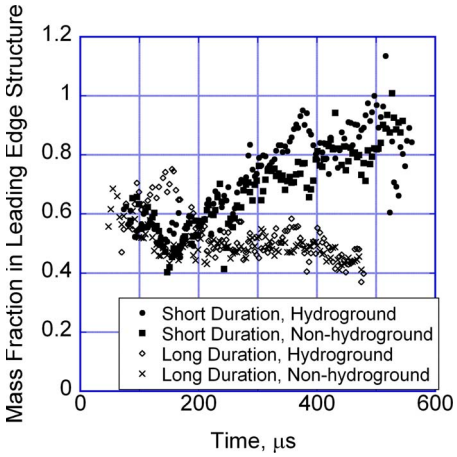

Fig. 18 Fraction of the fuel mass located in the leading-edge structure versus time

penetration speed. For both spray durations, the difference between the trailing edge speeds for the different nozzle geometries is not statistically significant.

Compared to previous X-ray radiography measurements of trailing-edge speed [18], these trailing-edge speed values are quite low. There are several reasons for this difference. First, the injection pressure is only half of that used in Ref. [18]; if the trailing-edge speed scales as the Bernoulli speed (i.e., as the square root of the pressure difference across the orifice [6]), the speeds in this study would be expected to be around 70% of the values seen in Ref. [18]. The higher injection pressure used in Ref. [18] may also cause the needle to lift more fully, resulting in an even greater increase in spray velocity, and by extension trailing edge speed. In addition, the measurements in Ref. [18] were taken only for $x < 15$ mm and used the edge-detection method. As stated previously, it appears that the finite time period required for the injector to close makes it difficult to define the trailing edge so close to the injector orifice.

As the two-dimensional plots of the projected mass density show, the leading edge of the spray contains a structure of concentrated fuel. The leading-edge structure may have an important influence on how fuel sprays mix with their surroundings, especially for short-duration injections. Thus, it is desirable to determine the total quantity of fuel in the leading-edge structure and its fraction of the total mass. To quantify the amount of fuel in this leading-edge structure, the flow field is partitioned in software using a strategy based on the TIM. For every time step until the leading edge reaches the edge of the measurement domain, the slice with the maximum TIM is located. Except for very early in the spray, this location corresponds to the location of the center of the leading-edge structure. All of the mass downstream of this point is assumed to be part of the leading-edge structure. Mass upstream of the center of the leading-edge structure, however, will be mixed with trailing jet fluid. To define the amount of mass in the leading-edge structure, the leading-edge structure is assumed to be mirror symmetric about the peak TIM position. The mass upstream of the peak TIM is determined and this value is doubled to yield the total mass of the leading-edge structure. The method is illustrated in Fig. 17. Tests of the procedure have shown that the results match the appearance of the two-dimensional radiography data (i.e., Figs. 3–8) quite well.

The results of this analysis are shown in Fig. 18. The analysis is only performed until the spray leading edge reaches the downstream end of the measurement domain. All of the sprays initially have roughly 60% of the fuel residing in the leading-edge structure. While nozzle geometry does not seem to significantly affect these results, the spray duration has a large effect. The fraction of the fuel residing in the leading-edge structure slowly decreases and levels off at approximately 50% for the long-duration sprays. For the short-duration sprays, the fraction of fuel in the leading-edge structure increases as the spray develops, reaching roughly 80% as the leading edge reaches the downstream edge of the measurement domain. It appears that for the short-duration sprays, the vast majority of the spray mass collects in the leading-edge structure. Conversely, for the long-duration sprays, the injector continues to supply mass to the trailing jet, and the fraction of mass in the leading-edge structure does not significantly exceed 50% of the total near the end of the data record.

Discussion

The preceding data provide important insights into diesel spray behavior. Both injection duration and nozzle hydrogrinding have important effects on the mass distribution of the spray. Short-duration injections produce relatively slow-moving sprays with pronounced leading-edge structures. Long-duration injections have a concentrated jet extending from the nozzle to the leading-edge structure. Nozzle hydrogrinding seems to make little difference in the mass distribution of the short-duration injection sprays. For the long-duration injections, the nonhydroground nozzle produced a stable spray with a moderate cone angle. On the other hand, the hydroground nozzle produced a wide spray that transitioned into a narrow spray as the spray reached steady state.

The existence of this leading-edge structure has important implications for the analysis of diesel sprays. Even after the spray tip has penetrated tens of millimeters into the ambient gas, a majority of the spray mass in all of these sprays resides in the leading-edge structure. An accurate model of spray plume combustion and mixing must take into account that a large fraction of the fuel in these sprays resides, not in a thin, spreading jet, but in a concentrated, rounded structure. It should be reiterated, however, that the spray structure under the current nonvaporizing conditions may not be representative of the spray structure under vaporizing conditions.

There are two particularly important implications of the existence of this leading-edge structure. First, the existence of a highly concentrated parcel of fluid at the leading edge of the spray may make it more likely that liquid fuel would impact the piston surface in an engine. On the other hand, the penetration speed of these short-duration injections is lower than that of the long-duration injections. In addition, pilot injection is a popular method to reduce combustion noise and soot emissions from diesel engines. These data show that short-duration injections induce particularly pronounced leading-edge structures. Understanding the mixing and combustion behavior of such structures is thus especially important to better understand the behavior of pilot injec-

tion. More study is needed to determine whether such leading-edge structures remain important at density values more representative of engine cylinder conditions.

Another question regards the character of this concentrated leading-edge structure. The fluid dynamics literature reports that a head vortex will form at the leading edge of an impulsively started jet [28]. The appearance of the spray in Figs. 3–8 is similar to that of impulsively started jets in the literature. Without measurements of the velocity vectors of individual parcels of fluid, however, the authors cannot conclusively prove the existence of a head vortex. Also, the head vortex in impulsively started laminar jets penetrates into the surrounding fluid at about $\frac{1}{2}$ of the steady-state jet velocity at that location [29]. The velocity of the fluid in these sprays is unknown; few reliable spray velocity measurements are available in the high-density region probed in this experiment. Recent transient velocity measurements in these sprays indicate injection velocities of 150–200 m/s for the long-duration sprays when the spray tip is near the end of the measurement domain [26]. Thus, the penetration speed values of 80–130 m/s are consistent with the behavior of a head vortex. Moreover, previous laser Doppler velocimetry data of the ambient gas surrounding a diesel spray suggest rotational flow in the ambient gas around the head of the diesel spray [11]. While not entirely conclusive, these data all suggest that a head vortex exists at the tip of these diesel sprays. Further research is needed to investigate how changes in injection pressure and density ratio between the jet fluid and the ambient gas affect the formation and development of this head vortex.

These data also illustrate the limitation of measurements of steady-state sprays in describing the behavior of diesel injectors. In an engine operating at 3000 rpm, each crank angle represents a time span of only 56 μs. The injection duration is on the order of a millisecond or less in duration. As shown by the data in this work, transient effects, such as the propagation of the leading-edge structure and the transition in the behavior of the long-duration spray from the hydroground nozzle, significantly impact the mass distribution in the sprays. This is expected to have a direct impact on the mixing and combustion of the fuel in applied injectors. Moreover, recent trends toward using more numerous, shorter injection events in diesel engines may make the understanding of these transient events more important. On the other hand, the use of a higher injection pressure might accelerate the development of the spray and reduce the time period for which these transient effects are important. Nevertheless, the study of steady-state spray behavior gives at best an incomplete depiction of the phenomena acting in diesel sprays.

Conclusions

The behavior of four fuel sprays from commercial common-rail diesel injectors has been examined with X-ray radiography, which provides quantitative measurements of the injected-fluid distribution in the spray. The spray structure generally consists of a thin jet terminated by a concentrated leading-edge structure. Long-duration injection with a hydroground nozzle yielded a spray that, while initially quite wide, transitioned into a very narrow jet. The nonhydroground nozzle, on the other hand, showed no such transition. Penetration speed measurements were significantly higher for long- than short-duration injections. The penetration speed for all positions, however, was significantly lower than the theoretical Bernoulli exit velocity of sprays from the injector orifice. The trailing-edge speed was significantly higher than the leading-edge penetration speed for the long-duration injections, but slower for the short-duration injections. Analysis of the amount of fuel in the leading-edge structure showed that for times where the spray was within the measurement domain a majority of the fuel resided in this structure for all of the injections, with a particularly large fraction seen in the short-duration injections after the spray event had ended. The appearance of the leading-edge structure suggests that it may be a head vortex, though the present data cannot prove this hypothesis.

Acknowledgment

This research was performed at the 1-BM-C beamline of the Advanced Photon Source, Argonne National Laboratory. This work and the use of the APS are supported by the U. S. Department of Energy under Contract No. DE-AC02-06CH11357 and by the Department of Energy Vehicle Technologies Program, with Gurpreet Singh as a team leader.

References

[1] Tow, T. C., Pierpont, D. A., and Reitz, R. D., 1994, "Reducing Particulate and NOx Emissions by Using Multiple Injections in a Heavy Duty Diesel Engine," SAE Paper No. 940897.
[2] Han, Z., Uludogan, A., Hampson, G., and Reitz, R., 1996, "Mechanism of Soot and NOx Emission Reduction Using Multiple-Injection in a Diesel Engine," SAE Paper No. 960633.
[3] Qin, J.-R., Dan, T., Lai, M.-C., Savonen, C., Schwartz, E., and Brkyzik, W., 1999, "Correlating the Diesel Spray Behavior to Nozzle Design," SAE Paper No. 1999-01-3555.
[4] Kampmann, S., Dittus, B., Mattes, P., and Kirner, M., 1996, "The Influence of Hydro Grinding at VCO Nozzles on the Mixture Preparation in a DI Diesel Engine," SAE Paper No. 960867.
[5] Hoffmann, J., Khatri, F., Martin, J., and Coates, S., 1998, "Mass-Related Properties of Atomizers for Direct-Injection SI Engines," SAE Paper No. 980500.
[6] Desantes, J., Payri, R., Salvador, F. J., and Gimeno, J., 2003, "Measurements of Spray Momentum for the Study of Cavitation in Diesel Injection Nozzles," SAE Paper No. 2003-01-0703.
[7] Naber, J., and Siebers, D., 1996, "Effects of Gas Density and Vaporization on Penetration and Dispersion of Diesel Sprays," SAE Paper No. 960034.
[8] Chang, C., and Farrell, P., 1997, "A Study on the Effects of Fuel Viscosity and Nozzle Geometry on High Injection Pressure Diesel Spray Characteristics," SAE Paper No. 970353.
[9] Blessing, M., König, G., Krüger, C., Michels, U., and Schwarz, V., 2003, "Analysis of Flow and Cavitation Phenomena in Diesel Injection Nozzles and Its Effects on Spray and Mixture Formation," SAE Paper No. 2003-01-1358.
[10] Siebers, D., 1998, "Liquid-Phase Fuel Penetration in Diesel Sprays," SAE Paper No. 980809.
[11] Araneo, L., Coghe, A., Brunello, G., and Cossali, G. E., 1999, "Experimental Investigation of Gas Density Effects on Diesel Spray Penetration and Entrainment," SAE Paper No. 1999-01-0525.
[12] Sick, V., and Stojkovic, B., 2001, "Attenuation Effects on Imaging Diagnostics of Hollow-Cone Sprays," Appl. Opt., **40**(15), pp. 2435–2442.
[13] Bruneaux, G., Verhoeven, D., and Baritaud, T., 1999, "High-Pressure Diesel Spray and Combustion Visualization in a Transparent Model Diesel Engine," SAE Paper No. 1999-01-3648.
[14] Smallwood, G., and Gülder, O., 2000, "View on the Structure of Transient Diesel Sprays," Atomization Sprays, **10**, pp. 355–386.
[15] Linne, M., Paciaroni, M., Hall, T., Walters, E. B., and Parker, T., 2005, "The Structure of the Very Near Field for a Diesel Spray: Results From a Ballistic Imaging Study," *18th Annual Conference on Liquid Atomization and Spray Systems*, Irvine, CA.
[16] Powell, C. F., Ciatti, S. A., Cheong, S.-K., Liu, J., and Wang, J., 2004, "X-Ray Absorption Measurements of Diesel Sprays and the Effects of Nozzle Geometry," SAE Paper No. 2004-01-2011.
[17] Yue, Y., Powell, C. F., Poola, R., Wang, J., and Schaller, J., 2001, "Quantitative Measurements of Diesel Fuel Spray Characteristics in the Near-Nozzle Region Using X-Ray Absorption," Atomization Sprays, **11**, pp. 471–490.
[18] Cheong, S.-K., Liu, J., Shu, D., Wang, J., and Powell, C. F., 2004, "Effect of Ambient Pressure on Dynamics of Near-Nozzle Diesel Sprays Studied by Ultrafast X-Radiography," SAE Paper No. 2004-01-2026.
[19] Cai, W., Powell, C. F., Yue, Y., Narayanan, S., Wang, J., Tate, M., Renzi, M., Ercan, A., Fontes, E., and Gruner, S., 2003, "Quantitative Analysis of Highly Transient Fuel Sprays by Time-Resolved X-Radiography," Appl. Phys. Lett., **83**(8), pp. 1671–1673.
[20] Kastengren, A., and Powell, C. F., 2007, "Spray Density Measurements Using X-Ray Radiography," Proc. Inst. Mech. Eng., Part D (J. Automob. Eng.), **221**, pp. 653–662.
[21] Ohrn, T., Senser, D., and Lefebvre, A., 1991, "Geometrical Effects on Discharge Coefficients for Plain-Orifice Atomizers," Atomization Sprays, **1**(2), pp. 137–153.
[22] Kastengren, A., Powell, C. F., Wang, Y.-J., and Wang, J., 2007, "Study of Diesel Jet Variability Using Single-Shot X-Ray Radiography," *ASME Internal Combustion Engines Fall Conference*, Charleston, SC, Paper No. ICEF2007-1663.
[23] Pope, S., 2001, *Turbulent Flows*, Cambridge University Press, Cambridge.
[24] Su, T., Farrell, P., and Nagarajan, R., 1995, "Nozzle Effect on High Pressure Diesel Injection," SAE Paper No. 950083.
[25] Sotieriou, C., Andrews, R., and Smith, M., 1995, "Direct Injection Diesel

Sprays and the Effect of Cavitation and Hydraulic Flip on Atomization," SAE Paper No. 950080.
[26] Kastengren, A., Powell, C. F., Riedel, T., Cheong, S.-K., Wang, Y.-J., Im, K.-S., Liu, X., and Wang, J., 2007, "Improved Method to Determine Spray Axial Velocity Using X-Ray Radiography," *20th Annual Conference on Liquid Atomization and Spray Systems*, Chicago, IL.
[27] Lai, M.-C., Wang, T.-C., Xie, X., Han, J.-S., Henein, N., Schwarz, E., and Bryzik, W., 1998, "Microscopic Characterization of Diesel Sprays at VCO Nozzle Exit," SAE Paper No. 982542.
[28] Krueger, P., and Gharib, M., 2003, "The Significance of Vortex Ring Formation to the Impulse and Thrust of a Starting Jet," Phys. Fluids, **15**(5), pp. 1271–1281.
[29] Abramovich, S., and Solan, A., 1973, "The Initial Development of a Submerged Laminar Round Jet," J. Fluid Mech., **59**(4), pp. 791–801.

Numerical Analysis of Cavitation Instabilities in Inducer Blade Cascade

Benoît Pouffary
Centre National d'Etudes Spatiales,
Evry 91023, France

Regiane Fortes Patella
INPG-LEGI,
Grenoble 38041, Cedex 9, France

Jean-Luc Reboud
CNRS-LEMD,
University of Grenoble,
Grenoble 38042, France

Pierre-Alain Lambert
Snecma,
Vernon 27208, France

The cavitation behavior of a four-blade rocket engine turbopump inducer was simulated by the computational fluid dynamics (CFD) code FINE/TURBO™. The code was modified to take into account a cavitation model based on a homogeneous approach of cavitation, coupled with a barotropic state law for the liquid/vapor mixture. In the present study, the numerical model of unsteady cavitation was applied to a four-blade cascade drawn from the inducer geometry. Unsteady behavior of cavitation sheets attached to the inducer blade suction side depends on the flow rate and cavitation number σ. Numerical simulations of the transient evolution of cavitation on the blade cascade were performed for the nominal flow rate and different cavitation numbers, taking into account simultaneously the four blade-to-blade channels. Depending on the flow parameters, steady or unsteady behaviors spontaneously take place. In unsteady cases, subsynchronous or supersynchronous regimes were observed. Some mechanisms responsible for the development of these instabilities are proposed and discussed.
[DOI: 10.1115/1.2903823]

Introduction

One of the most prejudicial consequences of the cavitation in the rocket engine turbopump inducers is the generation of system and machinery instabilities. Machinery instabilities may appear for a particular range of the cavitation number, near to the performance drop. These unsteady phenomena are associated with different rotating nonsymmetrical cavitation patterns, which are characterized by sub- or supersynchronous frequencies.

Cavitation instabilities lead to downstream and upstream pressure fluctuations, which may be at the origin of system instabilities. They induce also axial and radial forces on the blades and shaft, which can disturb the bearings working and endanger the turbopump running.

For these reasons, inducer cavitation instabilities have been studied for many years in the aim of observing, better understanding, quantifying, and predicting such phenomena. Extensive studies have been carried out mainly from the viewpoint of system instability [1–3]. Several experimental works have been performed to visualize global cavitation patterns and to measure the radial loads on the shaft due to cavitation instabilities [4–8]. More recently, theoretical and numerical models have been developed to predict these instabilities and to analyze their origin [9–15].

In spite of those relevant works, more detailed cavitating flow analyses are needed for the understanding of local cavitation instabilities.

Through collaborations between the laboratory LEGI-Laboratoire des Ecoulements Géophysiques et Industriels, the Rocket Engine Division of Snecma, the French Space Agency CNES, and NUMECA International, a cavitation physical model was implemented in the commercial code FINE/TURBO™. The code allows steady and unsteady cavitating flows calculations in two-dimensional (2D) or three-dimensional (3D) geometries, as presented in Refs. [16–20], and it can be used as a tool to analyze inducer instabilities.

In this context, and in complement to previous work [13,14], the main target of the present study is to propose a qualitative analysis of cavitation instabilities. The presented analyses are based on some numerical results obtained with the unsteady numerical code in a blade cascade geometry, derived from a 3D inducer. Subsynchronous and supersynchronous cavitation regimes have been simulated and analyzed. This paper illustrates numerical results obtained and proposes qualitative analyses of mechanisms responsible for these instability phenomena.

Models

The applied numerical code solves the conservative unsteady Reynolds-averaged Navier-Stokes (RANS) equations of a homogeneous fluid [16–21]. In the present study, the Spalart–Allmaras model was used to simulate turbulent behavior [22].

Associated with these basic equations, the barotropic state law proposed by Delannoy and Kueny [23] was implemented in the code to model mass transfer in cavitating flows. This simple model involves in the hypotheses of instantaneous vaporization and condensation phenomena, as well as the no-slip condition between liquid and vapor phases. It does not take into account thermal effects, i.e., the energy equation is not considered in the calculation. The liquid-vapor mixture is characterized by a mixture specific mass ρ given as a function of void ratio α, by the relation $\rho = \alpha\rho_v + (1-\alpha)\rho_l$.

This barotropic law depends on the minimum speed of sound, $c_{\min}$, in the mixture and on the value of the density ratio, ρ_v/ρ_l, as illustrated in Figs. 1 and 2.

In the present study, the Reynolds number is in the order of 10^6. The value of the minimum speed of sound $c_{\min}$ is taken equal to 4.7 m/s, which is higher than the values used in our numerical previous works concerning cavitating flows in a Venturi apparatus [24]. The density ratio ρ_v/ρ_l is imposed to be 0.1. These choices were made to improve the robustness of these first feasibility computations with FINE/TURBO™ code.

For the same blade cascade geometry considered in the present work, some numerical tests were carried out in a previous work to evaluate the influence of the speed of sound $c_{\min}$, the Reynolds number, and the used time step and mesh on the cavitation instability pattern. Most important results obtained from these influence analyses are described in Ref. [13].

Regardless of considered hypotheses, previous studies [24–27] pointed out that the barotropic approach can succeed to quantita-

Contributed by the Fluids Engineering Division of ASME for publication in the JOURNAL OF FLUIDS ENGINEERING. Manuscript received September 8, 2005; final manuscript received October 3, 2007; published online April 7, 2008. Assoc. Editor: Yoshinobu Tsujimoto.

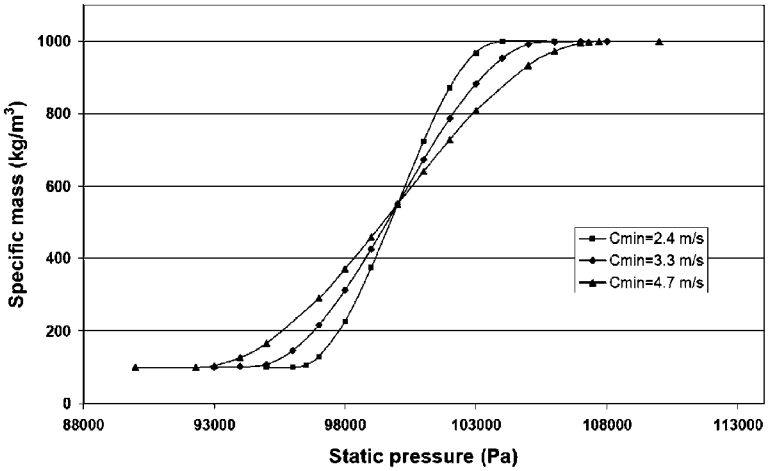

Fig. 1 Scheme of the barotropic state law $\rho=\rho(P)$. Illustration of the speed of sound influence.

tive and qualitative predictions of cavitating flow global parameters (i.e., characteristic frequencies, vapor structure size, and pump performance) as well as mean local parameters (void ratio and velocity distribution).

These physical models have been implemented in the code FINE/TURBO™ developed by NUMECA International. This three-dimensional structured mesh code solves the time dependent Reynolds-averaged Navier–Stokes equations. Time accurate resolutions use the dual time stepping approach proposed by Jameson [28]. Pseudotime derivative terms are added to the equations. They march the solution toward convergence at each physical time step.

This kind of resolution is devoted to highly compressible flows. In the case of low-compressible or incompressible flows, its efficiency decreases dramatically. This well-known problem has been addressed by many authors and solved by introducing a preconditioner [21]. This one is based on the studies presented in Refs. [29,30], and has been modified to take into account the cavitation model.

The discretization is based on a finite volume approach. We use a second order central scheme that must be associated with two artificial dissipation terms, respectively, of second and fourth orders as initially proposed by Jameson [28]. The first one is activated in the strong pressure and density gradient areas. The other one is used in the whole domain. The applied form of the artificial dissipation term leads to a central second order accurate convection scheme. The pseudotime integration is made by a four-step Runge–Kutta procedure.

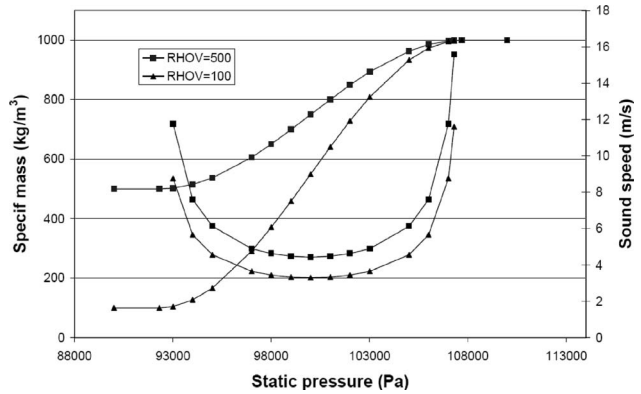

Fig. 2 Illustration of the ρ_v influence on the barotropic law $\rho=\rho(P)$ and on the speed of sound distribution

The physical time derivative terms are discretized with a second order backward difference scheme that ensures a second order accuracy in time.

A meaningful numerical work has been performed recently by Pouffary [17] to improve the preconditioner and the stability of numerical code for calculations of cavitating flows. A more detailed description of the code is given in Refs. [19–21]. Some influence tests of numerical parameters, including the effects of second and fourth order dissipation terms, are presented in Ref. [19].

Geometry and Mesh

An example of studied inducer geometry is given in Fig. 3. Because 3D unsteady calculations in inducer geometries are very time consuming, a 2D approached geometry was adopted (even if it cannot represent completely the original three-dimensional case).

The studied inducer was designed to operate, even at a nominal flow rate, with nonzero incidence angle. Nevertheless, in the range of running conditions, the angle of attack remains very small for the considered inducer geometry, because of the variable thread and the associated curvature of the blades. In these conditions, the inlet backflow is not relevant and a 2D geometry approach can be used for qualitative analyses. It is important to note that tip clearance and backflow effects are neglected and, consequently, the applicability of the approach proposed in this paper might be limited to high inducer flow rates.

Hence, computations are performed in a four-blade cascade derived from an entire inducer. The transformation from the 3D geometry to the 2D blade cascade leads us to neglect the peripheral cavitation in the inducer: Only cavitation sheets attached on

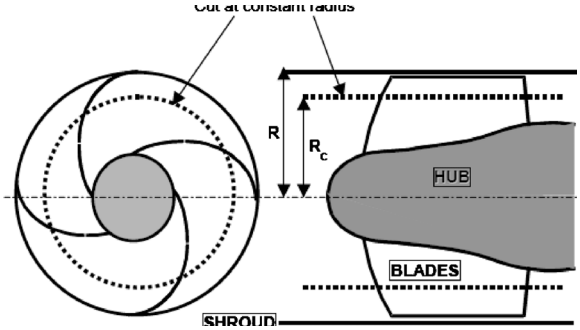

Fig. 3 Inducer 3D geometry—frontal and meridian planes

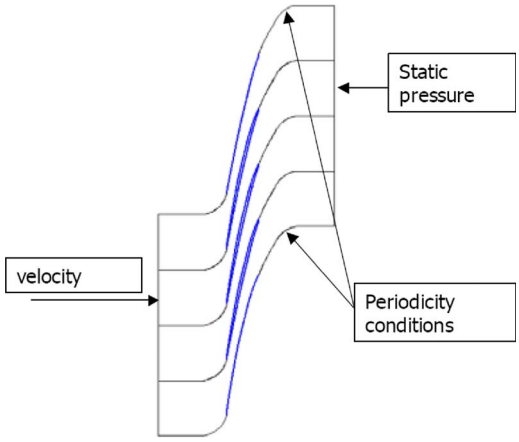

Fig. 4 Blade cascade corresponding to the cut at constant radius of the 3D inducer geometry. The mesh topology is *I*-type; calculations were carried out with 26,660 internal nodes corresponding to *y*+ values close to 10–20.

the blades will be considered. To obtain the 2D geometry, the 3D inducer (Fig. 3) is cut at a constant radius R_c equal to 70% of the tip radius R. The resulting shape of the blade cut in the plane $(R_c\theta, Z)$ is given in Fig. 4.

We use a 215×31 structured mesh per blade-to-blade channel, giving 26,660 internal nodes when calculating the four-blade cascade. The boundary conditions are imposed velocity at the mesh inlet, imposed static pressure at the outlet, and periodicity or connection conditions between the different channels of the blade cascade (Fig. 4). The distributions of the inflow velocity and the downstream pressure are uniform.

The time step, mesh, and turbulence model are chosen to put the attention on the low frequency fluctuations of the attached cavity, more than to the local unsteadiness in the cavitation sheet wake (cloud shedding).

Qualitative Results

Several four-channel computations are performed at the nominal flow rate, for different cavitation numbers σ (based on outlet reference pressure) varying from low cavitating conditions down to the final performance drop of the cascade. The corresponding head drop chart is drawn in Fig. 5 at a nominal flow rate.

Stable configurations correspond to cavitation numbers lower than 0.65 or higher than 0.8 (square dots in the figure). For $\sigma > 0.8$, cavitation sheets are small and identical on the four blades. For these flow conditions, the performance of the runner is only slightly affected by the presence of vapor. For $\sigma < 0.65$, the cavitation sheets are much more developed, and they are responsible for the important performance drop observed. The performance drop of the cascade is directly related to the evolution of the blade load illustrated in Fig. 6: The appearance of cavitation structures

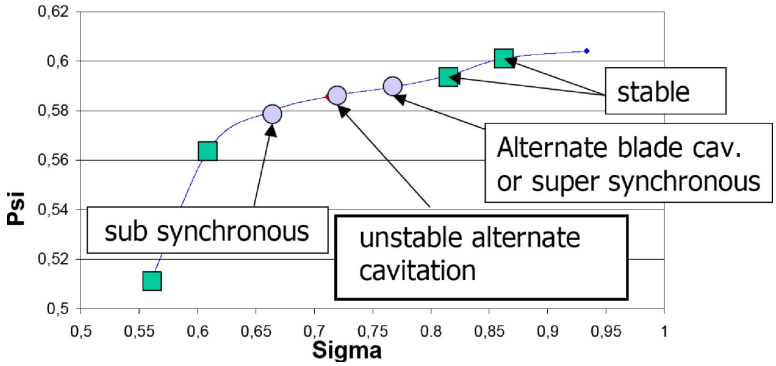

Fig. 5 Performance chart at a nominal flow rate. Static pressure coefficient ψ vs $\sigma_{downstream}$.

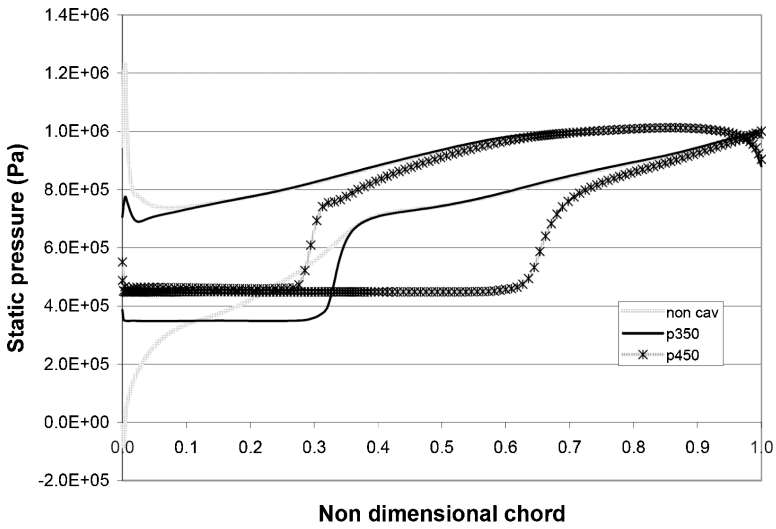

Fig. 6 Mean static load of the blade at midspan for three different cavitation numbers $\sigma_{downstream}$

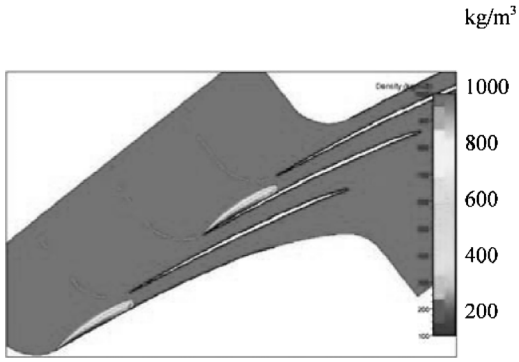

Fig. 7 Alternate blade cavitation ($\sigma \sim 0.75$). Density fields (kg/m³) calculated in the blade cascade.

at the pressure side of the blade leads to the decrease of the applied mechanical torque, and consequently to the performance drop.

Circular dots in Fig. 5 correspond to unsteady regimes and define the range of cavitation instabilities of the cascade. Three kinds of instabilities have been observed from our calculations: a supersynchronous behavior, a subsynchronous configuration, and an unstable alternate cavitation.

Calculations are done in relative referential: Sub- or supersynchronous configurations are determined by the unsteady visualization of the cavitation sheets. For example, if the nonsymmetrical cavitation sheet pattern rotates in the same direction as the inducer, the characteristic frequency of the instability is added to the inducer rotation frequency and a supersynchronous configuration is established. In another way, subsynchronous regimes are characterized by cavitation patterns that rotate in the opposite direction as the inducer.

Alternate Blade Cavitation. For $\sigma_{downstream} \sim 0.75$, two kinds of cavitation configurations have been observed. The first one is the alternate blade cavitation (Fig. 7). The system here is symmetrical, characterized by two radial opposite large vapor sheets and two opposite small ones.

For this cavitation number, the calculations pointed out also the appearance of another cavitation configuration, associated with a supersynchronous behavior.

Supersynchronous Configuration. Figure 8 illustrates this kind of instability. It is characterized by a nonsymmetrical rotating pattern of vapor sheets: We observe four different sizes of cavitation sheets in the four channels.

Calculations indicate that this cavitation pattern rotates in the blade cascade in the same direction as the inducer rotation, but more quickly.

Unstable Alternate Cavitation. For $\sigma_{downstream} \sim 0.7$, another type of alternate blade configuration has been observed. As illustrated in Fig. 9, for this cavitation number, the cavitation pattern is initially characterized by two opposite large sheets in Channels 1 and 3, separated by two channels without cavitation. During two periods of inducer rotation, this configuration shifts and the large vapor structures change to Channels 2 and 4.

This kind of configuration was studied in a previous work presented in Ref. [13].

Subsynchronous Configuration. For smaller cavitation numbers (~ 0.65), a subsynchronous configuration appears (Fig. 10). In this case, the cavitation pattern is not symmetrical: We observe four sheets of different sizes. The largest sheet occurring in Channel 3 obstructs the flow in this channel and leads to the increase of the cavitation sheet in the upper channel. This configuration rotates in the opposite direction as the inducer rotation.

Flow Qualitative Analyses

Based on the results presented here above, we propose in this paper a qualitative analysis of the mechanisms responsible for the instability phenomena observed.

Subsynchronous Configuration. According to our calculations, and by making an analogy with rotating stall phenomenon observed in compressor inlet [31], the subsynchronous configuration seems to be associated with the obstruction of a channel by the largest sheet, as schematized in Fig. 11. This obstruction deflects the flow and modifies the angle of attack of the neighboring upper channel, which leads to a pressure decrease and to the increase of the cavitation sheet size in this channel. Otherwise, as flow rate is imposed as a constant in the inducer, the flow angle of attack in the channel below the obstructed channel should decrease, which leads to the reduction of vapor structure size in this channel.

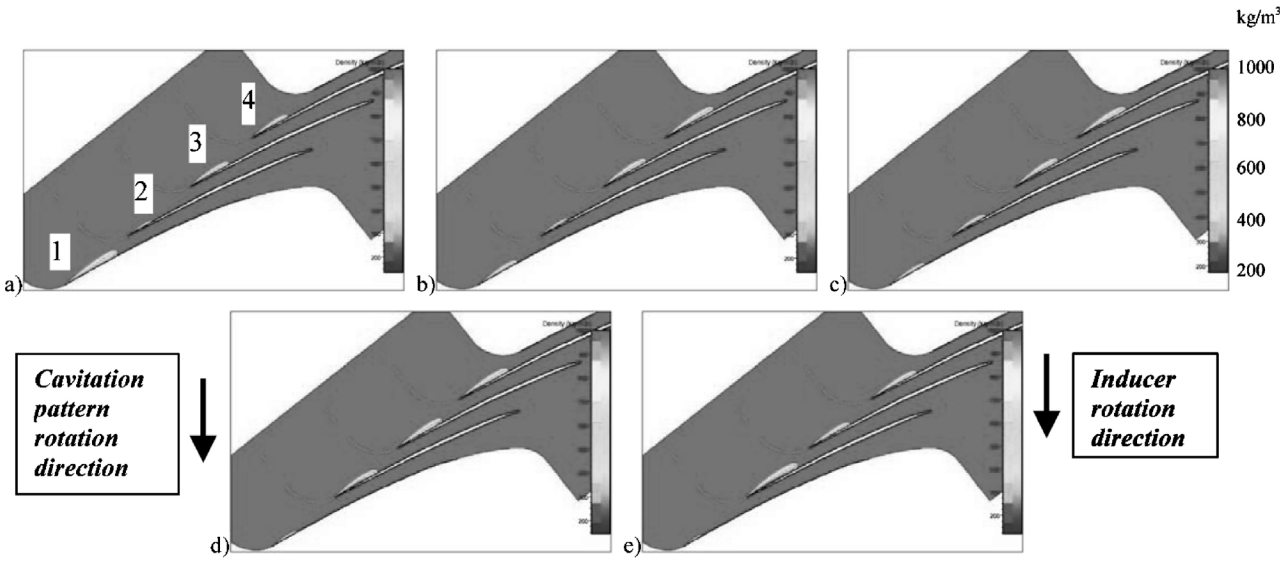

Fig. 8 Visualization, in the case of supersynchronous configuration, of the vapor structures (density fields) at five different times during a complete inducer rotation period

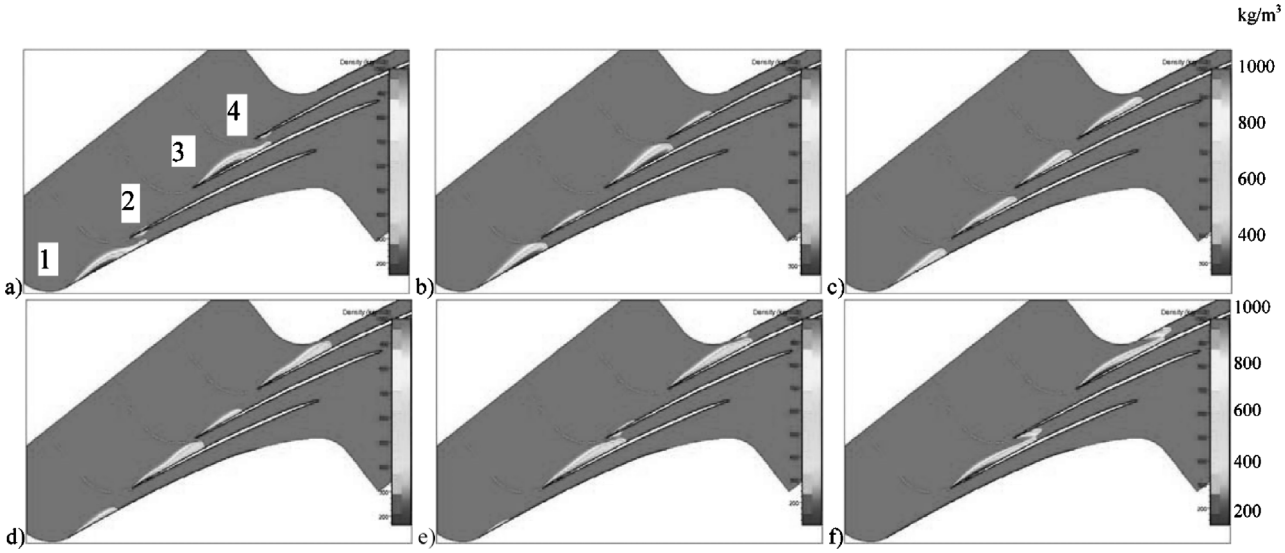

Fig. 9 Unstable alternate configuration: Figures illustrate density fields at six different times during approximately two inducer rotation periods

Hence, this kind of rotating cavitation configuration would be strongly coupled with the modification of the angle of attack due to the flow rate fluctuations in the channels.

Further works are needed to improve the comparison between cavitating subsynchronous configuration and rotating stall phenomena.

Supersynchronous Configuration. To identify and analyze the mechanism responsible for the supersynchronous instabilities, we will adopt the nomenclature introduced in Fig. 11.

First, we will study the time evolution of the inlet and outlet flow rates in each channel during an inducer rotation period (Fig. 12), as well as the corresponding transient evolution of the total pressure variation ΔP_{tot} (Fig. 13). The difference between outlet and inlet flow rates in a channel (Fig. 12) represents the variation of volume of the vapor structure in the channel. These results concern the unsteady cavitation pattern illustrated in Fig. 8.

These results point out the following.

— The rise of the cavitation sheet size in Channel 2 (between Blades 1 and 2) leads to a partial obstruction of this channel, which induces the mass flow rate decrease.
— As a consequence of the cavity length increase, we can observe the augmentation of total pressure variation in Channel 2. As a matter of fact, the cavitation sheet in Blade 1 does not reach the channel throat (i.e., the channel is not completely obstructed). The ΔP_{tot} (or blade load) increase is due to the rise of the angle of attack at Blade 1, which is associated with the flow rate decrease in Channel 2.
— During the rotation of the small sheet from Channel 2 to Channel 1, the flow rates and ΔP_{tot} in Channels 3 and 4 are slightly modified.

Contrarily to the subsynchronous configuration, the propagation

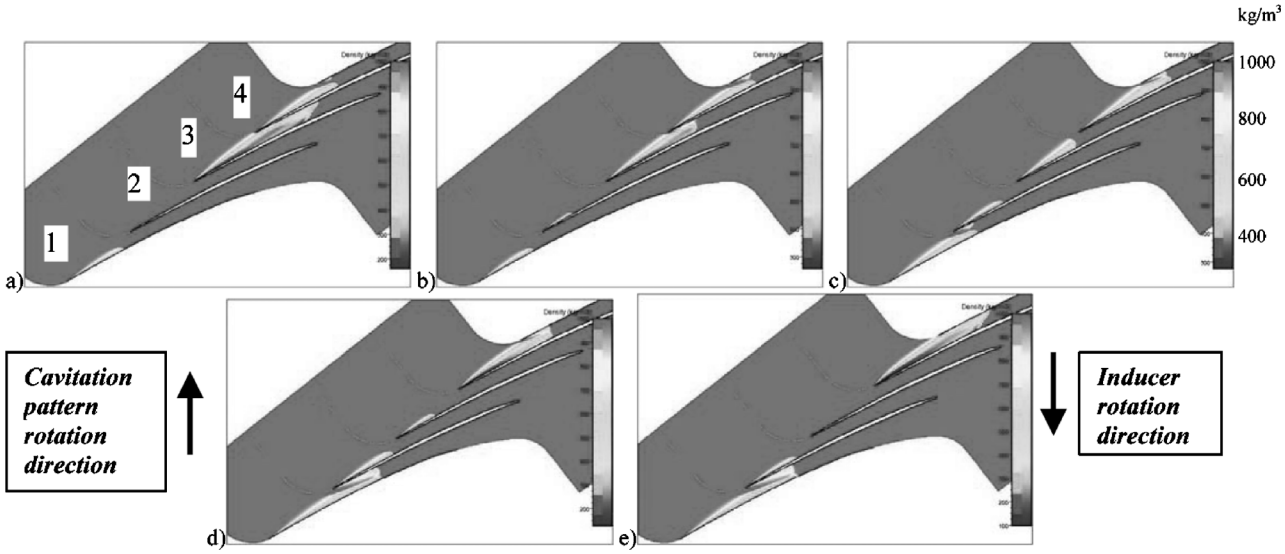

Fig. 10 Visualization, in the case of subsynchronous configuration, of the vapor structures (density fields) at five different times during a complete inducer rotation period

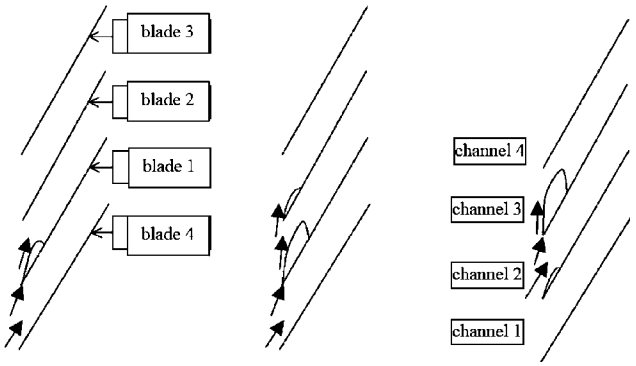

Fig. 11 Illustration of the propagation of the largest sheet in the case of subsynchronous configuration

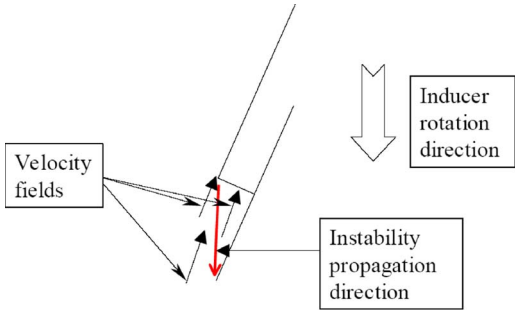

Fig. 14 Scheme of the flow velocity, instability propagation, and inducer rotation directions

of the supersynchronous instability seems not to be related only to the inlet flow velocity fields. Indeed, the instability moves in the opposite direction as the velocity fields, as schematized in Fig. 14.

Hence, we think that the mechanism responsible for this kind of instability should be related mainly to the pressure field in the blade cascade. To study pressure fields, Fig. 15 illustrates the time evolution of the blade loads during the propagation of supersynchronous instability for a complete inducer rotation period (corresponding to Fig. 8).

In agreement with the flow rates and ΔP_{tot} time evolution analyses, we note that the loads of Blades 2 and 3 are slightly modified. Concerning Blade 2 (Fig. 15(*a*)) the pressure along the blade pressure side decreases during the development of the cavi-

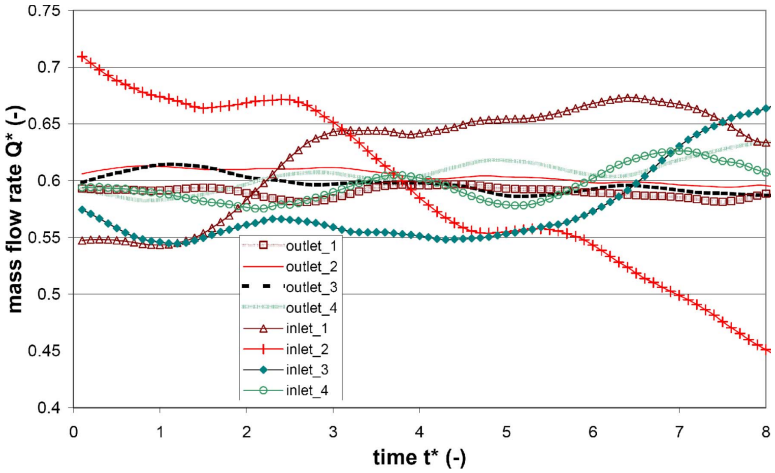

Fig. 12 Time evolution of the nondimensional mass flow rate in the four channels (σ=0.75; supersynchronous configuration). The lines represent the outlet and inlet flow rates in Channels 1–4.

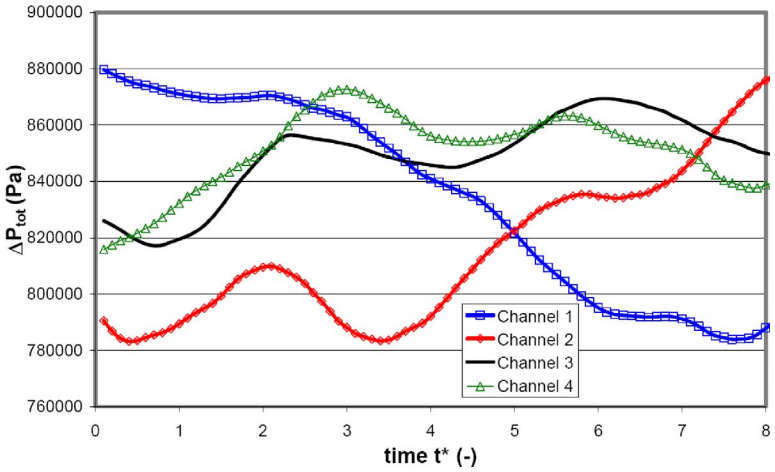

Fig. 13 Time evolution of the total pressure variation ΔP_{tot} for each channel. $\Delta P_{tot} = P_{downstream} - P_{upstream}$. Channels 1–4.

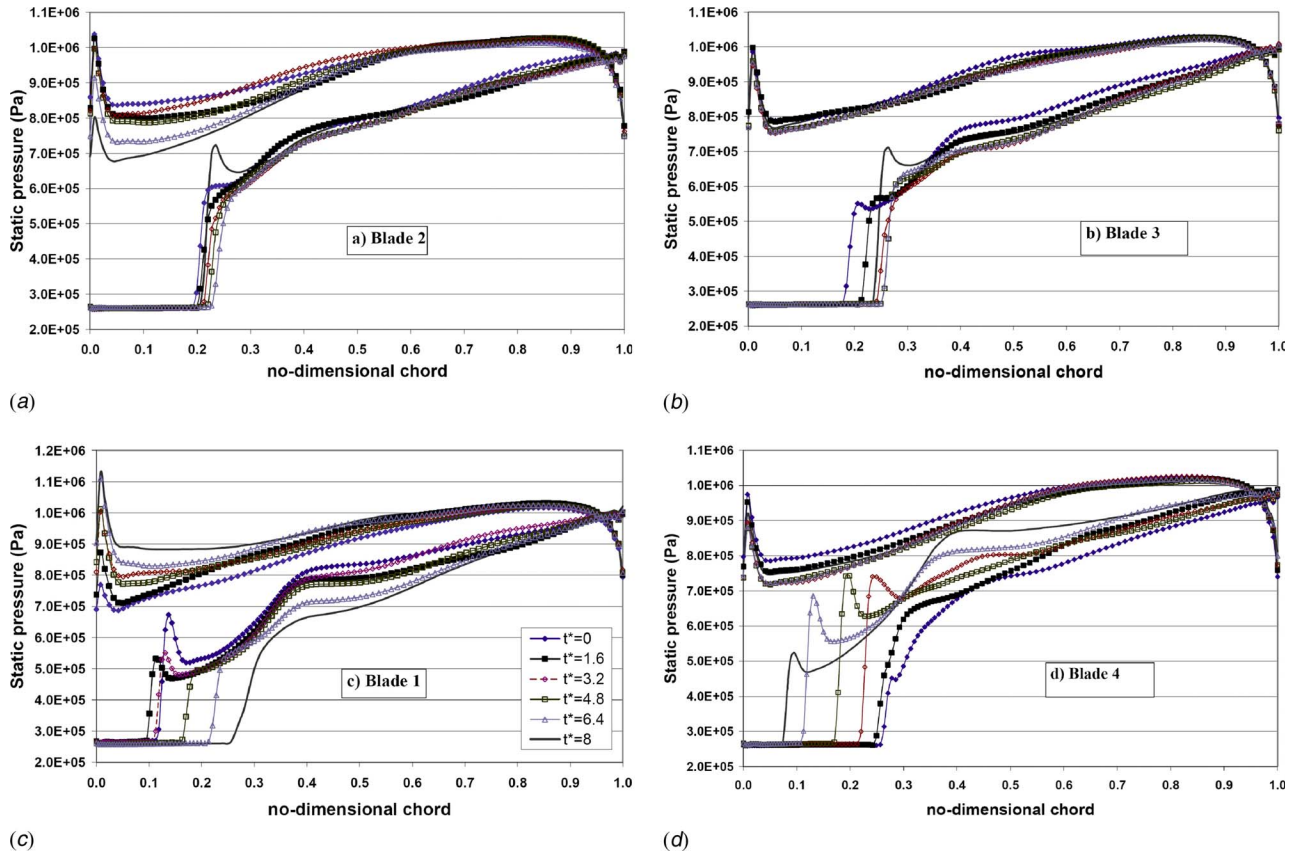

Fig. 15 Time evolution of the blade loads in the supersynchronous configuration

tation sheet in Channel 2. The load of Blade 3 (Fig. 15(*b*)) is slightly modified at the blade suction side (probably due to the decrease of the cavitation sheet in Channel 1).

The loads concerning Blades 1 (Fig. 15(*c*)) and 4 (Fig. 15(*d*)) are strongly modified by the cavitation instability. The increase of the vapor sheet length at the suction side of Blade 1 is associated with a strong pressure rise, on the pressure side, near to the leading edge. This peak pressure could be the mechanism responsible for the decrease of the sheet in Channel 1.

To summarize, from the analyses of the whole of these unsteady results, we can propose the following scenario in order to explain the cavitation supersynchronous configuration (Figs. 8 and 16).

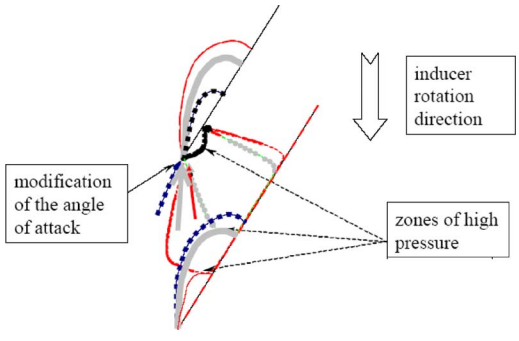

Fig. 16 Description of the physical mechanism supposed to be responsible for supersynchronous cavitation instability: The rise of the cavity on the upper blade increases the angle of attack and the pressure near the leading edge, at the pressure side. Then, the cavity facing this leading edge tends to vanish because of the pressure rise.

- The growth of the cavitation sheet on the Blade 1 suction side leads to the increase of the angle of attack on this blade.
- A consequence of this phenomenon is the rise of the pressure at the Blade 1 pressure side, near the leading edge.
- The pressure field in Channel 1, located below Blade 1, is modified by this pressure rise, which leads to the decrease of the cavitation sheet attached to Blade 4.
- The presence of the cavitation sheet in Channel 4 will change the Blade 4 angle of attack, inducing the progressive rise of the attached sheet cavitation, and the continuation of the instability propagation.

Conclusion

The Laboratory LEGI, in collaboration with the French Space Agency CNES and the rocket engine division of the Snecma, develops, for many years, numerical codes to simulate and analyze cavitation phenomena, mainly occurring in turbopump inducer geometries. In the scope of collaboration with NUMECA International, a cavitation model was implemented in the commercial code FINE/TURBO™. It has been successfully applied to perform calculations of 3D steady cavitating flows [18], as well as unsteady 2D simulations of cavitating flows [16].

In this paper, we presented first results obtained by 2D unsteady calculation in a four-blade cascade drawn from one inducer geometry. Computations were performed at the nominal flow rate for several cavitation numbers. The resulting performance chart was presented. A good agreement was found with previous work performed for the same geometry, by using another numerical code based on a different numerical scheme [13].

From the presented calculations, five different cavitation patterns were observed:

— symmetrical stable configurations (for $\sigma<0.65$ or >0.8) characterized by four identical cavitation sheets
— stable alternate blade cavitation (for $\sigma\sim0.75$)
— supersynchronous configuration (also for $\sigma\sim0.75$ by intermittency)
— unstable alternate cavitation (for $\sigma\sim0.7$)
— subsynchronous configuration (for $\sigma\sim0.65$)

Based on the qualitative analyses of numerical results (i.e., density, velocity, pressure fields, and time evolution of the mass flow rates and of the blade loads), the mechanisms responsible for cavitation instabilities were analyzed and described. An original scenario concerning supersynchronous instability origin was more particularly proposed and discussed.

The duration of the calculations presented in this paper does not allow us to perform reliable quantitative evaluation of the characteristic frequencies. In previous work [13], by using the same physical model and a different computational method, many time-consuming calculations have been carried out to evaluate the characteristic frequencies of instabilities in this same geometry. The main contribution of the present paper, in complement of the previous one, is to propose physical scenarios to describe cavitation instabilities. This study was also a test case used to evaluate the capability of the new 3D numerical code to perform unsteady calculations and to simulate cavitation instability. This step of the work is very important to prepare 3D unsteady calculation in the entire inducer geometries.

Further work is now needed to assess the prediction capability of the model. Presently, a detailed study is being performed to improve the applied physical models by taking into account thermodynamic effects [32]. Numerical model aspects are also in progress to succeed 3D unsteady cavitating calculations in inducer real geometries [33].

Acknowledgment

This research was supported by the French Space Agency CNES (Centre National d'Etudes Spatiales) and the Snecma company. The authors wish also to express their gratitude to NUMECA International for its cooperation to the development of the numerical code.

Nomenclature

$c_{\min}$ = minimum sound speed in the medium (ms^{-1})
P = local static pressure (Pa)
P_{ref} = reference pressure (Pa)
P_v = vapor pressure (Pa)
R_c = cut radius for the passage from three dimensions to two dimensions (m)
T_0 = inducer rotation period (s)
T_{ref} = reference time=blade passage time=$T_0/4$ (s)
V_{ref} = reference velocity ($=R_c\Omega$) (ms^{-1})
$y+$ = nondimensional distance to the boundary
α = void ratio
Ω = angular rotation speed of the inducer ($rd\,s^{-1}$)
ρ = mixture density (kg/m^3)
$\rho_l(=\rho_{\text{ref}})$, ρ_v = liquid (=ref), vapor density (kg/m^3)
σ = $(P_{\text{ref}}-P_v)/(\rho V_{\text{ref}}{}^2/2)$ cavitation number
ψ = static pressure coefficient=$(P-P_{\text{ref}})/(\rho_L V_{\text{ref}}{}^2/2)$
ΔP_{tot} = total pressure variation in a channel; $\Delta P_{\text{tot}}=P_{\text{downstream}}-P_{\text{upstream}}$ (Pa)

References

[1] Kim, J. H., and Acosta, A. J., 1975, "Unsteady Flow in Cavitating Turbopumps," ASME J. Fluids Eng., **96**(3), pp. 412–418.
[2] Brennen, C. E., and Acosta, A. J., 1976, "The Dynamic Transfer Function for a Cavitating Inducer," ASME J. Fluids Eng., **98**(2), pp. 182–191.
[3] Brennen, C. E., Meissner, C., Lo, E. Y., and Hoffmanns, G. S., 1982, ASME J. Fluids Eng., **104**(4), pp. 428–433.
[4] de Bernardi, J., Joussellin, F., and Von Kaenel, A., 1993, "Experimental Analysis of Instabilities Related to Cavitation in Turbopump Inducer," First International Symposium on Pump Noise and Vibrations, Paris, France, pp. 91–99.
[5] Goirand, B., Mertz, A., Joussellin, F., and Rebattet, C., 1992, "Experimental Investigation of Radial Loads Induced by Partial Cavitation With Liquid Hydrogen Inducer," Third International Conference on Cavitation, Cambridge, U.K., pp. 263–269, ImechE Paper No. C453/056.
[6] Joussellin, F., Maitre, T., and Morel, P., 1998, "3D Cavity Shape in an Inducer; Experimental Investigations and Numerical Predictions," Third International Symposium on Cavitation, Grenoble, France.
[7] Kamijo, K., Shimura, T., and Watanabe, M., 1977, "An Experimental Investigation of Cavitating Inducer Instability," ASME Paper No. 77-WA/FW-14.
[8] Pagnier, P., Morel, P., Spettel, F., Henry, C., and Champagne, J.-Y., 1995, "Conception and Experimental Study of an Inducer," in Cav'95 International Symposium, Deauville, France.
[9] Tsujimoto, Y., 2001, "Simple Rules for Cavitation Instabilities in Turbomachinery," Fourth International Symposium on Cavitation, Pasadena, CA.
[10] Watanabe, S., Sato, K., Tsujimoto, Y., and Kamijo, K., 1999, "Analysis of Rotating Cavitation in a Finite Pitch Cascade Using a Closed Cavity Model and a Singularity Method," ASME J. Fluids Eng., **121**(4), pp. 834–840.
[11] Horiguchi, H., Watanabe, S., Tsujimoto, Y., and Aoki, M., 2000, "Theoretical Analysis of Alternate Blade Cavitation in Inducers," ASME J. Fluids Eng., **122**(1), pp. 156–163.
[12] Joussellin, F., Courtot, Y., Coutier-Delgosha, O., and Reboud, J. L., 2001, "Cavitating Inducer Instabilities: Experimental Analysis and 2D Numerical Simulation of Unsteady Flow in Blade Cascade," Proceedings of the Fourth International Symposium on Cavitation, Pasadena, CA.
[13] Fortes Patella, R., Coutier-Delgosha, O., Perrin, J., and Reboud, J. L., 2007, "A Numerical Model to Predict Unsteady Cavitating Flow Behaviour in Inducer Blade Cascades," ASME J. Fluids Eng., **129**(1), pp. 128–135.
[14] Coutier-Delgosha, O., Courtot, Y., Joussellin, F., and Reboud, J. L., 2004, "Numerical Simulation of the Unsteady Cavitation Behavior of an Inducer Blade Cascade." AIAA J., **42**(3), pp. 560–56.
[15] Otsuka, S., Tsujimoto, Y., Kamijo, K., and Furuya, O., 1996, "Frequence Dependence of Mass Flow Gain Factor and Cavitation Compliance of Cavitating Inducers," ASME J. Fluids Eng., **118**(3), pp. 400–408.
[16] Pouffary, B., Fortes Patella, R., and Reboud, J. L., 2003, "Numerical Simulation of Cavitating Flow Around a 2D Hydrofoil: A Barotropic Approach," Fifth International Symposium on Cavitation, Osaka, Japan.
[17] Pouffary, B., 2004, "Simulation Numérique d'Écoulements 2D/3D Cavitants, Stationnaires et Instationnaires: Analyse Spécifique Pour les Turbomachines," Ph.D. thesis, Grenoble, France.
[18] Pouffary, B., Fortes Patella, R., and Reboud, J. L., 2005, "Numerical Simulation of 3D Cavitating Flows: Analysis of Cavitation Head Drop in Turbomachinery," Proceedings of FEDSM2005, Houston, TX, Jun. 19–23.
[19] Coutier-Delgosha, O., Fortes Patella, R., Reboud, J. L., Hakimi, N., and Hirsch, C., 2005, "Numerical Simulation of Cavitating Flow in 2D and 3D Inducer Geometries," Int. J. Numer. Methods Fluids, **48**(2), pp. 135–167.
[20] Coutier-Delgosha, O., Fortes Patella, R., Reboud, J. L., Hakimi, N., and Hirsch, C., 2005, "Stability of Preconditioned Navier–Stokes Equations Associated With a Cavitation Model," Comput. Fluids, **34**(3), pp. 319–349.
[21] Hakimi, N., 1997, "Preconditioning Methods for Time Dependent Navier–Stokes Equations," Ph.D. thesis, Vrije Universiteit Brussels, Belgium.
[22] Spalart, P. R., and Allmaras, S. R., 1992, "A One Equation Turbulence Model for Aerodynamic Flows," AIAA Paper No. 92-0439.
[23] Delannoy, Y., and Kueny, J. L., 1990, "Two Phase Flow Approach in Unsteady Cavitation Modelling," FED (Am. Soc. Mech. Eng.), **98**, pp. 153–158.
[24] Coutier-Delgosha, O., Reboud, J.-L., and Delannoy, Y., 2003, "Numerical Simulation of the Unsteady Behaviour of Cavitating Flows," Int. J. Numer. Methods Fluids, **42**, 527–548.
[25] Lohrberg, H., Stoffel, B., Fortes-Patella, R., and Coutier-Delgosha, O., Reboud, J.-L., 2002, "Numerical and Experimental Investigation on the Cavitating Flow in a Cascade of Hydrofoils," Exp. Fluids **33/4**, pp. 578–586.
[26] Coutier-Delgosha, O., Fortes Patella, R., Reboud, J. L., Hofmann, M., and Stoffel, B., 2003, "Experimental and Numerical Studies in a Centrifugal Pump With 2D-Curved Blades in Cavitating Conditions," ASME J. Fluids Eng., **125**(6), pp. 970–978.
[27] Coutier-Delgosha, O., Fortes Patella, R., and Reboud, J. L., 2002, "Simulation of Unsteady Cavitation With a Two-Equation Turbulence Model Including Compressibility Effects," J. Turbul., **3**, 058.
[28] Jameson, A., 1991, "Time Dependant Calculations Using Multigrid, With Application to Unsteady Flows Past Airfoils and Wings," AIAA Paper No. 91–1596.
[29] Turkel, E., 1987, "Preconditioning Methods for Solving the Incompressible and Low Speed Compressible Equations," J. Comput. Phys. **72**, pp. 277–298.
[30] Choi, D., and Merkle, C. L., 1993, "The Application of Preconditioning in Viscous Flows," J. Comput. Phys. **105**, pp. 207–223.
[31] Emmons, H. W., Pearson, C. E., and Grant, H. P., 1955, "Compressor Surge and Stall Propagation," Trans. ASME, **77**(4), pp. 455–469.
[32] Rolland, J., Boitel, G., Barre, S., Goncalves, E., and Fortes Patella, R., 2006, "Experiments and Modelling of Cavitating Flows in Venturi, Part I: Stable Cavitation," Sixth International Symposium on Cavitation, CAV2006, Wageningen, The Netherlands, Sept.
[33] Gonzalo-Flores, N., Rolland, J., Goncalves, E., Fortes Patella, R., and Rebattet, C., 2006, "Head Drop of Spatial Turbopump Inducer," Proceedings of CAV 2006 Symposium, Wageningen, The Netherlands, Sept.

Control of Vortex Shedding of Circular Cylinder in Shallow Water Flow Using an Attached Splitter Plate

Huseyin Akilli[1]
Cuma Karakus
Atakan Akar
Besir Sahin
N. Filiz Tumen

Department of Mechanical Engineering,
Faculty of Engineering and Architecture,
Cukurova University,
Balcali, Adana 01330, Turkey

In the present work, passive control of vortex shedding behind a circular cylinder by splitter plates of various lengths attached on the cylinder base is experimentally investigated in shallow water flow. Detailed measurements of instantaneous and time-averaged flow data of wake flow region at a Reynolds number of Re=6300 *were obtained by particle image velocimetry technique. The length of the splitter plate was varied from* $L/D=0.2$ *to* $L/D=2.4$ *in order to see the effect of the splitter plate length on the flow characteristics. Instantaneous and time-averaged flow data clearly indicate that the length of the splitter plate has a substantial effect on the flow characteristics. The flow characteristics in the wake region of the circular cylinder sharply change up to the splitter plate length of* $L/D=1.0$. *Above this plate length, small changes occur in the flow characteristics.* [DOI: 10.1115/1.2903813]

Keywords: flow control, splitter plate, shallow flow, formation region, PIV

1 Introduction

Vortex shedding and wake region of bluff bodies, especially cylinders, for a wide range of Reynolds numbers have been a topic of much interest due to their extensive use in engineering applications. A detailed review of the flow characteristics downstream of the circular cylinder was given by Williamson [1]. Another comprehensive review of the progress made during the past two decades on vortex induced vibration was reported by Sarpkaya [2]. His extensive review covers the fundamental aspect of bluff body flows, mostly vortex induced vibration of cylindrical structure subjected to steady uniform flow. The review includes a powerful theoretical discussion, experimental methods, and numerical models regarding the strengths and weaknesses of the current state of the understanding of complex fluid/structure interactions.

Structural vibrations and acoustic noise or resonance caused by the periodic surface loading have led investigators to concentrate on the control of the large-scale vortex shedding behavior behind bluff bodies. On the other hand, unsteady behavior of the vortex shedding downstream of the cylinder enhances the heat transfer. There are numerous techniques to control the vortex shedding downstream of the bluff bodies. These techniques are basically separated into two categories: passive and active controls. Passive control techniques suppress the vortex shedding by modifying the shape of the bluff body or by attaching additional devices in the flow field. Active control techniques use external energy to change the flow field. Since passive techniques are simple and easier to implement compared to the active control techniques, they are widely used for flow control applications [3]. The examples of passive control techniques are splitter plates, small rods, base bleed, roughness elements, and helical wires. Delaunay and Kaiktatsis [4] numerically investigated the effect of base suction and blowing on the stability of the cylinder wake at low Reynolds numbers. Their results indicated that a low level of blowing fluid can stabilize the wake. Namely, a reduction of backflow reduces the absolute instability in the near wake. On the other hand, high level of suction can also stabilize the wake at supercritical Reynolds numbers. Aerodynamic slot control for square prism was studied numerically by Hangan and Kim [5]. It is shown that penetration of slot flow in the near wake region generates a Kelvin–Helmholtz-type instability that attenuates the vortex shedding formation. Experimental and computational study of a square cylinder wake with planer jet injection from its base into the wake region conducted by Koutmos et al. [6] reported the slot jet and wake flow interactions. Kwon et al. [7] investigated the drag reduction caused by ribbons attached to circular cylinders. The position and length of ribbons have a significant effect on the drag reduction. Igarashi [8] found that the installation of a small rod upstream of a square prismatic cylinder decreased the drag approximately by 50–70% for the Reynolds number of $\mathrm{Re}=3.2\times10^4$. In the work of Lee et al. [3], a rod was set upstream for the purpose of controlling the flow around a circular cylinder in air stream. The flow pattern alters depending on the rod diameter and its position. Fujisawa and Takeda [9] reported that the active control techniques of vortex shedding have attracted the attention of researchers more recently. They introduced acoustic disturbances through a split to the flow over the cylinder in order to control the vortex shedding emanating from both sides of the cylinder. Conclusions were derived that flow control with acoustic excitation can reduce the drag about 30% compared to the stationary cylinder.

Among passive control techniques, the splitter plate has been one of the most successful devices for control of the vortex shedding [10]. Gerrard [11] investigated the effect of length of splitter plate, attached to the circular cylinder, on the wake flow characteristics. He showed that the Strouhal number decreased when the splitter plate length was smaller than the cylinder diameter, but it increased for $1<L/D<2$. Apelt et al. [12] reported that the drag force acting on the cylinder was significantly reduced and the value of Strouhal number became smallest at $L/D=1$. They also found that Strouhal number increased for $1<L/D<2$ and vortex shedding completely disappeared for the splitter plate lengths of $L/D>5$. Anderson and Szewczyk [13] concluded that the vortex shedding frequency from a circular cylinder with a splitter plate

[1]Corresponding Author.

Contributed by the Fluids Engineering Division of ASME for publication in the JOURNAL OF FLUIDS ENGINEERING. Manuscript received May 8, 2007; final manuscript received November 16, 2007; published online April 4, 2008. Assoc. Editor: James A. Liburdy.

was altered in different ways depending on the length of the splitter plate. They gave an explanation for the nonlinearity between Strouhal number and the splitter plate length. Due to the nonlinearity, they divided the variation in Strouhal number over the range of $L/D=0-1.75$ into four distinct regions where within each region a different flow phenomenon dominated the selection process of the shedding frequency. Kwon and Choi [14] conducted a numerical study on the control of vortex shedding in laminar flow downstream of the circular cylinder using splitter plates. They pointed out that the vortex shedding downstream of the circular cylinder completely disappears when the length of the splitter plate is longer than a critical length, which is found to be proportional to the Reynolds number. Prasad and Williamson [15] placed small flat plate upstream of the cylinder to reduce the drag acting on the cylinder. They concluded that the width of the plate had a significant effect on the total drag on the system. Hwang et al. [16] applied a detached splitter plate for the control of flow-induced forces on a circular cylinder in their numerical study of laminar flow. They observed the existence of an optimal location of the splitter plate by which the drag force was reduced significantly. Drag force increased sharply with the insertion of the splitter plate further downstream of the optimal location. A numerical study was carried out by Tiwari et al. [17] to investigate the flow and heat transfer characteristics of a circular tube with splitter plates attached on the rear side. It was found that these splitter plates alter the characteristics of the wake flow region; for example, stabilizing effect takes place, which reduces the heat transfer rate from the tube surface. However, the presence of the splitter plate substantially increases the total heat transfer by complementing for extended surface heat transfer. They also concluded that the splitter plate significantly reduces the pressure loss penalty.

A shallow water flow is described as the condition that the horizontal length scale of the flow is considerably larger than its depth. Many wake flows can be characterized as shallow flow in nature, such as those in wide rivers, lakes, estuaries, shallow coastal waters, mountains, or stratified atmosphere [18]. The detailed physics of vortex development in the shallow near wake is expected to be complex due to the effects of bottom and free surfaces and the relatively small distance between them [19]. Studies of Ingram and Chu [20] and Chen and Jirka [21] show that the flow structure behind bluff bodies in shallow water is different from that of deep water. Lloyd et al. [22] carried out experiments to investigate wake formation around conical island, circular cylindrical forms, and with gentle slopes in oscillating laminar shallow water flows. They identified four distinct types of wake pattern around circular cylinder and conical island, which are similar to those observed for unbounded cylinder wakes. Akilli and Rockwell [19] investigated the vortex formation behind a vertical circular cylinder in shallow water. Their study indicated that three-dimensional flow appears in the cylinder wake flow region and a horseshoe vortex system emanating from the upstream of the cylinder base interacts with the shear layers on both sides of the cylinder wake region causing additional patterns of Reynolds shear stress exterior to the shear layers. Flow patterns at the midplane elevation are remarkably similar to that occurring in the near wake of a cylinder of larger extent. Kahraman et al. [23] attached a narrow transverse strip of roughness elements on the bed surface downstream of the vertical cylinder in shallow water flow to demonstrate bed-friction influence on the formation of large-scale vortices in the wake flow regions. Fu and Rockwell [24] reported that instability of the horseshoe vortices emanating from the upstream of the vertical cylinder in shallow water flow activates the instability of the wake flow region. Fu and Rockwell [25] studied the control of vortex formation in the near wake of shallow water flow downstream of the vertical cylinder using a base water bleed through a very narrow slot. They concluded that a water bleed through this very small gap alters the flow data in upstream and downstream of the cylinder base. Experimental

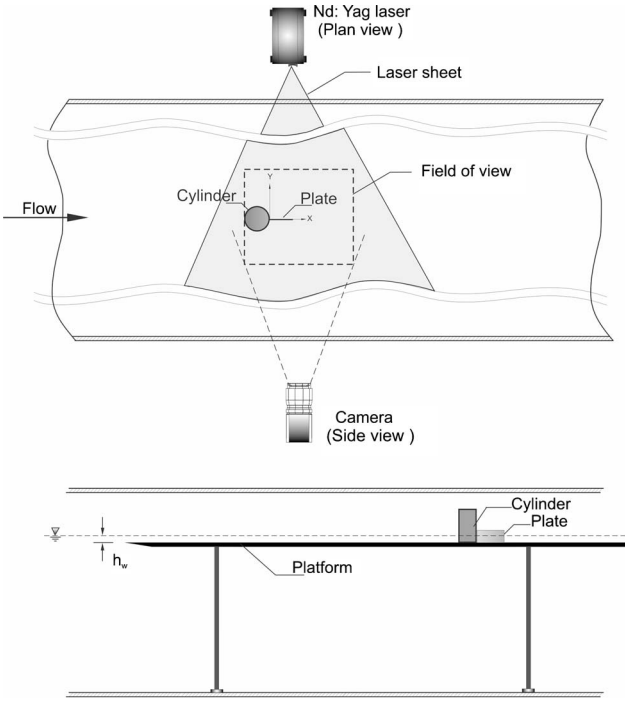

Fig. 1 Schematic of the experimental system

studies of Akilli et al. [10] revealed that a detached splitter plate located at various stations downstream of the vertical cylinder in shallow water flow has a drastic effect on the suppression of the vortex shedding for the gap ratio between $0.0D$ and $1.75D$.

In this study, controlling of the flow structure in the wake flow region downstream of the vertical circular cylinder placed in shallow water was experimentally investigated using the particle image velocimetry (PIV) technique. Vortex formation due to the vertical cylinder in shallow water layer was passively controlled by a placement of attached splitter plates with various lengths on the downstream base of the cylinder.

2 Test Facility

Experiments were conducted in a recirculating free surface water channel having dimensions of $8000\times1000\times750$ mm^3 located at Cukurova University, Fluid Mechanics Laboratory of Mechanical Engineering Department, Turkey.

A nonintrusive optical method PIV is a well known and commonly used technique for studying bluff body aerodynamics and can give quantitative information on the structure of the instantaneous velocity field in a flow plane of interest. In the present investigation, the PIV technique is employed to calculate instantaneous and mean velocity field behind a vertical cylinder in order to understand the effect of the length of attached splitter plate on the vortex shedding behavior in shallow water flow. By postprocessing, as well as Reynolds shear stress correlation, instantaneous, or mean vorticity maps, streamline topology could be obtained.

Plan view of the test section, position of the cylinder, dimensions of the test chamber, location of the laser sheet, and the view of camera as well as the coordinate system are shown in Fig. 1. The total depth of the water in the channel was set at a 600 mm. All experiments were carried out above a platform having a length of 2300 mm shown in Fig. 1. The length between the leading edge of the platform and the location of the cylinder was 1800 mm to obtain fully developed boundary layer. The water height between the base of the platform and the free surface was adjusted as 25 mm, which corresponds to half of the cylinder diameter ($D=50$ mm). The ratio between the cylinder diameter and the width

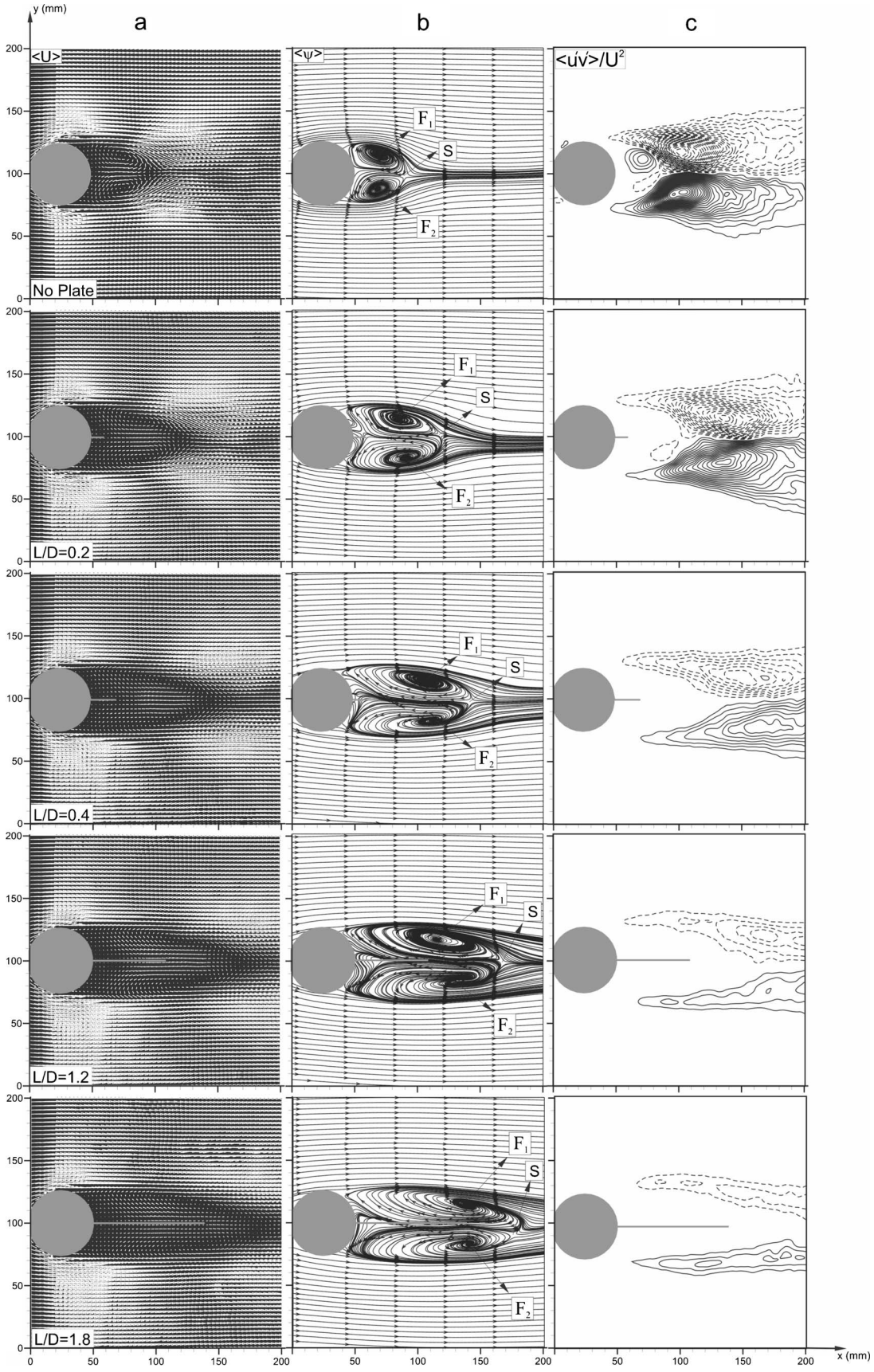

Fig. 2 (*a*) **Time-averaged-velocity vector field,** (*b*) **corresponding streamline topology, and** (*c*) **contours of normalized Reynolds shear stress**

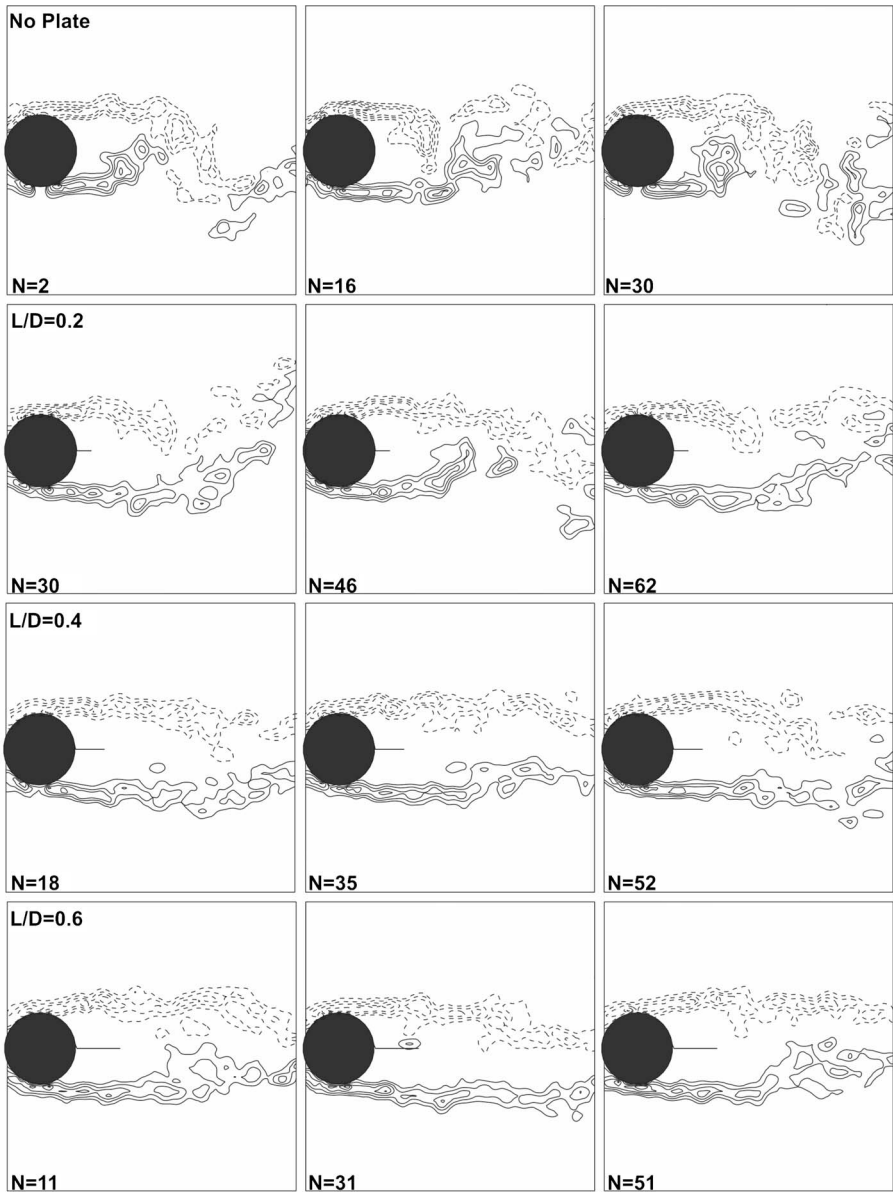

Fig. 3 Comparison of instantaneous spanwise vorticity contours for different splitter plate cases

of the test section, geometric blockage of the cylinder, was 5%. The movement of the water inside the water channel was provided using a pump driven by an electric motor having a variable speed controller. Depth-averaged velocity was $U=126$ mm/s corresponding to the Reynolds number of $\mathrm{Re}=6300$ based on the cylinder diameter. Splitter plates having three different thicknesses ($T=0.8$ mm, 2 mm, and 4 mm) were used and their lengths were varied from 10 mm to 120 mm with 10 mm increments. The splitter plates are kept in position along the axis of the cylinder. Both circular cylinder and splitter plates are made of transparent Plexiglas material to provide optical access for PIV measurements.

The experiments were performed and the measured data were processed using Dantec Dynamics PIV system and FLOW MANAGER software installed on a computer. The measurement field was illuminated by a thin and an intense laser light sheet by using a pair of double-pulsed Nd:YAG (yttrium aluminum garnet) laser units each having a maximum energy output of 120 mJ at 532 nm wavelength. The laser sheet was oriented parallel to the bottom surface of the water channel and the experiments were carried out both at the midplane of the water height ($h_L/h_w=0.5$) and very close to the bottom (bed) surface ($h_L/h_w=0.06$). The image capturing was performed by an 8 bit cross-correlation charge-coupled device (CCD) camera having a resolution of 1024×1024 pixels, equipped with a Nikon AF Micro 60 $f/2.8D$ lens. In the image processing, 32×32 rectangular interrogation pixels were used and an overlap of 50% was employed. A total of 3844 (62×62) velocity vectors were obtained for an instantaneous velocity field at a rate of 15 frames/s. The overall field of view was 200×200 mm^2 in physical size. The image magnification was 0.195 mm/pixel. The time interval between pulses was 1.5 ms for all experiments and the thickness of the laser sheet illuminating the measurement plane was approximately 2 mm. The time interval and the laser sheet thickness were selected such that the maximum amount of particles in the interrogation window was obtained. The number of particles in an interrogation area was in between 20 and 25. The uncertainty in velocity relative to depth-averaged velocity is about 2% in the present experiments. The water was seeded with 12 μm diameter hollow glass sphere par-

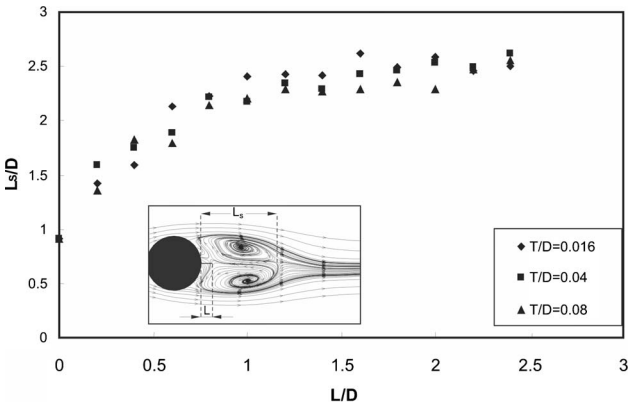

Fig. 4 Variation of saddle point location as a function of splitter plate length

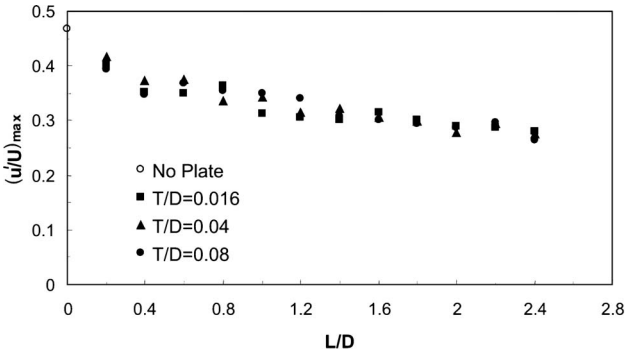

Fig. 5 Variation of normalized peak streamwise root-mean-square velocity fluctuations as a function of splitter plate length

ticles having 1100 kg/m^3 density. In each experiments, 300 instantaneous images were captured, recorded, and stored in order to obtain averaged-velocity vectors and other statistical properties of the flow field. Spurious velocity vectors (less than 3%) were removed using the local median-filter technique and replaced by using a bilinear least squares fit technique between surrounding vectors. The velocity vector field was also smoothed to avoid dramatic changes in the velocity field using the Gaussian smoothing technique. The vorticity value at each grid point was calculated from the circulation around the eight neighboring points.

3 Results and Discussion

Splitter plates having different thicknesses, $T/D=0.016$, 0.04, and 0.08, were attached at the base of the circular cylinder ($X/D=0.0$). The depth-averaged velocity was $U=126$ mm/s, which corresponds to a Reynolds number of Re=6300. Preliminary dye visualization and PIV experiments show that the plate thickness does not have a considerable effect on the flow structure; the overall form of the patterns of velocity vectors is generally similar for all plate thickness cases. Patterns of time-averaged velocity $\langle V\rangle$, streamline topology $\langle\psi\rangle$, and corresponding normalized Reynolds shear stress correlations $\langle u'v'\rangle/U^2$ at the midplane elevation ($h_L/h_w=0.5$) are given in Fig. 2 as a function of plate length L/D, for the thinnest plate thickness, $T/D=0.016$. The first row of figures is given for the case of no plate to compare this case with the presence of the splitter plate cases. Time-averaged flow characteristics shown in Fig. 2 have an almost symmetrical structure with respect to the centerline of the wake for all cases. A well-defined wake region is evident from velocity vector fields and corresponding streamline topologies. Since the splitter plates prevent the interaction of the separated shear layer on both sides of the cylinder, the wake region significantly elongates along the streamwise direction with increasing length of the splitter plate as shown in the first and second columns of Fig. 2. This elongation of the wake region is an indication of the substantial attenuation of the large-scale vortex formation. However, the spanwise extend of the wake region remains constant for all cases. Furthermore, two well-defined foci designated as F_1 and F_2, and a saddle point, S_1, occur downstream of the cylinder for all cases. The locations of both foci and saddle points significantly move in the downstream direction with increasing the splitter plate length. Two foci are located on both sides of the splitter plate and the saddle point is generally located downstream of the trailing edge of the splitter plate. The transverse distance between two foci, which is approximately $0.6D$, is not affected from the presence of the splitter plate in general. The third column of Fig. 2 depicts the corresponding Reynolds shear stress correlations normalized by the square of depth-averaged velocity as a function of splitter plate length, L/D. Here, the solid lines show the positive Reynolds shear stress correlations and the dashed lines depict the negative concentrations. Minimum and incremental values of Reynolds shear stress contours are ± 0.005 and 0.005, respectively. In terms of no-plate case, well-defined Reynolds shear stress correlations, which are characteristics of Karman vortex shedding, occur downstream of the circular cylinder. The Reynolds shear stress correlation shows an absence of pronounced concentrations in the base region because of the lack of significant correlation between the streamwise and cross-flow fluctuations and/or small magnitudes of the fluctuations in the near wake of the cylinder [26]. Nevertheless, the small-scale clusters of Reynolds shear stress located in the vicinity of the base region occur as a result of the entrainment of freestream flow into this base region. As the flow goes downstream, the Reynolds shear stress increases to a peak value of 0.1364 at a location of approximately $0.97D$, which coincides with the saddle point associated with the generation of intensive fluctuations in this location, from the base of the cylinder and then decreases. The overall form of the Reynolds shear stresses obtained at the midplane elevation is notably similar to the studies performed by Akilli and Rockwell [19] for the near wake of a circular cylinder located in shallow water flow and Lin et al. [27] and Mittal and Balachandar [28] for the near wake of a cylinder of larger spanwise extent.

The peak value of Reynolds shear stress decreases to 0.085 for $L/D=0.2$ case and the spatial location of peak concentration moves downstream and occurs at a location of approximately $1.7D$. The decrease in the peak concentration for the $L/D=0.2$ case as compared to the no-plate case indicates that the presence of even a very short splitter plate is effective in decreasing the peak value of the Reynolds shear stress. The low-level Reynolds shear stress correlation region located in the vicinity of the base of the cylinder gets larger and extends in streamwise direction. At $L/D=0.4$, the peak values of Reynolds shear stress are significantly attenuated and the location of the peak Reynolds shear stress moves further downstream with a substantial distance. The peak value of concentration of the Reynolds shear stress drops to a value of 0.035. The peak values of Reynolds shear stress for $L/D=1.2$ and 1.8 cases substantially decrease to 0.02 and 0.015, respectively. These values suggest that the velocity oscillations in the wake region are effectively suppressed and the direct interaction between separated shear layers is prevented by the splitter plate. It can be said that the considerable decrease in the Reynolds shear stress correlation is closely related to the reduction in the drag force of the circular cylinder [9,29]. The peak value of concentration of Reynolds shear stress obtained for $L/D=1.8$ case is smaller approximately by a factor of 9 than the concentrations occurred for no-plate case. Pronounced Reynolds shear stress correlations for $L/D=1.8$ are only obtained in the shear layer apparently due to the small-scale vortices occurring along the shear layer.

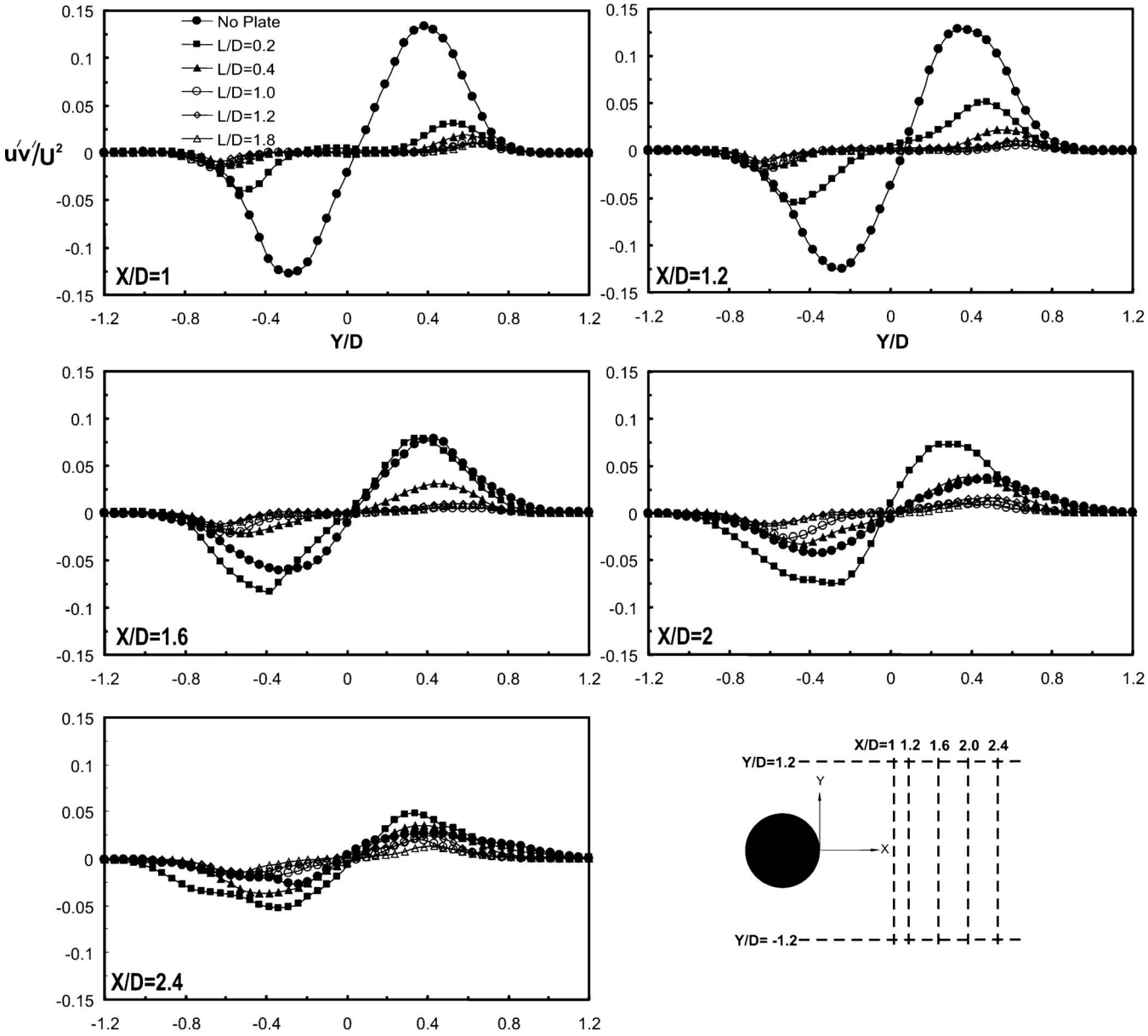

Fig. 6 Variation of Reynolds stress at various locations downstream of the cylinder

Figure 3 compares the instantaneous spanwise vorticity contours between the cases of no-plate and splitter plate, having $T/D=0.016$, with different lengths at the midplane elevation. Here, the solid and dashed lines show the positive (anticlockwise) and negative (clockwise) spanwise vorticity layers, respectively, and N represents the image number. For the case of no plate shown in the first row of Fig. 3, a large-scale Karman-like vortex structure occurs close to the base of the cylinder and small concentration of vortices detected from large-scale vortices are observed far away from the cylinder. The shear layers of the cylinder actually interact with each other just after the cylinder. The first image of the row is the second instantaneous image ($N=2$) in 300 instantaneous images. The middle image of the first row represents the image obtained half cycle later from the first image ($N=2$) and the third image of the first row shows the image 1 cycle later from the first image. The time interval between the two successive images is 66.6 ms. Meanwhile, spectra of streamwise velocity fluctuations evaluated at various locations in the flow field for no-plate case shows a clear and distinct peak, which shows the natural frequency of vortex shedding, approximately $f=0.529$ Hz. When the splitter plates are attached to the cylinder, instantaneous vorticity contours depict that the splitter plate has a significant influence on the wake flow structure. At $L/D=0.2$, the vorticity layers elongate in streamwise direction and the shear layers emanating on both sides of the circular cylinder interact with each other at a location further downstream of the cylinder at approximately $x/D=1.2D$. Nevertheless, the oscillation of the flow is obtained for this splitter plate length at a frequency of $f=0.47$ Hz, which is smaller than that of the no-plate case. The peak vorticity value for this plate length is slightly smaller compared to the case of no plate. For the plate lengths of $L/D=0.4$ and 0.6, the oscillation of the flow is still observed at frequencies of $f=0.455$ Hz and 0.410 Hz, respectively. The entrainment of the shear layers occurs further downstream of the cylinder for these plate lengths and the magnitude of the vorticity concentration, however, remains almost constant with increasing splitter plate length. The same vortex shedding frequencies were also obtained for other splitter plate thicknesses, $T/D=0.04$ and 0.08, for $0<L/D\leq 0.6$. For the splitter plate length greater than $L/D=1.0$, spectra of the streamwise velocity do not give any dominant fre-

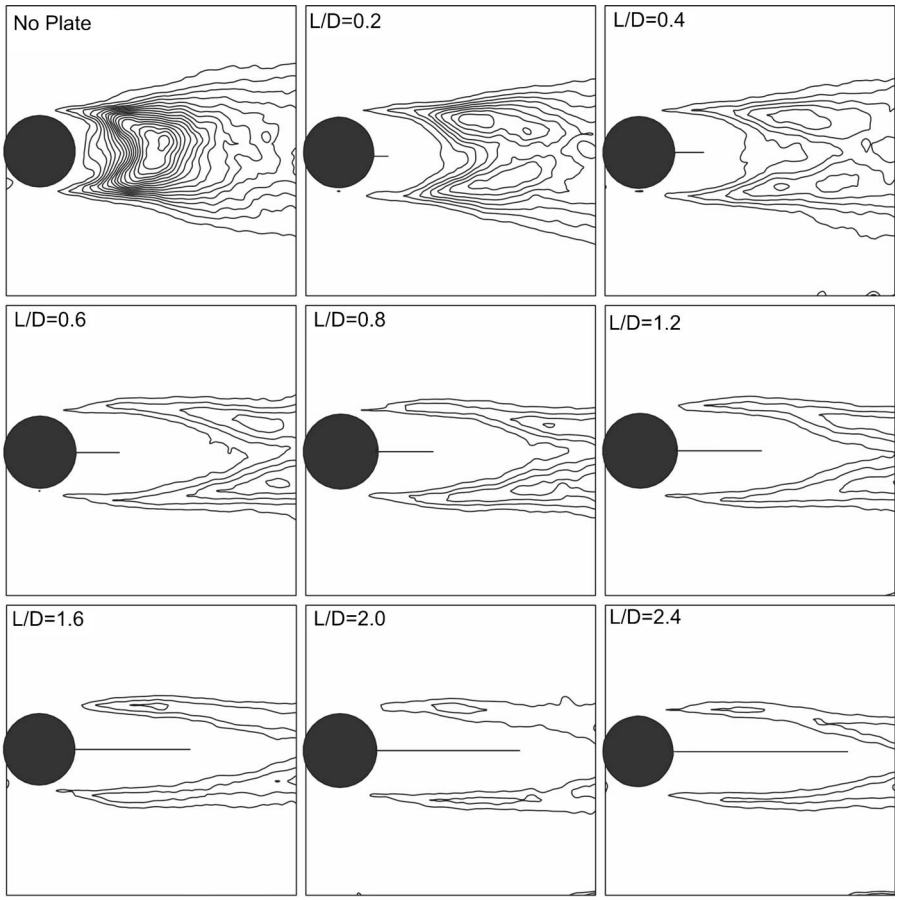

Fig. 7 Effect of splitter plate length on turbulent kinetic energy distribution downstream of the cylinder

quency in the flow field. Gerrard [11] observed that the dominant frequency of vortex shedding decreased when the length of the splitter plate attached on the cylinder in deep water was smaller than D, but it increased for $1<L/D<2$ at $\mathrm{Re}=2\times10^4$. Similar results were also reported by Apelt et al. [12] in deep water flow. Kwon and Choi [14] concluded that the reason for the increase in vortex shedding at $1<L/D<2$ was due to the generation of the secondary vortex at the tip of the splitter plate. Instantaneous images obtained from present experiments do not clearly show the presence of the secondary vortices occurring at the tip of the splitter plate most probably due to the strong effect of the bed and free surface on shallow flow characteristics. At $1.0<L/D\leq2.4$, the flow oscillations downstream of the trailing edge of the splitter plate are rarely observed. However, these oscillations are not periodic. Both positive and negative spanwise vorticity layers remain horizontal and further expanded in the streamwise direction for $L/D>1.0$ cases. This behavior of the flow prevents the momentum transfer from the freestream flow into the wake region. Finally, despite the unsteady structure of the flow, the variation of the vorticity layers is, in contrast to the case of no plate, similar for most of the instantaneous images.

Figure 4 presents the variation of saddle point location, which is an indication of vortex formation length, as a function of the splitter plate length for three different plate thicknesses at the midplane elevation ($h_L/h_w=0.5$). Saddle point for no-plate case occurs at approximately $0.93D$ from the base of the cylinder. Considerable increase in vortex formation length is obtained with the increase in the splitter plate length up to $L/D=1.2$. Above this plate length, the vortex formation length slightly increases. Figure 4 also shows that the plate thickness has a negligible effect on the vortex formation length.

The variation of normalized peak streamwise root-mean-square velocity fluctuations at the midplane elevation for different plate thicknesses as a function of splitter plate length is given in Fig. 5. First of all, the results obtained for different plate thicknesses verify that the thickness of the plate does not have much effect on the flow characteristics downstream of the cylinder. Second, it is evident that increasing splitter plate length results in a decrease in the peak value of the streamwise rms velocity fluctuation. Splitter plates located downstream of the circular cylinder strongly suppress the large-scale vortices, which carry fresh fluid from freestream region into the wake region behind the circular cylinder, and then velocity fluctuations downstream of the cylinder are weakened. While the peak fluctuation for no-plate case is 0.48, this value decreases approximately to 0.4 with the presence of the smallest splitter plate, $L/D=0.2$. When the splitter plate length is increased to $L/D=2.4$, the peak value of streamwise root-mean-square velocity fluctuation drops to a value of 0.26, which is about half that of the no-plate case.

The cross-sectional distribution of the Reynolds shear stress for various cases is displayed in Fig. 6 at five different locations, $X/D=1$, 1.2, 1.6, 2.0, and 2.4 downstream of the circular cylinder for $T/D=0.016$ at the midplane elevation. At $X/D=1$ location, Reynolds shear stress distribution for no-plate case is much larger than the other cases. Because of the suppression of the vortex shedding and elongation of the wake region for the presence of the splitter plate, the fluctuations of the velocity components are very low and Reynolds shear stress concentrations are negligible in this location except for $L/D=0.2$ case where the peak concentration of Reynolds shear stress is approximately equal to 0.04. Similar distribution of Reynolds shear stress are obtained for $X/D=1.2$ location. However, the peak concentration slightly in-

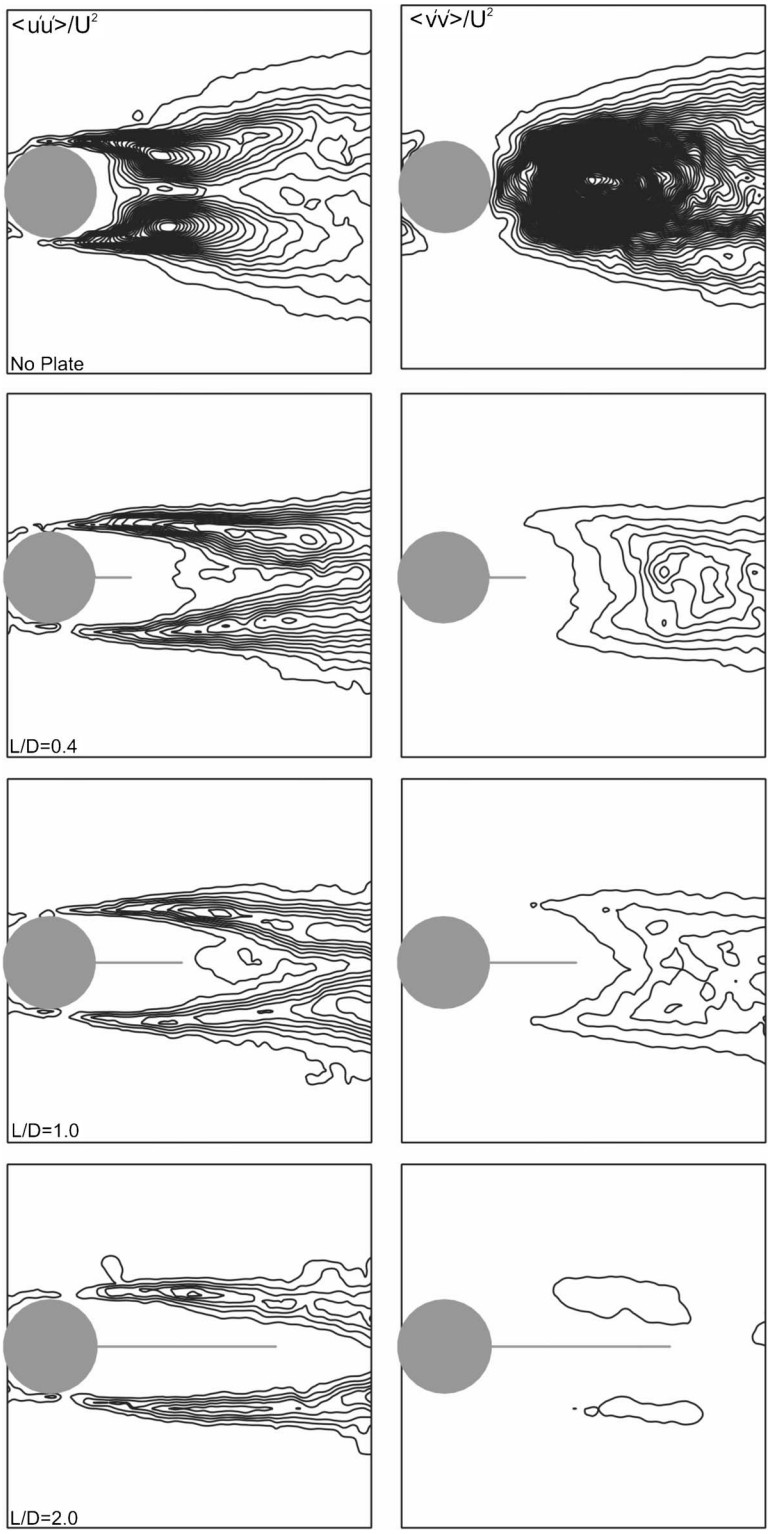

Fig. 8 Normalized Reynolds normal stresses $\langle u'u' \rangle / U^2$ and $\langle v'v' \rangle / U^2$ for different splitter plate lengths

creases for the plate having $L/D=0.2$. As mentioned earlier, Reynolds shear stress concentration reaches a peak value at $X/D=1$ and slightly drops after this location for no-plate case. Due to this fact, the peak concentration of Reynolds shear stress drops to a value of 0.079, while the peak concentration for $L/D=0.2$ increases to a value of 0.08 at the $X/D=1.6$ location. Beside this, slight changes are obtained for the $L/D=0.4$ case. Moreover, Reynolds shear stress distributions are very similar for the plate lengths of $L/D=0.8$, 1.2 and 1.8 for all downstream locations. However, very small changes are obtained in the distribution of Reynolds shear stress between $L/D=0.8$ and $L/D=1.2$ and 1.8 cases in the downstream locations of $X/D=2.0$ and 2.4. Finally, it

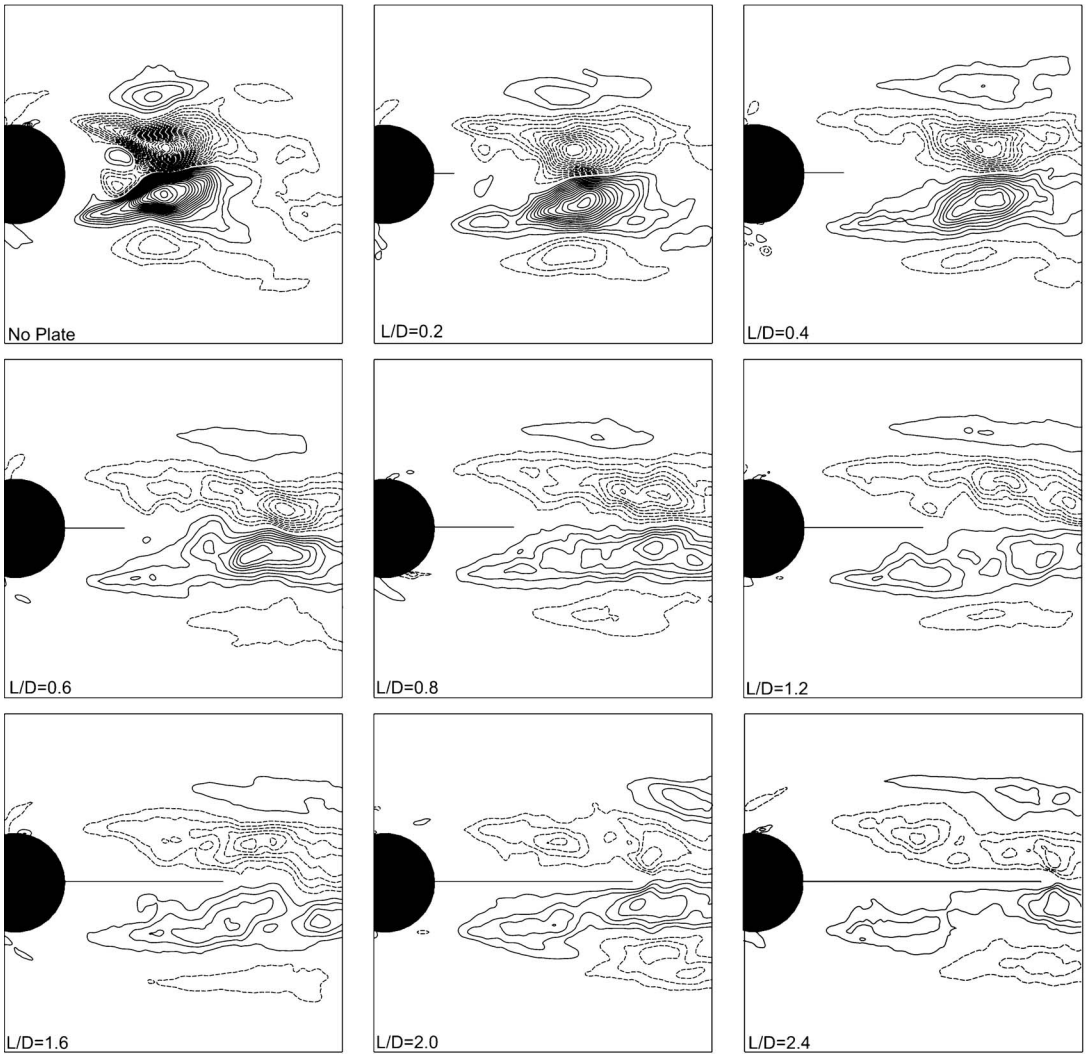

Fig. 9 Normalized Reynolds shear stress for different splitter plate lengths at the elevation adjacent to the bed surface

can be concluded from Fig. 5 that Reynolds shear stress distribution at various downstream locations along the transverse direction negligibly changes after the splitter plate length of $L/D=1.2$.

Figure 7 shows the contours of normalized turbulent kinetic energy for different splitter plate cases of $T/D=0.016$ at the midplane elevation. For all graphs, the minimum value of turbulent kinetic energy was kept the same in order to provide comparison. For the no-plate case, turbulent kinetic energy increases initially along the downstream direction starting from the base of the circular cylinder and reaches its peak value at a point very close to the saddle point location along the centerline in the wake region. Then, it decreases gradually along the downstream direction. Compared to the no-plate case, two maxima, which are located in shear layers both sides of the cylinder, are evident for the presence of the splitter plates in the flow field, instead of just one dominant peak obtained for no-plate case. Due to the fact that the formation of the large-scale vortices is suppressed by the splitter plates, the entrainment of the freestream flow into the wake flow region is prevented and the peak value of turbulent kinetic energy does not occur along the symmetry line anymore. For the splitter plate having the length of $L/D=0.2$, the peak value of turbulent kinetic energy decreases to approximately half of that of the no-plate case and the location of the peak turbulent kinetic energy moves in the downstream direction as a result of the elongation of the vortex formation region mentioned above. The decrease in the peak value of turbulent kinetic energy is rapid until the $L/D=1.2$ case. This peak value of turbulent kinetic energy for the $L/D=1.2$ case is approximately four times smaller than that of no-plate case. The peak value of the turbulent kinetic energy changes slightly after the plate length of $L/D=1.2$. For example, the peak value for $L/D=2.4$ case is less than half that of the $L/D=1.2$ case. The size of wake region with negligible kinetic energy is considerably longer in freestream direction for $L/D=2.4$ case compared to the no-plate case. This feature of the flow is consistent with the elongation of the vortex formation length and the prevention of the interaction of the separated shear layers with each other.

Figure 8 indicates streamwise and transverse Reynolds normal stresses for different splitter plate cases at the midplane elevation to reveal their effect on turbulent kinetic energy. The minimum and incremental values of the contours for streamwise Reynolds normal stress $\langle u'u' \rangle / U^2$ and for transverse Reynolds normal stress $\langle v'v' \rangle / U^2$ are the same and equal to 0.01 and 0.005, respectively. The peak value of both normal stresses decreases with increasing splitter plate length. However, as could be seen in Fig. 8, the rate of decrease in transverse Reynolds normal stress is greater than that of streamwise Reynolds normal stress. The peak values of normalized streamwise and transverse Reynolds normal stresses for no-plate case are 0.23 and 0.39, respectively. These values

decrease to 0.09 and 0.023 for $L/D=1$ and 0.06 and 0.009 for $L/D=2.0$. These numerical values indicate that transverse Reynolds normal stress has considerable effect on the weakening of turbulent kinetic energy compared to the effect of streamwise Reynolds normal stress.

Contours of normalized Reynolds shear stress for different splitter plate lengths at the elevation adjacent to the bed surface ($h_L/h_w=0.06$) are shown in Fig. 9. The minimum and incremental values of Reynolds shear stress $\langle u'v' \rangle / U^2$ are ± 0.005 and 0.005, respectively. Here, the solid and dashed lines represent the positive and negative Reynolds shear stress contours, respectively. Similar to the case at the midplane elevation, the peak values of Reynolds shear stress are significantly attenuated with increasing splitter plate length. The most important difference between Reynolds shear stress concentrations obtained at the bed and midplane elevation appears to be the formation of additional concentrations exterior to the near wake region and both sides of the cylinder at the bed. They are presumably due to the fluctuations related to horseshoe vortex formed immediately upstream of the cylinder's leading edge [19]. Reynolds shear stress contours in Fig. 9 also show that the existence of the splitter plate has negligible effect on horseshoe vortex system and the additional concentrations mentioned above.

4 Conclusions

The flow characteristics of the wakes behind the circular cylinder with attached splitter plates have been investigated experimentally in shallow water flow using the PIV technique. The effects of the splitter plate length, ranging from 10 mm ($0.2D$) to 120 mm ($2.4D$), on the suppression of vortex shedding were determined by the instantaneous and time-averaged-velocity vector field, corresponding vorticity field, streamline topology, and turbulent statistics. The splitter plates having different thicknesses exert the same influence on the flow characteristics. Increasing splitter plate length results in a decrease in the frequency of vortex shedding until $L/D=0.6$. After this splitter plate length, the dominant frequency of the shedding vortices is not obtained probably due to the stabilizing effect of the shallow water. Turbulent flow characteristics of wake region changes immediately even with the presence of the smallest splitter plate. Substantial changes in turbulent statistics, such as turbulent kinetic energy, Reynolds shear and normal stresses are obtained until the splitter plate length of $L/D=1.2$. The large-scale vortex shedding behind the circular cylinder completely disappeared when the length of the splitter plate was bigger than this critical length ($L/D=1.2$). After this length, inconsiderable changes occur in flow characteristics of the cylinder wake and despite the fact that the flow is unsteady and the variation of the flow characteristics is similar for most of the instantaneous images.

Acknowledgment

The authors would like to thank for the financial support of the Office of Scientific Research Projects of Cukurova University under Contract No. AAP20025.

Nomenclature

D = cylinder diameter
h_L = height of laser sheet from the bed (bottom surface)
h_w = water height
L = splitter plate length
L_s = location of saddle point
Re = Reynolds number
T = splitter plate thickness
U = depth-averaged velocity
u = horizontal component of velocity
v = vertical component of velocity
u' = velocity fluctuation in streamwise direction
v' = velocity fluctuation in transverse direction
$u'v'$ = Reynolds shear stress correlation
$u'u'$ = streamwise Reynolds normal stress
$v'v'$ = transverse Reynolds normal stress
X = streamwise coordinate
Y = transverse coordinate
ψ = streamline topology
ω = vorticity

References

[1] Williamson, C. H. K., 1996, "Vortex Dynamics in the Cylinder Wake," Annu. Rev. Fluid Mech., **28**, pp. 477–526.
[2] Sarpkaya, T., 2004, "A Critical Review of the Intrinsic Nature of Vortex-Induced Vibrations," J. Fluids Struct., **19**(4), pp. 389–447.
[3] Lee, S. J., Lee, S. I., and Park, C. W., 2004, "Reducing the Drag on a Circular Cylinder by Upstream Installation of a Small Control Rod," Fluid Dyn. Res., **34**, pp. 233–250.
[4] Delaunay, Y., and Kaiktsis, L., 1999, "Active Control of Cylinder Wakes: Use of Base Suction and Blowing," *ESAIM, Third International Workshop on Vortex Flows and Related Numerical Methods, Proceedings*, Vol. 7, pp. 104–119.
[5] Hangan, H., and Kim, J., 2003, "Aerodynamic Slot-Control for 2D Square Prisms," J. Wind. Eng. Ind. Aerodyn., **91**, pp. 1847–1857.
[6] Koutmos, P., Papailiou, D., and Bakrozis, A., 2004, "Experimental and Computational Study of Square Cylinder Wakes With Two-Dimensional Injection Into the Base Flow Region," Eur. J. Mech. B/Fluids, **23**, pp. 353–365.
[7] Kwon, S. H., Cho, J. W., Park, J. S., and Choi, H. S., 2002, "The Effects of Drag Reduction by Ribbons Attached to Cylindrical Pipes," Ocean Eng., **29**(15), pp. 1945–1958.
[8] Igarashi, T., 1997, "Drag Reduction of a Square Prism by Flow Control Using a Small Rod," J. Fluids Struct., **69**, pp. 141–153.
[9] Fujisawa, N., and Takeda, G., 2003, "Flow Control Around a Circular Cylinder by Internal Acoustic Excitation," J. Fluids Struct., **17**, pp. 903–913.
[10] Akilli, H., Sahin, B., and Tumen, N. F., 2005, "Suppression of Vortex Shedding of Circular Cylinder in Shallow Water by a Splitter Plate," Flow Meas. Instrum., **16**, pp. 211–219.
[11] Gerrard, H., 1966, "The Mechanics of the Formation Region of Vortices Behind Bluff Bodies," J. Fluid Mech., **25**, pp. 401–413.
[12] Apelt, J., West, G. S., and Szewczyk, A. A., 1973, "The Effects of Wake Splitter Plates on the Flow Past a Circular Cylinder in the Range $104<R<5\times104$," J. Fluid Mech., **61**, pp. 187–198.
[13] Anderson, A., and Szewczyk, A. A., 1997, "Effects of a Splitter Plate on the Near Wake of a Circular Cylinder in 2 and 3-Dimensional Flow Configurations," Exp. Fluids, **23**, pp. 161–174.
[14] Kwon, K., and Choi, H., 1996, "Control of Laminar Vortex Shedding Behind a Circular Cylinder Using Splitter Plates," Phys. Fluids, **8**(2), pp. 479–486.
[15] Prasad, A., and Williamson, C. H. K., 1997, "The Instability of the Shear Layer Separating From a Bluff Body," J. Fluid Mech., **333**, pp. 375–402.
[16] Hwang, J. Y., Yang, K. S., and Sun, S. H., 2003, "Reduction of Flow-Induced Forces on Circular Cylinder Using a Detached Splitter Plate," Phys. Fluids, **15**(8), pp. 2433–2436.
[17] Tiwari, S., Chakraborty, D., Biswas, G., and Panigrahi, P. K., 2005, "Numerical Prediction of Flow and Heat Transfer in a Channel in the Presence of a Built-In Circular Tube With and Without an Integral Wake Splitter," Int. J. Heat Mass Transfer, **48**, pp. 439–453.
[18] Akilli, H., Akar, A., and Karakus, C., 2004, "Flow Characteristics of Circular Cylinders Arranged Side-By-Side in Shallow Water," Flow Meas. Instrum., **15**, pp. 187–197.
[19] Akilli, H., and Rockwell, D., 2002, "Vortex Formation From a Cylinder in Shallow Water," Phys. Fluids, **14**, pp. 2957–2967.
[20] Ingram, R. G., and Chu, V. H., 1987, "Flow Around Island in Rupert Bay: An Investigation of the Bottom Friction Effect," J. Geophys. Res., **92**, pp. 14521–14533.
[21] Chen, D., and Jirka, H., 1995, "Experimental Study of Plane Turbulent Wakes in a Shallow Water Layer," Fluid Dyn. Res., **16**, pp. 11–41.
[22] Lloyd, P. M., Stansby, P. K., and Chen, D., 2001, "Wake Formation Around Islands in Oscillatory Laminar Shallow-Water Flows. Part 1. Experimental Investigation," J. Fluid Mech., **429**, pp. 217–238.
[23] Kahraman, A., Sahin, B., and Rockwell, D., 2002, "Control of Vortex Formation From a Vertical Cylinder in Shallow Water: Effect of Localized Rough-

ness Elements," Exp. Fluids, **33**, pp. 54–65.
[24] Fu, H., and Rockwell, D., 2005, "Shallow Flow Past a Cylinder: Transition Phenomena at Low Reynolds Number," J. Fluid Mech., **540**, pp. 75–97.
[25] Fu, H., and Rockwell, D., 2005, "Shallow Flow Past a Cylinder: Control of the Near Wake," J. Fluid Mech., **539**, pp. 1–24.
[26] Dong, S., Karniadakis, G. E., Ekmekci, A., and Rockwell, D., 2006, "A Combined Direct Numerical Simulation-Particle Image Velocimetry Study of the Turbulent Near Wake," J. Fluid Mech., **569**, pp. 185–207.
[27] Lin, J. C., Yang, Y., and Rockwell, D., 2002, "Flow Past Two Cylinders in Tandem: Instantaneous and Averaged Flow Structure," J. Fluids Struct., **16**, pp. 1059–1071.
[28] Mittal, R., and Balachandar, S., 1995, "Effect of Three-Dimensionality on the Lift and Drag of the Nominally Two-Dimensional Cylinders," Phys. Fluids, **7**, pp. 1841–1865.
[29] Kim, W., Yoo, J. Y., and Sung, J., 2006, "Dynamics of Vortex Lock-On in a Perturbed Cylinder Wake," Phys. Fluids, **18**, 074103.

Effect of Surface Roughness on Single Cryogen Droplet Spreading

Jie Liu
Department of Mechanical Engineering,
University of California,
Riverside, CA 92521
e-mail: liuj@engr.ucr.edu

Walfre Franco
Beckman Laser Institute and Medical Clinic,
University of California, Irvine,
1002 Health Sciences Road East,
Irvine, CA 92612
e-mail: wfranco@uci.edu

Guillermo Aguilar
Department of Mechanical Engineering,
University of California,
Riverside, CA 92521
e-mail: gaguilar@engr.ucr.edu

Cryogen spray cooling is an auxiliary procedure to dermatologic laser surgery, which consists of precooling the superficial skin layer (epidermis) during laser irradiation of subsurface targets to avoid nonspecific epidermal thermal damage. While previous studies have investigated the interaction of cryogen sprays with microscopically smooth human skin models, it is important to recognize that real human skin surface is far from smooth. With the objective to provide physical insight into the interaction between cryogen sprays and human skin, we study the effect of surface roughness on the impact dynamics of single cryogen droplets falling on skin models of various roughnesses (0.5–70 μm). We first develop a theoretical model to predict the maximum spread diameter (D_m) following droplet impingement based on a similarity approximation to the solution of a viscous boundary layer that incorporates friction as the major source of viscous dissipation on a rough surface. Then, we measure the droplet diameter, impact velocity, and D_m of cryogen droplets falling by gravity onto skin models. Experimental data prove that the proposed model predicts D_m with good accuracy, suggesting that the effects of surface roughness and friction on D_m are properly taken into account for the range of surface roughness studied herein. [DOI: 10.1115/1.2903810]

1 Introduction

Dermatological laser surgery is the treatment of choice for vascular lesions (e.g., hemangiomas [1] and port wine stain (PWS) birthmarks [2]) as well as cosmetic surgery (e.g., hair [3] and tattoo [4] removal). In these treatments, cryogen spray cooling (CSC) is an essential auxiliary method that protects the epidermis from excessive thermal damage during laser irradiation, while subdermic targets, such as PWS blood vessels located 100–500 μm below the skin surface [5], are thermally photocoagulated. The only FDA-approved cryogen used thus far for this purpose is Tetrafluoroethane-1,1,1,2 (R134a) [3], with a boiling temperature of −26 °C at atmospheric pressure. Short cryogen spurts (20–100 ms) [6,7] are released from a pressurized container through a spray valve/nozzle system. Well-atomized cryogen droplets with diameters of 3–20 μm [8] and velocities of 10–80 m/s [9,10] impact onto human skin and extract heat as they spread and evaporate.

The efficiency of heat extraction during spray deposition is largely dictated by the dynamics of droplet impact [8]. Ideally, micrometer-size cryogen droplets impact and spread on the skin surface, evaporating and extracting heat. Previous studies [5,11–13] used epoxy resins or Plexiglas substrates as skin models to measure the heat extraction induced by short cryogen spurts. These studies concluded that the thickness of the cryogen layer on the skin surface influences greatly the heat transfer during CSC. The skin models used in these studies were macroscopically smooth; however, the human skin surface is far from smooth. Moreover, human skin roughness varies with age, anatomical location, and environmental factors, such as sun exposure and humidity [14].

In the present study, we first use a simple but realistic experimental scenario where the liquid layer (formed by the coalescence of thousands or millions of droplets) that spreads on the human skin surface is represented and indirectly measured by the maximum spread diameter (D_m) of a single droplet [6]. This scenario allows us to maintain proper scaling while significantly simplifying the more complex spray problem. In this study, we investigate the dynamics of a single droplet impact onto flat rigid surfaces with surface roughnesses (Ra) in the range of 0.5–70 μm, which include those characteristic of human skin: 50–200 μm. Subsequently, we use these experimental results to develop a new semiempirical model to predict D_m without considering evaporation. Finally, we use discrete experimental data to obtain the free parameters required by our model and compare its predictions to those of previous models and to a comprehensive experimental data set.

2 History of Numerical Models

Figure 1 shows a schematic of the droplet geometry before and after the impact on a flat surface and the associated mass and energy conservation equations. Before the impact, the geometry of the droplet is close to a perfect sphere of diameter D moving with velocity V. The total energy of the droplet at this stage E_1 can be expressed as [15]

$$E_1 = (\tfrac{1}{2}\rho V^2)(\tfrac{1}{6}\pi D)^3 + \pi D^2 \sigma_{LV} \tag{1}$$

where the two terms on the right represent the kinetic energy and surface energy of the droplet, respectively.

After the impact, the cryogen droplet spreads along the surface until it reaches the maximum spread diameter D_m. At this stage, the geometry of the cryogen can be modeled as a disk of diameter D_m and thickness h, where $h = 2D^3/3D_m^2$ according to mass conservation. Since the kinetic energy of the droplet reduces to zero at maximum spreading, the total energy of the flattened droplet only consists of the surface energy [15],

$$E_2 = \left(\frac{\pi}{4}D_m^2 + \frac{2}{3}\pi\frac{D^3}{D_m}\right)\sigma_{LV} + \frac{\pi}{4}D_m^2(\sigma_{SL} - \sigma_{SV}) \tag{2}$$

The first term on the right of Eq. (2) represents the surface energy between the liquid and vapor at the top and peripheral areas of the flattened liquid droplet, while the second term represents the sur-

Contributed by the Fluids Engineering Division of ASME for publication in the JOURNAL OF FLUIDS ENGINEERING. Manuscript received April 18, 2006; final manuscript received October 8, 2007; published online April 11, 2008. Assoc. Editor: James A. Liburdy. Paper presented at the 2005 ASME Heat Transfer Summer Conference (HT2005), San Francisco, CA, July 15–22, 2005.

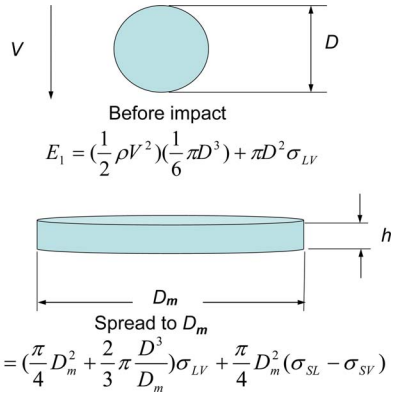

Fig. 1 Sketch of shape and energy of droplet before impact and at maximum spread diameter D_m

face energy of the droplet. The three surface tensions (σ_{LV}, σ_{SL}, and σ_{SV}) are related to each other through the static contact angle θ [16],

$$\sigma_{LV}\cos\theta = \sigma_{SL} - \sigma_{SV} \tag{3}$$

Substituting Eq. (3) into Eq. (2), the total energy at this stage can be rewritten as

$$E_2 = \left[\frac{\pi}{4}D_m^2(1-\cos\theta) + \frac{2}{3}\pi\frac{D^3}{D_m}\right]\sigma_{LV} \tag{4}$$

According to energy conservation, Eq. (1) must be written as

$$\left(\frac{1}{2}\rho V^2\right)\left(\frac{1}{6}\pi D^3\right) + \pi D^2\sigma_{LV} = \left[\frac{\pi}{4}D_m^2(1-\cos\theta) + \frac{2}{3}\pi\frac{D^3}{D_m}\right]\sigma_{LV} + W_{\text{diss}} \tag{5}$$

where W_{diss} is the energy dissipation during the spread process. Several papers have discussed how to evaluate this term. Chandra and Avedisian [15] suggested that W_{diss} could be solved using the following approximation:

$$W_{\text{diss}} = \int_0^{t_c}\int_\Omega \phi\, d\Omega\, dt \approx \phi\Omega t_c \tag{6}$$

where ϕ, the dissipation function, is defined as

$$\phi = \eta\left(\frac{V}{h}\right)^2 \tag{7}$$

where η is the dynamic viscosity and Ω is the liquid droplet volume, which, once the droplet reaches D_m, is defined as

$$\Omega = \tfrac{1}{4}\pi D_m^2 h \tag{8}$$

and t_c is the characteristic time from droplet impact to maximum spread, simply defined as [15]

$$t_c \approx D/V \tag{9}$$

Combining Eqs. (6)–(9) yields

$$W_{\text{diss}} = \tfrac{1}{4}\pi\eta(V/h)DD_m^2 \tag{10}$$

Inserting Eq. (10) into Eq. (5) and applying the definitions of Reynolds and Weber numbers ($\text{Re}=\rho DV/\eta$ and $\text{We}=\rho DV^2/\sigma$, where ρ is the density, D is the droplet diameter, V is the impact velocity, η is cryogen viscosity, and σ is the surface tension), the energy equation becomes

$$\frac{3}{2}\frac{\text{We}}{\text{Re}}\beta^4 + (1-\cos\theta)\beta^2 - \left(\frac{1}{3}\text{We} + 4\right) = 0 \tag{11}$$

where $\beta = D_m/D$ is the normalized maximum spread diameter. To get more accurate results, Pasandideh-Fard et al. [17] considered droplet spreading as an axisymmetric stagnation flow and used it to find W_{diss} as follows. In cylindrical coordinates, the simplified continuity equation becomes

$$\frac{V_r}{r} + \frac{\partial V_r}{\partial r} + \frac{\partial V_z}{\partial z} = 0 \tag{12}$$

and the Navier–Stokes equation in the radial direction (r) becomes

$$\frac{\partial V_r}{\partial t} + V_r\frac{\partial V_r}{\partial r} + V_r\frac{\partial V_z}{\partial z} = -\frac{1}{\rho}\frac{\partial P}{\partial r} + \nu\left[\frac{\partial^2 V_r}{\partial r^2} + \frac{1}{r}\frac{\partial V_r}{\partial r} + \frac{\partial^2 V_r}{\partial z^2} - \frac{V_r}{r^2}\right] \tag{13}$$

For a steady state axisymmetric stagnation flow, the similarity method can be used to find the thickness of the boundary layer δ. This method requires the introduction of a stream function ψ that satisfies the no-slip condition, a similarity variable α, and a similarity function $G'(\alpha)$ defined as

$$\psi = -Br^2 z, \quad \alpha = z\sqrt{\frac{B}{\nu}}, \quad G'(\alpha) = \frac{V_r}{Br} \tag{14}$$

where B is a constant parameter with units of $1/\text{s}$ that must be defined. In terms of ψ, the radial component of the velocity V_r may be expressed as

$$V_r = -\frac{1}{r}\frac{\partial\psi}{\partial z} = Br \tag{15}$$

$G'(\alpha)$ represents a dimensionless velocity, which takes a value of ~ 1 when $\alpha = 2.4$. Thus, the thickness of the boundary layer of an axisymmetric stagnation flow can be obtained [18] using Eq. (14). Pasandideh-Fard et al. [17] proposed the spread velocity V_r to be equal to the impingement velocity V ($V_r = V$) and assumed $B = V/D$. In this case, δ becomes

$$\delta = \frac{2.4D}{\sqrt{\text{Re}}} \tag{16}$$

and ϕ in Eq. (6) becomes

$$\phi \approx \eta\left(\frac{V}{\delta}\right)^2 \tag{17}$$

which differs from Eq. (7) since h is replaced by δ. Another significant difference from the model of Chandra and Avedisian [15] is the definition of t_c, which Pasandideh-Fard et al. defined as

$$t_c = \frac{8}{3}\frac{D}{V} \tag{18}$$

By combining Eqs. (5), (6), and (16)–(18), Pasandideh-Fard et al. obtained

$$4\frac{\text{We}}{\sqrt{\text{Re}}}\beta^3 + 3(1-\cos\theta)\beta^2 - (\text{We}+12) = 0 \tag{19}$$

Mao and Kuhn [19] subsequently modified the above equation according to experimental results and obtained

$$0.2\frac{\text{We}^{0.83}}{\text{Re}^{0.33}}\beta^3 + \frac{1}{4}(1-\cos\theta)\beta^2 - \left(\frac{\text{We}}{12}+1\right)\beta + \frac{2}{3} = 0 \tag{20}$$

In summary, the three models described above assume t_c as a parameter proportional to the ratio of droplet size (D) and impact velocity (V) (Eq. (9) for the Chandra and Avedisian model and Eq. (18) for Pasandideh-Fard et al. and Mao and Kuhn models) and the dissipation function ϕ defined by Eq. (7) to calculate W_{diss}, thus increasing the uncertainty of the prediction. Moreover, while all these models are capable of predicting D_m, they are only applicable to macroscopically smooth surfaces: $\text{Ra} < 5\ \mu\text{m}$, which are far from those of skin ($\text{Ra} = 50-200\ \mu\text{m}$). Previous models do not consider friction during droplet spreading, which is likely to

be a dominant factor for Ra approaching those of skin, i.e., Ra >50 μm. We suggest a new approach to evaluate W_{diss}.

3 Analytical Model

From Eqs. (14) and (15), the shear stress τ between the droplet and the impact surface during spreading can be expressed as

$$\tau = \eta \frac{\partial V_r}{\partial z} = \eta B r G''(0) \sqrt{\frac{B}{\nu}} \tag{21}$$

where B is an undetermined constant and $G''(0)$ represents the wall shear stress, $G''(0)=1.312$ [18]. Assuming axisymmetric radial spreading, the differential friction force F between the droplet and the impact surface can be expressed as

$$dF = \tau dA = \eta B r G''(0) \sqrt{\frac{B}{\nu}} 2r\pi dr \tag{22}$$

The overall energy dissipation W_{diss} due to friction can be expressed as

$$dW_{\text{diss}} = F dr \tag{23}$$

Employing Eq. (22) and integrating both sides of Eq. (23) yields

$$W_{\text{diss}} = \int_0^{D_m/2} \int_0^r \eta B \xi G''(0) \sqrt{\frac{B}{\nu}} 2\pi \xi d\xi dr = \frac{\pi}{96} \eta B G''(0) \sqrt{\frac{B}{\nu}} D_m^4 \tag{24}$$

Inserting W_{diss} into Eq. (5) and rearranging yields

$$\frac{G''(0)}{96} \frac{\text{We}}{\sqrt{\text{Re}}} \beta^5 D^{3/2} V^{-3/2} B^{3/2} + \frac{1}{4}(1-\cos\theta)\beta^3 - \left(\frac{\text{We}}{12}+1\right)\beta + \frac{2}{3} = 0 \tag{25}$$

In Eq. (25), all terms must be dimensionless, which again requires B to have dimensions of $1/\text{s}$. We propose

$$B = C_1 \frac{V}{D} \tag{26}$$

where C_1 is an undetermined constant. This enables the product $D^{3/2}V^{-3/2}B^{3/2}$ within the first term in Eq. (25) to become a constant C. Simplifying Eq. (25),

$$\frac{CG''(0)}{96} \frac{\text{We}}{\sqrt{\text{Re}}} \beta^5 + \frac{1}{4}(1-\cos\theta)\beta^3 - \left(\frac{\text{We}}{12}+1\right)\beta + \frac{2}{3} = 0 \tag{27}$$

4 Experimental Procedures

4.1 Droplet Impact Facilities. A schematic of our experimental setup is shown in Fig. 2. To minimize the evaporation of cryogen droplets during the experiments, the chamber was first pressurized to the saturation pressure of R-134a at room temperature (5.79 bars=84 psi) using cryogen vapor. Then, the pressure was increased slightly to 6.21 bars (90 psi) using pressurized air. After this, the chamber and droplet generator reservoir were cooled to approximately the same temperature ($\sim 5\,^\circ$C). Under these conditions, droplet spreading after the impact can be considered isothermal without evaporation. It took more than 30 s for a droplet to completely evaporate after the impact, which is at least three orders of magnitude higher than the time it takes a droplet to spread after the impact ($\sim$2–8 ms).

The impact surfaces were horizontally mounted at the bottom of the chamber, and transparent windows made of polycarbonate were positioned on the two sides of the chamber to allow for side illumination and imaging. Pressure valves, gauges, and safety instrumentation were mounted on the top cap of the polyvinyl chloride (PVC) chamber.

Falling cryogen droplets were formed at the tip of small nozzles (3), which were attached to a needle valve (12) connected to a small cryogen tank (2) pressurized to (6.48 bars) (94 psi), which is slightly above the chamber's pressure. For a proper comparison and analysis, it is necessary to maintain similarity between the smaller (3–20 μm) and faster (10–80 m/s) cryogen spray droplets and the larger and slower droplets that we generate within the chamber. The average droplet size and velocities of the R134a spurts we have characterized in the past [8,10] lead to ranges in Reynolds numbers (Re) of 200–9000 and Weber numbers (We) of 50–9000. Both of these dimensionless numbers are relevant to the physics of impact and spreading of liquids on solid surfaces [20]. By producing single droplets of R134a of 1.4–2.4 mm in diameter and 0.9–2.4 m/s in impact velocity, Re and We are in the ranges 9200–26,500 and 258–1670, respectively. Note that the use of R134a is not only supported by the initial motivation of this study, but also because the viscosity and surface tension of R134a are about five and ten times lower than those of water, respectively, which allows us to overlap, at least partially, the ranges of Re and We of spray and single droplets.

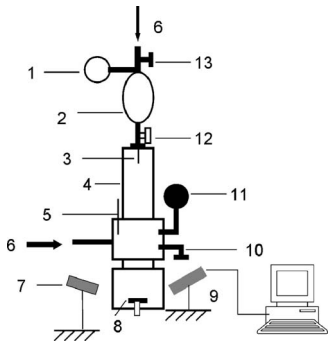

Fig. 2 Experimental facilities for experiments of cryogen droplet impact dynamics without evaporation. 1, pressure gauge; 2, cryogen tank; 3, nozzle; 4, clear PVC tower; 5, temperature sensor; 6, pressured gas; 7, illumination; 8, impact surface; 9, high speed camera; 10, pressure relieve valve; 11, pressure gauge; 12, needle valve; 13, ball valve.

The targeted flat surface was made of a mixture of 3100 epoxy resin and A210 Hardener (RBC Industries, Inc., Warwick, RI) with a ratio of 3:1 in weight. The mixture was poured into a Teflon mold with a presanded bottom that determines the surface roughness (Ra) of the targeted flat surface.

To fully scale the problem from the spray to the single droplet scenario, the surface roughness (Ra)—defined as half the distance between the average peak to valley separation of a rough surface [14]—would also need to be scaled. As mentioned above, Ra varies between 50 μm and 200 μm for human skin depending on the anatomical location, age, and race [14]. This means that the ratio of Ra of skin to a single spray droplet varies between 3 and 66, which would require the Ra of the human skin model to be 4–125 mm. However, Ra=70 μm was set as the upper limit because splashing occurs beyond that roughness, so the continuity of the spread no longer exists.

4.2 Imaging System. A high speed camera (Photron Fastcam PCI 10 K, Itronics, Westlake Village, CA) with a 90 mm zoom lens (V-HQ Macro MC 90 mm $f/2.5$, Elicar, Japan) was used to acquire digital images of single droplet impingement on the skin models. Image sequences were captured at a rate of 2000 frames/s with a pixel resolution of 128×64. Two Fiber-Lite illuminators (Edmund Industrial Optics, Barrington, NJ) were used as light sources, one in front and the other on the back of the chamber. To record droplet impingement dynamics, the camera was positioned at a 30 deg angle with respect to the horizontal level. To clearly record the static contact angle, the camera was also mounted at the same level as the impingement surfaces. The droplet velocity was obtained using the MOTION software (Itronics,

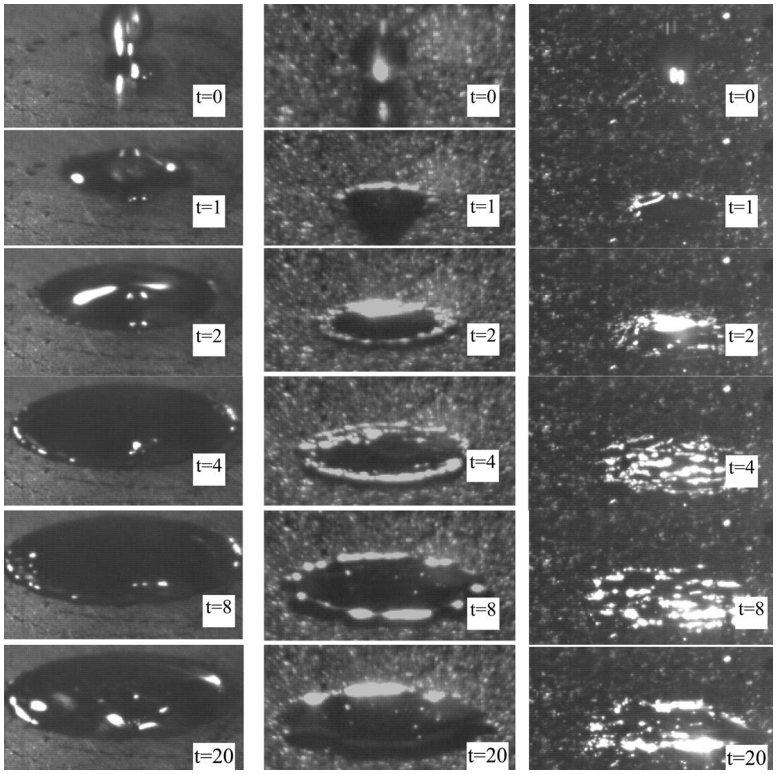

Fig. 3 Droplet with D=1.41 mm and V=0.9 m/s and Re=9200 and We =258 impact onto three surfaces with Ra=0.5 μm (left), Ra=30 μm (middle), and Ra=70 μm (right) for various times in the range of 0–20 ms

Westlake Village, CA) by comparing the same droplet in a series of consecutive frames. The velocity at which droplets break into smaller ones, or the breakup velocity, can be expressed as $V_b = 8\sigma/C_d\rho D$ [21], where C_d is the drag coefficient. It was found that droplet impact velocity was far below the breakup velocity for the droplet sizes studied, which is the regime in which the model is applicable.

5 Results and Analysis

Figure 3 shows the time sequences of cryogen droplets with size D=1.41 mm and V=0.9 m/s impacting on flat surfaces with Ra=0.5 μm, 30 μm, and 70 μm, respectively. The impact process can be divided into four continuous stages [21]. Stage 1: the droplet spreads due to the kinetic energy before impact. Stage 2: the droplet spreads to the maximum diameter D_m and the kinetic energy is zero at this time. Stage 3: the spread droplet begins to retreat due to surface tension. Stage 4: the droplet either statically stays on the surface or rebounds. These four stages can be clearly observed in the surface with Ra=0.5 μm. The near perfect spherical cryogen droplet impinges onto the surface at t=0.0 ms and spreads along the surface until reaching D_m at t=8 ms. The droplet then begins to retreat, but at a much slower pace than it spreads. It takes about 70 ms (not shown) to reach Stage 4 where the droplet stays static at the surface.

For the surface with Ra=30 μm, the impact dynamics exhibit some differences. Once the droplet impinges onto the surface, it spreads as in the previous case, but at the same intervals of t =1 ms, 2 ms, and 4 ms, the spread diameters are smaller than those of the surface with Ra=0.5 μm. Also, the time required for the cryogen to spread to D_m, is the same (8 ms), but after the cryogen reaches its D_m the retreat cannot be observed and the spread stays at almost the same position. For the surface with Ra=70 μm, the impact dynamics are close to those of Ra =30 μm.

Figure 4 shows spread diameter changes over time for different surface roughnesses of Ra=0.5 μm, 4.2 μm, 8.2 μm, 30 μm, 50 μm, and 70 μm. For all surfaces, the time required for the cryogen to spread to D_m was approximately 8 ms. D_m decreases as Ra increases from Ra=0.5–70 μm. The surface with Ra =0.5 μm displays a maximum spread distance D_m=6.31 mm; however, as the surface roughness increases to Ra=50 μm and 70 μm, D_m decreases to 4.9 mm and 4.6 mm, respectively. As pointed out above, once the cryogen spread reaches D_m, it begins to retreat for Ra=0.5 μm, but for other Ra, the spread diameters remain unchanged with time.

Figure 5 shows the spread velocity variation with time for the

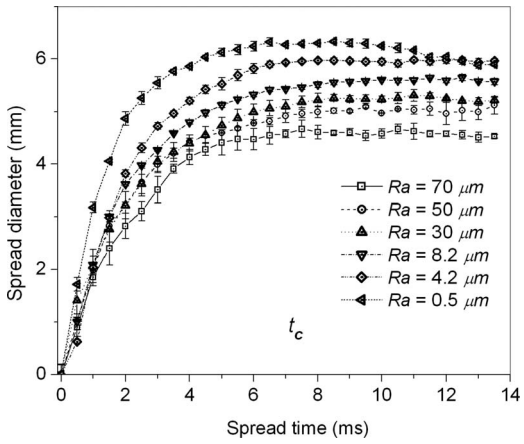

Fig. 4 Spread diameter versus spread time for surface roughnesses of Ra=0.5 μm, 4.2 μm, 8.2 μm, 30 μm, 50 μm, and 70 μm, with droplet with D=1.41 mm and V=0.9 m/s

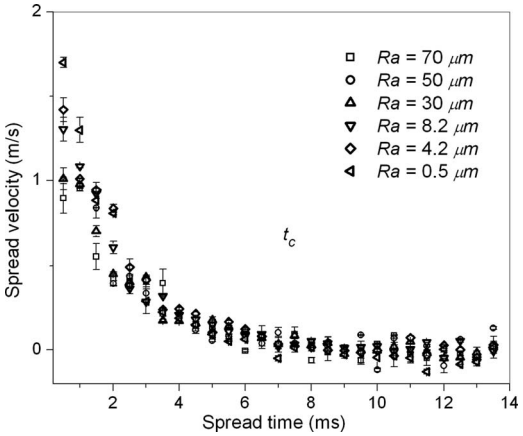

Fig. 5 Spread velocity versus spread time for surface roughnesses of Ra=0.5 μm, 4.2 μm, 8.2 μm, 30 μm, 50 μm, and 70 μm, with droplet with D=1.41 mm and V=0.9 m/s

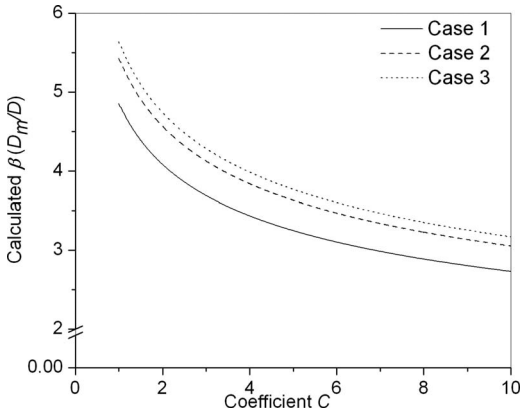

Fig. 6 Prediction of β with undetermined coefficient C in Eq. (27): Case 1: D=1.41 mm and V=0.9 m/s; Re=9200 and We=258. Case 2: D=1.41 mm and V=2.38 m/s; Re=20,000 and We=1210. Case 3: D=1.91 mm and V=2.38 m/s; Re=26,500 and We=1670.

six different surface roughnesses of Ra=0.5 μm, 4.2 μm, 8.2 μm, 30 μm, 50 μm, and 70 μm. For all six surfaces, the spread velocities after the impact quickly decrease within the first 4 ms, time after which the spread velocities slowly reduce to zero after D_m is reached (8 ms). The Ra also has an effect on the initial spread velocities, which are 1.7 m/s, 1.4 m/s, 1.3 m/s, 1.1 m/s, 1.0 m/s, and 0.9 m/s for Ra=0.5 μm, 4.2 μm, 8.2 μm, 30 μm, 50 μm, and 70 μm, respectively.

Two more series of experiments with D=1.91 mm and V=2.38 m/s were performed. Table 1 shows a comparison of the normalized maximum spread diameter (β) for the three sets of experiments. For a droplet with D=1.41 mm impacting a surface with Ra=0.5 μm (Sets 1 and 2), β increases from 4.51 to 5.11 as V changes from 0.9 m/s to 2.38 m/s. For the same V=2.38 m/s (Sets 2 and 3), β also increases from 5.11 to 5.35 as D increases from 1.41 mm to 1.91 mm. Altering Ra to 50 mm and 70 μm results in a similar phenomena: increasing Ra causes a corresponding decrease in β for a given set of Re and We values.

The first term on the left hand side of Eq. (27) is the energy dissipation term, which is the key factor influencing D_m. Figure 6 shows the effect of the undetermined coefficient C, which appears in the first term of Eq. (27) on β. As C increases, β decreases for all three experimental sets, meaning that as the energy dissipation increases, the maximum spread diameter must decrease. These results are also in agreement with previous research [19], which show that as Ra increases, the value of β decreases. Therefore, we used the following steps to associate Ra with the energy dissipation and to determine the value of C in the energy dissipation term of Eq. (27).

Table 1 Three experimental cases and results

Droplet parameters		Surface roughness Ra (μm)	β
Set 1:	Re=9200	0.5	4.51
	We=258	4.2	4.23
	D=1.41 mm	8.2	4.02
	V=0.9 m/s	30	3.74
		50	3.52
		70	3.26
Set 2:	Re=20,000	0.5	5.11
	We=1210	4.2	4.78
	D=1.41 mm	8.2	4.69
	V=2.38 m/s	30	4.1
		50	3.81
		70	3.58
Set 3:	Re=26,500	0.5	5.35
	We=1670	4.2	4.95
	D=1.91 mm	8.2	4.78
	V=2.38 m/s	30	4.4
		50	4.12
		70	3.9

From Eq. (24), the energy dissipation term can be expressed as

$$\frac{W_{\text{diss}}}{\pi D^2\sigma} = \frac{\frac{\pi}{96}\eta B G''(0)\sqrt{\frac{B}{\nu}}D_m^4}{\pi D^2\sigma} \tag{28}$$

Inserting Eq. (26) into Eq. (28) and rearranging in terms of Re and We, we obtain

$$\frac{W_{\text{diss}}}{\pi D^2\sigma} = \frac{CG''(0)}{96}\frac{\text{We}}{\sqrt{\text{Re}}}\beta^4 \tag{29}$$

Considering a perturbation of the energy dissipation term, Eq. (29) can be written as

$$\frac{W_{\text{diss}}}{\pi D^2\sigma} = c\frac{\text{We}}{\sqrt{\text{Re}}}\beta^4(1+\varepsilon) \tag{30}$$

where $c=CG''(0)/96$, and ε is a small perturbation which can be defined as

$$\varepsilon = K_1\left(\frac{\text{Ra}}{D}\right)^{K_2} \tag{31}$$

where K_1 and K_2 are constants that need to be found using experimental results. Inserting Eq. (31) into Eq. (27), we get

$$c\frac{\text{We}}{\sqrt{\text{Re}}}\left(1+K_1\left(\frac{\text{Ra}}{D}\right)^{K_2}\right)\beta^5 + \frac{1}{4}(1-\cos\theta)\beta^3 - \left(\frac{\text{We}}{12}+1\right)\beta + \frac{2}{3} = 0 \tag{32}$$

Note that if Ra=0, Eq. (27) can be recovered.

The coefficients c, K_1, and K_2 of Eq. (32) were adjusted based on our experimental data using an iterative algorithm. Figure 7 shows the flowchart of this algorithm using experimental set 1 as an example. Equation (32) has five solutions for β; however, only the largest real root is considered [15]. By comparing the computed coefficients c, K_1, and K_2 for the three sets using the least squares method, only one set was found, and the resulting equation for the prediction of β is,

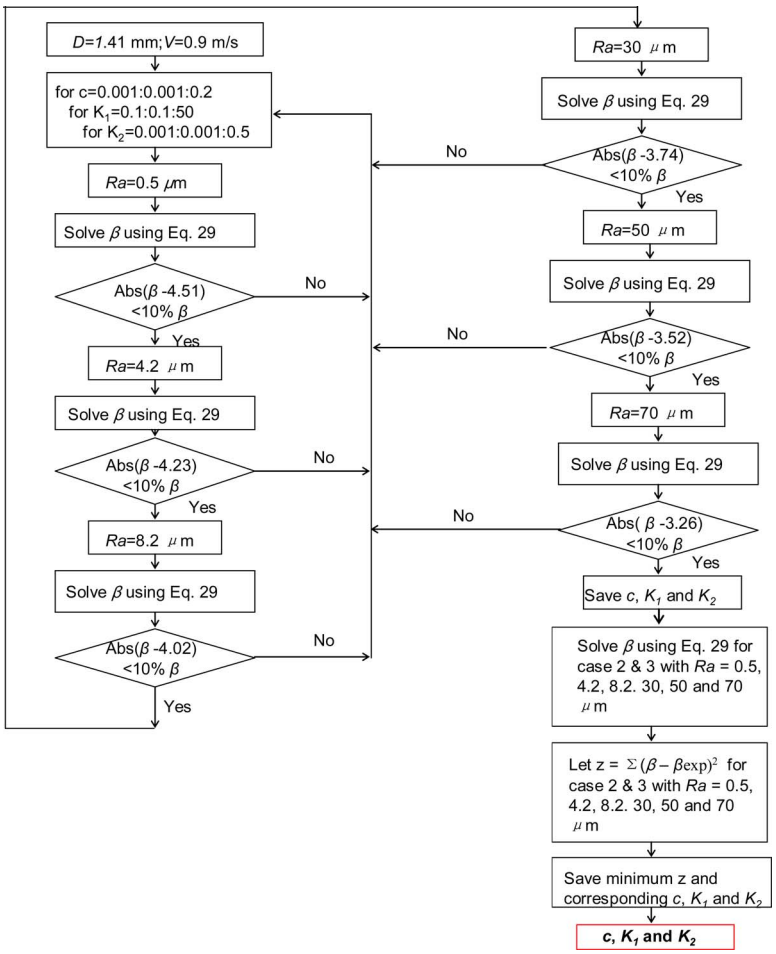

Fig. 7 Flowchart of algorithm to determine the coefficients c, K_1, and K_2 for experiment results

$$0.0018\frac{\mathrm{We}}{\sqrt{\mathrm{Re}}}\left(1+27.3\left(\frac{\mathrm{Ra}}{D}\right)^{0.76}\right)\beta^5+\frac{1}{4}(1-\cos\theta)\beta^3-\left(\frac{\mathrm{We}}{12}+1\right)\beta+\frac{2}{3}=0 \quad (33)$$

To make sure that the common solution set represents all experimental cases reasonably well, Fig. 8 shows a comparison of the experimental data and the predictions by Eq. (33). The uncertainty of the experimental data is described using error bars, while the model predictions are expressed by continuous lines. For all cases, it is apparent that as the surface roughness Ra increases, β decreases, and, as expected, the experimental and numerical results display consistency as the differences between them are less than 10%. To further verify our model, we used two additional Plexiglas surfaces Ra=0.1 m and 4.2 m and recorded the D_m resulting from 16 water droplets impacting under ambient pressure and temperature at ranges of Re=5500–24,000 and We =120–1330 (data not shown). A very good fit was found with confidence values within 10%. Table 2 shows the predicted values of β by the three models developed by other researchers and described above, plus the proposed model and the three sets of our experimental data.

Since the proposed model can be applied to surface roughnesses up to Ra=70 μm, while the other three cannot, Ra was limited to 0.5 μm for this comparison. For Set 1, the experimental results and most model predictions are close. The notable exception is the model of Chandra and Avedisian [15]. For Set 3, the predictions of the proposed model are also close to the experimental results, while the other models overpredict β by at least 20%.

6 Discussion

The cryogen droplet impact monitored over identical time intervals shows that surface roughness affects maximum spread di-

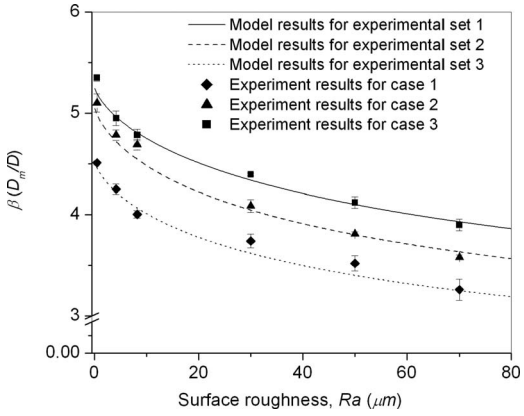

Fig. 8 Experimental and model predicted results of β for three cases: Case 1: D=1.41 mm and V=0.9 m/s; Re=9200 and We =258. Case 2: D=1.41 mm and V=2.38 m/s; Re=20,000 and We=1210. Case 3: D=1.91 mm and V=2.38 m/s; Re=26,500 and We=1670.

Table 2 Comparison of four models using present experimental results for Ra=0.5 μm

	Set 1 D=1.41 mm V=0.9 m/s β	Set 2 D=1.41 mm V=2.38 m/s β	Set 3 D=1.91 mm V=2.38 m/s β
Chandra and Avedisian [15]	6.45	6.95	8.82
Pasandideh-Fard et al. [17]	4.83	5.97	6.43
Mao and Kuhn [19]	4.68	5.42	6.40
Liu et al., proposed model	4.61	5.0	5.20
Experimental data (Eq. (33))	4.51	5.11	5.35

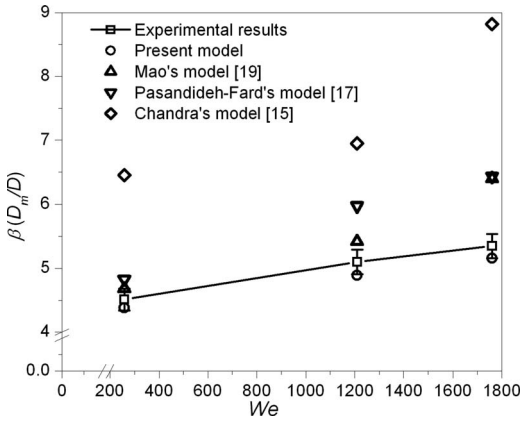

Fig. 9 Comparison of our experimental results with previous models [15,17,19] for the same three cases described in Table 2 with Ra=0.5 μm

ameters (D_m). As Ra increases, D_m dramatically reduces, as seen in Figs. 3 and 4. This phenomenon can be best explained through principles of energy conservation: during the spread process, the larger the Ra, the larger the portion of energy consumed by friction between the cryogen droplet and impact surface. In Fig. 3, all droplets have the same D=1.41 mm and V=0.9 m/s. It follows that the kinetic energies prior to impact are the same. The energy dissipation during the spread process is greater for Ra=30 μm than for Ra=0.5 μm. The energy lost influences the maximum spread diameter D_m. The droplet that dissipates more energy has less D_m. Therefore, for droplets with identical D and V values, increasing Ra of the impact surface will reduce D_m (or β).

Ra also affects the behavior after the liquid spreads to D_m. For the occurrence of the retreat phenomena, the surface energy should be large enough to overcome the energy consumed during the retreat process. Figure 3 shows pictures from spread to retreat after impact. It is obvious that the retreat phenomenon only occurs for Ra=0.5 μm, but for Ra=30 μm and 70 μm, this retreat phenomenon cannot be observed because the surface energy is not enough to overcome the energy lost by friction during the spreading and is also insufficient to coalesce the droplet after D_m has been reached. Therefore, for surfaces with Ra=50 μm and 70 μm, the cryogen droplet cannot retreat after spreading to D_m.

Also in Fig. 3, the geometries of the cryogen droplet spreads are different for various Ra. For Ra=0.5 μm, the droplet remains together during impact, spreads, and retreats. However, for Ra =30 μm and 70 μm, the droplet is separated into several parts after spreading to D_m. This shows that increasing Ra can assist in breaking up liquid cryogen droplets. Because the resulting surface energy of a spread cryogen droplet is not enough to hold the cryogen together, the droplet breaks into several parts after reaching D_m and cannot retreat.

An important feature of the proposed model is that it directly associates Ra with energy dissipation during the spread process without the need to define θ. In previous models designed to predict D_m, however, θ had to be measured for different Ra, although in all cases, Ra was limited to <5 μm. From Fig. 3, it is clear that for Ra=30 μm and 70 μm, the measurement of θ becomes quite difficult because of the irregularity of the surface roughness, resulting in loss of accuracy. However, the average value of θ for the different surfaces used in this study is the same: θ=15 deg, so only this constant value was used in our model. The effects of Ra on θ are subsequently and implicitly included in the first term of Eq. (33) because θ is a constant value for the same surface.

Figure 5 shows that the spread velocity is also affected by Ra. The energy dissipation can also explain why the initial spread velocity changes with Ra. For droplets with the same size and impact velocity, the spread velocity should be the same without consideration of wall friction. For Ra=0.5 μm, the spread velocity after 0.5 ms is 1.7 m/s, but for Ra=70 μm, this value is only 0.9 m/s. This means that the energy dissipation caused by friction is much less for Ra=0.5 μm than for Ra=70 μm during the first 0.5 ms after the impact. After t=4.0 ms, the spread velocities are almost the same for all Ra, suggesting that most of the energy dissipation occurs during the first half of the spread process.

Our results support the concept of a constant characteristic time t_c, representing the time from impact to maximum spread D_m. In previous models, this time was defined as D/V [15] or $\frac{8}{3}$ D/V [17,19] and was used to find the energy dissipation (W_{diss}). While our proposed model does not need an explicit definition of t_c, we can observe from our experimental results that t_c is essentially equal to 8.0 ms (Figs. 4 and 5), while the definitions of D/V and $\frac{8}{3}$ D/V result in shorter times (e.g., 0.8 and 2.1, respectively, for set 3), which would underestimate W_{diss} according to our model.

It is also noteworthy that while t_c might be a constant, the spread velocity and, consequently, the instantaneous W_{diss} are not. Figure 5 shows that the spread velocity shortly after the impact and up to about 4.0 ms is significantly higher for the smooth surfaces, but its rate of decrease is larger. After 4.0 ms, the spread velocity is the same for all surfaces. That is, the larger Ra is, the more significant the loss of kinetic energy is for the thin-spreading layer that exists during the first 4.0 ms, and, consequently, the velocity drop in that initial period is large relative to the one after 4.0 ms (Fig. 5). Since the energy dissipation after 4.0 ms is less, the spread velocity remains nearly constant and below 0.2 m/s, independent of Ra. Note that the spread velocities for all Ra are close to zero after 8.0 ms when the spread reaches the maximum value (D_m).

Figure 9 shows the comparison of β computed by the four models for Ra=0.5 μm as a function of We. For We=258 (minimum value), all model predictions are close to the experimental results, except for We=1680 (maximum value), where the error of some other models can be as large as twofold. Therefore, it appears that models that do not consider friction loss during the spread process may be accurate for predicting D_m for small droplets at low impact velocity (low Re and We), but lose accuracy for large droplets with high impact velocity (high Re and We).

Figure 10 shows the comparison of experimental results from four other sources according to Table 3 with the predicted β by the proposed model. Note that the present model is more accurate for droplets with higher impact velocity. For the experimental results of Prunet-Foch et al. [22], the droplets have the same impact velocity V=3.5 m/s, but with different surface roughness. The errors between the calculated β using the present model and the experimental data are only 5%.

For the experimental results of Mao and Kuhn [19], the proposed model is reliable for $V>1.86$ m/s but loses its accuracy for $V<1$ m/s. This can also be observed using the experimental results of Rioboo et al. [23]. With V=3.6 m/s, the errors between measured and calculated β are 10%. However, with an impact

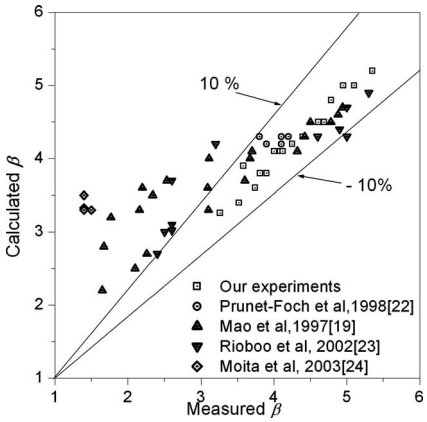

Fig. 10 Comparison of the β using the present model with experimental data from current and previous works [20,22–24]

velocity of 1.18 m/s, the error increases. For Moita and Moreira [24] experiments, the proposed model cannot predict the correct results for droplets with $V=0.44$ m/s.

In summary, increasing the droplet velocity or Ra makes friction effects on D_m more prominent. The spread velocity increases with increasing droplet impact velocity [21], but the effect of Ra is more prominent as the spread velocity increases. Therefore, the proposed model is more accurate, predicting D_m for droplets with large impact velocities (1.86–3.72 m/s) impinging on surfaces with a wide range of roughnesses (0.5–70 μm).

One of the most significant advantages of the presented model is that the effect of Ra on D_m is directly and explicitly associated with the surface roughness. Thus, the errors caused by estimating t_c could be reduced. Even though the scales between CSC of human skin and our experimental setup are not comparable, our study shows how droplet spread varies as a function of Ra and the effect of Ra on spread dynamics. In addition, we used our experimental results to build on the existing models of maximum spread by accounting for surface roughness during energy dissipation. To the best of our knowledge, this is the first study that considers surface roughness as a free parameter. Knowing the effect of surface roughness on liquid spread may enable engineers to appropriately modify either liquid or substrate properties to enhance many applications, e.g., addition of surfactants to sprays, peeling of the stratum corneum for improved skin cooling, or moisturizer penetration.

Table 3 Comparison of calculated β using our proposed model with experimental results from previous works

Diameter (mm)	Velocity (m/s)	Re	We	Ra (μm)	θ	Measured β	Calculated β		Ref.
2.7	3.5	9000	960	0.5	40	4.2	4.4	○	[22]
2.7	3.5	9000	960	2	15	3.9	4.1	○	[22]
2.7	3.5	9000	960	5	30	3.7	3.9	○	[22]
2.7	3.5	9000	960	0.5	55	4.1	4	○	[22]
2.7	3.5	9000	960	2	35	3.8	4.1	○	[22]
2.7	0.55	1485	12	5	97	1.65	2.2	△	[19]
2.7	0.82	2214	25	5	97	2.1	2.6	△	[19]
2.7	1	2700	37	5	97	2.26	2.8	△	[19]
2.7	1.58	4266	92	5	97	3.1	3.2	△	[19]
2.7	1.86	5022	127	5	97	3.6	3.5	△	[19]
2.7	2.77	7480	282	5	97	4.32	3.8	△	[19]
2.7	3.72	10,044	509	5	97	4.78	4.3	△	[19]
2.7	0.55	1485	12	0.5	67	1.67	2.8	△	[19]
2.7	0.82	2214	25	0.5	67	2.16	3.3	△	[19]
2.7	1	2700	37	0.5	67	2.34	3.5	△	[19]
2.7	1.58	4266	92	0.5	67	3.09	3.6	△	[19]
2.7	1.86	5022	127	0.5	67	3.67	4.1	△	[19]
2.7	2.77	7480	282	0.5	67	4.42	4.4	△	[19]
2.7	3.72	10,044	509	0.5	67	4.88	4.6	△	[19]
2.7	0.55	1485	12	0.2	37	1.77	3.2	△	[19]
2.7	0.82	2214	25	0.2	37	2.2	3.6	△	[19]
2.7	1	2700	37	0.2	37	2.53	3.7	△	[19]
2.7	1.58	4266	92	0.2	37	3.11	4	△	[19]
2.7	1.86	5022	127	0.2	37	3.7	4.1	△	[19]
2.7	2.77	7480	282	0.2	37	4.5	4.7	△	[19]
2.7	3.72	10,044	509	0.2	37	4.94	4.9	△	[19]
3.04	1.18	3587	58	0.003	10	3.2	5.1	△	[19]
3.17	3.6	11,412	563	0.003	10	5.3	5.7	▽	[23]
3.03	1.18	3587	58	3.6	78	2.6	3.7	▽	[23]
3.17	3.6	11,412	563	3.6	78	4.6	4.3	▽	[23]
3.03	1.18	3587	52	0.4	105	2.4	2.7	▽	[23]
3.17	3.6	11,412	563	0.4	105	5	4.7	▽	[23]
3	1.18	3587	57	25.6	105	2.5	2.7	▽	[23]
3.17	3.6	11,412	563	25.6	105	4.9	4.2	▽	[23]
2.65	1.22	3233	54	6.2	100	2.6	3.02	▽	[23]
3.42	3.62	12,380	614	6.2	100	5	4.3	▽	[23]
2.65	1.22	3233	54	6.2	90	2.6	3.1	▽	[23]
3.52	3.62	12,380	614	6.2	90	5.1	4.3	▽	[23]
3.2	0.44	1408	452	2	85	1.4	3.5	◇	[24]
3.2	0.44	1408	452	2.7	85	1.4	3.33	◇	[24]
3.2	0.44	1408	452	1.52	71	1.5	3.3	◇	[24]
3.2	0.44	1408	452	3	86	1.4	3.3	◇	[24]

7 Conclusion

Both the experimental and modeling results demonstrate that the surface roughness Ra affects the cryogen impact and spreading dynamics. For a droplet with the same size and velocity, the smaller the impact surface roughness Ra, the larger the spread diameter D_m. For impact surfaces with Ra greater than 30 μm, the cryogen retreat phenomenon cannot be observed. The proposed model appears to predict D_m for surfaces with large Ra, like human skin, better than previous models because it considers the effect of friction loss due to surface roughness and reduces the uncertainty of defining a spread time t_c. The comparison of the experimental and modeling results demonstrates the accuracy of this model to predict the maximum spread diameter (D_m) of droplet impingement onto surfaces with a large range of surface roughnesses (Ra).

Acknowledgment

This work has been supported in part by a NIH grant (K01-42057) and the UCR Academic Senate Grant No. 05-06. The authors also thank Dr. Wangcun Jia at the University of California, Irvine for helpful discussions.

Nomenclature

C_d = drag coefficient
D = droplet diameter (mm)
D_m = maximum spread diameter (mm)
g = gravity (m s^2)
G = similarity function
h = thickness of flattened cryogen at maximum spread diameter (mm)
r = radius of cryogen spread (mm)
Ra = surface roughness (μm)
Re = Reynolds number ($\rho VD/\eta$)
t = time (ms)
t_c = characteristic spread time (ms)
T = temperature (°C)
T_{sat} = saturation temperature of cryogen at 1 bar (°C)
V = droplet velocity (m/s)
V_b = droplet breakup velocity (m/s)
V_r = velocity along the radial direction (m/s)
V_Z = velocity along the vertical direction (m/s)
W_{diss} = energy dissipated during cryogen spread (m s)
We = Weber number ($D\rho V^2/\sigma$)

Greek Symbol

α = similarity variable
β = D_m/D (ratio of the maximum spread diameter over the droplet diameter)
δ = boundary layer thickness (mm)
η = dynamic viscosity (N s/m^2)
ϕ = dissipation function (N/m s)
ν = kinetic viscosity (m^2/s)
θ = static wetting angle (deg)
ρ = density [kg/m^3]
σ = surface tension (N/m)
σ_{LV} = surface tension between liquid and vapor (N/m)
σ_{SL} = surface tension between liquid and solid surface (N/m)
σ_{SV} = surface tension between vapor and solid surface (N/m)
τ = shear stress (N/m^2)
ψ = stream function

References

[1] Kelly, K. M., Nelson, J. S., Lask, G. P., Geronemus, R. G., and Bernstein, L. J., 1999, "Cryogen Spray Cooling in Combination With Nonablative Laser Treatment of Facial Rhytides," Arch. Dermatol., **135**(6), pp. 691–694.
[2] Nelson, J. S., Milner, T. E., Anvari, B., Tanenbaum, B. S., Kimel, S., Svaasand, L. O., and Jacques, S. L., 1995, "Dynamic Epidermal Cooling During Pulse-Laser Treatment of Port-Wine Stain: A New Methodology With Preliminary Clinical Evaluation," Arch. Dermatol., **131**(6), pp. 695–700.
[3] Goldman, M. P., and Fitzpatrick, R. E., 1999, *Cutaneous Laser Surgery*, Mosby, Chicago.
[4] Nelson, J. S., Milner, T. E., Anvari, B., Tanenbaum, B. S., Kimel, S., Svaasand, L. O., and Jacques, S. L., 1991, "Selective Photothermolysis and Removal of Cutaneous Vasculopthies and Tattoos by Pulsed Laser," Plast. Reconstr. Surg., **88**(4), pp. 723–731.
[5] Anvari, B., Milner, T. E., Tanenbaum, B. S., Kimel, S., Svaasand, L. O., and Nelson, J. S., 1995, "Dynamic Epidermal Cooling in Conjunction With Laser Treatment of Port-Wine Stains: Theoretical and Preliminary Clinical Evaluations," Lasers Med. Sci., **10**(2), pp. 105–112.
[6] Aguilar, G., Majaron, B., Pope, K., Svaasand, L. O., Lavernia, E. J., and Nelson, J. S., 2001, "Influence of Nozzle-to-Skin Distance in Cryogen Spray Cooling for Dermatologic Laser Surgery," Lasers Surg. Med., **28**(2), pp. 113–120.
[7] Aguilar, G., Vu, H., and Nelson, J. S., 2004, "Influence of Angle Between the Nozzle and Skin Surface on the Heat Flux and Overall Heat Extraction During Cryogen Spray Cooling," Phys. Med. Biol., **49**(10), pp. N147–N153.
[8] Aguilar, G., Majaron, B., Verkruysse, W., Zhou, Y., Nelson, J. S., and Lavernia, E. J., 2001, "Theoretical and Experimental Analysis of Droplet Diameter, Temperature, and Evaporation Rate Evolution in Cryogenic Sprays," Int. J. Heat Mass Transfer, **44**, pp. 3201–3211.
[9] Aguilar, G., Majaron, B., Karapetian, E., Lavernia, E. J., and Nelson, J. S., 2003, "Experimental Study of Cryogen Spray Properties for Application in Dermatologic Laser Surgery," IEEE Trans. Biomed. Eng., **50**(7), pp. 863–869.
[10] Franco, W., Vu, H., Jia, W., Nelson, J. S., and Aguilar, G., 2007, "Fluid and Thermal Dynamics of Cryogen Sprays Impinging on a Human Tissue Phantom," ASME J. Biomech. Eng., accepted for publication.
[11] Aguilar, G., Wang, G. X., and Nelson, J. S., 2003, "Dynamic Behavior of Cryogen Spray Cooling: Effects of Spurt Duration and Spray Distance," Lasers Surg. Med., **32**(2), pp. 152–159.
[12] Gasljevic, K., Aguilar, G., and Matthys, E. F., 2001, "On Two Distinct Types of Drag-Reducing Fluids, Diameter Scaling, and Turbulent Profiles," J. Non-Newtonian Fluid Mech., **96**(3), pp. 405–425.
[13] Tunnell, J. W., Torres, J. H., and Anvari, B., 2002, "Methodology for Estimation of Time-Dependent Surface Heat Flux Due to Cryogen Spray Cooling," Ann. Biomed. Eng., **30**(1), pp. 19–33.
[14] Manuskiatti, W., Schwindt, D. A., and Maibach, H. I., 1998, "Influence of Age, Anatomic Site and Race on Skin Roughness and Scaliness," Dermatology (Basel, Switz.), **196**(4), pp. 401–407.
[15] Chandra, S., and Avedisian, C. T., 1991, "On the Collision of a Droplet With a Solid-Surface," Proc. R. Soc. London, Ser. A, **432**(1884), pp. 13–41.
[16] Frohn, A., and Roth, N., 2000, *Dynamics of Droplets*, Springer, New York.
[17] Pasandideh-Fard, M., Qiao, Y. M., Chandra, S., and Mostaghimi, J., 1996, "Capillary Effects During Droplet Impact on a Solid Surface," Phys. Fluids, **8**(3), pp. 650–659.
[18] White, F. M., 1991, *Viscous Fluid Flow*, McGraw Hill, New York.
[19] Mao, T., and Kuhn, D., 1997, "Spread and Rebound of Liquid Droplets Upon Impact on Flat Surfaces," AIChE J., **43**(9), pp. 2169–2179.
[20] Lavernia, E. J., and Wu, Y., 1996, *Spray Atomization and Deposition*, Wiley, New York.
[21] Rein, M., 1993, "Phenomena of Liquid Drop Impact on Solid and Liquid Surface," Fluid Dyn. Res., **12**(2), pp. 61–93.
[22] Prunet-Foch, B., Legay, F., Vignes-Adler, M., and Delmotte, C., 1998, "Impacting Emulsion Drop on a Steel Plate: Influence of the Solid Substrate," J. Colloid Interface Sci., **199**(2), pp. 151–168.
[23] Rioboo, R., Marengo, M., and Tropea, C., 2002, "Time Evolution of Liquid Drop Impact Onto Solid, Dry Surfaces," Exp. Fluids, **33**(1), pp. 112–124.
[24] Moita, A., and Moreira, A., 2003, "Influence of Surface Properties on Dyanmic Behavior of Impacting Droplet," *Ninth International Conference on Liquid Atomization and Spray System*, Sorrento, Italy.

A Model of Piston Sliding Process for a Double Piston-Actuated Shock Tube

I. da S. Rêgo
e-mail: rego@aees.kyushu-u.ac.jp

T. Ando

K. Misumi

T. Miyazaki

S. Nishiyori

Interdisciplinary Graduate School of Engineering Sciences,
Kyushu University,
6-1 Kasuga Koen,
Fukuoka 816-8580, Japan

K. N. Sato
e-mail: satcho@triam.kyushu-u.ac.jp

M. Sakamoto

S. Kawasaki

Research Institute for Applied Mechanics,
Kyushu University,
6-1 Kasuga Koen,
Fukuoka 816-8580, Japan

A double piston-actuated structure designed for replacing the use of diaphragms in conventional shock tubes has been recently developed. In order to clarify the piston sliding process for this structure, a simplified model based on the motion equation of its main sliding piston has been developed. Calculated piston sliding time against pressure ratio has been numerically obtained and indirectly evaluated by examining the experimental curves of the performance of the diaphragmless structure.
[DOI: 10.1115/1.2903521]

1 Introduction

A newly designed double piston-actuated structure [1,2], which is a variation of the design reported by Oguchi et al. [3], has been developed for diaphragms that are usually employed to separate the high- and low-pressure sections in conventional shock tubes. This has been highly motivated by the fact that, in general, the use of rupturing diaphragms results in (a) an uncontrollable amount of impurities inside the shock tube, (b) a relatively low reproducibility of shock conditions, and (c) very costly and time-consuming tasks of replacing the ruptured diaphragm after each and every shot.

In order to clarify the piston sliding process for the double piston-actuated structure, a simplified model based on the motion equation of its main sliding piston has been developed. Such a model allows the piston sliding time to be estimated. The piston sliding time is of importance mainly because it may influence the distance where the shock wave will be formed downstream and the characteristics of the shock wave itself [4,5].

2 Diaphragmless Structure and Modeling

Such a diaphragmless structure is shown in Fig. 1. The scheme for generating normal shock waves through this diaphragmless structure is as follows: (i) High-pressure nitrogen gas (N_2) is supplied to the actuating-gas chamber, which contains both the main sliding piston and the auxiliary sliding piston (with a low conductance pinhole in its base) made of high-density plastic material; (ii) As the inside of the chamber is filled, the pistons slide forward. The main piston shuts a passage between the driver-gas chamber and the shock tube; (iii) Since the pressure of the driver gas (P_4) introduced into its chamber is slightly lower than that in the actuating-gas chamber, the driver gas is then sealed in its chamber with the main piston; (iv) By rapidly purging N_2 gas from the rear of the auxiliary piston via a fast-opening valve, the auxiliary piston is quickly actuated backward due to a pressure imbalance across its base. This allows the rest of the N_2 gas to escape massively through various high-conductance orifices on the piston tube open to the ambient air; (v) Because of this, the main piston backs rapidly driven by P_4, opening that passage for the driver gas, which discharges into the shock tube.

The equation of motion of the main sliding piston is formulated next. The main piston experiences a driving force F_d due to the pressure differential across the piston base and a friction force F_f in the opposite direction due to the compression force on two piston rings (for simplicity, F_f is negligible). Thus, the net force or resultant force F_n on the main piston is estimated as

$$F_n(t) \simeq A_b P_4(t) - A_b[P_r(t) - fP_1] \tag{1}$$

where A_b is the base area of the main piston (the actual A_b is about 0.02 m^2), $P_4(t)$ is the driver-gas pressure, which drops rapidly over time (immediately after the beginning of the sliding process of the main piston), f is about 0.41 (percentage of A_b pressed by P_1), P_1 is the driven-gas pressure (ranging from 0.1 kPa to 2.7 kPa), $P_r(t)$ is the pressure at the rear of the main piston, i.e., the pressure of N_2 gas in the actuating-gas chamber, which decreases rapidly over time (immediately after the auxiliary piston starts being actuated backward). Thus, the net acceleration of the main piston is

$$a_n(t) \simeq F_n(t)/m_p \tag{2}$$

where m_p is the mass of the main piston (the actual m_p is about 1.5 kg). To obtain an adequate net acceleration to simulate the motion of the main piston, $P_4(t)$ and $P_r(t)$ need to be determined. For simplicity, both drop adiabatically as N_2 gas rapidly exhausts out and helium gas (used as the driver gas) discharges into the shock tube. Thus, the drop in pressure of the driver gas is

$$P_4(t) \simeq P_4(0)\left\{\frac{1}{1 + t\dfrac{\pi d_p \Delta z}{V_4(0)}\sqrt{\dfrac{2[P_4(0) - P_1]}{\rho_4}}}\right\}^{\gamma_4} \tag{3}$$

where $\pi d_p \Delta z$ is an increasing lateral area (d_p=0.127 m is the actual minor piston diameter and Δz corresponds to the increasing stroke distance whose maximum is about 0.04 m, as shown in Fig. 1), $P_4(0)$ is the initial pressure of the driver gas in its chamber (before actuating the main piston), and ρ_4=0.16 kg/m^3 and γ_4 =1.66 are the density and adiabatic index for He gas, respectively

Contributed by the Fluids Engineering Division of ASME for publication in the JOURNAL OF FLUIDS ENGINEERING. Manuscript received July 5, 2007; final manuscript received October 8, 2007; published online April 1, 2008. Assoc. Editor: Phillip M. Ligrani.

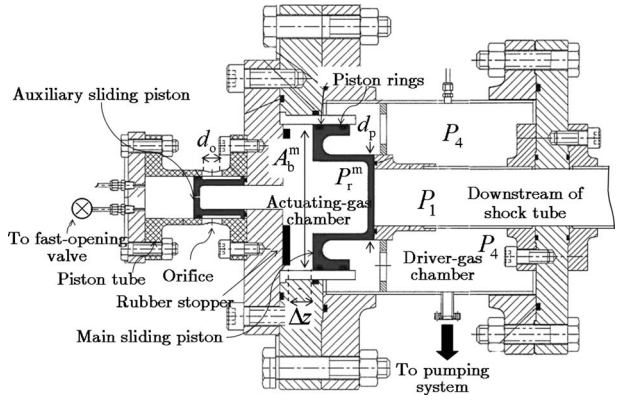

Fig. 1 Scale drawing of the double piston-actuated structure

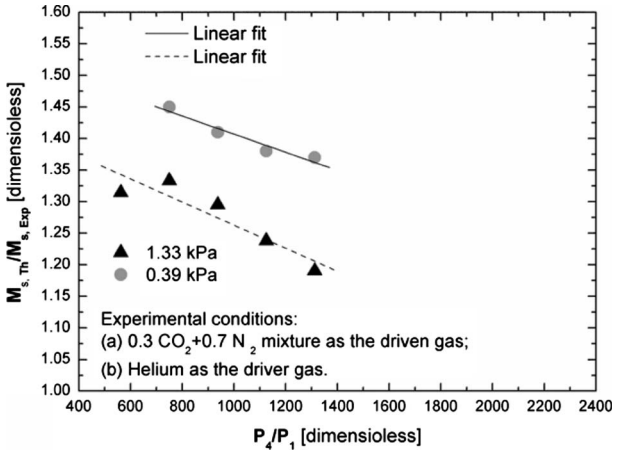

Fig. 3 Variation of $M_{s,\text{theor}}/M_{s,\text{expt}}$ with P_4/P_1. Shock waves in the 0.3 CO_2+0.7 N_2 mixture using He as the driver gas and N_2 as the actuating gas, taking P_1 as a parameter.

at normal temperature and pressure. The velocity of flowing gas is calculated by means of the Bernoulli equation under assumptions of incompressible flow, horizontal streamline, and large chamber and is held constant over the piston sliding process for simplicity.

The drop in pressure of N_2 gas at the rear of the main piston can be similarly estimated by counting that N_2 gas flows out across a total area given by the area of four high-conductance orifices (πd_o^2, where d_o=0.033 m is the diameter of the orifice) immediately after the auxiliary sliding piston is actuated backward, the initial volume occupied by N_2 gas in the chamber is $V_r(0)$, N_2 gas exhausts against ambient air at P_{atm}, and the density (ρ_{act}) and the adiabatic index (γ_{act}) for N_2 gas at normal temperature and pressure are 1.16 kg/m^3 and 1.404, respectively. Thus, the drop in pressure of N_2 at the rear of the main piston is

$$P_r(t) \simeq P_r(0)\left\{\frac{1}{1+t\dfrac{\pi d_o^2}{V_r(0)}\sqrt{\dfrac{2[P_r(0)-P_{\text{atm}}]}{\rho_{\text{act}}}}}\right\}^{\gamma_{\text{act}}} \quad (4)$$

Finally, the desired net acceleration of the main sliding piston is obtained by combining Eqs. (1) and (2) with Eqs. (3) and (4), which results in a second-order ordinary differential equation involving functions that depend only on t. The solutions (stroke distance covered at a certain time instant t) for them were computed under the initial conditions of z=0 and dz/dt=0 at t=0. Figure 2 shows the calculated values of the total sliding time of the piston required to cover a fixed stroke distance of $\Delta z/2$ (i.e., 50% of the passage opened) against the pressure ratio (P_4/P_1), taking P_1 as a parameter. In general, the piston sliding time (roughly one order of magnitude higher than that of the diaphragm opening time) shortened as P_4/P_1 increased. This numerical trend suggests that the pressure of the driver gas may simultaneously drive the incident shock wave downstream of the shock tube and the main piston upstream of the shock tube. This was indirectly evaluated by confirming the experimental decrease of the ratio of the theoretical to experimental values of the incident-shock Mach number ($M_{s,\text{theor}}/M_{s,\text{expt}}$) with increasing values of P_4/P_1, as shown in Fig. 3. Note that the values of $M_{s,\text{theor}}/M_{s,\text{expt}}$ are always higher than 1. This is probably due to variations of properties of the driven gas with rise in temperature behind the incident shock, friction forces that attenuates the flow near the inside wall of the tube, and noninstantaneous piston sliding times. However, the decrease in $M_{s,\text{theor}}/M_{s,\text{expt}}$ as P_4/P_1 increases has to do with shorter opening times and means that data approach theory, where the opening time is considered as instantaneous. Experimentally, this decrease was observed and has been attributed to the fact that at higher P_4, the piston sliding motion was faster and, consequently, the piston sliding time shortened, as numerically suggested in Fig. 2. This may be the experimental evidence that confirms that P_4 drives not only the incident shock wave downstream of the shock tube but also the main piston in the opposite direction. Direct measurements of piston sliding time were not performed yet because of constraints on instrumentation access.

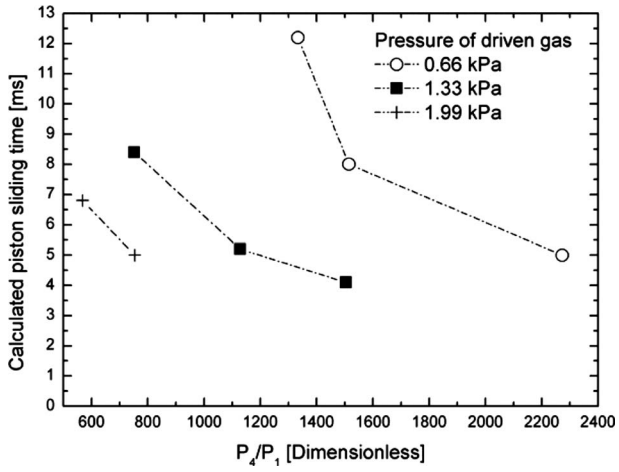

Fig. 2 Calculated piston sliding time against pressure ratio, taking the pressure of the driven gas as a parameter

3 Conclusions

In short, a newly designed double piston-actuated structure has been developed for diaphragms in conventional shock tubes. A simplified model based on the motion equation of its main sliding piston has been developed. It was numerically found that the pressure of the driver gas drives simultaneously the incident shock wave downstream of the shock tube and the main sliding piston upstream in the opposite direction. This numerical finding was indirectly supported by confirming the experimental decrease of the ratio of the theoretical to experimental values of the incident-shock Mach number with increasing values of pressure ratio. Direct measurements of piston sliding time still need to be performed.

Acknowledgment

This research is sponsored by the Ministry of Education, Culture, Sports, Science, and Technology (MEXT).

References

[1] Sato, K. N., Kawasaki, S., Kugimiya, S., Nourgostar, S., Aoki, T., and TRIAM Exp. Group, 2005, "Development of a New Non-Diaphragm Type Shock Tube for High Density Plasmas," *Proceedings of the 32nd EPS Conference on Plasma Physics*, Tarragona, Vol. 29C, p. 5.128.

[2] da S. Rêgo, I., Sato, K. N., Kugimiya, S., Aoki, T., Miyoshi, Y., Ando, T., Goto, K., and Sakamoto, M., 2007, "Development of a Large Diameter Diaphragmless Shock Tube for Gas-Dynamic Laser Studies," Mater. Sci. Forum, **566**, pp. 9–13.

[3] Oguchi, H., Funabiki, K., and Sato, S., 1975, "An Experiment on Interaction of Shock Wave With Multiple-Orifice Plate by Means of a Snap-Action Shock Tube," *Proceedings of the Tenth International Shock Tube Symposium*, Kyoto, Vol. 35, p. 386.

[4] Ikui, T., Matsuo, K., and Yamamoto, Y., 1979, "Fast-Acting Valves for Use in Shock Tubes (Part, 2, Formation of Shock Waves)," Bull. JSME, **22**(167), pp. 693–699.

[5] White, D. R., 1958, "Influence of Diaphragm Opening Time on Shock-Tube Flows," J. Fluid Mech., **4**, pp. 585–599.